

**Convection in an African Easterly Wave
over West Africa and the Eastern Atlantic:
a Model Case Study of Hurricane Helene (2006)
and its Interaction with the Saharan Air Layer**

Zur Erlangung des akademischen Grades eines
DOKTORS DER NATURWISSENSCHAFTEN
von der Fakultät für Physik des
Karlsruher Instituts für Technologie (KIT)

genehmigte

DISSERTATION

von

Dipl.-Met. Juliane Schwendike
aus Brodowin

Tag der mündlichen Prüfung:	30.04.2010
Referent:	Prof. Dr. S. C. Jones
Korreferent:	Prof. Dr. K. D. Beheng

Abstract

Convective systems embedded in an African Easterly wave (AEW) over West Africa and the eastern Atlantic in September 2006 are investigated. AEWs are wave-like disturbances propagating along the midlevel African easterly jet (AEJ). The study is based on COSMO (COntortium for Small scale MOdelling) model runs with a horizontal resolution of 2.8 km. Over land, the developing, mature and decaying phases of a mesoscale convective system can be clearly distinguished. This is not the case over the ocean, where the convection is characterised by the development and decay of short-lived systems. There are significant differences between the structure of convection over land and water. The convective cores, in which the updraught speed, the heating rate and the vertical velocity attain maximal values, and which are collocated with regions of high positive relative vorticity, are upright over water, but tilted over land. Over land, the atmosphere is drier at midlevels and the shear is stronger leading to stronger downdrafts and, hence, to the development of a distinct cold pool. No cold pool is detected for the convective systems over the ocean. Due to their smaller size and smaller motion the convection is harder to sustain. Although the environment is favourable, only a sequence of smaller, short-lived convective systems develops over the ocean whereas long-lived MCSs form over land. The influence of the convective systems on their environment is assessed by means of potential temperature and relative vorticity budgets for regions encompassing the convective systems. During the convective system's life-cycle, the relative vorticity increases at the height of the African easterly jet over land due to the eddy flux term (i.e. the horizontal advection of perturbation absolute vorticity) whereas the relative vorticity maximum over the ocean moves downwards with time due to stretching. The low-level circulation that develops as a positive low-level vorticity anomaly associated with the westward extension of the Saharan heat low, moves over the Atlantic and southwestwards. In addition, positive vorticity associated with the low-level monsoon flow contributes to this circulation. The

cyclogenesis of Hurricane Helene is initiated when the mid-level vorticity anomaly of the AEW moves over the low-level circulation, initiating convection and enhancing the low-level vorticity through vortex stretching.

The tropical cyclogenesis of Helene was accompanied by several marked dust outbreaks. Thus, the second part of this study investigates the transport of mineral dust and the impact of the dust-radiation feedback for the AEW out of which Hurricane Helene (2006) developed. We use the model system COSMO-ART (Aerosols and Reactive Trace gases) in which the dust emission and dust transport as well as the radiation feedback are taken into account. The low-level positive vorticity anomaly described above associated with the westward extension of the Saharan heat low over West Africa leads to high wind speeds near the surface and, thus, to the emission of significant amounts of mineral dust. Dust is also emitted by the gust fronts of the convective systems over land, due to orographical effects at the Algerian Mountains, Atlas Mountains and the Hoggar, as well as by the Atlantic Inflow, and at the interface between the hot and dry Harmattan and the moist and cool monsoon flow. The dust is lifted up and transported over the Atlantic in the Saharan Air Layer (SAL). The mineral dust is both lifted up into the AEW trough and transported westwards, and advected at lower levels by the monsoon flow into the centre of the low-level monsoon circulation. At low-levels the dust laden air moves to the north and northwest of the convective system that develops into a tropical depression, and is present in the vicinity of the storm during the whole genesis period of Helene. The dust concentrations are relatively high within the centre of the developing tropical cyclone also. The influence of the dust-radiation interaction on the processes leading to the formation of Helene is investigated using two COSMO-ART model runs with a horizontal resolution of 28 km. In the first run the dust-radiation interaction is taken into account, in the second run it is not. In the run including the dust-radiation interaction the low-level monsoon trough is enhanced. Additionally, the low-level circulation, and hence, the tropical depression as well as the tropical storm out of which Hurricane Helene developed were stronger in this model run. The position of the storm in both model runs differed by about 2° , where the storm in the run without the dust-radiation interaction was located further to the southwest. Thus in this case taking the dust-radiation interaction into account facilitated the development of a tropical cyclone.

Zusammenfassung

Im ersten Teil dieser Arbeit wurden konvektive Systeme über Westafrika und dem östlichen Atlantik im September 2006 untersucht, die in so genannte afrikanische östliche Wellen (engl. African Easterly Waves, AEWs) eingelagert sind. AEWs sind wellenartige Störungen, die entlang des afrikanischen östlichen Strahlstroms (engl. African Easterly Jet, AEJ) propagieren. Die Arbeit basiert auf COSMO (COntortium for Small scale MOdelling) Modellläufen mit einer horizontalen Auflösung von 2.8 km. Über Land waren die Entwicklungs-, die Reife- und die Zerfallsphase von mesoskaligen konvektiven Systemen klar zu erkennen. Über dem Ozean war dies nicht der Fall, da hier die Konvektion durch die Entwicklung und den Zerfall von kurzlebigen Systemen charakterisiert war. Die Struktur der konvektiven Systeme über Land und über Wasser unterschied sich deutlich. Die konvektiven Kerne, in denen die Geschwindigkeit des Aufwindes, die Heizraten und die positive Vorticity maximale Werte erreichten, waren über dem Wasser aufrecht, über dem Land jedoch geneigt. Die mittlere Atmosphäre über Land war trockener als über Wasser und die Scherung war stärker was zu stärkeren Abwinden und damit zu einem deutlich ausgebildeten Kaltluftsee (engl. Cold Pool) führte. Über Wasser konnte kein Kaltluftsee beobachtet werden. Aufgrund der geringeren Größe und der kleineren Geschwindigkeit der konvektiven Systeme über Wasser war es schwieriger die Konvektion aufrechtzuerhalten. Obwohl die Umgebungsbedingungen günstig waren, entstanden über Wasser nur kleine, kurzlebige konvektive Systeme und über Land langlebige mesoskalige konvektive Systeme. Der Einfluß der konvektiven Systeme auf ihre Umgebung und umgekehrt wurde mit Hilfe von Haushaltsrechnungen der potentiellen Temperatur und der relativen Vorticity für Regionen, die das konvektive System umgaben, untersucht. Während des Lebenszyklusses des untersuchten konvektiven Systems über Land nahm die relative Vorticity auf der Höhe des AEJs aufgrund des Eddyflußterms, d.h. der horizontalen Advektion von absoluter Vorticity, zu. Das Maximum der relativen Vorticity über dem Ozean verlagerte sich

hingegen aufgrund von Wirbelstreckung mit der Zeit weiter nach unten. Die bodennahe Zirkulation über dem Atlantik, die sich aus einer positiven bodennahen Vorticityanomalie entwickelte, die mit der westlichen Ausdehnung des Sahara Hitzetiefes verbunden war, lieferte einen wichtigen Beitrag zur Auslösung der Zyklognese von Helene. Die positive Vorticity der bodennahen Monsunströmung verstärkte die bodennahe Zirkulation zusätzlich. Die Zyklognese von Hurrikan Helene begann, als sich die positive Vorticityanomalie der AEW in der mittleren Atmosphäre über die bodennahen Zirkulation bewegte. Von diesem Zeitpunkt an wurde Konvektion ausgelöst und die bodennahe Vorticity wurde durch Wirbelstreckung verstärkt.

Während der tropische Zyklognese von Helene kam es zu einigen starken Staubausschüben. Daher wurde im zweiten Teil der Arbeit der Transport von Mineralstaub und der Einfluss der Staub-Strahlungs-Wechselwirkung auf die AEW, aus der sich Hurrikan Helene entwickelte, untersucht. Dazu wurde das Modellsystem COSMO-ART (Aerosols and Reactive Trace gases) verwendet, in dem die Emission und der Transport des Staubs, sowie der Einfluß auf die Strahlung berücksichtigt sind. Die oben beschriebene bodennahe Vorticityanomalie, die mit der Ausweitung des Sahara Hitzetiefes über Westafrika nach Westen verbunden war, führte zu hohen Windgeschwindigkeiten in Bodennähe und somit zur Emission von erheblichen Mengen an Mineralstaub. Staub wurde ebenfalls emittiert durch die Böenfronten der konvektiven Systeme über Land, durch orographische Effekte am Atlasgebirge und dem Hoggar, sowie durch den so genannten "Atlantic Inflow", und an der Grenze zwischen dem heißen und trockenen Harmattan (Nordostpassat) und der feuchten und relativ kühlen Monsunströmung. Der Staub wurde angehoben und mit dem so genannten Saharan Air Layer (SAL) über den Atlantik transportiert. Darüberhinaus gelangte der Staub zum einen durch Hebung in den Trog der AEW und zum anderen wurde er mit der bodennahen Monsunströmung nach Nordwesten und in das Zentrum des Monsuntrogs transportiert. Während der gesamten Entstehungsperiode von Helene traten relativ hohe Staubkonzentrationen im Norden und Nordwesten des Sturms auf. Auch im Zentrum der sich entwickelnden tropischen Zyklone waren die Staubkonzentrationen relativ hoch.

Der Einfluß der Staub-Strahlungs-Wechselwirkung auf die Prozesse, die zur Bildung von Helene führten, wurden mit Hilfe zweier COSMO-ART Modellläufe untersucht, die mit

einer horizontalen Auflösung von 28 km durchgeführt wurden. Im ersten Lauf wurde die Strahlungswechselwirkung berücksichtigt, im zweiten war sie nicht enthalten. Im Modelllauf mit Strahlungswechselwirkung war der bodennahe Monsuntrog stärker ausgeprägt. Darüber hinaus zeigte dieser Lauf eine stärker entwickelte bodennahe Zirkulation, und sowohl die tropische Depression als auch der tropische Sturm, aus dem sich Hurrikan Helene entwickelte, waren stärker. Die Lage des Sturmzentrums unterschied sich in den beiden Modellläufen um ungefähr 2° , wobei die Berücksichtigung der Strahlungs-Wechselwirkung eine Verschiebung nach Nordosten bewirkte. In diesem Fall begünstigte die Berücksichtigung der Strahlungswechselwirkung des Mineralstaubs also die Bildung eines tropischen Wirbelsturms.

Contents

Abstract	ii
Zusammenfassung	v
1 Introduction	1
2 West African Monsoon System	5
2.1 African Easterly Jet (AEJ)	8
2.2 African Easterly Waves (AEWs)	10
2.3 Mesoscale Convective Systems (MCSs)	12
2.4 Tropical Cyclogenesis	21
2.4.1 “Bottom–Up” Cyclogenesis	22
2.4.2 “Top–Down” Cyclogenesis	23
2.5 Saharan Air Layer (SAL)	25
2.5.1 Dust Sources and Emission over West Africa	25
2.5.2 Characteristics of the SAL	28
2.5.3 Impact of the SAL on Tropical Cyclones	31
3 COSMO Model, Configurations and Diagnostics	35
3.1 COSMO	35
3.1.1 Basic Equations	36
3.1.2 Numerical Solution	38
3.1.3 Parametrisation	39
3.1.4 Initial- and Boundary Conditions	40
3.2 Code Adaption for Budget Calculations	41
3.2.1 Relative Vorticity Budgets	45

3.2.2	Potential Vorticity Budgets	47
3.3	COSMO-ART	49
3.3.1	Transport of Mineral Dust in COSMO-ART	50
3.3.2	Radiation in COSMO-ART	51
3.4	Trajectory Calculations	53
4	Convective Systems over West Africa and the eastern Atlantic	55
4.1	Synoptic Situation and COSMO simulations	58
4.1.1	Synoptic Situation	58
4.1.2	COSMO Simulations	62
4.1.3	Methodology for Budget Calculations	70
4.2	Convective Systems over West Africa and the Atlantic	72
4.2.1	Structural Features	73
4.2.2	Potential Temperature Budget	85
4.2.3	Vorticity Budget	92
4.3	Summary and Discussion	112
5	The Saharan Air Layer and Hurricane Helene (2006)	115
5.1	Synoptic Situation and the pre-Helene system	115
5.1.1	Model Setup and Observations	117
5.1.2	Dust Emission and Transport over West Africa	119
5.1.3	Comparison with Observational Data	127
5.2	The Impact of the Dust-Radiation Feedback	144
5.3	Summary and Discussion	149
6	Summary and Conclusions	155
	Symbols	165
	Abbreviations	170
	Bibliography	188

1

Introduction

West Africa is one of the most drought–threatened and food–insecure regions in the world. An improvement of the forecast of precipitation in West Africa is crucial for the vulnerable rainfall–dependent economies and the growing population. As mesoscale convective systems (MCSs) contribute to about 80% to the annual rainfall (Eldridge, 1957; Omotosho, 2003; Laurent et al., 1998; Mathon et al., 2002; Fink et al., 2006), they play a key role in the water cycle of West Africa. Mesoscale convective systems which consist of several thunderstorms, cover an area with a horizontal extent of up to several hundreds of kilometres (Maddox, 1980). They are embedded in African easterly waves (AEWs), which are wave–like disturbances propagating along the midlevel African easterly jet. Over the ocean, AEWs are the main precursors for Atlantic and East Pacific tropical cyclones (Avila and Pasch, 1992). The embedded mesoscale convective systems act as seed disturbances for the development of tropical cyclones.

Each year tropical cyclones cause a considerable amount of damage due to their destructive winds, heavy precipitation, storm surge, wind waves, and swell. In the United States alone, landfalling tropical cyclones cause an average damage of US\$ 5 billion to property every year (Willoughby and Rahn, 2004). In 1992, Hurricane Andrew caused damage on the order of US\$ 25 billion. As the cyclone–prone coasts are growing more populated, it is vital to analyse these storms in as much detail as possible to improve the ability to forecast them.

Significant amounts of mineral dust are emitted in the Sahara and transported westwards across the Atlantic. The effect of the mineral dust on AEWs, MCSs and tropical cyclones is yet not fully understood. The dust might act to strengthen or weaken tropical cyclones. It is important to improve the knowledge about the tropical cyclone and dust interaction to better forecast them. The present study investigates the AEW–MCS interaction and the effect of the mineral dust on the tropical cyclogenesis.

There are still many unanswered questions concerning the interaction between AEWs and MCSs. On the one hand, previous studies found that MCSs are important in the initiation of AEWs (Hodges and Thorncroft, 1997; Hill and Lin, 2003; Lin et al., 2005; Berry et al., 2007). On the other hand, the AEW troughs provide a favourable environment for the development of new MCSs. The manner in which the MCSs embedded in the AEW influence the AEW itself has been addressed only recently by very few studies.

From satellite images it can be seen, that the convection over land takes the form of MCSs which move across West Africa. A number of MCSs may develop and decay within an AEW over the continent. Over the ocean, the convection has the form of large convective bursts. The organised convection within the AEW may develop into a tropical cyclone.

When an AEW moves out over the ocean the characteristics of convection may change. Recent studies of tropical cyclogenesis have emphasised the role that might be played by individual intense convective cores in the pre–tropical–depression phase (Hendricks et al., 2004; Montgomery et al., 2006). The merger of these individual vorticity anomalies or vortical hot towers may be an integral part of tropical cyclogenesis, although the precise route by which this occurs is still under investigation (Ritchie and Holland, 1997; Montgomery et al., 2006).

A systematic study of the various interactions that can take place between AEJ, AEW, MCSs, and tropical cyclones is beyond the scope of this study. Instead we focus on one case and investigate the interaction between AEW and MCSs for the AEW out of which Hurricane Helene (2006) developed. We contrast the different nature and evolution of MCSs over West Africa and the eastern Atlantic in one AEW to gain a better understanding of the interaction between the processes on the synoptic and the convective scale. Such differences have been investigated in previous studies. The novel aspect of

our study is the direct comparison of convection over land and water within the same easterly wave and using the same model and diagnostic tools. We examine the net impact of convection on its environment as a first step towards investigating the role of the convection in modifying the AEW. In particular, we can carry out a direct comparison of the budgets of various quantities. We analyse the potential temperature and relative vorticity budgets for different parts of the convective systems.

The second part of this thesis analyses the influence of the mineral dust on the tropical cyclogenesis of Hurricane Helene (2006). North Africa is the largest source of mineral dust (Engelstaedter and Washington, 2007), which has a significant influence on the earth's radiation budget (Haywood et al., 2003). Dust aerosol plumes emanating from this region are the most wide spread, persistent and dense (Prospero et al., 2002). The dust is emitted from the desert regions and transported into the atmosphere (Karyampudi and Carlson, 1988; Karyampudi and Pierce, 2002). These processes are highly variable in time and space with an annual peak during summer (Prospero et al., 2002; Engelstaedter and Washington, 2007). The Saharan air layer (SAL) consists of the well-mixed layer above the Saharan desert reaching from the surface up to about 500 hPa, and the elevated Saharan planetary boundary layer which is located at the height of the AEJ with the monsoon flow underneath it and the free atmosphere aloft. It is characterised by a significant amount of mineral dust aerosols, relatively dry and warm air. The SAL, which conserves the thermodynamic structure of the Saharan planetary boundary layer, can be transported across the Atlantic and into the Caribbean (Carlson and Prospero, 1972).

The interactions of the SAL with AEWs, MCSs, and its influence on the genesis of tropical cyclones is not yet fully understood and is a topic of ongoing research. Some studies state that the SAL has a negative effect on tropical cyclones by inhibiting the formation, or reducing the intensity of tropical cyclones (Dunion and Velden, 2004; Carlson and Benjamin, 1980; Wong and Dessler, 2005; Lau and Kim, 2007). Other studies found a positive impact (e.g. Shu and Wu, 2009). Several investigations even claim that the effect of the Saharan dust is rather weak (Braun and Shie, 2008). Most of the previous studies are based on satellite data whereas only very few studies use numerical models to analyse the effect of the SAL.

In the present study we investigate the emission and the transport of mineral dust from West Africa to the Atlantic during the pre-Hurricane Helene phase¹. We consider how the SAL modifies the environment of the developing tropical depression. For this purpose the model system COSMO-ART (COnsortium for Small scale MOdelling-Aerosols and Reactive Trace gases) is used to perform model runs with and without the dust-radiation feedback.

The study is arranged as follows. An overview of the West African monsoon systems and tropical cyclogenesis is given in chapter 2. The numerical model, the configurations and the diagnostics are introduced in chapter 3. In chapter 4, the synoptic situation for our case study is introduced and the model-based methodology presented. The evolution of convection over West Africa and the eastern Atlantic is compared. Potential temperature and relative vorticity budgets are used to quantify the differences. The emission and the transport of the mineral dust, during the period analysed in this study, are described in chapter 5. The effect of the SAL on the environmental condition for the convective system over water are investigated. A summary and conclusions are provided in chapter 6.

The present study was conducted in the scope of the African Monsoon Multidisciplinary Analyses (AMMA) project (Redelsperger et al., 2006). The AMMA project aims to advance the knowledge about the West African monsoon system to improve the numerical weather prediction. A large measurement campaign was conducted between May and September 2006 to increase the number of observations in this usually data sparse region.

¹We are not aware of any published studies in which mineral dust transport and dust-radiation feedback is modelled explicitly for a real case of Atlantic tropical cyclogenesis.

2

West African Monsoon System

The West African monsoon (WAM), an annually varying and thermally direct circulation, is the dominant atmospheric system which controls the weather over West Africa. The region affected by the WAM extends from the Guinean coast in the south to the southern edge of the Sahara at 20°N and from Cap Verde in the west to the Ethiopian highlands in the east. The WAM is determined by the interaction between its subsystems, namely the African easterly jet (AEJ), its perturbations, the African easterly waves (AEWs), the Saharan air layer (SAL), the northeasterly Harmattan, as well as by the low level monsoon flow and mesoscale convective systems (MCSs) (Fig. 2.1).

The West African monsoon results from the differential heating of the land and ocean surface in tropical North Africa, caused by the different heat capacities of land and water. During boreal summer the zone of maximum surface heating is shifted northwards following the intertropical convergence zone (ITCZ), which is the zone where strongest insolation occurs. The ITCZ reaches its northernmost position in August at about 11°N and moves back to the equator in the northern hemisphere winter. The strong insolation at the ITCZ leads to a convective-driven circulation in which hot moist air ascends at the ITCZ, and forms deep convection, resulting in a low-level near-equatorial trough. In the upper troposphere the air moves polewards and partly subsides in the subtropics, where the subtropical anticyclones form. At mid- and low-levels the air flows back to the ITCZ. These convective circulations are named Hadley cells (Hadley, 1735). The Coriolis force superposes the meridional flow with a zonal component. Poleward flow is linked with a

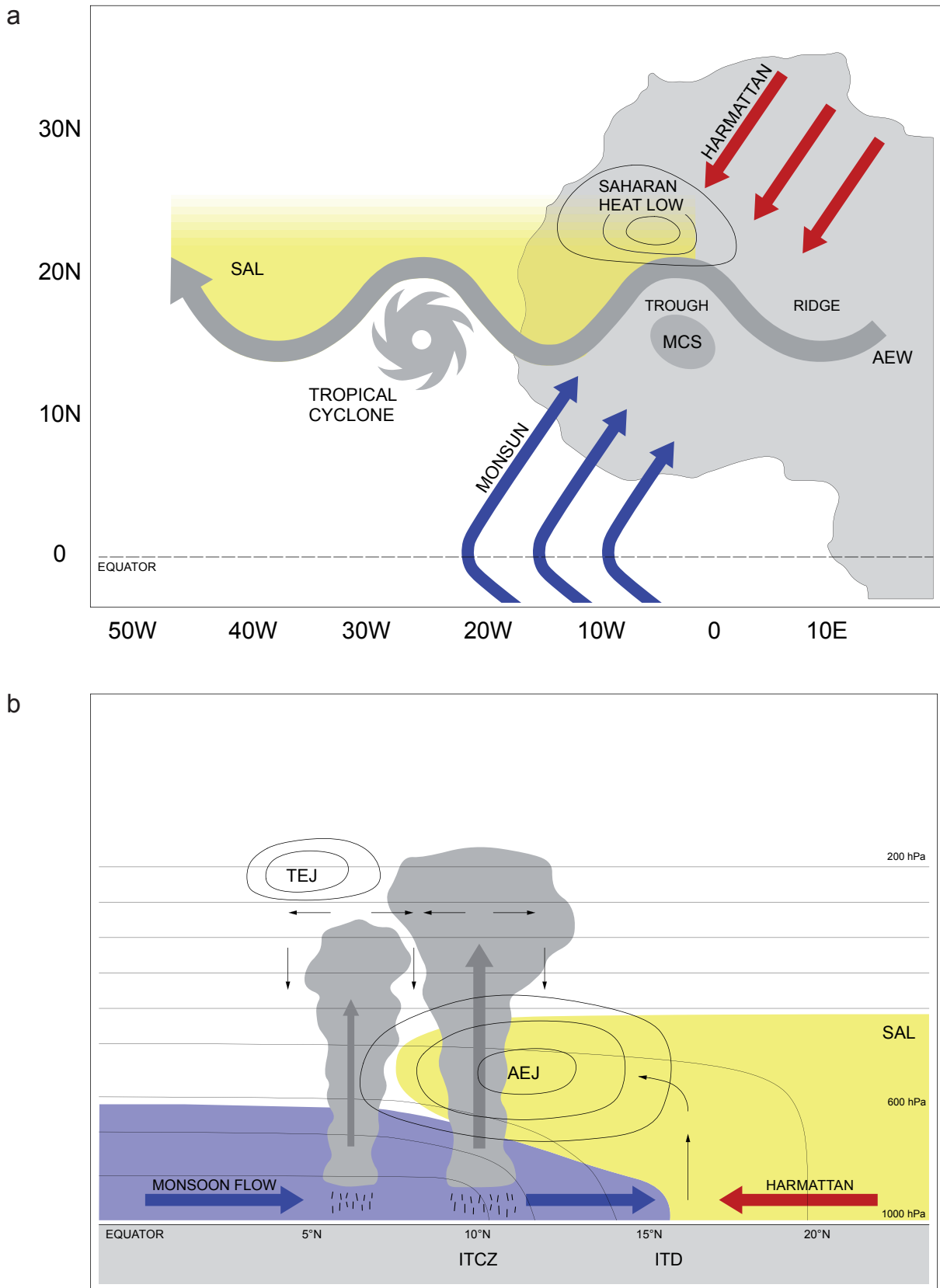


Figure 2.1: The main weather systems in West Africa and the Eastern Atlantic during boreal summer in (a) a horizontal plane and (b) in a north–south cross section. The thin contours in (b) display the potential temperature isotherms with relatively cool temperatures in the monsoon flow and warm temperatures at upper levels. Adapted from Mohr and Thorncroft (2006).

westerly component, equatorward flow with an easterly component. Thus the low-level equatorward winds become the north–eastern and south–eastern so–called trade winds (Fig. 2.1a). In boreal summer when the ITCZ is located north of the equator the south–easterly trade winds cross the equator and become southwesterlies under the influence of the Coriolis force. The northeasterly trade winds are often referred to as the Harmattan and the southwesterly trade winds as the monsoon flow. As the temperatures over the ocean are lower than over land, the monsoon flow penetrating West Africa is relatively cool and moist. In the ITCZ the northern and southern branches converge and deep moist convection occurs. The ITCZ moves between the tropic of Cancer and Capricorn following the largest insolation, but it lags it by about 4 to 6 weeks. It leads to the summer monsoon regime in West Africa that brings precipitation into this region, and the winter monsoon, that is characterised by dry conditions as the Harmattan is the dominant flow pattern in West Africa. The monsoon onset in West Africa is marked by an abrupt shift of the ITCZ from a quasi–stationary location at 5°N in May and June to 10°N in July and August (Janicot and Sultan, 2006).

The Inter Tropical Discontinuity (ITD) which is often also referred to as the Inter Tropical Front (ITF), marks a sharp density gradient resulting from the temperature and humidity differences in the Harmattan and monsoon layer. The ITD is also the convergence zone between the moist and cool monsoon flow and the dry and hot Harmattan. It can be detected in the low–level wind field and by dew–point temperatures less than 14°C (Buckle, 1996). It is best defined during the night when no turbulent mixing in the planetary boundary layer (PBL) occurs and the monsoon flow progresses northward. This leads to the existence of a sharp density gradient across the monsoon–Harmattan interface. During the day, the turbulence in the PBL tends to mix the opposing flows, i.e., the southwesterly monsoon flow and the northeasterly Harmattan flow. Hence, the density gradient across the monsoon–Harmattan interface decreases. As a result, the ITD moves further south. The ITD is located at about 20°N between July and August, which is about 10° north of the ITCZ, where the deep convection occurs (Fig. 2.1b).

The tropical easterly jet (TEJ) (Fig. 2.1b) occurs in the upper troposphere at about 200 hPa and 7°N over west Africa. The TEJ is the result of the increasing geopotential

gradient at the southern fringe of the upper-level anticyclone over the Sahara, and partly due to the outflow of the deep moist convection (Fink, 2006).

The Saharan heat low (SHL) (Fig. 2.1a,b) is a shallow low-pressure system covering major parts of the Sahara desert. It extends vertically from the surface up to about 700 hPa. Above, strong subsidence due to the northern branch of the Hadley cell occurs. The main heat source over the Sahara is the dry convective heating and the adiabatic compression due to the descending air in the Hadley cell.

The AEJ is characterised by an easterly wind maximum at mid levels resulting from baroclinity between the relatively cool monsoon air in the south and the hot air over the Sahara (Fig. 2.1a). The AEJ is maintained by two diabatically forced meridional circulations: one associated with surface fluxes and dry convection in the Saharan heat-low region and one associated with deep moist convection in the ITCZ equatorward of this (Thorncroft and Blackburn, 1999). The AEWs are wave-like disturbances propagating along the jet. Over the ocean, AEWs are the main precursor for Atlantic and East Pacific tropical cyclones (Avila and Pasch, 1992; Landsea, 1993).

Mesoscale convective systems are deep, organised thunderstorms with a horizontal extent of several hundreds of kilometres. They are embedded within the AEWs (Fig. 2.1a) and modulate the West African rainfall significantly (Omotosho, 2003; Mathon and Laurent, 2001). In the African Sahelian (12°N–18°N) and Sudanian climate zone (9°N–11°N) convective systems contribute to about 80–90% and about 50%, respectively, to the annual rainfall (Eldridge, 1957; Omotosho, 2003; Laurent et al., 1998; Mathon et al., 2002; Fink et al., 2006). The WAM system's components will be explained in detail in the following.

2.1 African Easterly Jet (AEJ)

The African easterly jet (AEJ) is a mid-tropospheric jet with a typical wind speed of about 10–15 m s^{-1} (Burpee, 1974; Parker et al., 2005b; Fink, 2006) (Fig. 2.1b). It occurs between 10–15°N and at a height of about 600–700 hPa (Burpee, 1972; Reed et al., 1977; Thorncroft and Blackburn, 1999; Nicholson and Grist, 2003). The AEJ fulfils the necessary conditions for barotropic–baroclinic instability (Charney and Stern, 1962). The vertical

shear along the AEJ helps to organise moist convection and to generate MCSs (e.g. Houze and Betts, 1981).

Three distinct layers occur in the AEJ region (Parker et al., 2005b). The monsoon layer is located near the surface and is characterised by moist and relatively cool air from the Gulf of Guinea, extending into the Sahel and decreasing in depth towards the north (Fig. 2.1b). Within the monsoon layer, a diurnally-varying boundary layer develops. Usually, the atmosphere is close to dry adiabatic in the planetary boundary layer and close to pseudoadiabatic above. The hot and dry Saharan air layer (SAL), which becomes thinner towards the equator, is located above the monsoon layer and characterised by low static stability and low potential vorticity (PV). Above the SAL, the free atmosphere prevails, which is almost pseudoadiabatic and contains little baroclinicity.

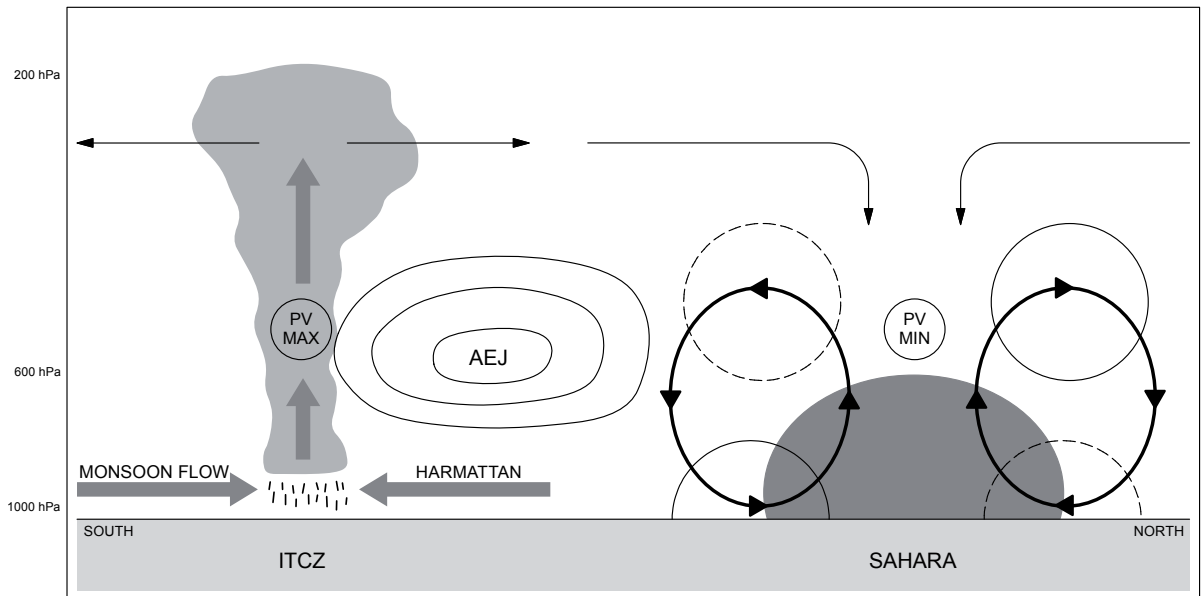


Figure 2.2: A schematic illustrating the deep moist convection at the ITCZ and the response in the wind field to deep sensible heating in the Saharan region. The shading indicates dome-shaped heating region, thick solid lines with arrowheads show resulting meridional circulations which form at the northern and southern fringes of the Sahara as a response to this heating. The poleward and equatorward branches of these overturning cells result in westerly (thin solid lines) and easterly (dashed lines) acceleration due to the conservation of angular momentum. The ascending branches of the overturning cells “overshoot” the region of heating, resulting in the adiabatic cooling necessary for maintaining the thermal–wind balance above the AEJ maximum around 600–700 hPa. Adapted from Thorncroft and Blackburn (1999).

The AEJ is maintained by two adiabatically forced meridional circulations (Thorncroft and Blackburn, 1999). The first circulation occurs at the southern flank of the Sahara and is caused by the surface fluxes and the dry convection of the Saharan heat low, that reaches the height of the AEJ (Fig. 2.2). The second circulation is associated with the deep moist convection in the ITCZ taking place on the southern flank of the jet. This is reflected in the meridional PV structure. A positive mid-tropospheric PV anomaly occurs near 10°N and is related to the ITCZ. Potential vorticity values near-zero can be found in the dry convective region of the Saharan heat low. At mid-levels between both regions, a strong negative meridional PV gradient is distinct.

A baroclinic zone exists between the relatively cold and moist monsoon flow (south of 5°N) and the hot, dry, and well-mixed air over the Saharan heat low (17-30°N). Due to the thermal wind relation, the positive surface temperature gradient induces easterly shear over the surface monsoon southwesterlies. The height of the jet is determined by the level at which the surface-induced positive temperature gradient is replaced by the free atmosphere's negative temperature gradient. Cook (1999) showed that a thermally direct ageostrophic circulation leads to an acceleration of the largely geostrophic zonal flow and to the maintenance of the jet.

Synoptic-scale disturbances, which are referred to as African easterly waves (AEWs), grow on the AEJ (Burpee, 1972). The meridional gradient of the PV and the meridional temperature gradient in the lower troposphere are important for the development of AEWs (Burpee, 1972; Thorncroft and Hoskins, 1994a,b; Thorncroft, 1995). The observed AEJ is a combination of the diabatically forced meridional circulations which maintain it and the AEWs which weaken it.

2.2 African Easterly Waves (AEWs)

African easterly waves are synoptic-scale disturbances that develop on the African easterly jet (AEJ). They propagate westwards across tropical West Africa into the eastern Atlantic and the east Pacific. The AEWs have propagation speeds of 7-9 ms⁻¹, a period of 2-5 days, a wavelength of about 2000-4000 km, and a mean latitude of 11-12°N (Carlson,

1969b,a; Burpee, 1972, 1974; Reed et al., 1977; Duvel, 1990; Berry et al., 2007). African easterly waves form over central Africa in the zone of cyclonic wind shear on the southern flank of the mid-tropospheric AEJ with their maximum intensity at the height of the jet core (~ 650 hPa). The disturbances have a cold core below the level of the jet maximum and a warm core above.

The necessary condition for the instability of an internal jet is a reversal in sign of the meridional gradient of the PV (Charney and Stern, 1962). This condition is satisfied in the region of formation of AEWs. Additionally, a reversal in the meridional gradient of absolute vorticity (condition for barotropic instability) can be observed in that region. The growth of the AEWs is traditionally attributed to this mixed barotropic–baroclinic instability (Carlson, 1969b; Burpee, 1972, 1974, 1975). However, more recent studies indicate that barotropic–baroclinic instability alone cannot explain the initiation and intermittence of AEWs but that the formation of waves requires a finite–amplitude initial perturbation to a stable basic state (Hall et al., 2006). African easterly waves are often triggered by orographically induced convection in east Africa (Hodges and Thorncroft, 1997), in particular by convective complexes that originate over the Ethiopian Highlands (Hill and Lin, 2003; Lin et al., 2005; Berry et al., 2007). Horizontal and vertical shear are important for the growth of the AEWs (e.g. Burpee (1972); Thorncroft and Hoskins (1994a,b); Paradis et al. (1995)).

African easterly waves can also be found north of the AEJ core. Pytharoulis and Thorncroft (1999) showed that the maximum amplitude of the AEW occurs at the level of the AEJ (around 700 hPa), at Bamako (12.58°N , 8.08°W) whereas at Dakar (14.78°N , 17.58°W) the waves are characterised by maxima between 850 and 950 hPa. The occurrence of the low-level waves to the north of the AEJ are associated with baroclinic interactions between the negative meridional PV gradients in the jet core and the positive low-level gradient of potential temperature, θ , enhanced by the presence of low-static-stability air north of the AEJ. These waves propagate along the positive meridional θ -gradients over northern Africa (low-level temperature wave) in contrast to the jet-level AEWs that propagate along the meridional PV gradients at the level of the AEJ. Cross-correlation analysis shows that there is strong coherence between the low-level AEWs north of the

jet and the well-known cold core AEWs that propagate south of the jet (Pytharoulis and Thorncroft, 1999).

The life cycle of AEWs can be divided into three phases (Berry and Thorncroft, 2005). The first phase is the initiation, where by convective events composed of several MCSs or elevated terrain in the Sudan lead to the development of AEW. The second phase is baroclinic growth during which a low-level warm anomaly, is generated close to the initial convection, and interacts with a mid-tropospheric jet. This interaction is reinforced by the generation of subsynoptic-scale PV anomalies by deep convection that is embedded within the baroclinic AEW structure. The third phase is the west coast development. The baroclinic structure weakens near the West African coast, but the convection is maintained. The mid-tropospheric PV anomalies embedded within the AEW merge with each other and with PV anomalies that are generated by convection over topography ahead of the system. That results in the production of a significant PV feature that leaves the West African coast.

The location of convection within AEWs can vary depending on the nature of the convection and the geographic location (Payne and McGarry, 1977; Machado et al., 1993; Fink and Reiner, 2003). For AEWs propagating along 10°N , Kiladis et al. (2006) found that convection occurs in the northerly flow of an AEW when the wave is east of 0° and that the convection shifts into the wave trough west of 0° . As the wave propagates offshore into the Atlantic ITCZ the convection is located in the southerly flow. In contrast, AEWs propagating along 15°N show convection which remains in the southerly flow throughout the wave's trajectory. The largest convective activity and amounts of precipitation are observed ahead of the AEW trough and along and south of the disturbance path. The AEWs modulate West African rainfall and are the main precursors of Atlantic (Riehl, 1954; Frank, 1970; Landsea, 1993) and East Pacific tropical cyclones (Avila and Pasch, 1995).

2.3 Mesoscale Convective Systems (MCSs)

Mesoscale convective systems (MCSs) are organised cumulonimbus cloud systems with cloud tops that usually cover a large area with a horizontal extent of several hundred kilometres (Maddox, 1980). They produce precipitation in an area of about 100km^2 .

The area of cold cloud tops often exceeds the size of an individual cumulonimbus by 2-3 orders of magnitude (Houze, 2004). According to Maddox (1980), they can be classified as linearly-oriented tropical squall lines and as mesoscale convective complexes with a circular shape. Conditional instability, vertical wind shear in the lower troposphere, as well as a moist PBL and dry air at mid-levels are favourable conditions for MCSs to form. Over West Africa, significant vertical shear occurs due to the low-level monsoon flow, which is typically southwesterly, undercutting the easterly flow of the AEJ. The instability is usually released by convective scale motions which are triggered by surface heating, soil moisture inhomogeneity, and/or topography (Rowell and Milford, 1993; Redelsperger et al., 2002; Berry and Thorncroft, 2005; Laing et al., 2005; Gantner and Kalthoff, 2010).

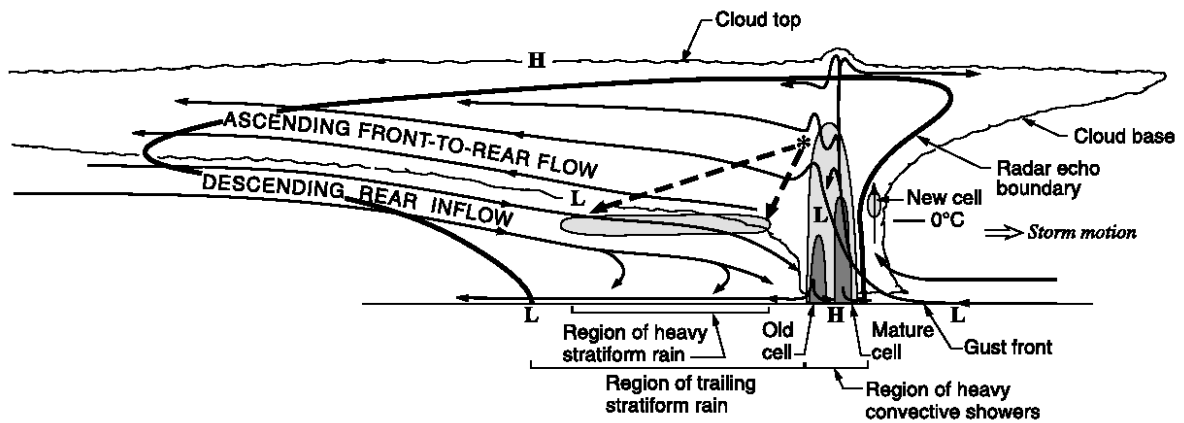


Figure 2.3: Vertical cross section oriented perpendicular to a convective line in the midlatitudes. Kinematic, microphysical, and radar echo structure of a convective line with trailing-stratiform precipitation are shown. Intermediate and strong radar reflectivity is indicated by medium and dark shading. H and L indicate centres of positive and negative pressure perturbations. Dashed-line arrows indicate fallout trajectories of ice particles passing through the melting layer. Taken from Houze (2004).

Most information about the diurnal cycle and lifetime of MCSs is based on satellite data (Fortune, 1980; Reed and Jaffe, 1981; Machado et al., 1993; Mathon and Laurent, 2001). A strong dependence of MCS generation on the diurnal solar cycle has been noted. Often, small cells or thunderstorms develop in the mid-afternoon, followed by MCS genesis during the late evening or early night hours (Laing and Fritsch, 1993). A peak in initiation has been detected during the mid- or late-afternoon hours when the conditional instability of the PBL reaches a maximum. The MCSs usually propagate westwards towards the low-

level high equivalent-potential temperature air that feeds the convective systems (Laing and Fritsch, 1993).

Knowledge about the inner structure of MCSs is based mainly on data from the Atlantic tropical experiment GATE data (McGarry and Reed, 1978) and over the West African continent from campaigns like HAPEX-Sahel in Niger 1992 (Goutorbe et al., 1997), COPT 81 (Sommeria and Testud, 1984), JET 2000 Thorncroft et al. (2003) and IMPETUS (Fink et al., 2006). Houze (1977) formulated a conceptual model of squall-line systems (Fig. 2.3), which was modified slightly by Gamache and Houze (1982). The main characteristics of a squall-line system, as summarised by e.g., Hastenrath (1994), are a convective squall-line region and a stratiform or anvil region. The convective region is characterised by boundary-layer convergence, which feeds deep convective updraughts. The buoyant updraughts carry air with high moist static energy from the PBL to the middle and upper troposphere (Fig. 2.3). These active centres of cumulonimbus convection are accompanied by heavy precipitation. Evaporation into comparatively dry mid-tropospheric and PBL air leads to cooling and strong downdraughts. The negatively buoyant air reaches the surface as part of the storm's downdraught and spreads out as a gravity current. The leading edge of this density current lifts conditionally unstable environmental air upward past its level of free convection. Thus new clouds are generated at the leading edge of the storm. The movement of small convective cells can be attributed to the spreading of the cold pool. MCSs consist of multiple intense convective cells that are accompanied by an anvil region. Cold pools are generated by these individual convective cells in an MCS. They spread out at the surface and combine to form a large mesoscale cold pool covering a contiguous area on the scale of the entire MCS. This combined cold pool acts as a gravity current and can influence the MCS propagation velocity by forcing unstable air upward in the vicinity of the MCS.

Usually, the forward edge of the squall line moves slightly faster than the maximum easterly jet speed (Bolton, 1984). The anvil region has a predominantly stratiform structure. These trailing anvils of the cumulonimbus clouds produce horizontally uniform, lighter rains. In MCSs with a leading line of convection with a trailing-stratiform region, descent occurs below the cloud base of the stratiform clouds due to the cooling of mid tropospheric environmental air by sublimation, melting, and evaporation of precipitation

particles falling out of the stratiform clouds aloft. This results in a mid-level rear-to-front flow which is a gravity wave response to heating in the convective line (Schmidt and Cotton, 1990). This rear inflow is a layer of low equivalent-potential air which enters the MCS from the rear below the trailing anvil cloud of the stratiform region and descends toward the leading convective line. The descent occurs gradually across the stratiform region. A sudden downward jump can occur when it reaches the rear of a region of active convective cells. Typical post-squall line conditions are the “onion”-shaped temperature and moisture structure below 600 hPa in the skewT-logP diagram (Zipser, 1977; Dudhia et al., 1987), i.e., cool and moist conditions at the surface, warm and dry conditions near 850 hPa, and saturated conditions above 600 hPa.

Key factors for long-lived convective systems are given by Weisman (1993). They comprise convective available potential energy (CAPE) values of around $2000 \text{ m}^2 \text{ s}^{-2}$, vertical wind shear between the surface and about 500 hPa of about 20 m s^{-1} , a line of convective cells with strong rear-inflow jets, as well as cyclonic and anticyclonic vortices on the northern and southern flanks of the bow segments that have a length of about 40 to 100 km (Fig. 2.4). About three hours into the lifetime of an MCS this structure develops and remains coherent.

The lifetime of an MCS and its strength depend on the storm-generated cold pool and the circulation related to the ambient vertical wind shear perpendicular to the orientation of the convective system (Rotunno et al., 1988; Weisman et al., 1988; Weisman and Rotunno, 2004). The strongest lifting at the leading edge and most effective convective retriggering occurs when the circulation associated with the storm-generated cold pool and the circulation associated with the ambient shear are in near balance. MCSs often develop a rear-inflow jet originating through collective cooling and heating patterns of convective cells (Lafore and Moncrieff, 1989). Such a situation is illustrated in Fig. 2.4. The velocity C represents the strength of the cold pool and Δu represents the magnitude of the low-level ambient vertical wind shear. The convective cells embedded in an MCS tilt predominantly in the downshear direction before a distinct cold pool develops ($C \ll \Delta u$). When a cold pool develops a more upright convective structure ($C \sim \Delta u$) can be observed because the circulation associated with the low-level shear can turn and produce deeper lifting at lower levels. When the development of the cold pool reaches a

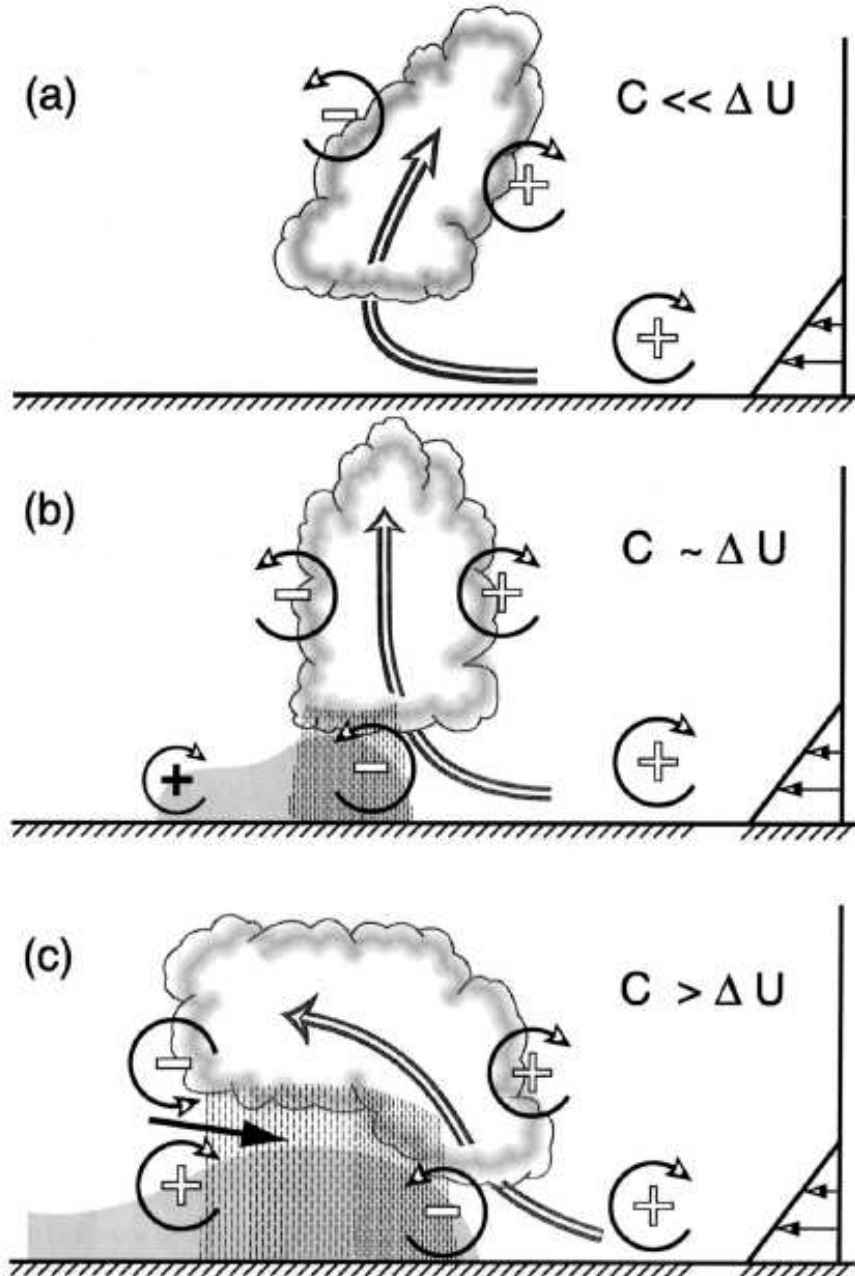


Figure 2.4: Three stages in the evolution of a convective system. (a) An initial updraught leans downshear in response to the ambient vertical wind shear, which is shown on the right. (b) The circulation generated by the storm-induced cold pool balances the ambient shear, and the system becomes upright. (c) The cold-pool circulation overwhelms the ambient shear and the system tilts upshear, producing a rear-inflow jet. The updraught current is denoted by the thick, double-lined flow vector, and the rear-inflow current in (c) is denoted by the thick solid vector. The shading denotes the surface cold pool. The thin, circular arrows depict the most significant sources of horizontal vorticity, which are either associated with the ambient shear or which are generated within the convective system, as described in the text. Regions of lighter or heavier rainfall are indicated by the more sparsely or densely packed vertical lines, respectively. The scalloped line denotes the outline of the cloud. Here, C represents the strength of the cold pool while Δu represents the strength of the ambient low-level vertical wind shear, as described in the text. The convective systems moves eastwards, i.e. to the right of this figure. Taken from Weisman and Rotunno (2004).

state with $C > \Delta u$, the circulation associated with the cold pool dominates the circulation due to the ambient shear. Convective cells and the regions of heating and cooling are shifted rearward, where they generate the rear-inflow jet. Rotunno et al. (1988) define the “optimal” state of a long-lived MCS by $C/\Delta u$ being close to 1. This means the convective system is upright and the largest lifting is produced at the leading edge of the cold pool. An isolated updraught growing in a vertically sheared environment deforms a horizontal vortex line upward within the ambient shear. Cyclonic and anticyclonic vortices are produced on the flank of the cell (Fig. 2.5a). They are often referred to as line-end vortices (Weisman, 1993). Downdraughts develop and further deform this pattern. The downdraught gradient provides an additional source of tilting and the downdraught acceleration leads to stretching of the vertical vorticity. When the environmental vertical wind shear and the convective available energy are strong enough, cell splitting may occur. The right cell of the splitting pair has a cyclonic updraught and an anticyclonic downdraught at mid-levels, whereas the left cell is characterised by anticyclonic updraught and cyclonic downdraught (Fig. 2.5b).

In the stratiform region a mesoscale convective vortex (MCV) often forms at mid-levels at the base of the stratiform cloud (Davis and Weisman, 1994; Knievel and Johnson, 2002). MCVs have a diameter of about 100-300 km and are several kilometres deep. The strength and scale of MCVs depend on the strength of the ambient shear, the strength of the system’s cold pool, the scale of the convective line segments, and the phase within the life cycle of the MCS in an environment with weak to moderate shear (Weisman and Davis, 1998). In environments with strong shear, however, line-end vortices, which are confined to the lowest 3 km (Weisman, 1993) and have a horizontal scale of 20-50 km, are often generated by tilting of the horizontal vorticity generated within the systems cold pool as the vortex lines are lifted within the front-to-rear ascending flow. Due to the planetary rotation an asymmetric structure forms with the cyclonic vortex dominant on the northern end of the line.

For a rear-to-front feeding MCS (Fig. 2.6) occurring in an environment with a low-level jet and a deep layer of weak flow and weak shear in the middle and upper troposphere, a diabatically produced PV maximum occurs in the mid-troposphere. A PV minimum occurs aloft as well as ahead of and behind the cold pool (Fritsch et al., 1994; Raymond

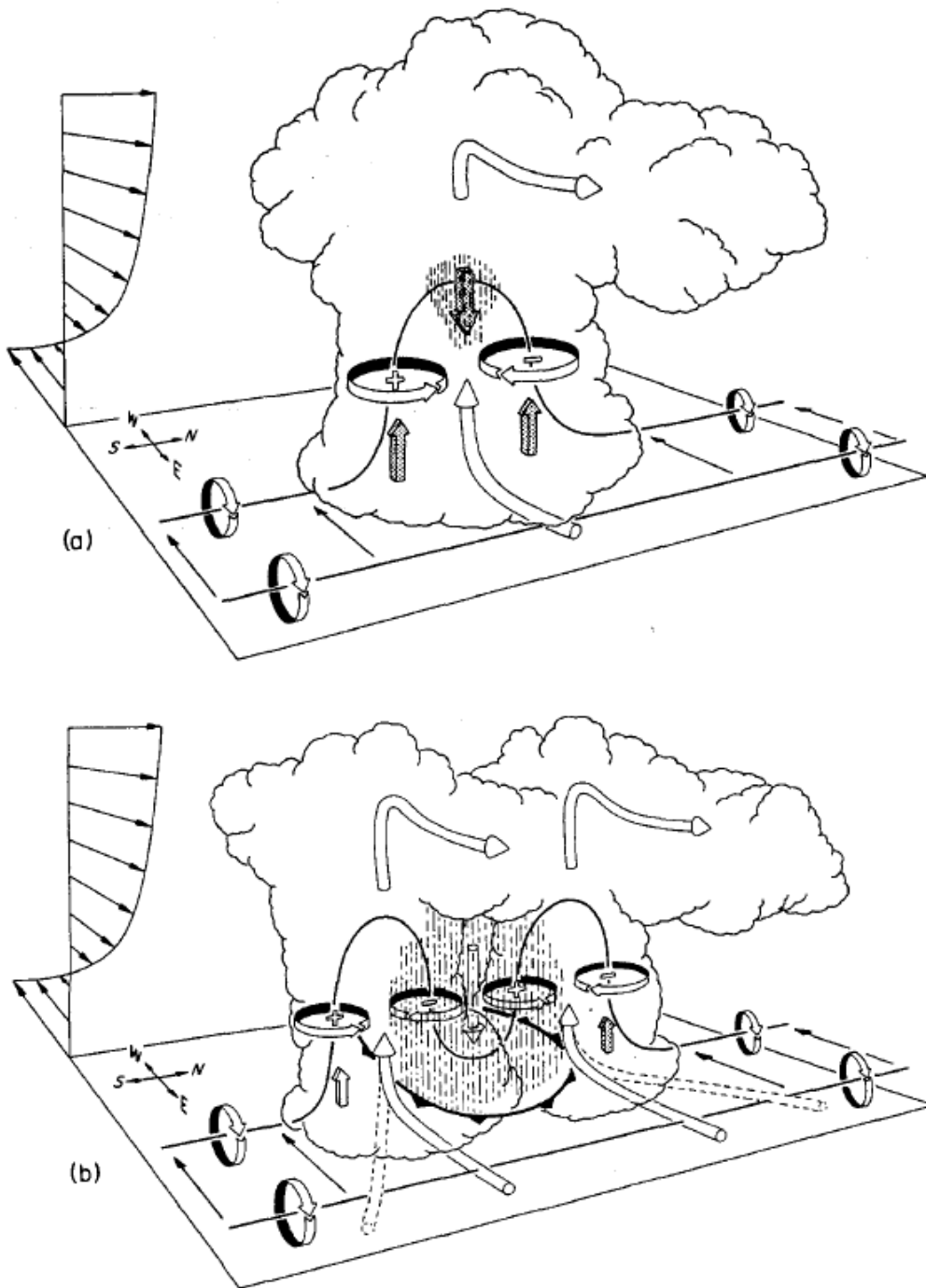


Figure 2.5: Schematic on how a typical vortex tube contained within (westerly) environmental shear is deformed as it interacts with a convective cell (viewed from the southeast). Cylindrical arrows show the direction of cloud–relative airflow, and heavy solid lines represent vortex lines with the sense of rotation indicated by circular arrows. Shaded arrows represent the forcing influences that promote new updraught and downdraught growth. Vertical dashed lines denote regions of precipitation, (a) Initial stage: vortex tube loops into the vertical as it is swept into the updraught. (b) Splitting stage: downdraught forming between the splitting updraught cell tilts vortex tubes downward, producing two vortex pairs. The barbed line at the surface marks the boundary of the cold air spreading out beneath the storm. Taken from Klemp (1987).

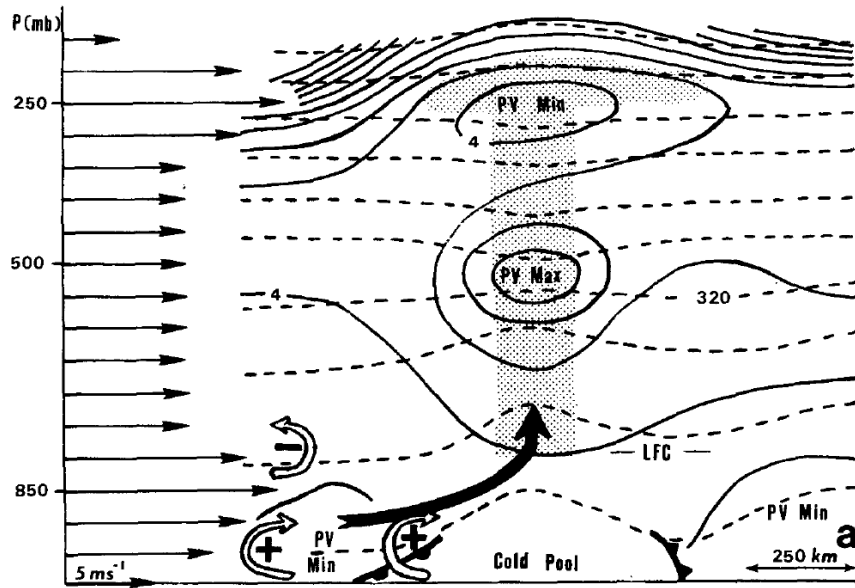


Figure 2.6: Structure and redevelopment mechanism of a mesoscale warm core vortex. Thin arrows along the ordinate indicate the vertical profile of the environmental wind. Open arrows with plus or minus signs indicate the sense of vorticity produced by the cold pool and by the environmental vertical wind shear. Thick solid arrows indicate updraught axes created by the vorticity distribution. Frontal symbols indicate the outflow boundaries. Dashed lines are potential temperature (5-K intervals) and solid lines display the potential vorticity ($2 \times 10^{-7} \text{m}^2 \text{s}^{-1} \text{K kg}^{-1}$ intervals). The system is propagating from the left to the right at about $5\text{--}8 \text{ms}^{-1}$. The low-level high- θ_e air in the low-level jet overtakes the system. Air overtaking the vortex ascends isentropic surfaces, reaches its level of free convection (LFC), and thereby initiates deep convection. Taken from Fritsch et al. (1994).

and Jiang, 1990; Rotunno et al., 1988). In regions where the air from the rear overtakes the outflow boundary, the vorticity of the downdraughts that create the cold pool, and the vorticity of the ambient shear have the same sign. This would lead to weak lifting along the outflow boundary (Rotunno et al., 1988), but as the air flows isentropically into the interior of the disturbance the overtaking air is lifted up (Fritsch et al., 1994). When the parcels have reached the level of maximum wind at the jet height the sign of the shear related vorticity changes. New convection is often initiated below the PV maximum and initiates a new MCS, that is likely to strengthen the disturbance. A front-to-rear jet (not shown) is associated with mesoscale upward motion and a rear-to-front jet is associated with evaporatively induced sinking. They could be caused by the non-advective transport of PV associated with latent-heat release in the updraught and evaporative cooling or

melting in the underlying downdraught. In most cases, the ambient shear associated with MCSs has a strong rear-to-front component (Raymond, 1992).

There are still many unanswered questions concerning the interaction between AEWs and MCSs. As discussed above, it has been proposed that MCSs are important in the initiation of AEWs. However, the AEW troughs provide a favourable environment for the development of new MCSs. The manner in which the MCSs embedded in the AEW influence the AEW itself has been addressed only recently by very few studies.

Diongue et al. (2002) conducted a numerical study of a Sahelian squall line and observed that the AEJ is accelerated behind the squall line over the whole cloud area and not only below the trailing stratiform region. The horizontal shear on the AEJ flanks above the rear inflow is very strong and generates a dipole of counter rotating vortices. They also observed an enhancement of barotropic instability on the northern flank of the AEJ. Organised convection in the vicinity of the jet core provoked a weakening of the AEJ ahead of the squall line and a strengthening behind it. In addition, squall lines affect the synoptic scale by bringing rain into the Sahelian region, generating density currents via mesoscale downdraughts, which can modify the low-level monsoon flow, generating a mesoscale vortex in the stratiform region, and by generating mesoscale vorticity that is advected toward the rear of the convective system and where it might aggregate with the AEW behind the squall line (Chaboureau et al., 2005). The latter could lead to a reinforcement of the AEW.

The overall structure of MCSs over West Africa has been analysed using potential temperature budgets (Lafore et al., 1988; Caniaux et al., 1994). The circulation and the precipitation of MCSs can be associated with the convective and stratiform regions (Houze, 2004). Intense, deep cores can be found in the convective region whereas the stratiform region is characterised by a more uniform cloud texture and lighter precipitation. The mid-tropospheric environmental air is cooled by melting and evaporation of precipitation particles falling out of the stratiform cloud. Thus, the region below the stratiform cloud base is characterised by descent. Typically there is net warming at all levels in the convective region, although adiabatic cooling largely compensates the diabatic heating. A net warming occurs in the stratiform region where ascent and condensation take place. Melting and evaporation are the dominant processes in the lower-troposphere leading to

a net cooling in the stratiform region. The thermal profiles of MCSs are also modified by radiation due to their long lifetime.

2.4 Tropical Cyclogenesis

The formation of tropical cyclones, which are called hurricanes in the Atlantic and East Pacific, is initiated when some general criteria are fulfilled (Gray, 1968, 1979):

- the ocean temperature must exceed 26.5°C throughout a depth of at least 50 m;
- the atmosphere needs to be potentially unstable to moist convection;
- the existence of relatively moist layers near the mid-troposphere (500 hPa) is important to allow the continuing development of widespread thunderstorm activity;
- the low-level disturbances can only develop into a tropical cyclone if they are at least 500 km away from the equator as significant values of planetary vorticity are required for this process;
- the vertical shear of the horizontal wind between the surface and the upper troposphere must be low (less than about 10 m s^{-1});
- tropical cyclones form in association with MCSs near the trough region of synoptic-scale weather disturbances, such as AEWs. The AEWs serve as seed disturbances for tropical cyclones in the Atlantic and the east Pacific (Gray, 1968; Frank, 1970; Avila and Pasch, 1992; Landsea et al., 1998; Thorncroft and Hodges, 2001).

The primary energy source for the genesis and maintenance of tropical cyclones is diabatic heating, i.e. the latent heat release in clouds, surface sensible heating and radiation. Most of the latent heat energy that drives the large-scale circulation of the tropical cyclone is evaporated from the ocean's surface. The evaporation rates increase in proportion to the wind speed as the cyclone intensifies.

As an AEW moves out over the ocean the characteristics of convection may change in character. Recent studies of tropical cyclogenesis have emphasised the role that might be played by individual intense convective cores in the pre-tropical-depression phase (Hendricks et al., 2004; Montgomery et al., 2006). The development of these so-called

“hot towers” (Riehl and Malkus, 1958) in an environment characterised by weak cyclonic vorticity can lead to them developing a marked positive vertical vorticity signature. The merger of these individual vorticity anomalies or vortical hot towers may be an integral part of tropical cyclogenesis, although the precise route by which this occurs is still under investigation (Ritchie and Holland, 1997; Montgomery et al., 2006).

Two possible routes to tropical cyclogenesis are the so called “bottom–up” and “top–down” hypotheses. The “bottom–up” theory assumes that a low–level circulation forms first and that the associated PV anomaly grows from the surface to upper levels. The “top–down” theory instead states that a PV anomaly at midlevels extends downwards, thus forming the low–level circulation. The reality, however, is likely to be a mixture between both.

2.4.1 “Bottom–Up” Cyclogenesis

Mesoscale convective vortices provide the necessary quasi–balanced forcing for the initiation and organisation of deep convection and for the initial concentration of low–level cyclonic vorticity (Zhang and Bao, 1996a,b; Montgomery and Enagonio, 1998). The deep convection contributes to the enhancement of the low–level positive vorticity anomaly through stretching in the presence of intensifying flows. Through merging with neighbouring vortical hot towers (VHTs), the MCVs contribute to the acceleration of the main vortex. This process is called the mean–eddy interaction. It can spin up a mesoscale vortex in a barotropic model as shown by Montgomery and Kallenbach (1997).

A two–stage process for creating a near–surface tropical storm vortex was suggested by Hendricks et al. (2004). The first step is the vortical preconditioning of the lower troposphere by the generation of multiple VHTs and their competition with each other for ambient CAPE and angular momentum. VHTs have only short convective lifetimes and have maximum tangential velocities near the ocean surface at the time of their maximum intensity. In the second step multiple VHTs merge. The warm–core formation and tangential momentum spinup are dominated by the organisation of diabatically generated PV anomalies. The strong vertical vorticity in the VHT cores traps the latent heat from moist convection. Additionally, the tropical cyclogenesis is enhanced by the accumulated diabatic heating associated with the VHT, which produces a net influx of low–level mean

angular momentum throughout the genesis, i.e. the diabatically and frictionally forced secondary circulation in the vicinity of the VHTs enhances the near-surface inflow. The VHTs tend to merge near the surface first. The diabatic concentration at these levels produces an intensification of near-surface PV.

Montgomery et al. (2006) found that within the cyclonic vorticity-rich environment of MCVs, small-scale cumulonimbus towers have intense cyclonic vorticity in their cores. VHTs emerge as the preferred coherent structures. They acquire their vertical vorticity through a combination of tilting of MCV horizontal vorticity and stretching of MCV and VHT-generated vertical vorticity. A quasi-balanced secondary circulation develops on the system scale that converges cyclonic vorticity of the initial MCV and small-scale vorticity anomalies generated by subsequent VHT activity.

Recently, Kieu and Zhang (2009) computed relative vorticity and PV budgets and found that when a fast moving MCV captures a slowly drifting MCV, high PV values are concentrated near the merger's centre with the peak amplitude occurring above the melting level. Meanwhile, the surface heat fluxes, the low-level convergence, the latent heat release and upward motion increase, while the lower tropospheric PV, and the surface pressure decrease. The cyclonic vorticity grows from the bottom upward. Kieu and Zhang (2009) found that storm-scale rotational growth results from increased flux convergence of absolute vorticity during the merging phase. The largest growth rates were found in the bottom layers due to the frictional convergence.

Tory et al. (2007) argues that tropical cyclogenesis follows the so called primary and secondary vortex enhancement mechanisms. The primary mechanism generates PV cores on the scale of the updraughts, and provides net heating and vertical mass flux to the system (Tory et al., 2006a). The secondary mechanisms organise the PV cores into one big PV core and enhances the system-scale vortex (Tory et al., 2006b). Vertical shear can inhibit the development of the PV cores or tear them apart. Insufficient large-scale cyclonic environmental vorticity also inhibits the genesis.

2.4.2 “Top-Down” Cyclogenesis

The top-down hypothesis, in contrast, says that the midlevel vorticity is increased through the merging of the MCVs. This process can maintain or even strengthen the vorticity in

the AEW. In order to undergo tropical cyclogenesis, the environment must support the development of strong convective bursts. The top-down hypothesis further says that the merging mid-level MCVs within a larger-scale low-level background flow are accompanied by a downward extension of cyclonic vorticity. The interactions between midlevel vortices results in a combined vortex of greater depth. Additionally, the interaction between midlevel vortices and the low-level circulation produces a development downward of the midlevel vorticity (Ritchie and Holland, 1997; Simpson et al., 1997). This results in an amplification of the surface rotation.

The MCVs affect the low-level circulation and the large-scale in two ways (Ritchie and Holland, 1997). The primary vortex forms and extends downward when two or more MCSs interact. Each MCS spins up its own MCV in the stratiform region. When these MCVs are in close proximity, they begin to rotate around a common axis and combine into a single vortex. At first, the interaction between the MCVs produces a combined vortex of greater depth, and the interaction between mid-level vortices and the low-level circulation results in a downward development of the mid-level vorticity. This process strengthens the vortex near the surface, and a closed circulation extending from the surface to the mid-troposphere forms. Ritchie et al. (2003) found that the interaction between unequal MCVs results in a stronger vortex that absorbs most of the circulation associated with the weaker vortex. It becomes stronger, thickens vertically, and joins with the preexisting surface low. Simpson et al. (1997) also points out that it is the interaction of several MCVs with each other and with the monsoon trough and its low-level circulation that leads to the development of the tropical depression. (A tropical depression is the first form of organised convection on the way to tropical cyclogenesis which is characterised by a closed low-level circulation and wind speed values larger than 17 m s^{-1} .) Bister and Emanuel (1997) found for an MCS with an extensive stratiform precipitation region that the diabatic heating in the upper troposphere and cooling at and below the melting level lead to the formation of a midlevel vortex. Evaporation of rain increases the relative humidity in the lower troposphere and leads to downdraughts that advect the vortex downward. The convection redevelops, leading to a further increase of vorticity below the maximum heating and a formation of a warm core. When the MCV extends low enough it can connect with the boundary layer and develop into a tropical depression.

Several theories exist about the formation of tropical cyclones, but it still remains a question of ongoing research to explain how a tropical depression forms out of a preexisting mesoscale convective system.

2.5 Saharan Air Layer (SAL)

West African dust aerosol plumes are the most wide spread, persistent and dense (Prospero et al., 2002). The processes which are responsible for the dust uplift are highly variable in time and space with an annual peak during summer (Prospero et al., 2002; Engelstaedter and Washington, 2007). The dust has a significant influence on the earth radiation budget (Haywood et al., 2003).

The Saharan heat low (SHL) is a shallow low pressure system, owing to the strong daytime insolation, covering major parts of the Sahara desert. It has a vertical extent from the surface up to about 700 hPa and is overlain by strong subsidence due to the northern branch of the Hadley cell. The dry convective heating, the descending vertical motion, adiabatic compression, and the absorption of solar radiation through mineral dust layers are the main heat sources in this region.

The Saharan air layer (SAL) consists of the well-mixed layer above the Saharan desert reaching from the surface up to about 500 hPa, and the elevated Saharan planetary boundary layer which occurs at a height of the AEJ with the monsoon flow underneath it and the free atmosphere aloft. It is characterised by a significant amount of mineral dust aerosols, relatively dry and warm air, and a weakly-stable stratification (Prospero and Carlson, 1972; Carlson and Prospero, 1972; Diaz et al., 1976; Karyampudi and Carlson, 1988; Parker et al., 2005a).

2.5.1 Dust Sources and Emission over West Africa

The main source regions of mineral dust over West Africa are the Bodélé Depression, the West Africa, the Nubian and the Libyan desert (Fig. 2.7). These deserts have a large diurnal and monthly variability. The largest monthly mean dust load over West Africa occurs between May and August (Fig. 2.8). Large dust events related to, for instance,

cold surges take place during wintertime. Such an example is the dust event that occurred in March 2006 (Stanelle et al., 2010).

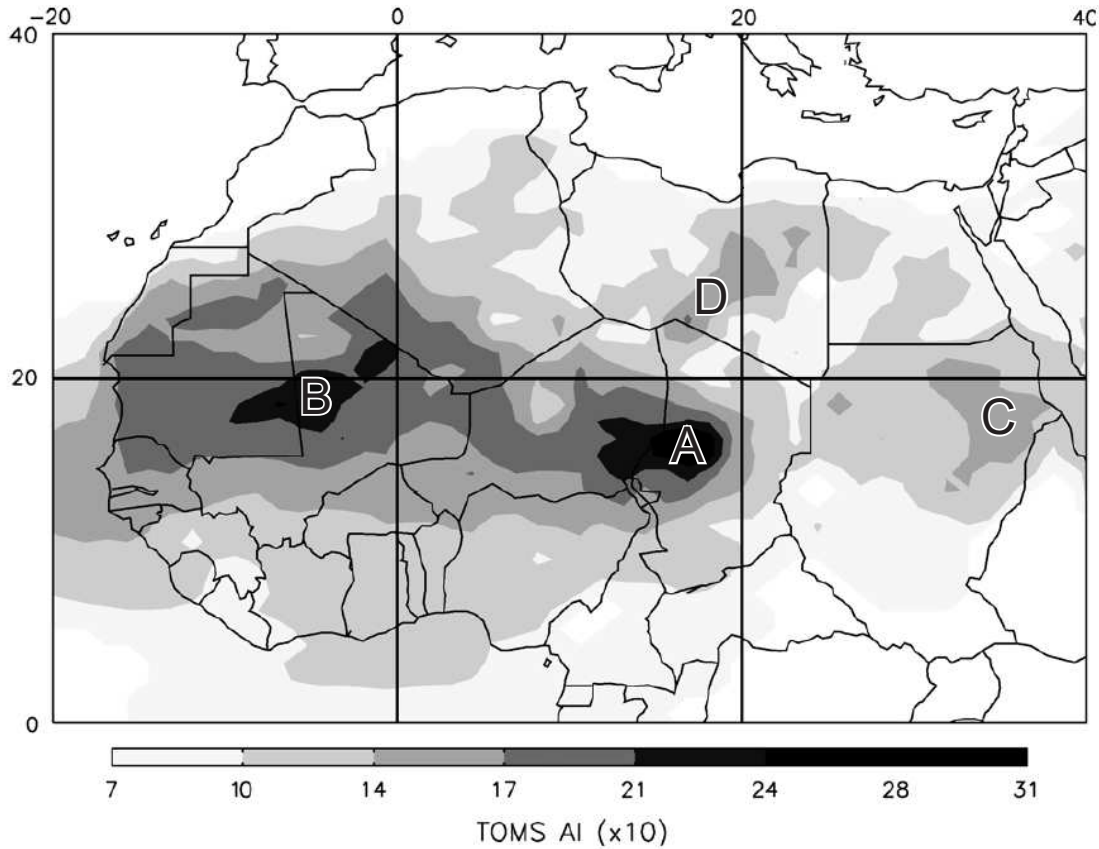


Figure 2.7: Long-term mean TOMS (Total Ozone Mapping Spectrometer) aerosol index ($AI \times 10$) between 1980-1992 highlighting the main sources of mineral dust in Africa: (A) Bodélé, (B) West Africa, (C) the Nubian desert and (D) the Libyan desert (Engelstaedter et al., 2006). The TOMS aerosol index gives the relation of how much the wavelength dependence of backscattered UV radiation from an atmosphere containing aerosols (Mie scattering, Rayleigh scattering, and absorption) differs from that of a pure molecular atmosphere (pure Rayleigh scattering). Under most conditions, the AI is positive for absorbing aerosols and negative for non-absorbing aerosols (pure scattering).

Dust emission over North Africa can occur in association with a variety of different weather systems. Mechanisms for dust emission over North Africa are, for instance, associated with high near-surface wind speeds resulting from the downward mixing of momentum from nocturnal low-level jets. (Nocturnal jets form when the lower part of the PBL becomes stable and has weaker turbulence as it moves over a cooler surface at night. The wind speed can increase with height reaching maximum values, which can even be higher than the geostrophic wind speed, at the top of the stable layer (Blackadar, 1957).) They can

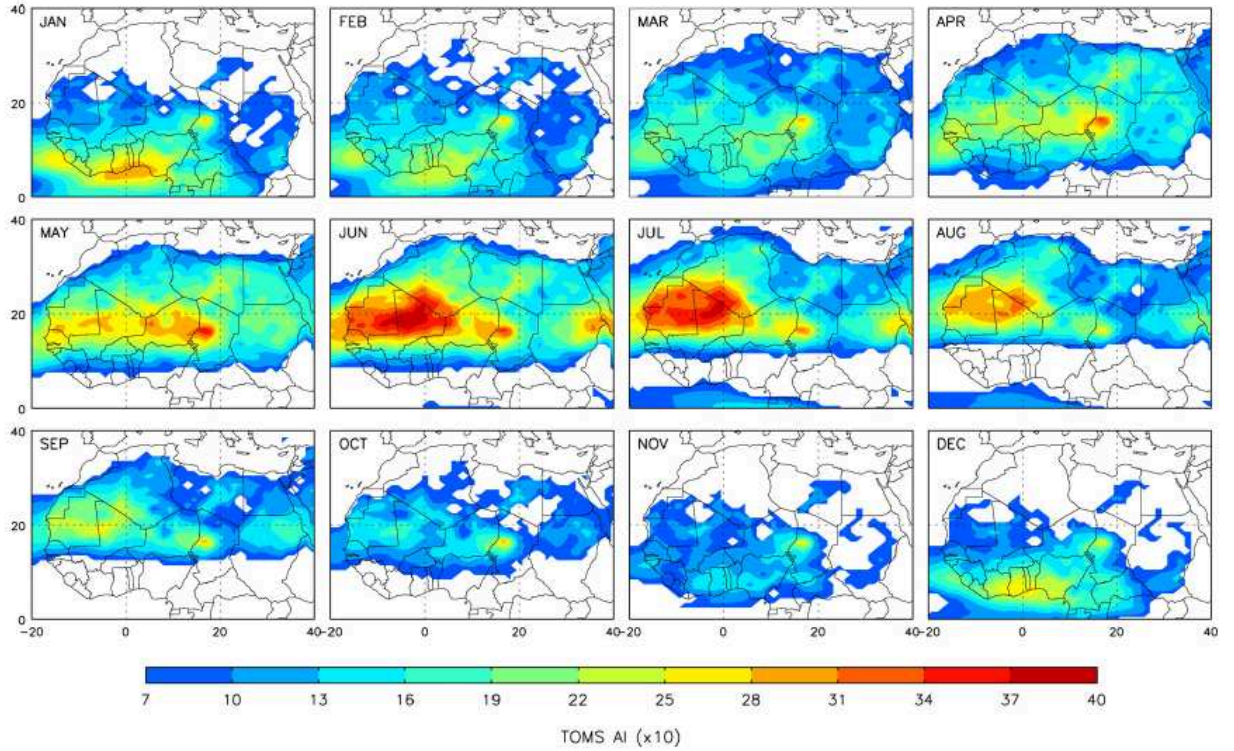


Figure 2.8: Monthly mean TOMS AI ($\times 10$)(1980-1992). Taken from Engelstaedter et al. (2006).

occur in connection with SHL dynamics (Knippertz, 2008). Further, low-level jets are generated in the lee of complex terrain, e.g. the Bodélé region in Northern Chad (region A in Fig. 2.7) (Washington and Todd, 2006; Todd et al., 2008).

North of the Inter Tropical Discontinuity (ITD), the northeasterly flow is often modulated by the occurrence of nocturnal low-level jets. The strongest near-surface winds occur during the night and shortly before sunrise, because at this time of the day there is no thermally driven turbulence in the planetary boundary layer. Hence, a strong density gradient across the monsoon-Harmattan interface is present. This density gradient is due to the temperature and humidity differences between the monsoon and Harmattan flow. Large dust uplifts are caused by the strong low-level jets north of the ITD in the morning hours just after sunrise (Bou Karam et al., 2008). As the turbulent mixing starts, momentum from the nocturnal low-level jets is transferred downward to the surface. South of the ITD, the emission of mineral dust occurs during the night and in the early morning

hours before sunrise. The circulation in the head of the monsoon density current lifts the mobilised dust towards the rear along an isentropic surface. The stable stratification north of the ITD prevents the dust from reaching altitudes at which it could be transported over long distances by the Harmattan. However, later in the day turbulent mixing throughout the planetary boundary layer takes place. Bou Karam et al. (2008) showed that the shear above the monsoon layer plays a key role in the mixing of dust across the top of the monsoon layer and the southward transport by the Harmattan. Density currents at the leading edge of the Atlantic inflow (Grams et al., 2010) in association with dust uplift were observed by Klüpfel (2008).

The penetration of upper level troughs to low latitudes and density currents due to strong evaporational cooling along precipitating cloud bands over the northern Sahara (Knippertz and Fink, 2006) and along the Saharan side of the Atlas Mountain chain in southern Morocco lead to high wind speeds in that region (Knippertz et al., 2007).

The density currents due to mesoscale convective systems (MCSs) are very effective for the emission of dust and its injection to altitudes favourable for long-range transport. This process is of particular importance at the beginning of the monsoon season, before the growing vegetation rapidly inhibits local dust emission (Flamant et al., 2007) and when greater energy is available to the downdraughts from the convective systems (Marshall et al., 2008).

2.5.2 Characteristics of the SAL

The deep well-mixed planetary boundary layer over the Sahara (Saharan PBL) extends up to about 500 hPa (Fig. 2.9). Two major internal layers are distinguishable (Messenger et al., 2010). These are the well-mixed convective boundary layer (CBL) growing from the surface within the Saharan PBL, overlain by the so-called Saharan residual layer (SRL). Surface heating leads to turbulent mixing and dry convection at daytime, and at nighttime the outgoing long wave radiation results in shallow stably-stratified low levels. The Saharan PBL is elevated from the ground at the edges of the Saharan heat low and is referred to as the SAL. The SAL/Saharan PBL can be transported across the Atlantic and into the Caribbean conserving its thermodynamic structure (Carlson and

Prospero, 1972). The boundaries of the SAL can be approximated as isentropic surfaces. Shallow altocumulus often results from high amounts of relative humidity at the capping inversion at the top of the SAL/Saharan PBL (Parker et al., 2005a). The thermodynamic characteristics of the dusty layer at the leading edge of the monsoon flow over the Sahel are described by Marsham et al. (2008). They show that higher dust concentrations can be found in the monsoon layer than in the Harmattan layer.

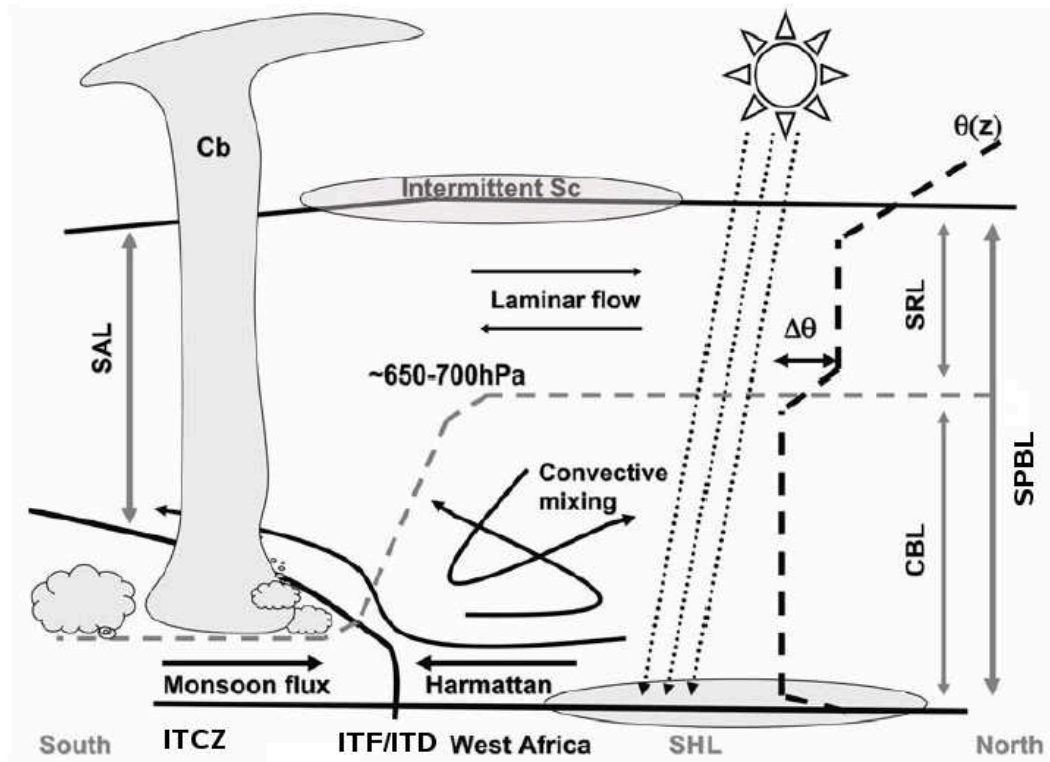


Figure 2.9: A schematic view of the diurnal cycle, the mixing process and the growth of the convective Boundary Layer (CBL) within the Saharan Residual Layer (SRL), both forming the Saharan Air Layer (SAL) also referred as Saharan Aerosol Layer. Taken from Messenger et al. (2010).

Approximately 20% of the dust entrainment into the atmosphere over a broad region of North Africa is associated with easterly wave activity (Jones et al., 2003), suggesting that easterly waves may regulate desert dust entrainment into the atmosphere.

Carlson and Prospero (1972) developed a model which depicts the movement of Saharan air from Africa to the Caribbean and its interaction with African disturbances. The lower part of the SAL may be about 5 to 6°C warmer than the normal tropical atmosphere.

This might have a strong suppressive influence on cumulus convection. The advancing dust pulse is often marked by rapid clearing behind the disturbances. Karyampudi et al. (1999) proposed a Saharan dust plume conceptual model that was based on the previous models by Carlson and Prospero (1972) and Karyampudi and Carlson (1988).

The dust plume over the West African coastline is composed of two narrow but separate plumes. One originates over the northern Sahara and the other over the Lake Chad region in the east. Maximum dust concentrations occur near the AEJ axis with downward extension of heavy dust into the marine boundary layer and a relatively dust-free trade wind inversion layer to the north of the dust layer over the eastern Atlantic region. The aerosol optical depths decreases rapidly away from land with maximum optical depths still located close to the AEJ. The ITD acts to raise the mineral dust layer over the south-westerly monsoon flow into the AEJ core (Flamant et al., 2009), and the AEJ transports the dust across West Africa and the Atlantic. Here, it can affect the tropical cyclogenesis and tropical cyclone intensity.

Mineral dust particles affect the atmospheric radiation budget directly (e.g. Tegen et al., 1996) and indirectly (e.g. Hoose et al., 2008). The direct radiative forcing of the dust involves absorbing and scattering of incoming solar radiation, as well as absorbing and re-emitting outgoing longwave radiation. The dust particles can affect the radiation budget indirectly by increasing the number of cloud-condensation and ice nuclei. An increase in cloud-condensation nuclei enhances the cloud albedo and extends the life time of the clouds. The indirect aerosol affect and the scattering of solar radiation lead to a cooling of the atmosphere, whereas the absorption of radiation by aerosols leads to a warming of the atmosphere and to a suppression of convection, which is called the semi-direct effect (e.g. Helmert et al., 2007).

Stanelle et al. (2010) investigated a West African dust storm in March 2006 and one in June 2007. They used the same model system as applied in the present study. They showed that the height range and the vertical extension of the dust layer determine the effect of dust particles on the 2 m temperature. When the dust layer is adjacent to the surface and lasts for several days it leads to an increase of the surface temperature even during the daytime. In the case of an elevated dust layer there is a decrease in 2 m temperature of up to 4 K at around noon. Furthermore, Stanelle et al. (2010) found for

their June 2007 case that the meridional temperature gradient at the surface is increased during the day due to the different influence of a near-surface (at 950 hPa) and elevated dust layer (at the height of the AEJ, i.e 600 hPa). Due to the radiative effect of the dust layer, the north becomes warmer and the south cooler, resulting in an increased temperature gradient and leading to an intensification of the secondary circulation in the region of the inner tropical front.

Tegen et al. (2006) observed a decrease in maximum daytime temperatures of about 5 K during the initial stage of a dust storm in March 2005 in West Africa. A surface temperature reduction of up to 4 K over regions with high AOT was found by Mallet et al. (2009). Helmert et al. (2007) computed the regional average over the southern Sahara and detected a decrease of about 3 K for more reflecting particles and of 3.3 K for more absorbing particles.

It is still an open question as to whether the atmospheric feedbacks associated with the presence of dust are more likely to increase or decrease precipitation over the Sahelian region. In addition, the uplifted dry and mineral dust particle enriched air, the SAL, is transported over West Africa and over the Atlantic, where it can affect the cyclogenesis of tropical cyclones (Dunion and Velden, 2004).

2.5.3 Impact of the SAL on Tropical Cyclones

It is not yet fully understood how the SAL interacts with AEWs and influences the genesis and intensity of tropical cyclones. Some studies state that the SAL has a negative effect on tropical cyclones, some say it has a positive impact, while others claim that the effect of the Saharan dust is overrated.

Based on the analysis of several case studies of individual tropical cyclone events, Dunion and Velden (2004) suggested that the SAL could inhibit the formation, or reduce the intensity of tropical cyclones in the North Atlantic through three mechanisms: (i) The convectively driven downdraughts are enhanced by the dry air at mid levels. This leads to a cooling of the planetary boundary layer and, hence, to a weakening of the tropical cyclone intensity or a disruption of the developing TC. (ii) The AEJ which can be found at the boundary of the the SAL increases the local vertical wind shear, which can de-

couple the storm's low-level circulation from its supporting mid- and upper-level deep convection. (iii) The radiative effects of mineral dust in the SAL may enhance the pre-existing trade wind inversion and act to stabilise the environment and, hence, suppress deep convection. The extremely dry air seems to undergo only little modification as it moves across the North Atlantic. The temperature inversion typically found at the SAL's base may contribute to the longevity of this dry air.

Karyampudi and Carlson (1988) and Karyampudi and Pierce (2002) assume an AEW growth related to the SAL. At the SAL's leading and southern borders convection is supported. The SAL is important for the growth and maintenance of some AEWs due to a stronger meridional circulation and greater latent heat release in cumulus convection due to stronger baroclinity along the lateral boundary of the SAL. Additionally, the SAL increases the strength of the AEJ. This leads to weak or negative potential vorticity north of the AEJ and positive potential vorticity south of it. The enhanced potential vorticity gradient leads to the growth of the wave due to barotropic instability. Both studies also state that SAL supports tropical cyclone development.

The shortwave radiative heating of the dust layer can lead to reduced ascent south of the jet when the dust concentrations are too high (Carlson and Benjamin, 1980), suppressing deep convection. Wong and Dessler (2005) also showed that the SAL is associated with suppressed convection and that this warm and dry air layer raises the lifting condensation level and the level of free convection, and increases the energetic barrier to convection that leads to reduced occurrence of deep convection.

Developing storms are typically located south of the AEJ with the SAL north of it. Braun and Shie (2008) argue that the jet is usually located on the northern side of the storm so that warmer air and greater thermodynamic stability is confined to this region. This highly stable air does not impact precipitating regions of the storm. Braun and Shie (2008) state further that the presence of dry air in the environment of tropical cyclones is not a good indicator of whether they intensify or not, based on the fact that some storms are weakened by the presence of SAL and others are not.

The early development of Hurricane Erin (2001) was characterised by unfavourable environmental and inner-core conditions (Jones et al., 2007) which are moderate shear and

mid- to upper-level dry air due to the presence of SAL. The lack of sustained heating and sustained deep convection inhibited the intensification of the disturbance. As Erin moved over warmer waters and away from the SAL, the storm intensified rapidly.

The idealised modelling study of Zhang et al. (2007) showed that an increase of cloud condensation nuclei (CCN) between 1 and 5 km lead to an increase in average cloud droplet number concentration and a decrease in cloud droplet mean mass diameter. When the CCNs represent the dust in the SAL then changes in the hydrometeor properties, diabatic heating distribution, and thermodynamic structure change the TC intensity through complex dynamical responses. Zhang et al. (2007) found that the impact of the CCN on the tropical cyclone intensity depends on the background CCN concentration.

According to the empirical study by Shu and Wu (2009), the SAL can act to intensify tropical cyclones when it occurs predominantly in the northwestern part of the storm, and it leads to a weakening of tropical cyclones when the dry air intrudes within 360 km of the tropical cyclone's centre, mostly in the southwest and southeast. The weakening is attributed to the stabilising effect of the SAL. Additionally, SAL is favourable for the initial development of tropical cyclones but unfavourable for their subsequent intensification. Shu and Wu (2009) argue that the tropical cyclones intensify due to an induced transverse circulation that promotes the upward motion and convection. In addition, weakening tropical cyclones are found to have a stronger averaged initial intensity, dry intrusions closer to the cyclones centre, and can be found further north than the intensifying tropical cyclones.

Sun et al. (2009) showed that dust aerosols are negatively associated with hurricane activity in the Atlantic in the long-term relationship between dust and tropical cyclones. They observed that during the NAMMA (NASA (National Aeronautics and Space Administration) AMMA) period, tropical disturbances form out of AEWs and south of the SAL in the vicinity of the ITCZ. When the dry and warm SAL is advected into the core of a developing cyclone, it leads to a suppression of convection and a decrease in vortical circulation, resulting in a weakening of the cyclone. Their analysis showed a low-level inversion and an increase in stability and vertical shear associated with the SAL. They further state that the warm SAL temperatures may indirectly increase vertical wind shear, evaporative cooling, and initiated mesoscale downdraughts, which bring dry air to lower levels.

The aerosols' surface radiative forcing has a net cooling effect on tropical Atlantic Ocean temperatures (Evan et al., 2006b). The surface aerosol forcing during the hurricane season is larger in magnitude than forcing associated with anthropogenic increases in greenhouse gases or sulfate aerosols, both of which have been linked to the recent increases in tropical cyclone activity. Evan et al. (2006b) suggest that, due to a distinctive reduction in dust cover over the last 30 years, the effect of dust is also to enhance the recent upward trend in Atlantic sea-surface temperature and the resultant increases in tropical cyclone intensity and frequency. Evan et al. (2006a) found that mean dust coverage and tropical cyclone activity are strongly (inversely) correlated over the tropical North Atlantic based on the analysis of satellite data for the years 1982–2005. They could not demonstrate a direct causal relationship, but they showed a link between tropical cyclone activity and dust transport over the Tropical Atlantic. Lau and Kim (2007), however, related the reduction in hurricane activity in 2006 and 2007 compared to the hurricane activity 2004 and 2005 to increased excursions of the SAL over the Atlantic.

The question as to how the SAL interacts with mesoscale convection and tropical cyclogenesis is a topic of ongoing research. Most of the previous studies are based on satellite data and only very few studies use numerical models to analyse the effect of the SAL. We are not aware of any published studies in which mineral dust transport and dust-radiation feedback is modelled explicitly for a real case of Atlantic tropical cyclogenesis.

3

COSMO Model, Configurations and Diagnostics

The numerical weather prediction model COSMO (**CO**nsortium for **S**mall scale **MO**delling) is used to simulate convection over West Africa and the eastern Atlantic in the same African easterly wave. The model system COSMO-ART (Aerosols and Reactive Trace gases) was developed to model the spatial and temporal distribution of reactive trace gases and particulate matter. Here, COSMO-ART is used to simulate the emission and transport of dust particles in West Africa. The trajectory mode LAGRANTO (LAG-Rangian ANalysis TOol) is employed to analyse the transport of mineral dust.

3.1 COSMO

The COSMO non-hydrostatic limited-area numerical model was initially developed by the German Weather Service (DWD) and was called Lokal Model (LM). It was further improved by the members of the consortium for small scale modelling, amongst them Germany, Switzerland, Italy, Greece, Poland and Romania. Since 1999 these countries have used the LM as their operational weather prediction model. In spring 2008 LM was renamed COSMO model.

COSMO was designed for operational numerical weather prediction and scientific applications on the meso- β (5-50 km) and meso- γ (500 m - 5 km) scale. It is based on the

primitive thermo–hydrodynamical equations, which describe the compressible flow in the atmosphere. A detailed model description can be found in Doms and Schättler (2002). In the following, the main implementations are summarised briefly.

3.1.1 Basic Equations

The COSMO model equations are based on the full Eulerian equations for a moist atmosphere. The Reynold’s averaging provides the formulation by which the sub–grid scale is separated from the resolved scale¹. The prognostic equation for vertical motion is used instead of the commonly used diagnostic one to take the vertical acceleration of the small–scale meteorological systems into account. Molecular fluxes, except for diffusion of liquid and solid forms of water, are neglected because they are much smaller than turbulent fluxes. The molecular fluxes of liquid water and ice are approximated by sedimentation fluxes, i.e. precipitation. The specific heat of moist air is approximated by that of dry air. The effect of phase changes and diffusion fluxes of water on the pressure tendency equation are neglected. Additionally, the mean dissipation rate due to viscous stress and the buoyancy term in the heat equation are neglected.

The equations describing the evolution of the non–hydrostatic compressible mean flow in COSMO are thus:

$$\text{momentum:} \quad \rho \frac{d\vec{v}}{dt} = -\nabla p + \rho \vec{g} - 2\vec{\Omega} \times (\rho \vec{v}) - \nabla \cdot \mathbb{T}, \quad (3.1)$$

$$\text{pressure:} \quad \frac{dp}{dt} = -\frac{c_{pd}}{c_{vd}} p \nabla \cdot \vec{v} + \left(\frac{c_{pd}}{c_{vd}} - 1 \right) Q_h, \quad (3.2)$$

$$\text{temperature:} \quad \rho c_{pd} \frac{dT}{dt} = \frac{dp}{dt} + Q_h, \quad (3.3)$$

$$\text{specific humidity:} \quad \rho \frac{dq_v}{dt} = -\nabla \cdot \vec{F}_v - (I_l + I_f), \quad (3.4)$$

$$\text{cloud water:} \quad \rho \frac{dq_{l,f}}{dt} = -\nabla \cdot (\vec{P}_{l,f} + \vec{F}_{l,f}) + I_{l,f}, \quad (3.5)$$

$$\text{equation of state:} \quad \rho = p \left[R_d \left(1 + \left(\frac{R_v}{R_d} - 1 \right) q_v - q_l - q_f \right) T \right]^{-1}, \quad (3.6)$$

$$\text{diabatic heating:} \quad Q_h = L_V I_l + L_S I_f - \nabla \cdot (\vec{H} + \vec{R}). \quad (3.7)$$

¹In the following, we omit the overbars and hats used to indicate the Reynolds and mass–weighted (Hesselberg) averaging.

The variables are defined as follows:

$\rho = \sum_{x=d,v,l,f} \rho_x$	total density of air mixture
$x = d, v, l, f$	index for mixture constituent: dry air (d), water vapour (v), liquid (l), and frozen water (f)
ρ_x	partial density of mixture constituent x
$\frac{d}{dt} = \frac{\partial}{\partial t} + \vec{v} \cdot \nabla$	total (Lagrangian) time derivative operator
$\frac{\partial}{\partial t}$	local (Eulerian) time derivative operator
$\vec{v} = (u, v, w)$	velocity relative to rotating earth
∇	gradient operator
p	pressure
\vec{g}	apparent acceleration due to gravity
$\vec{\Omega}$	constant angular velocity of earth rotation
$\mathbb{T} = \overline{\rho \vec{v}'' \vec{v}''}$	Reynolds stress tensor (turbulent flux of momentum)
$\Psi = \overline{\Psi} + \Psi'$	Reynolds average where $\overline{\Psi}$ denotes the mean value and Ψ' the deviation
$\Psi = \widehat{\Psi} + \Psi''$	mass-weighted average where $\widehat{\Psi}$ denotes mass-weighted mean and Ψ'' the deviation from $\widehat{\Psi}$
c_{pd}, c_{vd}	specific heat of dry air at constant pressure, volume
Q_h	diabatic heating/cooling
T	temperature
$q_x = \rho_x / \rho$	mass fraction of constituent x
$\vec{F}_x = \overline{\rho \vec{v}'' q_x}$	turbulent flux of water constituent x
$I_{l,f}$	phase transition rate for liquid water and ice
$\vec{P}_{l,f} = \rho q_{l,f} \vec{v}_{l,f}^T$	precipitation flux for liquid water and ice

$\vec{v}_{l,f}^T$	terminal velocity of constituent l, f
R_d, R_v	gas constant for dry air, water vapour
L_V, L_S	latent heat of vaporisation and sublimation
$\vec{H} = c_{pd}\overline{\rho\vec{v}''T}$	turbulent flux of sensible heat
\vec{R}	flux of solar and thermal radiation.

This set of equations is valid in a frame rotating with the earth.

3.1.2 Numerical Solution

For the numerical solutions the model equations are formulated in geographical coordinates and a generalised terrain following vertical coordinate χ is used, which is not time dependent. The thermodynamic variables are defined as the sum of reference state variable and the deviation from the reference state. The reference state is characterised by horizontal homogeneity, stationarity, hydrostatic balance, and it is dry and at rest. The reference pressure $p_0(z)$, temperature $T_0(z)$, and density $\rho_0(z)$ profiles are prescribed.

Due to the convergence of the meridians, the size of the grid cells decreases towards the North and South Poles. Rotated coordinates are used in the horizontal plane to avoid strong variations in the grid cell sizes. The North Pole is displaced in such a way that the equator crosses the model domain. In the present work, we do not use rotated coordinates, as the model region covers West Africa and the eastern Atlantic, i.e., is close to the equator.

The equations (3.1)-(3.7) are spatially discretised using second-order finite differences. An Arakawa C-grid with Lorenz vertical grid staggering (Arakawa and Lamb, 1981) is used. The scalars are defined at the centre of the grid box and the normal velocity components are defined on the corresponding cell faces (see Fig. 3.1).

The time integration is performed with a second-order leapfrog (horizontally explicit, vertically implicit) time split integration scheme. The model equations allow for sound

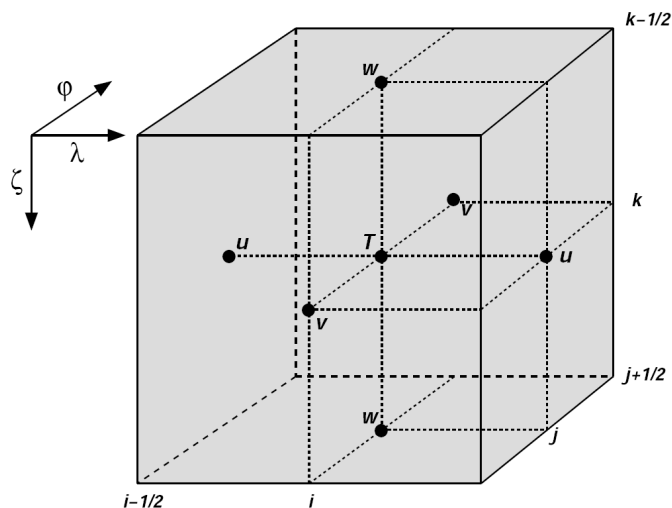


Figure 3.1: A grid box volume $\Delta V = \Delta x \Delta \lambda \Delta \varphi$ showing the Arakawa-C/Lorenz staggering of the dependent model variables. Taken from Doms and Schättler (2002).

waves, even though they are meteorologically unimportant, which has the advantage that there is an independence between different scales. However, the presence of sound waves severely limits the time step of the integration due to their fast propagation speed. It is necessary that the Courant–Friedrich–Levi (CFL) criterion, $u\Delta t/\Delta x < 1$, is fulfilled to ensure numeric stability (u is the propagation speed, Δt the numerical time step and Δx the horizontal grid scale). The time–splitting scheme of Klemp and Wilhelmson (1978) is used to accelerate the numerical integration while maintaining the required accuracy. In this approach, the prognostic equations are separated into terms which are directly linked to fast sound waves and terms representing slow modes of motion. The time step of the slow modes is divided into a number of small time steps. The fast term is computed at every small time step while slow terms are only computed at every large time step. So only a limited set of equations has to be solved using the small time step.

3.1.3 Parametrisation

With current computer resources not all processes that are relevant for the problems considered in this thesis can be resolved. A common approach to reduce the computational

costs is to choose a grid length that leads to an acceptable computational effort and to parametrise processes that occur on sub-grid scales. A detailed description of all parametrisation schemes implemented in COSMO can be found in Doms et al. (2005).

In this thesis two different model configurations are used. One set up includes a horizontal resolution of 28 km and the other of 2.8 km. For the 28-km resolution runs the subgrid-scale moist convection is parametrised using the Tiedtke mass-flux scheme (Tiedtke, 1989) with equilibrium closure based on moisture convergence. For the high-resolution model runs (2.8 km) the parametrisation of convection is switched off. The turbulent fluxes represent the exchange of momentum, heat and humidity due to turbulence. The resolvable and nonresolvable fluctuations of motion are linked by the sub-grid scale turbulence scheme. The horizontal components are neglected and the vertical diffusion is determined by using the 2.5 Mellor–Yamada closure (Mellor and Yamada, 1974). The calculation of the vertical turbulent diffusion is carried out using the semi-implicit Crank–Nicolson (Crank and Nicolson, 1947) scheme. Precipitation formation is treated using a Kessler-type bulk microphysics parametrisation (Kessler, 1969) including water vapour, cloud water, cloud ice, snow and rain with column equilibrium for the precipitating phase. The subgrid-scale clouds, are parametrised by an empirical function depending on relative humidity and height. A δ -two-stream radiation scheme (Ritter and Geleyn, 1992) with eight spectral bands is used for the short and longwave fluxes and the full cloud radiation feedback is included. The surface layer is parametrised by a stability-dependent drag-law formulation of momentum, heat and moisture fluxes according to similarity theory. A two-layer soil model (Jacobsen and Heise, 1982) employs the extended force-restore method.

3.1.4 Initial- and Boundary Conditions

Regional weather forecast models need initial and boundary data to incorporate the larger scale processes outside the model domain. This information is obtained from global models which usually have a lower resolution than the regional model. At every time step, the regional model receives information at the lateral boundaries, to ensure consistency with the large-scale flow.

External data sets, for instance, from lower resolution global models or other COSMO runs provide the initial and boundary data. The boundary conditions are updated periodically. These data are interpolated onto the model grid using the preprocessor programme INT2LM. The lateral boundary relaxation scheme of Davies (1976, 1983) is used to avoid numerical noise at the boundaries. Numerical smoothing is done with a 4th-order linear horizontal diffusion filter. The upper boundary is a lid at the top half level ², i.e. at a fixed height above the mean sea level. The lower boundary is the bottom half level, that follows the surface terrain. Rayleigh damping is applied in the upper layers. Three-dimensional divergence damping and off-centering in split time steps are also used.

In this study, the analyses from the global model IFS (Integrated Forecast System) of the ECMWF (European Centre for Medium Range Weather Forecast) are used to provide initial and boundary conditions for the regional COSMO model. Operational ECMWF analyses were available every 6 hours. All external parameters (e.g. surface data) for the model region are generated by the DWD with a preprocessor program using high-resolution global data sets.

3.2 Code Adaption for Budget Calculations

The model source code was adapted to provide information for specific humidity, temperature and momentum budgets. The specific humidity and temperature budget was implemented for COSMO 4.0 following the adaption described in Grams et al. (2010) and Grams (2008) for COSMO 3.19. Additionally, the model code was modified to output the terms of the momentum budget.

For numeric efficiency, tendency terms are split into contributions from fast-modes, FAST_Ψ , containing sound waves and gravity waves, and slow-modes, SLOW_Ψ :

$$\frac{\partial \Psi}{\partial t} = \text{SLOW}_\Psi + \text{FAST}_\Psi, \quad (3.8)$$

²The plane containing w in Fig. 3.1

where Ψ denotes a prognostic variable u, v, w, p, T , and q_v . The slow modes are related to the tendencies due to advection, mixing, Coriolis force, diabatic heating, and phase changes. The fast wave term represents changes due to the divergence term in the pressure tendency equation (Eqs. (3.2) and (3.3)), to the pressure gradient force in the horizontal and vertical equation of motion, to the buoyancy term due to pressure perturbation p' in the equation of vertical motion (Eq. (3.1)) and to the vertical advection of the base state pressure p_0 (Eq. (3.2)). The fast wave terms are integrated on the small time steps, and the slow modes can be evaluated on a bigger time step.

The total time derivative operator $\frac{d}{dt} = \frac{\partial}{\partial t} + \vec{v} \cdot \nabla$ is applied to the momentum (Eq. 3.1), temperature (Eq. 3.3), and water vapour (Eq. 3.4) equations. The Coriolis term in the momentum equation is reformulated as $2\vec{\Omega} \times \vec{v} = (lw - fv, fu, -lu)$ with $l = 2\Omega \cos\varphi$ and $f = 2\Omega \sin\varphi$. Thus the components of the momentum equation and their simplified notation are given as:

temperature tendency:

$$\frac{\partial T}{\partial t} = -\vec{v}_h \cdot \nabla_h T - w \frac{\partial T}{\partial z} + \frac{1}{\rho c_{pd}} \frac{dp}{dt} + \frac{1}{\rho c_{pd}} Q_h, \quad (3.9)$$

$$\frac{\partial T}{\partial t} = \text{HADV}_T + \text{VADV}_T + \text{FAST}_T + \text{MTD}_T + \text{MMC}_T + \text{RAD} + \text{SQ}_T + \text{COMP}_T, \quad (3.10)$$

specific humidity tendency:

$$\frac{\partial q_v}{\partial t} = -\vec{v}_h \cdot \nabla_h q_v - w \frac{\partial q_v}{\partial z} - \nabla \cdot \vec{F}_v - (I_l + I_f), \quad (3.11)$$

$$\frac{\partial q_v}{\partial t} = \text{HADV}_{q_v} + \text{VADV}_{q_v} + \text{MTD}_{q_v} + \text{MMC}_{q_v} + \text{SQ}_{q_v} + \text{COMP}_{q_v}, \quad (3.12)$$

tendency of zonal wind:

$$\frac{\partial u}{\partial t} = -\vec{v}_h \cdot \nabla_h u - w \frac{\partial u}{\partial z} - \frac{1}{\rho} \frac{\partial p}{\partial x} - fv - \frac{1}{\rho} (\nabla \cdot \mathbb{T}) \cdot \vec{i}, \quad (3.13)$$

$$\frac{\partial u}{\partial t} = \text{HADV}_u + \text{VADV}_u + \text{FAST}_u + \text{MTD}_u + \text{COMP}_u, \quad (3.14)$$

tendency of meridional wind:

$$\frac{\partial v}{\partial t} = -\vec{v}_h \cdot \nabla_h v - w \frac{\partial v}{\partial z} - \frac{1}{\rho} \frac{\partial p}{\partial y} + fu - \frac{1}{\rho} (\nabla \cdot \mathbb{T}) \cdot \vec{j}, \quad (3.15)$$

$$\frac{\partial v}{\partial t} = \text{HADV}_v + \text{VADV}_v + \text{FAST}_v + \text{MTD}_v + \text{COMP}_v, \quad (3.16)$$

tendency of vertical wind:

$$\frac{\partial w}{\partial t} = -\vec{v}_h \cdot \nabla_h w - w \frac{\partial w}{\partial z} - \frac{1}{\rho} \frac{\partial p}{\partial z} - g, \quad (3.17)$$

$$\frac{\partial w}{\partial t} = \text{HADV}_w + \text{VADV}_w + \text{FAST}_w + \text{B}_q + \text{COMP}_w, \quad (3.18)$$

with \vec{v}_h being the horizontal velocity, ∇_h the horizontal gradient operator, \vec{i} the unit vector along the x axis, and \vec{j} the unit vector along the y axis. When introducing the reference state $-\frac{1}{\rho} \frac{\partial p}{\partial z} - g$ can be written as $-\frac{1}{\rho} \frac{\partial p'}{\partial z} - \text{B}_q$, where the buoyant acceleration is given as $\text{B}_q = g \frac{\rho_0}{\rho} \left(\frac{T'}{T} \frac{T_0 p'}{T p_0} + \left(\frac{R_v}{R_d} - 1 \right) q_v - q_l - q_f \right)$. In the subgrid turbulent closure scheme horizontal homogeneity is assumed, resulting in a vertical velocity $w = 0$ and thus $\text{MTD}_w = 0$.

The tendencies due to physical processes are:

FAST_ψ : fast waves

HADV_ψ : horizontal advection

VADV_ψ : vertical advection

MTD_ψ : turbulent mixing from sensible heat flux

MMC_ψ : sub gridscale moist convection

RAD_ψ : solar and thermal radiation

SQ_ψ : cloud condensation and evaporation

B_q : contribution of water substance to the buoyancy

whith $\psi = T, q_v, u, v, w$.

The tendencies due to numerical filters are combined into the computational term, $\text{COMP}_\psi = \text{MCM}_\psi + \text{MLB}_\psi + \text{MRD}_\psi$, where:

MCM_ψ : computational mixing (horizontal diffusion)

MLB_ψ : lateral boundary relaxation

MRD_ψ : Rayleigh damping scheme within upper boundary.

The horizontal advection is given as $\text{HADV}_{T,q_v,u,v,w} = -\vec{v}_h \cdot \nabla_h(T, q_v, u, v, w)$ and the vertical advection as $\text{VADV}_{T,q_v,u,v,w} = -w \frac{\partial(T, q_v, u, v, w)}{\partial z}$. The Coriolis terms in the momentum equation for the u and v component is given as $-fv$ and fu , respectively. For the formulation of the basic model equations in the rotated spherical coordinate system several simplified assumptions are made. For instance, it is assumed that all spherical surfaces of a constant vertical coordinate have the same curvature. For consistency reasons this implies that both the Coriolis effect due to horizontal motion and the Coriolis effects on the vertical motion have to be neglected. Thus the term $-lu$ in the momentum equation for w and $-lw$ in the momentum equation for u are neglected. The pressure gradient term in the momentum equation ($\text{FAST}_u, \text{FAST}_v$) = $-\frac{1}{\rho} \nabla p$ and the total pressure derivative in the temperature equation $\text{FAST}_T = \frac{1}{\rho c_p} \frac{\partial p}{\partial t}$ represent the fast wave term. No fast mode exists for the specific humidity tendency equation. Tendencies due to Rayleigh damping, lateral boundary relaxation and computational mixing occur for each variable and are referred to as the computational terms $\text{COMP}_{T,q_v,u,v,w} = \text{MCM}_{T,q_v,u,v,w} + \text{MLB}_{T,q_v,u,v,w} + \text{MRD}_{T,q_v,u,v,w}$.

The heat equation in COSMO is written as a temperature tendency equation derived from the first law of thermodynamics. The contributions of turbulent diffusion (sensible heat flux) (MTD_T), radiation (RAD), sub-grid scale moist convection (SQ_T), grid scale moist convection (MMC_T) are combined in Q_T . In the tendency equation for the specific humidity, the latent heat flux determines the vertical diffusion, MTD_{q_v} , and specific humidity tendencies due to the grid scale and sub-grid scale moist convection are given by MMC_{q_v} and SQ_{q_v} , respectively.

For our application it is more convenient to analyse the budget of the potential temperature $\Theta = T \left(\frac{p_0}{p} \right)^{\frac{R}{c_p}}$ with $p_0 = 1000$ hPa being the standard sea-level pressure, $R = 287 \text{ J kg}^{-1} \text{ K}^{-1}$ the gas constant for dry air, $c_p = 1004 \text{ J kg}^{-1} \text{ K}^{-1}$ the specific heat of dry air at constant pressure. Following Grams (2008), the potential temperature budget can be written as:

$$\frac{\partial \Theta}{\partial t} = \frac{\Theta}{T} \left[\text{HADV}_T + \text{VADV}_T + \text{FAST}_T + \text{MTD}_T + \text{MMC}_T + \text{RAD} + \text{SQ}_T + \text{COMP}_T \right]. \quad (3.19)$$

3.2.1 Relative Vorticity Budgets

In this study, the relative and potential vorticity budgets are calculated offline based on individual terms of the temperature and momentum budgets. As the output from COSMO model is interpolated onto pressure levels, the relative and potential vorticity equations are given in pressure coordinates.

The local change of the vertical component of the relative vorticity $\zeta = \vec{k} \cdot \nabla \times \vec{v}_h$ (henceforth referred to as relative vorticity) is

$$\frac{\partial \zeta}{\partial t} = -\vec{v}_h \cdot \nabla \eta - \eta \nabla \cdot \vec{v}_h - \omega \frac{\partial \zeta}{\partial p} - \frac{\partial \omega}{\partial x} \frac{\partial v}{\partial p} - \frac{\partial \omega}{\partial y} \frac{\partial u}{\partial p} + \vec{k} \cdot \nabla \times \vec{F}, \quad (3.20)$$

where $\vec{v}_h = \vec{v}_h(u, v)$ is the horizontal wind vector, $\eta = \zeta + f$ is the vertical component of the absolute vorticity, f is the Coriolis parameter, $\omega = \frac{dp}{dt}$ is the vertical velocity in pressure coordinates (x, y, p) , \vec{F} is the frictional force, \vec{k} is the unit vector in the vertical, and ∇ is the gradient operator. As shown by Haynes and McIntyre (1987), equation 3.20 can be cast into

$$\frac{\partial \zeta}{\partial t} = -\nabla \cdot \left(\vec{v}_h \eta - \omega \vec{k} \times \frac{\partial \vec{v}_h}{\partial p} + \vec{k} \times \vec{F} \right) \equiv -\nabla \cdot \vec{K}, \quad (3.21)$$

as the flux of the relative vorticity \vec{K} has no vertical component in pressure coordinates. After integrating equation 3.21 over a closed region and applying Gauss's theorem we obtain

$$\frac{\partial C}{\partial t} = - \oint \vec{K} \cdot \vec{n} dl = - \oint \eta \vec{v}_h \cdot \vec{n} dl + \oint \omega \left(\vec{k} \times \frac{\partial \vec{v}_h}{\partial p} \right) \cdot \vec{n} dl - \oint (\vec{k} \times \vec{F}) \cdot \vec{n} dl, \quad (3.22)$$

where C is the circulation, and \vec{n} is the unit vector normal to the boundary of the closed region.

Following Davis and Galarneau (2009) (hereinafter DG09), we consider a closed region on a surface of constant pressure. For simplicity this is assumed to be a square box. In the following the overbars define the average value around the perimeter of the box, the primes denote the deviation from this value³, and the tildes indicate the average over the area of the box. The first term on the right hand side of equation 3.22 can be written as:

$$\begin{aligned} \oint (\bar{\eta} + \eta') (\bar{\vec{v}}_h + \vec{v}'_h) \vec{n} dl &= \iint \nabla \cdot ((\bar{\eta} + \eta') (\bar{\vec{v}}_h + \vec{v}'_h)) dA & (3.23) \\ &= \iint \nabla \cdot (\bar{\eta} \bar{\vec{v}}_h + \bar{\eta} \vec{v}'_h + \eta' \bar{\vec{v}}_h + \eta' \vec{v}'_h) dA \\ &= \bar{\eta} \iint \nabla \cdot (\vec{v}'_h + \bar{\vec{v}}_h) dA + \iint \nabla \cdot (\eta' \bar{\vec{v}}_h) dA + \iint \nabla \cdot (\eta' \vec{v}'_h) dA \\ &= \bar{\eta} \tilde{\delta} A + \oint \eta' \vec{v}_h \cdot \vec{n} dl. \end{aligned}$$

Thus equation 3.22 can be expressed as

$$\frac{\partial C}{\partial t} = -A \bar{\eta} \tilde{\delta} - \oint \eta' \vec{v}_h \cdot \vec{n} dl + \oint \omega \left(\vec{k} \times \frac{\partial \vec{v}_h}{\partial p} \right) \cdot \vec{n} dl - \oint (\vec{k} \times \vec{F}) \cdot \vec{n} dl. \quad (3.24)$$

The first term on the right hand side (henceforth rhs) is the mean stretching term consisting of the product of the average values of vorticity $\bar{\eta}$ and divergence $\tilde{\delta}$ over the area A .

³These primes are not to be confused with those used earlier for the Reynolds averaging.

The second term on the rhs is the eddy flux term which can increase the circulation within the box if inward flow is correlated with positive vorticity perturbations and outward flow with negative vorticity perturbations. This term is identified with the horizontal vorticity advection. The third term on the rhs describes vortex tilting and the fourth term friction. According to Stokes's theorem the circulation divided by a finite area A gives the average value of relative vorticity in this region.

3.2.2 Potential Vorticity Budgets

The Ertel potential vorticity (PV) (Ertel, 1942) combines the thermodynamic and dynamic properties of the atmospheric flow and is useful to diagnose dynamical processes. The PV is conserved in adiabatic, frictionless flow, and can be inverted, i.e. all interesting dynamic and thermodynamic fields can be recovered from the PV, given a basic state, a balance assumption, and suitable boundary conditions (Hoskins et al., 1985; Haynes and McIntyre, 1987, 1990; Bishop and Thorpe, 1994; Herbert, 2007). We use the PV in pressure coordinates:

$$q = -g(f\vec{k} + \nabla \times \vec{v}_h) \cdot \nabla\theta, \quad (3.25)$$

where q is the PV, g the acceleration due to gravity, f the Coriolis parameter, \vec{v}_h the two-dimensional wind vector, and θ the potential temperature. The PV tendency equation shows that the PV of a given air parcel can only be modified by diabatic or frictional processes (Hoskins et al., 1985):

$$\frac{dq}{dt} = \frac{\partial q}{\partial t} + v_h \cdot \nabla q + \omega \frac{\partial q}{\partial p} = -g(f\vec{k} + \nabla \times \vec{v}_h) \cdot \nabla\dot{\theta} - g(\nabla \times \vec{F}) \cdot \nabla\theta, \quad (3.26)$$

where \vec{F} is the frictional force and $\dot{\theta}$ the diabatic heating or cooling due to moist processes, turbulence and radiation.

The PV tendency equation in flux form is given as

$$\frac{\partial q}{\partial t} = -\nabla \cdot (q\vec{v}) - g \nabla \cdot [\dot{\theta} (f\vec{k} + \nabla \times \vec{v}_h)] - g \nabla \cdot [\theta (\nabla \times \vec{F})] \equiv -\nabla \cdot \vec{J}, \quad (3.27)$$

where $\vec{J} = q\vec{v} + g \dot{\theta} (f\vec{k} + \nabla \times \vec{v}_h) + g \theta (\nabla \times \vec{F})$. We see that the volume integral of the PV tendency for a given box only has contributions from the boundary terms. If the PV tendency is calculated with a finite-difference version of COSMO output on a latitude-longitude grid and standard centred differences the integral property discussed above is not satisfied. Thus we calculate the PV budget using equation 3.27.

In isentropic coordinates there is no net flux of density weighted PV (Haynes and McIntyre (1987, 1990)'s PV substance) across an isentropic surface. In pressure coordinates there can be, but the fact that, the isentropes are fairly flat shows that the net flux is small. Following Davis and Weisman (1994) we write the \vec{J} without a vertical component.

The friction was also neglected for the PV budget. Therefore, we will focus on the diabatic PV changes in the following. Thus we express the diabatic PV modification in component form as:

$$\frac{\partial q}{\partial t} = -\nabla \cdot (q\vec{v}) - g \left[-\frac{\partial}{\partial x} \left(\dot{\theta} \frac{\partial v}{\partial p} \right) + \frac{\partial}{\partial y} \left(\dot{\theta} \frac{\partial u}{\partial p} \right) \right]. \quad (3.28)$$

When the temperature anomalies are small and the isentropes approximately horizontal, there is a strong cancellation between the potential temperature tendencies due to diabatic heating and vertical advection. Thus the net flux of density-weighted PV across a pressure surface is small, and the description of the dynamical evolution using vorticity is analogous to that using PV. For our study, in which our model output is primarily on pressure levels, it is advantageous to analyse the relative vorticity budget since the vorticity flux across pressure surfaces is identically zero and we avoid the difficulties associated with calculating and interpreting the differences between two large terms of opposite sign.

3.3 COSMO-ART

The model system COSMO-ART includes the COSMO model described above and the aerosol model ART (Aerosol and Reactive Trace gases). It was developed at the Institut für Meteorologie und Klimaforschung (IMK) of the Universität Karlsruhe and the Forschungszentrum Karlsruhe, now Karlsruhe Institute of Technology. The interaction between meteorological fields and gaseous as well as particulate trace elements can be studied with fully online coupled COSMO-ART simulations. The same methods (numerical schemes and parametrisations) is used for calculating the transport of all scalars (e.g. temperature, humidity, concentrations of gases and aerosols) (Vogel et al., 2009).

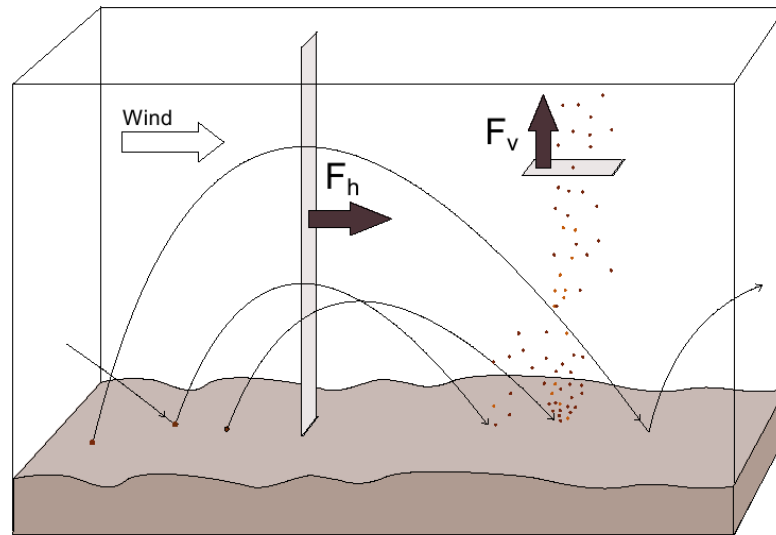


Figure 3.2: Vertically integrated horizontal flux of saltation particles F_h and the vertical flux of emitted dust particles F_v (Vogel et al., 2006).

Mineral dust particles are brought into the atmosphere by saltation processes (Vogel et al., 2006). Large particles with diameters larger than $50 \mu\text{m}$ are lifted into the atmosphere due to the Bernoulli effect. Due to gravitational forces they rapidly fall down, releasing smaller particles with a small settling velocity allowing them to remain in the atmosphere. The applied emission module for mineral dust particles was developed by Vogel et al. (2006).

A parametrisation of the threshold friction velocity (u_*) after Lu and Shao (1999) was combined with the parametrisation of the saltation processes following Alfaro and Gomes (2001) to calculate the emission of mineral dust particles. Additionally, it is necessary to

determine the vertically integrated flux of the saltation particles parallel to the surface, F_h , henceforth referred to as the horizontal saltation flux, and the vertical flux of the smaller particles in the atmosphere, F_v . Both fluxes are illustrated in Fig. 3.2. The horizontal saltation flux depends on the threshold friction velocity which depends on the particle diameter.

In COSMO-ART a grid cell can contain up to five different soil types. Information about the soil type (13 different classifications of sandy soil, the mass median diameter, the standard deviation of the particle distribution at the surface) are given by a data set (Chatenet et al., 1996). Further information about the parametrisation for the emission of mineral dust particles can be found in Vogel et al. (2006, 2009) and Hoose (2004).

3.3.1 Transport of Mineral Dust in COSMO-ART

Additional prognostic equations, the so called aerosol dynamic equations, are solved in COSMO-ART to calculate the transport of the aerosols. The changes of the particle size distribution are calculated in the module MADEsoot (Modal Aerosol Dynamics Model for Europe extended by Soot) (Ackermann et al., 1998; Riemer et al., 2003). Processes like coagulation, condensation and evaporation can be neglected for mineral dust particles. Besides, mineral dust particles do not take part in chemical reactions and chemical reactions do not take part on them within COSMO-ART (Stanelle, 2008).

The deposition can be divided into dry and wet deposition. The sedimentation, which has the strongest influence on the size distribution of the mineral dust particles, and the Brown diffusion are taken into account when computing the dry deposition (Slinn and Slinn, 1980). The parametrisation of the wet deposition has recently been included into COSMO-ART by Rinke (2008) but is not applied for the model runs in this study.

The aerosol dynamic equations are solved based on a modular approach in the module MADEsoot for certain moments of the particle distribution (Vogel et al., 2009). Three overlapping distributions describe the total distribution of the mineral dust particles where a single mode is approximated by a continuous distribution function (Stanelle, 2008). These functions are log-normal distribution. The applied values for the distribution function are listed in Tab. 3.1.

Table 3.1: Parameters of the distribution function for the mineral dust particle modes in COSMO-ART (Alfaro and Gomes, 2001).

Mode	Geometrical standard deviation	Mass median diameter of the mass density distribution
1	1.5	1.7 μm
2	1.6	6.7 μm
3	1.7	14.2 μm

3.3.2 Radiation in COSMO-ART

The parametrisation scheme for radiation in COSMO is called GRAALS (General Radiative Algorithm Adapted to Linear-type Solutions) and is based on the parametrisation of Ritter and Geleyn (1992). The parametrisation scheme is based on the solution of the δ -two stream version of the radiative transfer equation incorporating the effects of scattering, absorption, and emission by cloud droplets, aerosols, and gases in each part of the spectrum. The transfer of long- and shortwave radiation for cloud and non-cloud conditions is calculated separately. Three solar and five terrestrial bands are used. A detailed description can be found in Stanelle (2008); Stanelle et al. (2010).

Mineral dust particles are part of the continental aerosol type. Their distribution is constant in time. For the COSMO-ART simulations in this study we assumed a constant mineralogical composition of the mineral dust particles in the whole model domain. Additionally, the size distribution of the mineral dust particles is assumed to be constant in time and space for each mode in the Mie-calculation. The variation of the mass median diameter of the size distribution during the transport is not taken into account.

Mineral dust events in Africa have a high spatial and temporal variability and can lead to an optical thickness of over 3.0. The optical properties of the current mineral dust distribution are used in COSMO-ART (Stanelle, 2008). The extinction coefficient, the single scattering albedo, and the asymmetry factor have to be computed for every model level and the 3 shortwave and 5 longwave spectral bands because they are necessary to solve the radiative transfer equation. Mie-calculation is applied using the refraction indices to compute the specific extinction coefficient (mass extinction coefficient), the single scattering albedo and the asymmetry parameter for the three dust modes, and the

eight spectral bands. As the Mie-calculation is quite costly, it is carried out once off-line (Fig. 3.3).

COSMO-ART

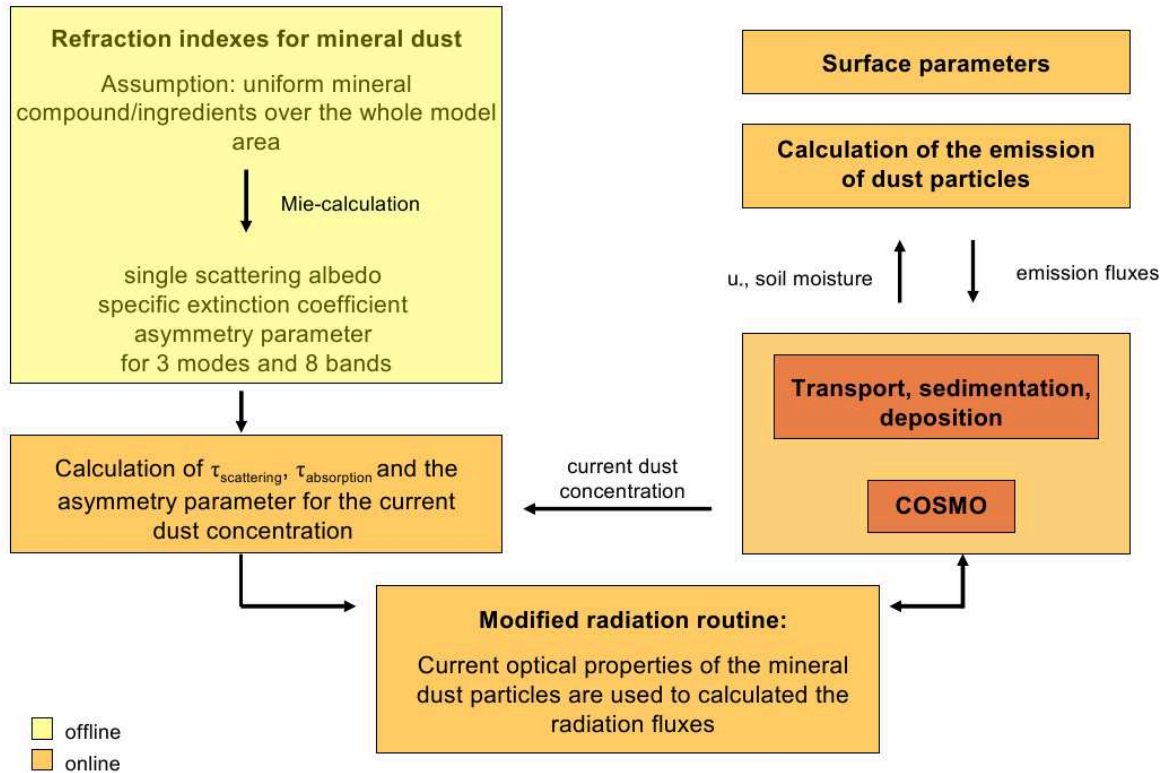


Figure 3.3: The interaction between the current mineral dust distribution and the state variables of the atmosphere in COSMO-ART (adapted from Stanelle (2008)).

The numerical code for the Mie-calculation is based on Bohren and Huffman (1983). The parameters obtained from the Mie-calculation are used to determine the optical thickness of mineral dust, the optical thickness of scattering, $\tau_{scatter}$, the optical thickness of absorption, τ_{absorb} , and the asymmetry factor of the total distribution for every grid cell (Stanelle et al., 2010).

The total aerosol optical thickness is calculated using the current optical properties of the mineral dust distribution, and the optical properties of the other aerosols. The results are taken into account when calculating the radiant flux density. For each call of the radiation routine the optical properties are computed.

3.4 Trajectory Calculations

Forward and backward trajectories are calculated using the trajectory model LAGRANTO (Wernli and Davies, 1997). The Lagrangian scheme is used to diagnose the origin and the nature of the spatial evolution of the Saharan air layer (SAL). It also helps to illustrate the proximity of relatively dry air to the tropical cyclone centre.

The flow in a Lagrangian framework is described by the position \vec{r} of an air particle as a function of its label, \vec{s} , and time, t , i.e. $\vec{r} = \vec{r}(\vec{s}, t)$. The label, \vec{s} , refers to a spatial location at a defined reference time. So the framework moves with the individual air parcels. LAGRANTO determines the physical properties and the spatial coordinates of the air parcels at a reference time. It collects all the locations and properties for the same air parcel for prior or subsequent times. Typical physical variables are, for example, potential temperature, humidity, and potential vorticity. The kinematic evolution in LAGRANTO is based on the work of Petterssen (1956); Whitaker et al. (1988); Kuo et al. (1992) and Reed et al. (1992).

The trajectories start from every model grid point within a predefined three-dimensional domain whose size and domain depends on the specific application. Time traces are determined for the horizontal and vertical position (longitude, latitude, pressure) as well as the physical properties for each trajectory. A limited number of trajectories is selected by applying one or more specific dynamically based criteria.

The first possibility is to use *a priori* criteria, where the selected trajectories describe macro air parcels that stream out from a domain characterised at a reference time by values of a field variable (e.g. potential vorticity) that exceed, or fail to exceed, a specific threshold. *A posteriori* criteria, on the other hand, is based upon the time trace of the air-parcel path (e.g. significant ascent or descent during a certain time interval) or of physical characteristics along the path (e.g. significant increase of potential vorticity). For each criterion a threshold value for significance has to be defined. The other possibility is to apply *a priori* and *a posteriori* criteria at the same time. For instance, one could define air with potential vorticity values larger than 2 PVU (1 PVU = $10^{-6} \text{ K kg}^{-1} \text{ m}^2 \text{ s}^{-1}$) with an *a priori* criteria, and with an ascent larger than a specific value with an *a posteriori* criteria.

The trajectory calculations are based on the European Centre for medium-range Weather Forecasts (ECMWF) operational analysis and COSMO runs. The fields of temperature, specific humidity, surface pressure, and the three wind components are interpolated onto a regular latitude-longitude grid with a grid spacing of 28 km. Secondary diagnostic variables like relative humidity, potential temperature, potential vorticity, and the diabatic heating rate can be determined, too. Further descriptions and applications of LAGRANTO can be found in Wernli (1997) and Stohl et al. (2001).

4

Convective Systems over West Africa and the eastern Atlantic

Mesoscale convective systems (MCSs) embedded in African easterly waves (AEWs) are responsible for about 80% of the rainfall in West Africa (Eldridge, 1957; Omotosho, 2003; Laurent et al., 1998; Mathon et al., 2002), and they are the seed disturbances for the development of tropical cyclones (Gray, 1968; Frank, 1970; Avila and Pasch, 1992; Landsea et al., 1998; Thorncroft and Hodges, 2001). To improve our understanding of the interaction between AEWs and MCSs, we analyse convective systems over West Africa and over the Atlantic that occur in the same AEW, by contrasting their nature and evolution. We use the COSMO model to simulate the convective systems, and apply the same analysis techniques for all systems. Additionally, we analyse the potential temperature and relative vorticity budgets for different parts of the convective systems to address the question as to how the MCS modifies its environment. The content of this chapter is published in Schwendike and Jones (2010).

The case study we have chosen is the AEW out of which Hurricane Helene (2006) developed. It occurred in September 2006 during the special observation period of the African Monsoon Multidisciplinary Analyses (AMMA) project (Redelsperger et al., 2006).

On 10 September 2006 at around 00 UTC a MCS embedded in the AEW out of which Hurricane Helene developed was located over West Africa (Fig. 4.1 A). It moved across West Africa (Fig. 4.1 B) and the associated clouds changed from a circular shape to a

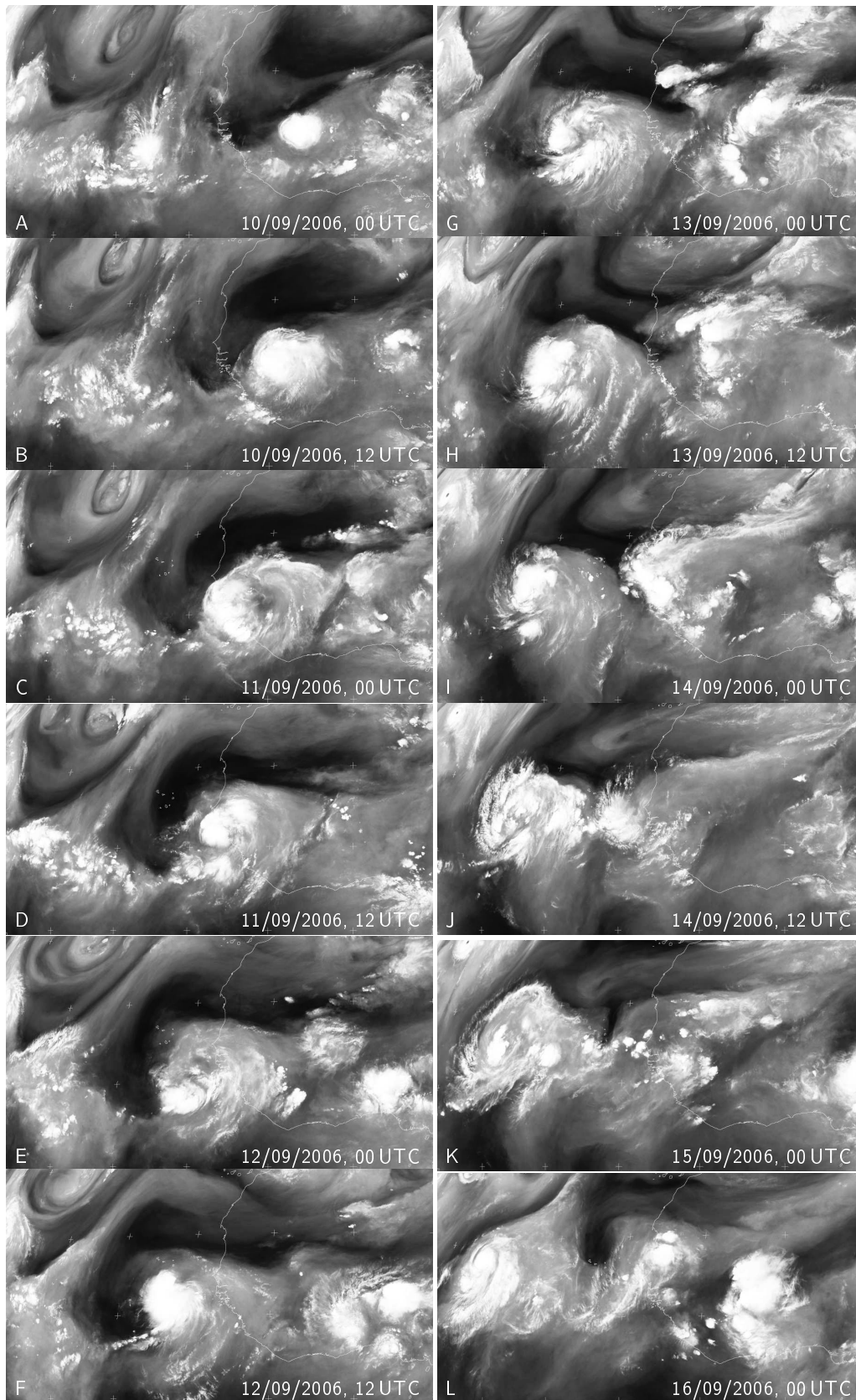


Figure 4.1: A convective system over West Africa and the eastern Atlantic is shown in the METEOSAT water vapour images from channel 5, starting on 10 September 2006, 00 UTC every 12h until 15 September, and 16 September, 00 UTC. The latitude ranges from 0°N to 30°N and the longitude 10°E to about 45°W.

comma shape (Fig. 4.1 C), when the convective system was crossing the West African coastline on 11 September 2006 at around midnight. Another MCS was initiated afterwards that passed Dakar, Senegal, on 11 September at 12 UTC (Fig. 4.1 D). Over the eastern Atlantic the convective activity was initially weak (Fig. 4.1 E) but several intense convective bursts occurred between 12 and 14 September 2006 (Fig. 4.1 F-I). Helene's track (Fig. 4.2) shows that the convective system was organised enough to be classified a tropical depression on 12 September 2006 at 12 UTC (Fig. 4.1 F). It was upgraded a tropical storm on 14 September 2006 at 00 UTC (Fig. 4.1 I), and reached hurricane intensity on 16 September 2006 at 12 UTC. Helene's minimum pressure of about 955 hPa occurred on 18 September. Between 21 and 22 September, Hurricane Helene made recurvature and became extratropical on 14 September 2006. Helene is analysed from a kinetic energy point of view by Arnault and Roux (2009).

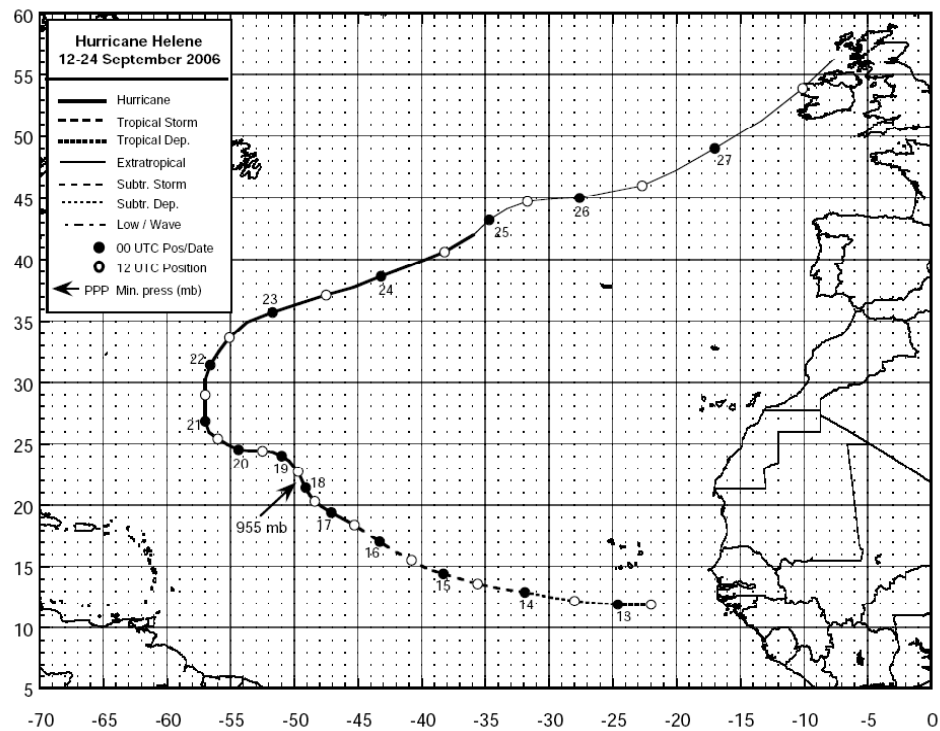


Figure 4.2: The best-track for Hurricane Helene (2006) from the U.S. National Hurricane Center (NHC). The position of the storm is shown at 12 hourly intervals. The open circle displays the the position at noon, and the filled circle the position at midnight for the time period between 12 September 2006, 12 UTC, and 27 September 2006, 12 UTC. The estimation of the minimum central pressure (mb) is indicated by the arrow.

4.1 Synoptic Situation and COSMO simulations

The synoptic conditions for the period between 9 and 14 September 2006 in which the convective systems analysed in this study took place, the model setup, and the methodology for the budget calculations are presented in the following.

4.1.1 Synoptic Situation

An AEW was generated over West Africa on 2 September 2006 in the early morning hours at about 33°E (Fig. 4.3). The trough of the AEW is characterised by high relative vorticity. This AEW propagated westward across West Africa and reached 40°W on 15 September 2006 at around midnight. Its genesis appeared to be related to a large region of convection which was initiated west of the Ethiopian Highlands, at about $30\text{--}34^{\circ}\text{E}$ and $12\text{--}15^{\circ}\text{N}$, on 1 September 2006. This can be seen in the METEOSAT water vapour imagery of that day (not shown). Convection was apparent in this region and its environment for the following 24 h. Previous studies (e.g. Burpee (1972) and Hodges and Thorncroft (1997)) have indicated that the orography in eastern Africa is important for the triggering of AEWs. More recent studies (e.g. Hill and Lin (2003) and Berry et al. (2007)) showed AEW genesis associated with a large convective complex that was originated over the Ethiopian Highlands. Two additional AEWs with less intense vorticity maxima can be seen in Fig. 4.3 as well. The first one was initiated on 2 September at about 20°E and reached 40°W on 12 September, and the second wave was initiated on 6 September at about 38°E and was located around 20°W on 15 September. In the following we will focus on the AEW initiated on 2 September at around 33°E , out of which Hurricane Helene developed.

At around 15 UTC on 9 September 2006, convection was initiated ahead of the trough of the AEW with maximum vorticity values occurring in a region around $3^{\circ}\text{W}\text{--}4^{\circ}\text{W}$ and $13^{\circ}\text{N}\text{--}15^{\circ}\text{N}$, including the northwestern part of Burkina Faso and the adjacent region in Mali (not shown). The large-scale environment on that day was similar to that observed in Parker et al. (2005b) except that the relatively moist monsoon flow had a very large westerly component and the AEJ had a very strong northeasterly component in the region

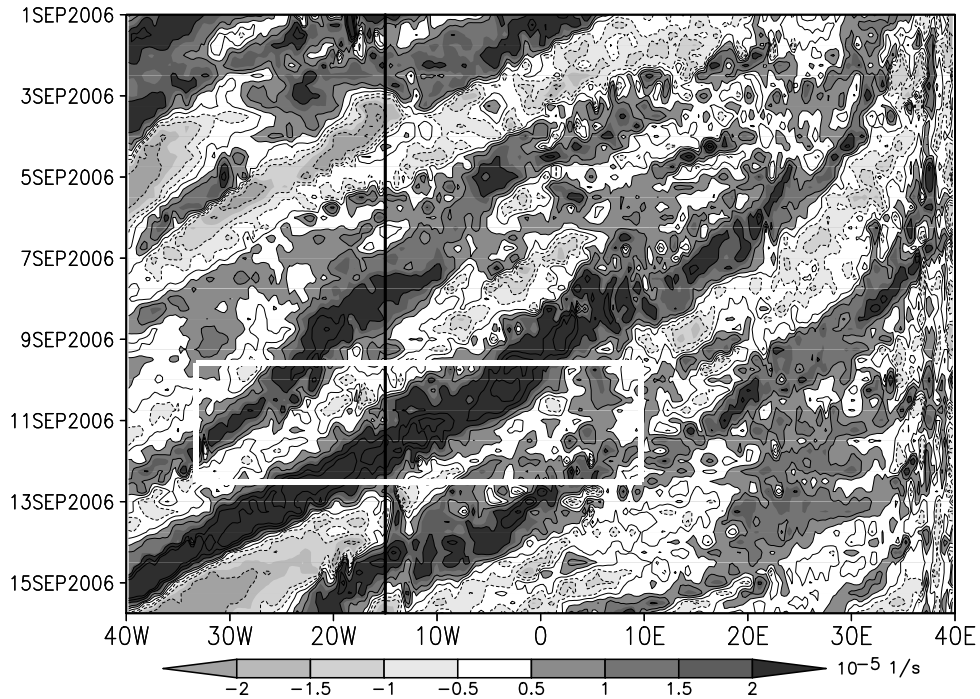


Figure 4.3: The 700-hPa relative vorticity (10^{-5}s^{-1}) Hovmöller diagram from the ECMWF operational analysis between 1 September 2006, 00 UTC and 15 September 2006, 18 UTC. The relative vorticity is averaged between 6°N and 16°N . The white frame depicts the area and time this study focuses on.

where the convection occurred. As the convective system moved across West Africa it kept its position relative to the AEW. The maximum of the AEJ occurred at a height of about 600 hPa and was located to the northwest of the convective system.

The convective system grew rapidly into a mature MCS which reached its peak intensity during the late evening hours (Fig. 4.4a). In the early morning on 10 September, the system began to decay slowly (Fig. 4.4c and e). In the following hours, a new convective burst occurred in the region of the decaying westward moving system. In the late afternoon, a squall line formed at around 10°W . The convection was enhanced as the system crossed the Guinea Highlands and it reached the West African coast line at around midnight. Over the eastern Atlantic, this system decayed. On 11 September at around 00 UTC, a new convective system was triggered southeast of Dakar at around $12\text{--}14^{\circ}\text{W}$ and $13\text{--}14^{\circ}\text{N}$. It grew rapidly into a mature MCS over land and decayed as it crossed the West African coast (Fig. 4.4g). Afterwards, the convective activity was generally relatively low. A few hours later, several large convective bursts occurred and by 11 UTC on 12 September (Fig. 4.4k) the system was organised enough to be classified as

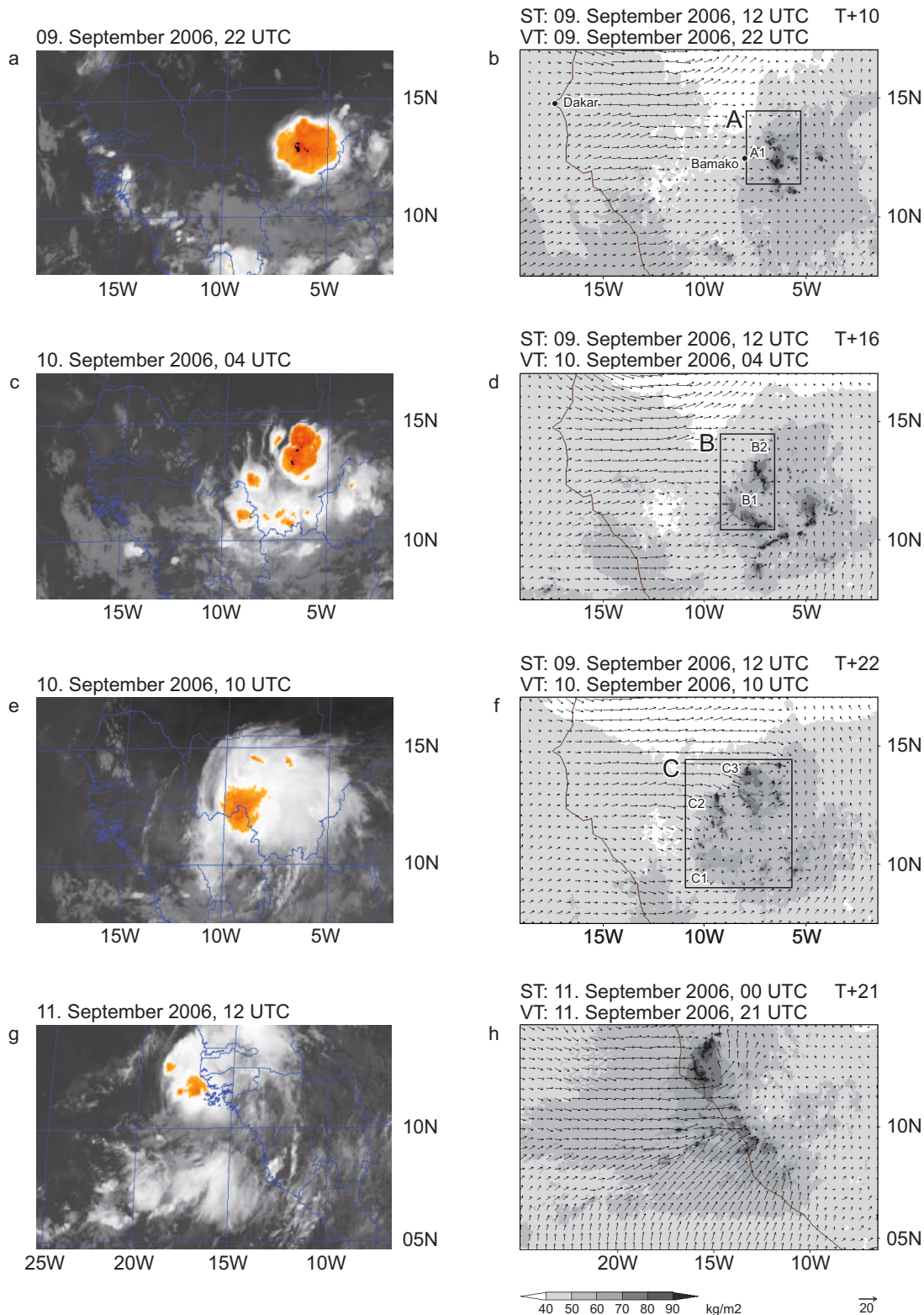


Figure 4.4: Left column: Meteosat 8 infrared images ($10.8 \mu\text{m}$ channel) where convective objects are superimposed using shadings of grey above -64°C , orange–red colours between -64° and -82°C , and black below -82°C . Right column: The vertical integral of cloud water, cloud ice and humidity (kg m^{-2}) as well as the horizontal wind (m s^{-1}) at 975 hPa based on the 2.8–km COSMO runs are shown at selected stages of the life cycle of the convective systems at the date and time given above the image. ST denotes the starting time of the simulation, and VT denotes the verification time. Details for the COSMO model regions are listed in Tab. 4.1. The subplots b, d, f correspond to model run 2, h to run 3, j, l, n belong to run 4, and p is a section of model run 5.

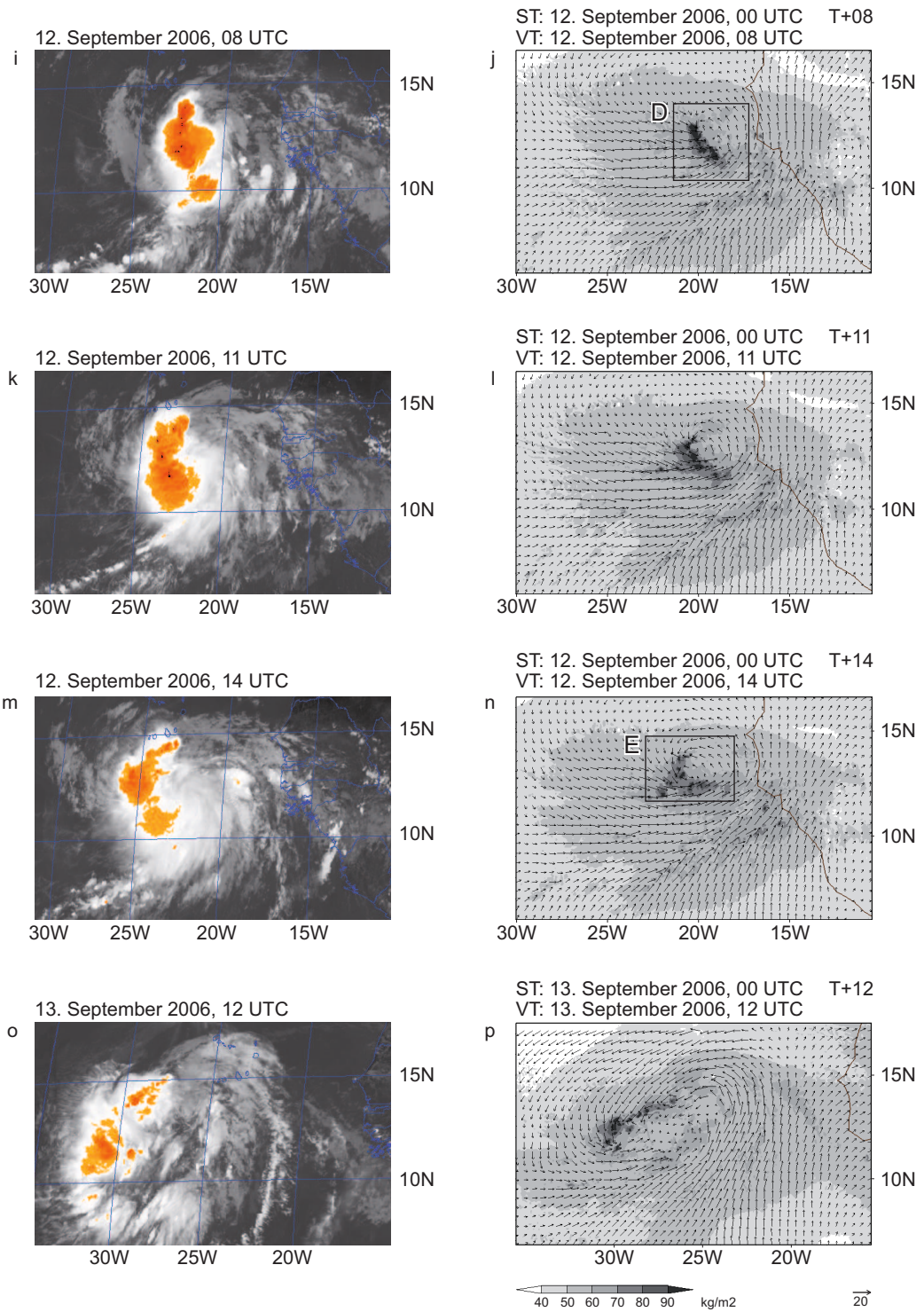


Figure 4.4: (Continued.)

a tropical depression while the centre was located approximately 370 km south–southeast of the Cape Verde Islands (Braun, 2006). During this period the convection moved into the trough of the AEW and kept this position throughout the cyclogenesis. From this time on it is no longer the high positive relative vorticity of the AEW that can be seen in Fig. 4.3, but that of the strengthening Tropical Depression which moved westward within the trough of this AEW. When the system was about 140 km south of the Cape Verde Islands, the circulation remained rather large and broad. Along with some easterly shear this was likely to delay the strengthening during the early stage of the system. On 13 September, convective banding began to increase in the northwestern part of the circulation (Fig. 4.4o). The convective system was upgraded to Tropical Storm Helene at 00 UTC on 14 September. Moving west–northwestward, Helene steadily intensified and became a hurricane at 12 UTC on 16 September. Helene continued to strengthen and became a category 3 storm on the Saffir–Simpson scale. Six hours later it reached its peak intensity with maximum sustained surface wind of about 54 m s^{-1} .

4.1.2 COSMO Simulations

For our case study we use the **CO**nsortium for **S**mall scale **MO**delling (COSMO) non–hydrostatic limited–area numerical model.¹ COSMO is based on the primitive thermo–hydrodynamic equations which describe compressible flow in a moist atmosphere (Doms and Schättler, 2002). A generalised terrain–following height coordinate with rotated geographical coordinates and a grid stretching in the vertical are used for the coordinate system.

The initial and boundary conditions for all runs are taken from 6–hourly European Centre for Medium Range Weather Forecasts (ECMWF) operational analyses. The different model regions for this study are given in Fig. 4.5 and Tab. 4.1. The COSMO run with a horizontal resolution of 28 km (area 1 in Fig. 4.5 and Tab. 4.1) covers a domain from -60 – 20°E and 0 – 45°N . The coordinates are not rotated. A series of high–resolution runs with 2.8 km horizontal resolution were carried out such that the first model region (area 2 in Fig. 4.5) was centred around the MCS over Burkina Faso. As the system moved across

¹www.cosmo-model.org

Table 4.1: Details of COSMO runs giving the initiation time, longitudinal and latitudinal extent of the domain and the horizontal resolution. The duration of each run is 72 h.

COSMO run	Initialisation	Longitude	Latitude	Resolution
1	9 Sep 2006, 12 UTC	60.0°W-12.0°E	1.0-40.0°N	28.0 km
2	9 Sep 2006, 12 UTC	19.5-1.025°W	7.0-17.5°N	2.8 km
3	10 Sep 2006, 12 UTC	24.5-6.025°W	5.0-15.975°N	2.8 km
4	11 Sep 2006, 00 UTC	30.0-6.025°W	4.0-14.975°N	2.8 km
5	12 Sep 2006, 00 UTC	32.0-10.025°W	5.0-16.975°N	2.8 km

West Africa the position of the model region was adjusted for each subsequent run. All the runs are 72-h in duration and the model region is always centred around the convective system. This model setup includes 50 vertical levels. The top level in this study is at 20 hPa. The vertical resolution in the boundary layer is enhanced. The model source code was adapted to provide information for moisture, temperature and momentum budgets (Grams et al., 2010).

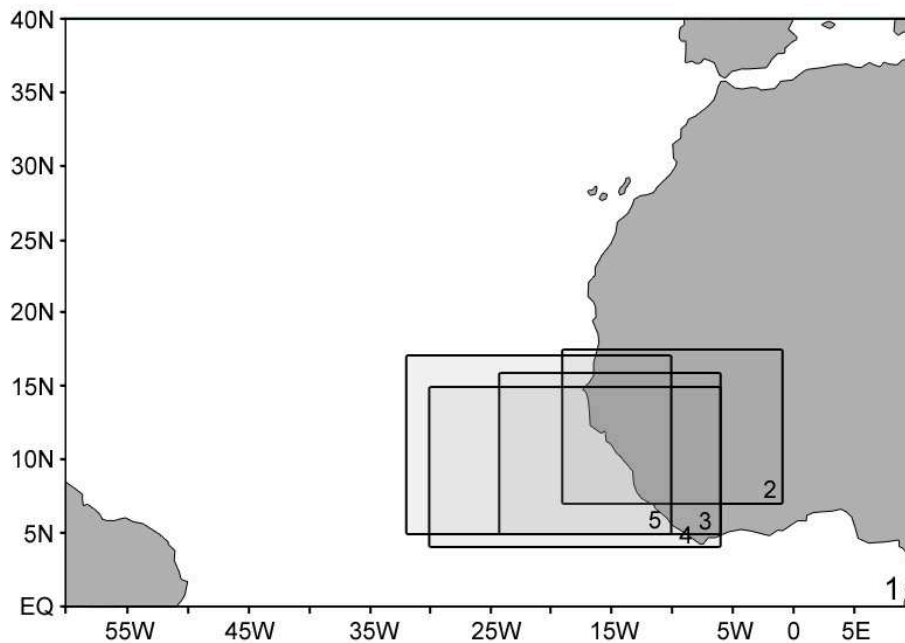


Figure 4.5: The different model regions are displayed here. Further description can be found in Tab. 4.1.

For the 28-km resolution runs, the subgrid-scale moist convection is parametrised using the Tiedtke mass-flux scheme (Tiedtke, 1989) with equilibrium closure based on moisture convergence. For the high-resolution model runs the parametrisation of convection is switched off.

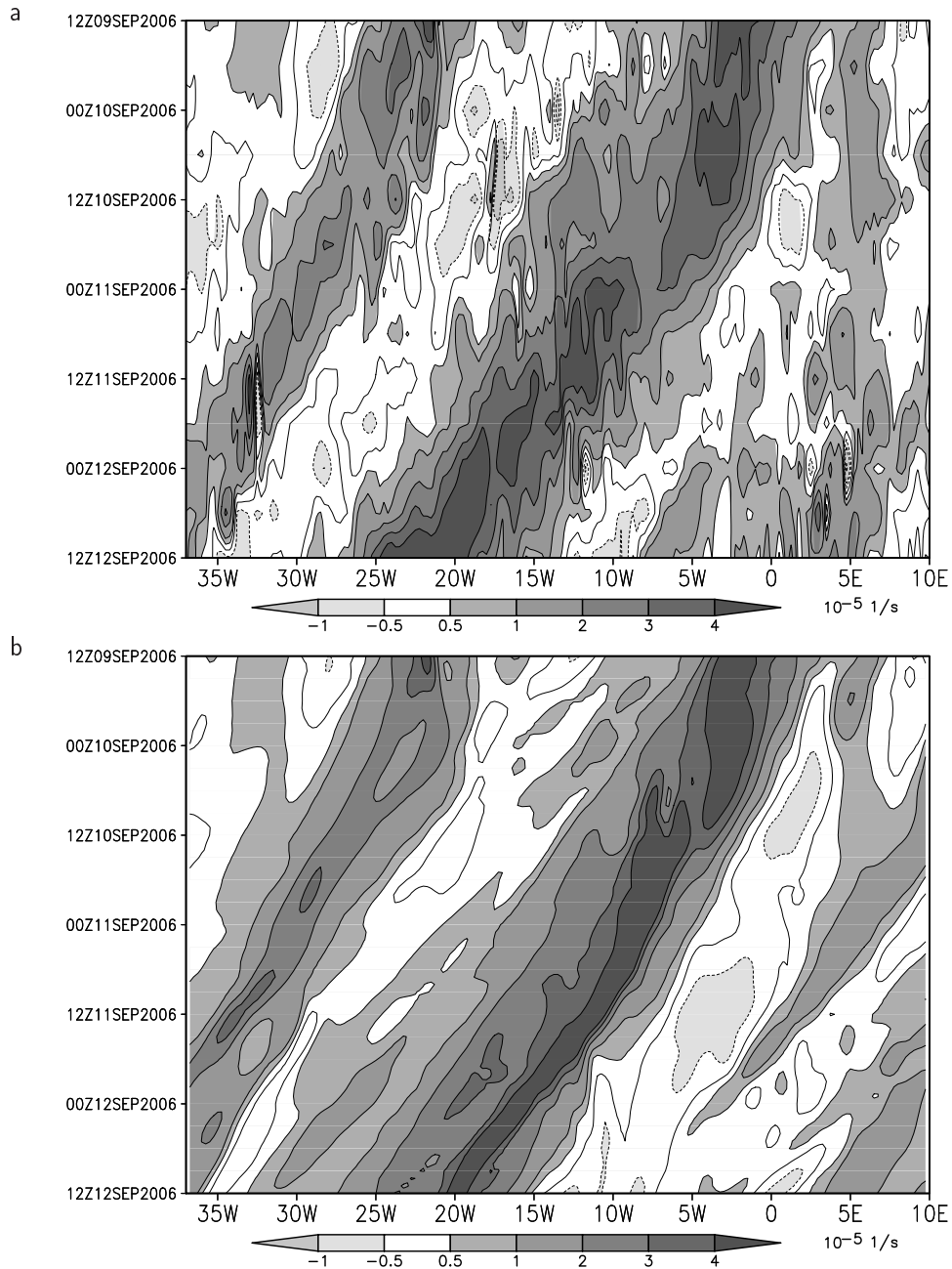


Figure 4.6: Hovmöller diagram of the 700-hPa relative vorticity (10^{-5}s^{-1}) (a) in the ECMWF analysis and (b) in the COSMO run initialised at 12 UTC on 9 September 2006 with a resolution of 28 km. The time starts at 9 September 2006, 12 UTC and ends at 12 September 2006, 12 UTC. The relative vorticity is averaged between 6°N and 16°N . The ECMWF analysis is available at 6 hourly intervals and the COSMO model output at hourly intervals.

The ability of the model to reproduce the observed AEW is illustrated with a comparison of the analysed and forecast Hovmöller plots (Fig. 4.6) for the period indicated by the white frame in Fig. 4.3. Two AEWs are seen in this period. The AEW preceding the one from which Hurricane Helene develops is depicted very well by the model with its maximum of the vertical component of the relative vorticity occurring on 9 September 12 UTC at about 23°W and on 12 September 00 UTC at around 37°W . The second AEW with the much stronger relative vorticity was generated over West Africa on 2 September at about 33°E as mentioned in the previous section. This is the AEW out of which Hurricane Helene developed which is well captured by the model.

The main difference between the simulated AEW and the AEW in the ECMWF analysis is the position of the maximum of the relative vorticity. In the COSMO 28-km run the maximum relative vorticity on 12 September, 12 UTC covers a region between 19 and 21°W whereas in the ECMWF analysis the relative vorticity maximum covers a region from about 19°W to 25°W . The difference in the extent of the vorticity maximum could be seen already on 10 September at around noon when the maximum was located between 3°W - 7°W in the ECMWF analysis and between 2°W - 5°W in the simulation.

The AEW in the ECMWF analysis has a phase speed of about 9 m s^{-1} , whereas the AEW in the 28-km horizontal resolution COSMO simulation has a phase speed of about 8 m s^{-1} and is therefore slightly slower. Note, the vorticity maximum seen in the Hovmöller plot is not only that of the wave but also of the convective system.

The Meteosat 8 infrared imagery and the model derived vertically integrated cloud ice, water vapour and humidity (total water) are used to assess the ability of the high-resolution model runs to simulate the convective system. High values of total water, which indicate the convective updraught cores, are compared to the convective regions in the satellite images, highlighted by the orange-red colours. In general, the total water images indicate the convective updraught cores whereas the water vapour images illustrate the cirrus shield of the system (Fig. 4.4). However, we are still able to compare the size, the position and the shape of the convective systems.

A large MCS, which was initiated at around 15 UTC on 9 September 2006 over Burkina Faso, is evident in the COSMO run initialised at 9 September 2006 at 12 UTC. After

the initiation the system intensified quickly and its leading edge can be seen in Fig. 4.4b as a north south orientated band with an area of deep convection (A1). The near-surface winds depict the mostly westerly monsoon flow. The regions with maximum total water content resemble the dark orange and black regions in the infrared images where a circularly shaped MCS is visible. The two regions of high total water in Fig. 4.4d (B1 and B2) are located in a similar position to the leading edge of the convective region in the infrared image (Fig. 4.4c). One hour later a third convective cell could be observed within the MCS, which reached its mature state shortly afterwards in the COSMO run. The convective system C1 decayed, followed by C2 and then C3 (Fig. 4.4f.) The COSMO run was able to capture these structural changes well.

It is not possible to distinguish in the infrared imagery between the individual convectively active regions seen in the modelled total water fields. However, a circular-shaped MCS with a large cirrus shield is seen. This MCS was decaying and, as it approaches the Highlands of Guinea, new convective cells were initiated and the structure of the system changed from a circular shape to a comma shape (not shown). In the evening hours of 10 September the system was a squall line, that crossed the West African coast at around 11 September, 00 UTC. This change in structure and intensity was observed also in the model simulation. The main difference is that the modelled system moved more slowly than in reality. It reached the same position as in the satellite image but about 6 hours later and not with the same intensity. A similar effect was observed by Chaboureaud et al. (2005) who simulated an MCS over West Africa with the Meso-NH model initialised with ECMWF analyses. They found that the simulated squall line propagated more slowly than the observed one. Diongue et al. (2002) used the same model but initialised it with the ERA-15 data and observed a squall line that reached the same location as in the observations 3 hours later.

When the squall line system reached the eastern Atlantic the convection decayed. This was simulated by the model as well, but it occurred several hours later. Meanwhile, a new convective system was initiated south east of Dakar and grew rapidly into a mature MCS. When it crossed the coastline it decayed over the ocean. Again, this process was delayed by about 9 hours in the model compared to the observations (Fig. 4.4g,h).

Over the Atlantic the AEW moved over a large-scale southwest–northeast oriented monsoon trough with strong southwesterly flow to the southeast and subsequently a surge of northeasterly flow to the north (Fig. 4.4j,l,n,p). The synoptic environment has been described in more detail by Arnault and Roux (2010). At this time the character of the convective system changed. It was no longer one large MCS with either a circular or comma shape, but several large convective bursts occurred embedded in a mesoscale circulation. Most of the times the convective bursts were initiated in the northwestern part of the circulation and grew very rapidly. As they moved around the circulation centre towards the southwest they decayed more slowly. While the old system decayed, a new convective burst was initiated in the north–northeast which moved in the same manner. One example of these big convective bursts is shown in Fig. 4.4j, l, n and a second one is shown in Fig. 4.4p. The low-level circulation intensified, the northeasterly trade winds in the north–west of the convective system extended southwards to almost 12°N , and the southwesterly flow on the western and southwestern side of the circulation strengthened. After 12 September, 12 UTC, the convective systems embedded in the circulation were organised enough for the circulation to be classified as a tropical depression. The model was able to capture these structure and intensity changes very well.

The evolution over the Atlantic, in which a series of convective bursts within a monsoon trough lead to the genesis of a tropical cyclone, resembles the case studied by Harr et al. (1996). In their case a series of MCSs developed within a large-scale monsoon depression, enhancing its vorticity, reducing the scale of the low-level circulation, and thus, in concert with interactions with large-scale circulations, promoting the cyclogenesis event. The evolution of the low-level circulation in the Helene case will be discussed later.

Radiosoundings from Dakar (Senegal) and Bamako (Mali)², which were obtained during the special observation period SOP3 of the AMMA campaign were used to validate the model results (Fig. 4.4a). The temperature, wind speed and relative humidity profiles

²The sounding from Bamako launched at 2232 UTC at 7.95°W , 12.53°N and ended at 2324 UTC will be referred to in the following as the “23 UTC” sounding. At this time Bamako was ahead of the AEW trough axis. The second sounding from Bamako is released on 10 September at 1033 UTC at 7.95°W , 12.53°N and ended at 1157 UTC and will be called the “11 UTC” sounding. It was also located ahead of the AEW axis and at the southern side of the stratiform region of the convective system C3. The first Dakar sounding is launched on 9 September 2006 at 2232 UTC at 17.49°W , 14.75°N , ended at 2344 UTC and is also referred to as the “23 UTC” sounding. At this time the AEJ maximum is slightly north of Dakar, which is close to the ridge of the preceding AEW. The second Dakar sounding is released on 11 September at 1037 UTC at 17.49°W , 14.75°N and ended at 1159 UTC and is also referred to as the “11 UTC” sounding. Again, the AEJ maximum occurs just over Dakar, ahead of the AEW trough axis.

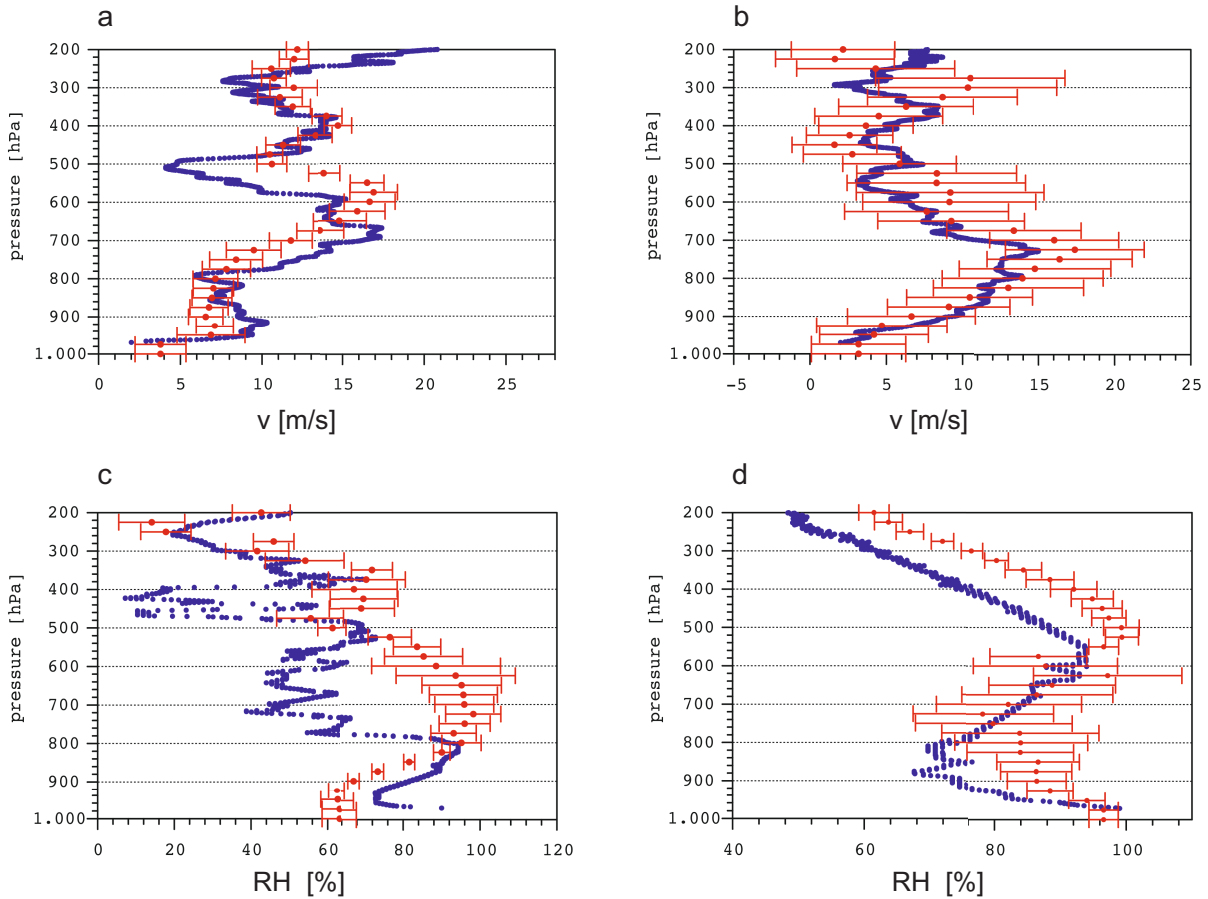


Figure 4.7: Profiles of horizontal wind speed (m s^{-1}) (upper row) and relative humidity (%) (lower row) from radiosondes, released at Bamako (7.95°W , 12.53°N), Mali, at (a, c) 09 September 2006, 2232 UTC and at (b, d) 10 September 2009, 1033 UTC (blue dots), together with the corresponding model output from the 72-hour COSMO forecast initialised at 12 UTC on 9 September 2006 (red dots). The horizontal bars indicate the standard deviation of the model output in a $0.5^\circ \times 0.5^\circ$ square centred on the closest grid point. Pressure (hPa) is used as the vertical coordinate.

from the radiosoundings at these stations were compared with profiles from the COSMO runs. The agreement between the model results and the observations for the temperature profiles is good. The departure of the observed temperature profile from that of the closest model grid point is generally within the standard deviation of the neighbouring grid points (not shown).

Soundings from Bamako and Dakar on 9 September 2006 at around 23 UTC, illustrating the pre-MCS conditions at both stations, can be found in Figs. 4.7 and 4.8. The AEJ occurs at around 700 hPa over Bamako with wind speed values of about 17 m s^{-1} . In Dakar, however, the AEJ occurs at slightly higher altitudes, i.e. 600-650 hPa, with wind

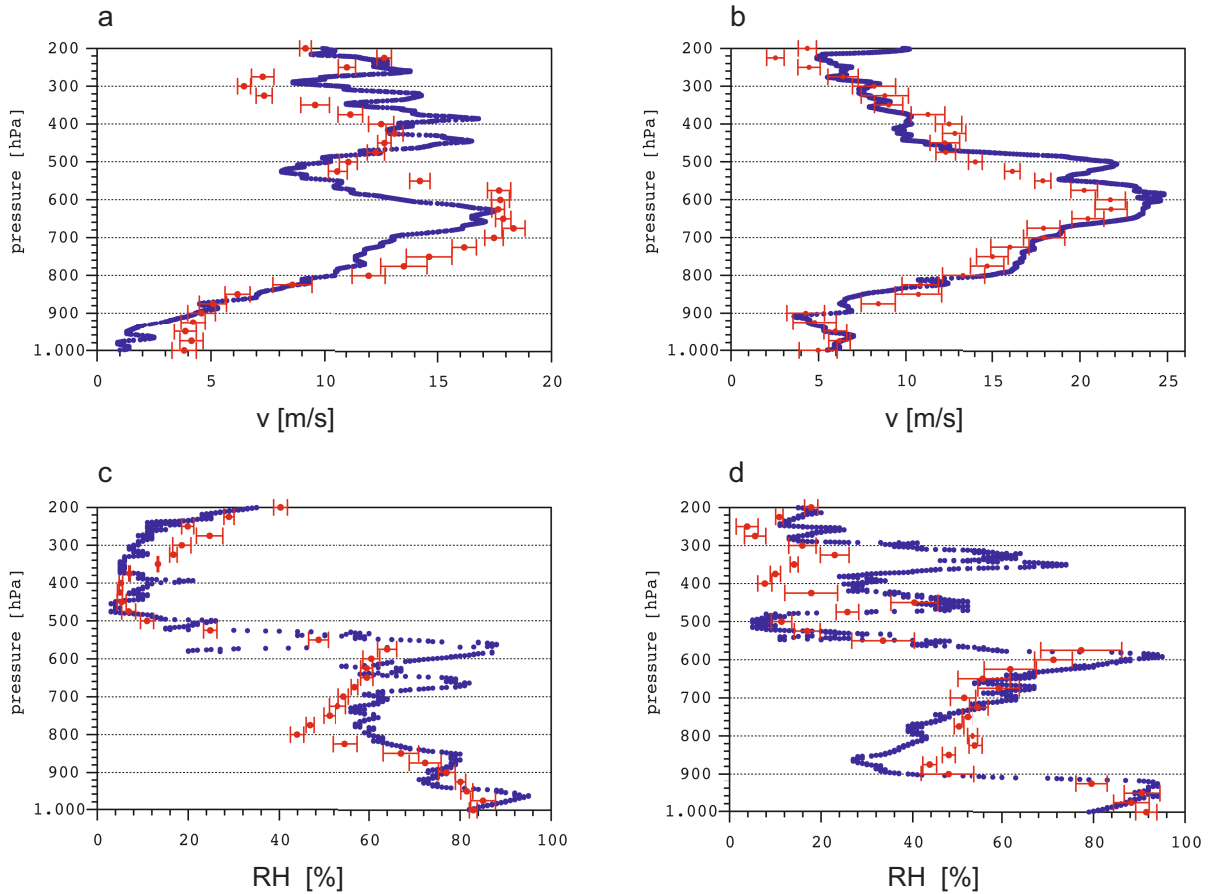


Figure 4.8: Profiles of horizontal wind speed (ms^{-1}) (upper row) and relative humidity (%) (lower row) from radiosondes, released at Dakar (17.49°W , 14.75°N), Senegal, at (a, c) 09 September 2006, 2232 UTC and at (b, d) 11 September 2009, 1037 UTC (blue dots), together with the corresponding model output from the 72-hour COSMO forecast initialised at 12 UTC on 9 September 2006 (red dots). The horizontal bars indicate the standard deviation of the model output in a $0.5^\circ \times 0.5^\circ$ square centred on the closest grid point. Pressure (hPa) is used as the vertical coordinate.

speed of about the same magnitude as in Bamako. The profiles of relative humidity show dryer air at the height of the jet and relatively moist conditions near the surface. The radiosounding from Bamako on 10 September at around 11 UTC is chosen because it is the only radiosonde that performed measurements in the vicinity of the convective system C3. A wind speed maximum occurs just below 700 hPa. The air is relatively moist near the surface due to precipitation evaporation and between 500 and 700 hPa due to the presence of clouds. At the time of the 9 September sounding Bamako is situated in the cloud free region ahead of the convective system (Fig. 4.4a one hour prior to the sounding shown in Fig. 4.7a,c). Inspection of the model fields showed that the leading edge of the convective system has already reached Bamako in the model. This results in higher model

relative humidity values between 500 and 800 hPa compared to the radiosounding. At the time of the 10 September sounding (Fig. 4.7b,d) Bamako was located in a region with a sharp temperature and moisture gradient at the southern fringes of the convective system C3 (Fig. 4.4f, one hour prior the radiosounding). The proximity of Bamako to a region with a strong moisture gradient leads to the large standard deviation. Dakar, however, was located in a region with uniform moisture at these times resulting in a much smaller standard deviation. Note, that of all the soundings investigated the sounding that shown in Fig. 4.7a,c is the one with the poorest agreement between observations and model results.

The highest wind speed of about 25 m s^{-1} is reached on 11 September 2006 in the sounding from Dakar at 11 UTC. The calculation of the trough and jet axes by the method of Berry et al. (2007) (not shown) shows that these high wind speed values occur because at this time the AEJ core is situated almost directly over Dakar. At the time of the sounding a major MCS crossed the West African coast line. Additionally, Dakar is located in the vicinity of the MCS over West Africa, analysed in the following, and relatively close to the boundary of the high-resolution model region, and thus represents the large-scale environment. Unfortunately, no measurements were available directly in the convective system that crossed West Africa.

Good agreement was seen between model results and observations concerning the position of the AEJ and the position and the shape of the convective systems. However, after a forecast time of 36 hours the convective systems moved more slowly than observed in the satellite images. Those convective systems, which were initiated over West Africa and crossed the coastline during their life cycle, developed several hours later in the simulation. The overall comparison of the COSMO runs with satellite and observational data showed that the model representation of the the convective systems in this AEW is realistic enough for the COSMO runs to form the basis for further analysis.

4.1.3 Methodology for Budget Calculations

The aim of this study is to investigate how the convective systems described above modify their environment and to relate these modifications to the structure of the convection it-

self. We assess the influence on the environment by calculating the potential temperature and the vorticity budgets for regions encompassing the convective systems. These regions were determined according to the position and size of the system as follows. Firstly, a region of organised convection was identified using the vertically integrated specific humidity, cloud water and cloud ice. Budget calculations are carried out for boxes enclosing regions with values larger than 60 kg m^{-3} . If necessary, these boxes were enlarged so that they include also the regions with high vertical velocities ($|\omega| > 2 \text{ Pa s}^{-1}$) related to the convective systems. The aim was to include one region of organised convection. For each budget calculation the box size was adjusted to the position of the convective system. The individual components of the budget equations on a given pressure level were then averaged over this area and averaged over 2 hours. Sensitivity experiments were carried out and it was found that the results of the budget calculation are not sensitive to the box size. The results changed by about 6% when the box size was increased by 50%. The profiles still had the same shape but were slightly smoothed.

The potential temperature budget consists of the potential temperature tendency due to phase changes of water on the grid-scale (referred to hereafter as “moist processes”), vertical and horizontal advection, the parametrisation of turbulence, radiation and the computational terms (computational mixing, the nudging terms at the lateral boundaries and Rayleigh damping at the upper boundary). The magnitude of the horizontal advection and radiation tendencies are always less than 0.5 K h^{-1} . The contribution of the computational terms is even smaller and, is therefore, not shown.

The local change of the circulation is calculated as described in chapter 3, section 3.2.1. Friction was neglected in the relative vorticity budget. Even without it the budgets are nearly balanced. The budgets were not calculated below 950 hPa because in some regions in the domain the levels below 950 hPa are below ground level. Additionally, friction cannot be neglected so close to the surface.

The potential vorticity structure was investigated also (chapter 3, section 3.2.2), but as will be discussed in section 3, due to the properties of the system being studied the vorticity and potential vorticity approaches give analogous pictures of the dynamical evolution. Thus we concentrate on the relative vorticity in the following.

Table 4.2: Details of boxes around the convective system over land used for budget calculations based on the COSMO run initialised at 12 UTC on 9 September 2006 giving longitudinal and latitudinal extent, time of simulation over which averaging was performed, corresponding real time, and number of grid points in a horizontal plane within the box.

Box	Longitude	Latitude	Forecast Hour	Verification Time	Grid points
A	10.5-14.0 °N	8.0-5.5 °W	9-11	21-23 UTC on 9 September	14 000
B	10.4-14.5 °N	9.5-6.4 °W	15-17	03-05 UTC on 10 September	20 336
C	9.0-14.5 °N	11.0-5.8 °W	21-23	09-11 UTC on 10 September	45 760

4.2 Convective Systems over West Africa and the Atlantic

In this section we focus on two convective systems embedded in the same AEW: one over the West African continent and the other over the eastern Atlantic. The period analysed for the convective system over land encompasses 9 September 2006 21 UTC to 10 September 11 UTC. Our analysis is based on the model run that was initialised on 9 September 2006 at 12 UTC (Run 2 in Fig. 4.5 and Tab. 4.1). We identified three different stages of the life cycle of this MCS: the growing phase (A), the mature stage (B) and the dissipating stage (C) (Fig. 4.4b,d,f).

The second convective system is embedded in the developing tropical depression over the eastern Atlantic. On 12 September at about 12 UTC, the system was classified a tropical depression. Two boxes were selected to represent different stages in the evolution of the convective bursts: the growing (D) and the decaying (E) phase (Fig. 4.4j,n). The basis for the analysis of this convective system, which was initiated by a zone of enhanced convergence in the northwest of the mid-level circulation, is a model run that was initialised on 12 September 2006 at 00 UTC (Run 5 in Fig. 4.5 and Tab. 4.1).

In the following, we describe the structural features of both systems that are relevant for our budget calculations, and then present the potential temperature and relative vorticity budgets. Details of the boxes used for the budget calculations can be found in Tabs. 4.2 and 4.3.

Table 4.3: As Tab. 4.2 but for the convective system over the eastern Atlantic based on the COSMO run initialised at 00 UTC on 12 September 2006.

Box	Longitude	Latitude	Forecast Hour	Verification Time	Grid points
D	10.5-14.0°N	21.5-17.5°W	7-9	7-9 UTC on 12 September	22 400
E	11.5-14.5°N	23.0-18.0°W	13-15	13-15 UTC on 12 September	24 000

4.2.1 Structural Features

The evolution of the convective systems in the region of interest is illustrated using vertical velocity at 650 hPa and at 900 hPa (Fig. 4.9). During the growing phase there are two north-south oriented convective systems, A1 and A2 (Fig. 4.9a and d), with system A1 being the larger and more intense one. The leading edge at 900 hPa is characterised by ascent. Distinct descent regions are already present. Low-level convergence occurs at the leading edge with the low-level flow primarily northwesterly in the north and westerly in the south. During the next hours the systems intensify and the systems B1 and B2 have reached their mature state (Fig. 4.9b and e). A new system B3 has formed and is not as strong as the others. System B1 has a length of about 160 km and a very clear arc-like shape with ascent at the leading edge and descent to the rear. System B2 still has a north-south orientation and is about the same length as system B1. In the two strongly developed systems the ascent region coincides with convergence between the predominantly westerly monsoon flow and the rear-to-front inflow. The vertical shear is reduced markedly behind the system due to the inflow from the rear. During the dissipating stage (Fig. 4.9c and f) of the whole convective complex all three convective systems, C1, C2 and C3, are clearly distinguishable and have a comma shape-structure. System C3 is most intense. At 650 hPa regions of ascent and descent are also evident. These systems occur ahead of the AEW trough and the jet axis is northeast of the system. In all the boxes the environmental flow is northeasterly and the wind speed is strongest in the northwestern part.

Over land the convection takes the form of MCSs with a life time of about 3 days. In contrast, successive convective bursts are embedded in the mesoscale circulation over the Atlantic each with a lifetime between 6 and 24 hours. A large convectively active region

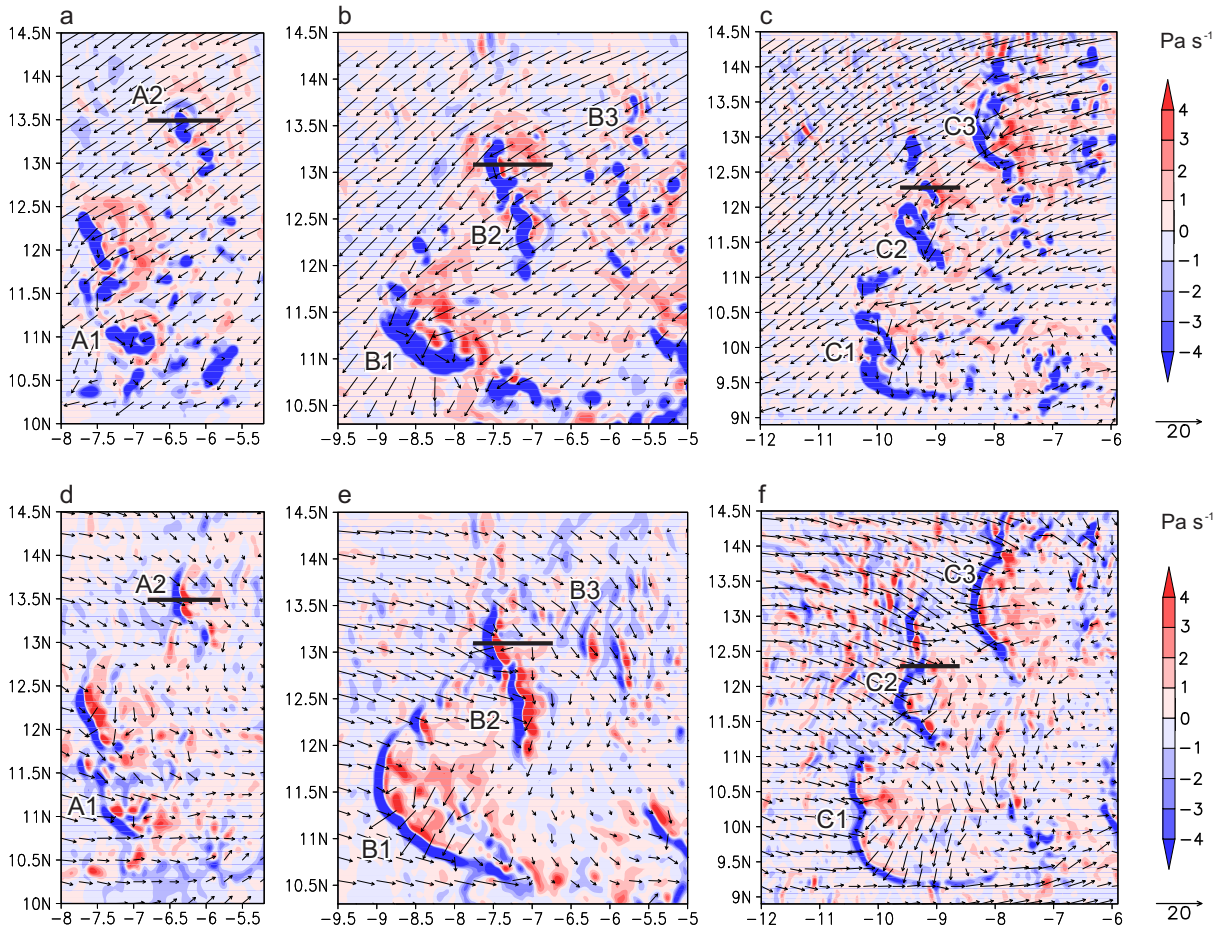


Figure 4.9: Convection over West Africa. The vertical velocity (Pa s^{-1}) and the horizontal wind (m s^{-1}) at 650 hPa (upper row) and at 900 hPa (lower row) for box A (a, d) at a forecast hour of T+13, box B (b, e) at T+16 and box C (c, f) at T+22 based on the COSMO run initialised at 9 September 2006, 12 UTC. Ascent is displayed in blue and descent in red.

is seen centred on $11.0\text{--}13.5^\circ\text{N}$, $21.0\text{--}18.0^\circ\text{W}$ (Fig. 4.10a,c). Low-level convergence is evident between $20.6\text{--}19.8^\circ\text{W}$ and $12.6\text{--}13.5^\circ\text{N}$ where the monsoon flow at the western edge of the system impinges on the easterly flow to the north of the circulation centre. Four hours later the regions of strong updraught are much smaller and convective cells occurred in different parts of the tropical depression (Fig. 4.10b,d). Additionally, north-northeasterlies occur to the northwest of the convective system (Fig. 4.10b) and ahead of the system as it decays (Fig. 4.10d). The descent is generally weaker and extends over a larger area than that of the marked mesoscale downdraught over land.

Due to the combination of the low-level monsoon flow and the AEJ, the convection over land develops in strong easterly shear. During the growing phase, low-level convergence occurs between a strong westerly inflow and an easterly flow from behind the system

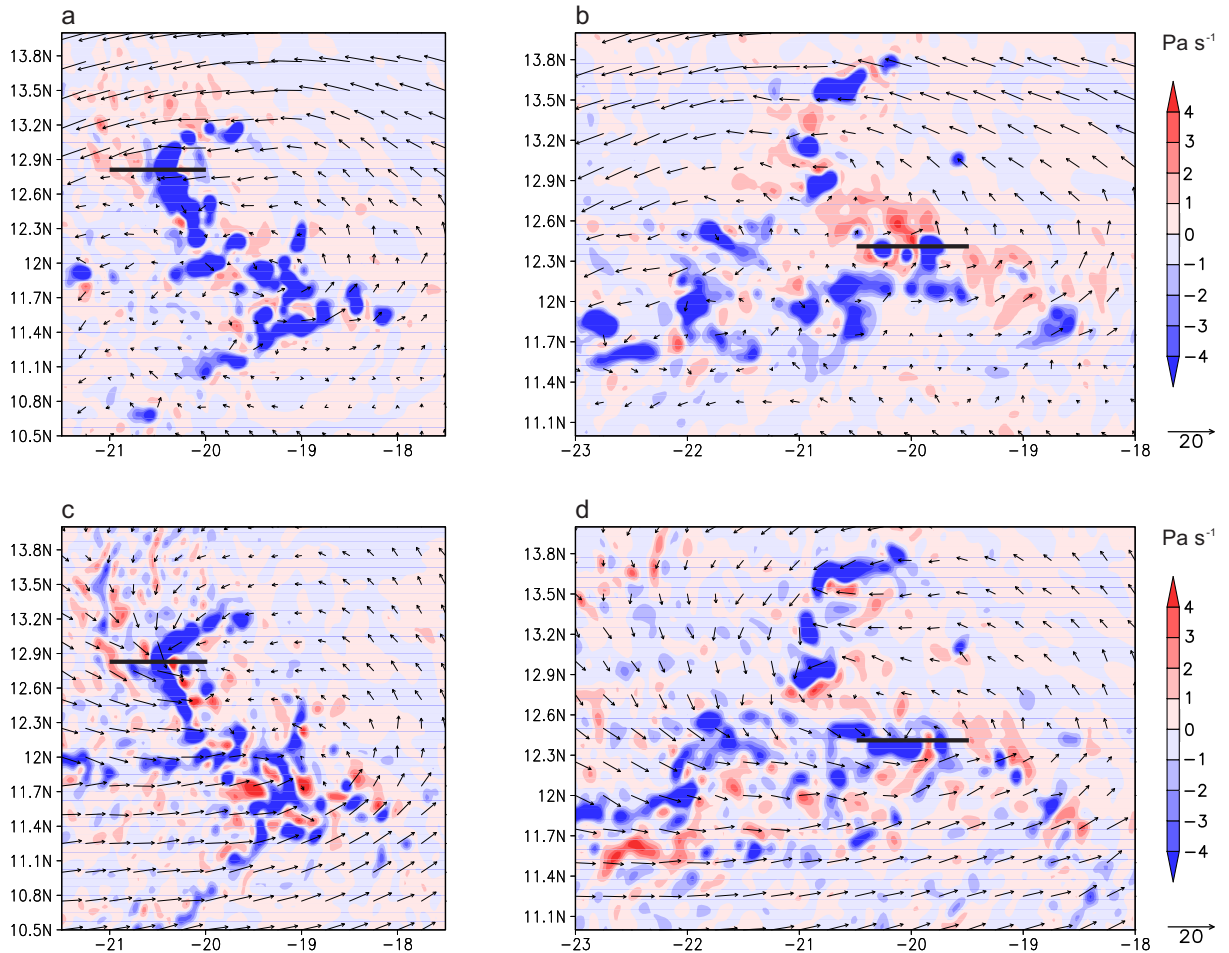


Figure 4.10: Convection over the ocean. The vertical velocity (Pa s^{-1}) and the horizontal wind (m s^{-1}) at 650 hPa (upper row) and at 900 hPa (lower row) for box D at a forecast hour of T+9 (a, c) and for box E at T+13 (b, d) based on the COSMO run initialised at 12 September 2006, 00 UTC. Ascent in blue and descent in red.

between about 6.5 and 6.35°W^3 . The associated ascent region extends up to about 150 hPa and tilts eastwards slightly with height (Fig. 4.11a). The convergence continues up to 500 hPa. Below 750 hPa a small descending area can be seen just behind the ascent region indicating the developing downdraughts. This region is characterised by divergence. The maximum of the relative vorticity is collocated with regions of maximum heating and maximum updraught. Negative relative vorticity occurs only at the upper levels west of the developing convective systems (Fig. 4.11b). A couplet of positive and negative relative vorticity develops below about 850 hPa and increases in vertical extent by the mature phase (Fig. 4.11b,d).

³The discussion of convergence and divergence here is based on a calculation of the total horizontal divergence (not shown) and not on the zonal wind field in the cross-section alone.

During the mature phase (Fig. 4.11c) the westerly inflow becomes much stronger and reaches deep into the system up to 550 hPa. The near surface region between about 7.65 and 7.52°W up to about 800 hPa is characterised by strong convergence. The region of strong divergence occurring at the leading edge of the convective system between about 800 and 400 hPa is also tilted with height. Divergence associated with the upper-level outflow can be seen at around 250 hPa with stronger westerly winds to the rear and weaker easterly winds ahead of the system. Thus there is strong mid-level convergence east of the tilted updraught. The westerly inflow can also be seen from Fig. 4.9 and has northwesterly direction for the convective system. The region of maximum heating moved towards lower levels (Fig. 4.11d). The low-level convergence has intensified also due to the descending air from the rear of the system. At this stage strong downdraughts have developed around 7.5°W behind the tilted updraught where a zonal system-relative wind minimum is located just behind the the low-level convergence zone characterised by a wind maximum at around 7.7°W. The downdraught region is characterised also by a very weak cooling. Between 200 and 300 hPa, the strongest outflow from the system is to the east and weaker outflow to the west (Fig. 4.11c) giving a region of strong outflow that extends about 100 km. An elongated horizontal band with negative relative vorticity develops through vortex compression in the region of strong divergence and is then advected to the west. This negative vorticity anomaly is seen along the upper-level region of strong outflow in each system. Positive relative vorticity that develops through vortex stretching in the vortex core is advected upwards and towards the east in the tilted updraught, leading to an upper-level vorticity dipole (Fig. 4.11d). A dipole of opposite sign occurs at low-levels but this appears to develop due to vortex stretching in the updraught region and vortex compression in the region of the strong downdraughts. Below 400 hPa weaker descent occurs. The easterly system-relative wind speed maximum at around 450 hPa ahead of the convective system can be related to air that came from the inflow region, was lifted upwards and then exited the convective region at about 450 hPa or slightly lower. The weakly subsiding air leads to an enhancement of the AEJ. This was evident from trajectory calculations.

In the decaying phase, the system is even more tilted. The increasing tilt of the convective system during its life cycle could be observed for all the systems embedded in this MCS.

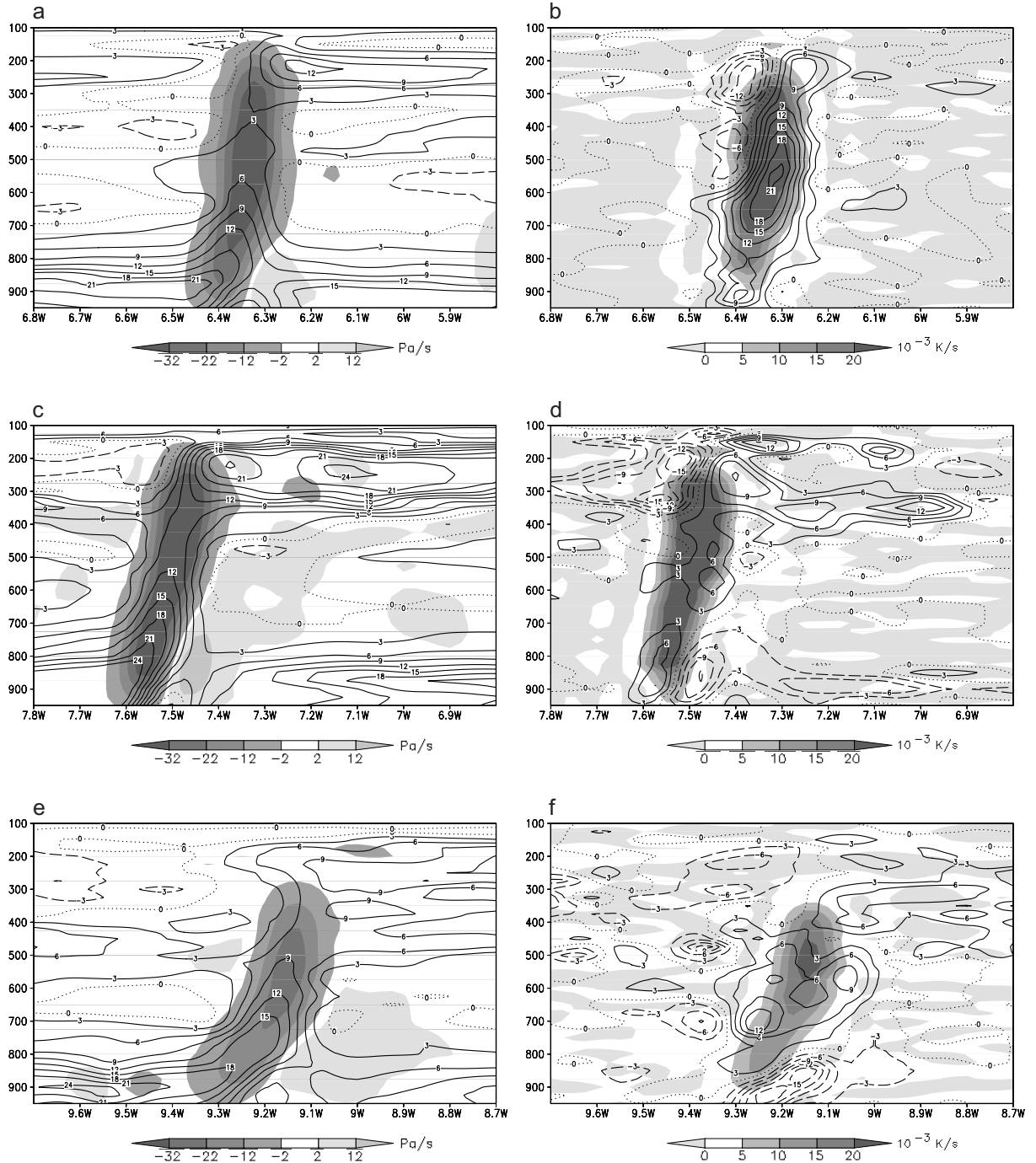


Figure 4.11: Cross sections through the convective system over West Africa of (a, c, e) vertical velocity (shaded) and system–relative zonal wind (contour interval is 3 m s^{-1}) and (b, d, f) total diabatic heating rate (shaded) and the vertical component of the relative vorticity (contour interval $3 \times 10^{-4} \text{ s}^{-1}$) based on the COSMO run initiated at 12 UTC on 9 September 2006. The convective system moved westwards with a translation speed of about 12.2 m s^{-1} during the developing stage (a,b), 15.3 m s^{-1} during the mature stage (c,d) and 10.7 m s^{-1} during the decaying stage (e,f). The cross sections (a,b) are along 13.5°N at T+13 in box A, (c,d) along 13.1°N at T+16 in box B, and (e,f) along 12.3°N at T+22 in box C. The location of the cross sections is shown in Fig. 4.9. Pressure (hPa) is used as the vertical coordinate.

For all the other times, the region of maximum heating is collocated with the region of the strongest ascent. A small region of upward motion occurred at around 900 hPa between 9.5 and 9.4°W (Fig. 4.11e). This can be attributed to small convective cells initiated by the system's downdraught. Just behind the tilted updraught the region of descent now extends over a larger horizontal area but is confined below 600 hPa and the maximum values have decreased. The region just behind and beneath the tilted updraught is characterised by high values of negative relative vorticity (Fig. 4.11f), associated with the system's cold pool. Maximum positive relative vorticity values can be found in the region of maximum heating and weaker values at upper levels behind the system. A region with weak negative relative vorticity occurs ahead of the system.

The convective system over the ocean at a time close to its peak intensity is shown in Fig. 4.12a,b. The northern convective burst (Fig. 4.10a,c; 21.0-19.4°W, 12.1-13.5°N) at the beginning of the period shown still displays some MCS-like character, as it has a bow-like form, moves toward the west and develops weak downdraughts. It occurs in a region that is close to the AEJ, which is located to the northwest. Thus the shear profile is similar to that of the MCS over West Africa. However, the region of maximum heating and ascent is only tilted below 700 hPa (Fig. 4.12a,b) rather than through its entire depth, as in the convective system over land and is collocated with a deep tower of positive vertical vorticity, so that this convective system could be described as a vortical hot tower. It is evident that the upper level outflow is much weaker and covers a smaller region than over land. Additionally, the downdraughts are weaker and smaller-scale than for the system over land. As time proceeds, the system decays (Fig. 4.10b,d) and south of it a large region of convective systems with strong updraughts occurs. A cross section through one of these convective systems (Fig. 4.12c,d) shows a tower of high positive relative vorticity collocated with the updraught region and the region of maximum heating at about 19.8°W. Again, the system is tilted below 700 hPa. The highest values of relative vorticity occur between the surface and 700 hPa whereas the maximum heating can be found above. The ascent region is elevated, and diabatic cooling and downdraughts are seen near the surface and at midlevels. The shear for the system in box E (Fig. 4.10d) is much smaller than for the system in box D (Fig. 4.10b). This is one of the main reasons

why the convection is less organised over water. The convective systems over the ocean are moulded by the monsoon inflow from the west, which became stronger with time.

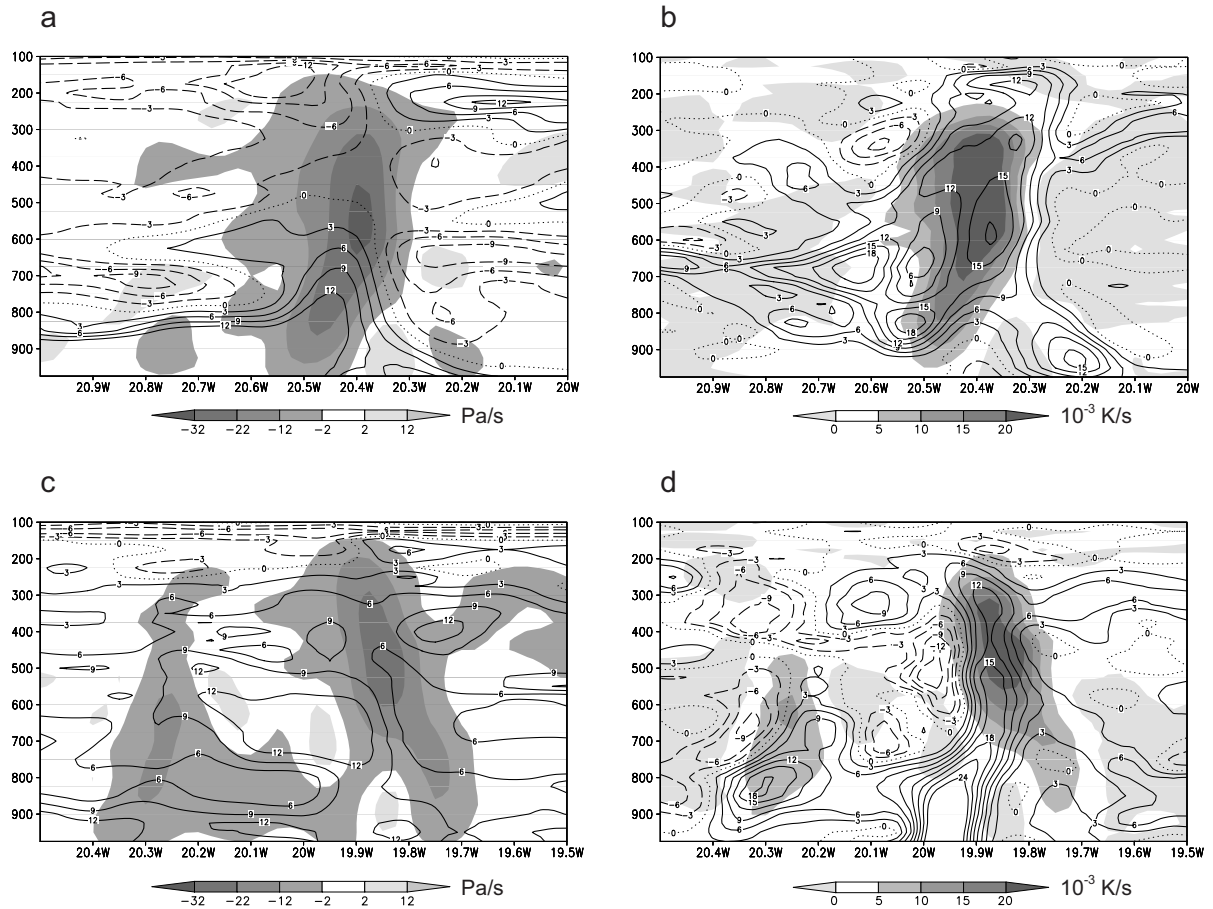


Figure 4.12: The same as Fig. 4.11 but for a convective system over the eastern Atlantic based on the COSMO run initialised on 12 September 2006, 00 UTC. During its life cycle the convective system moved westward with a translation speed of around 4.6 m s^{-1} . The cross sections are along (a, c) 12.8°N through box D on 12 September 2006, 09 UTC (T+9) and along (b, d) 12.4°N at 13 UTC (T+13) trough box E. Details can be found in Fig. 4.10 and Tab. 4.3.

The mean divergence profiles for the convective system over land and over the ocean (Fig. 4.13) show that low-level convergence over the ocean is stronger than over land. Over land the convergence is strongest at around 900 hPa. It increases as the system develops. The depth of the low-level convergence also increases with time. The divergence above 300 hPa becomes stronger with time as the system develops a distinct outflow region. Over the ocean, however, the largest convergence occurs near the surface. During the first 9 hours into the simulation the low-level convergence increases and as the convective system starts to decay it decreases. A region of divergence can be observed between 400 and 600 hPa and above 300 hPa related to the outflow region. The mid-level divergence

decreases with time and shows negative values after 13 forecast hours. This convergence seen between 300 and 500 hPa is associated with the outflow from a northeast–southwest orientated line of convection (Fig. 4.4m) in the monsoon flow to the south of the box.

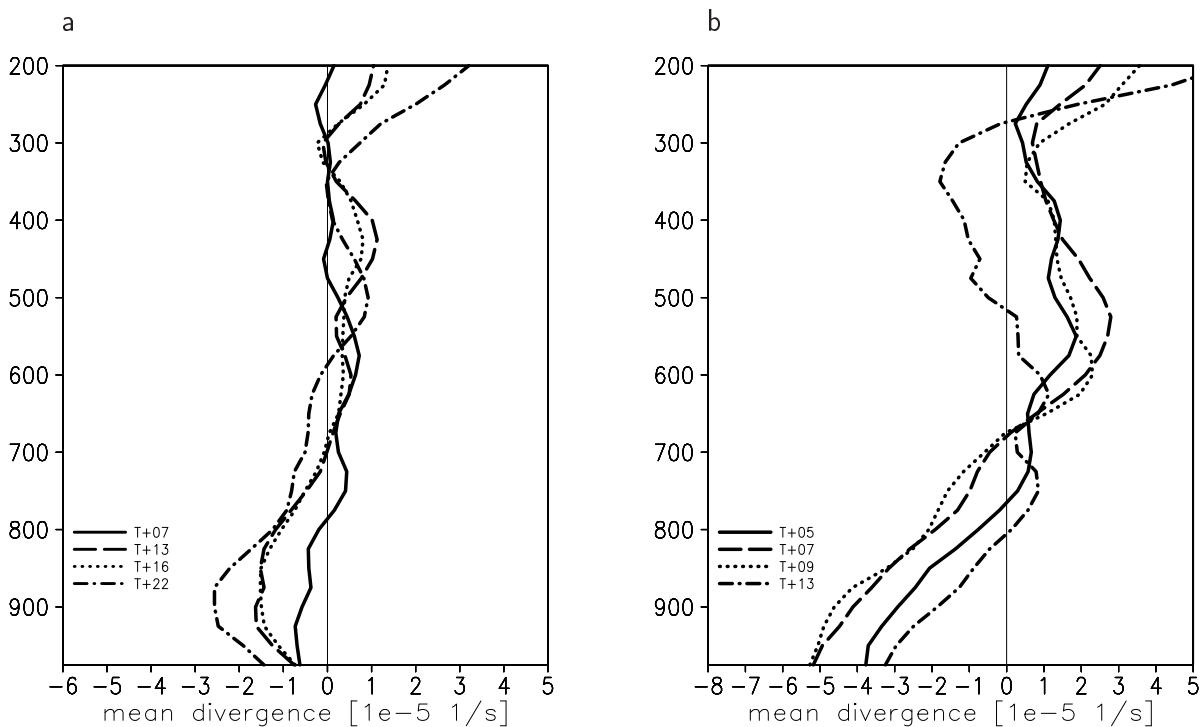


Figure 4.13: (a) Mean horizontal divergence for the convective system over West Africa averaged over $8.5\text{--}14.5^\circ\text{N}$, $1.0\text{--}5.4^\circ\text{W}$ based on the COSMO run initialised at 12 UTC on 9 September 2006, are displayed for selected times. (b) Mean horizontal divergence for the convective system over the eastern Atlantic averaged over $11.0\text{--}13.8^\circ\text{N}$, $21.2\text{--}18.0^\circ\text{W}$, for different times. Pressure (hPa) is used as the vertical coordinate.

The convection embedded in the AEW over land and over the ocean exhibits rather different structural characteristics. In order to assess how these differences arise we first consider the properties of the environment in which they develop. The primary environmental characteristics to consider are the moisture, the vertical shear and the convective available potential energy.

The mean relative humidity was calculated for a region encompassing all the convective systems described above over land and for a second region over the ocean (Fig. 4.14). The profile of the mean relative humidity for the convective system over land shows the relatively moist monsoon flow from near the surface up to about 800 hPa, where clouds on top of this layer lead to an increase in relative humidity. The relative humidity decreases with height above this layer. Local maxima occur at around 550 hPa due to the deep

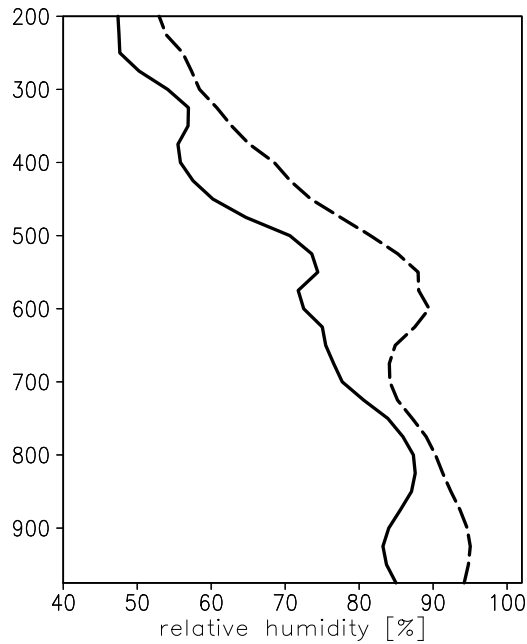


Figure 4.14: Solid line: Mean relative humidity of the convective system over land averaged over $8.5\text{--}14.5^\circ\text{N}$, $11.0\text{--}5.4^\circ\text{W}$ from 9 h to 24 h forecast time, based on the COSMO run initialised on 9 September 2006, 12 UTC. Dashed line: Mean relative humidity for the convective system over the eastern Atlantic averaged over $10.5\text{--}14.0^\circ\text{N}$, $22.5\text{--}17.5^\circ\text{W}$, from 7 h to 15 h forecast time, based on the COSMO run initialised on 12 September 2006, 00 UTC. Pressure (hPa) is used as the vertical coordinate.

convection and at around 350 hPa where the stratiform convection occurs as can be seen later. The maximum at around 600 hPa is due to the main convection within the box and the minimum below can be related to subsidence at this level. Above the 600 hPa level the relative humidity decreases.

The atmosphere is markedly drier over land than over water. In particular, the mid-level (700–500 hPa) relative humidity is noticeably lower over land. The MCS over land redistributes the moist air from lower levels to mid-levels. Inspection of the evolution of the moisture profiles over land (not shown) indicates that the moistening of the mid-troposphere is particularly marked during the period illustrated in Fig. 4.4b,d as the MCS develops to its mature phase. Over the ocean the redistribution of moisture continues during the frequent sequence of convective bursts over the Atlantic. The evolution of the moisture profiles is consistent with the drier air at mid-levels leading to stronger downdraughts over land.

Over land, the maximum mean zonal wind with values of about -15 m s^{-1} (Fig. 4.15a) occurs at around 600 hPa, which is due to the AEJ. As the convective systems grow, the

magnitude of the mid-level mean zonal wind maximum decreases whereas the magnitude of the low-level mean zonal wind maximum at around 900 hPa increases, as the low-level inflow into the convective system strengthens. The mean low-level zonal wind first increases quite rapidly, then starts to decrease towards the end of the mature phase of the MCS. After 25 hours into the simulation the wind speed below 800 hPa is lower than after 7 hours. The height of the mid-level wind maximum is reduced with time but the influence of the AEJ is still apparent. However, the shear is reduced between 800 and 600 hPa but increased below this layer. The mean zonal wind has a similar profile with a maximum at about 600 hPa (Fig. 4.15c) that is reduced and lowered with time. The low-level southerly flow is relatively weak and increases slightly with time.

The profile of the mean zonal wind is similar over land and over the ocean, although the wind speed maximum at low-levels over the ocean does not change with time and the zonal wind maximum at around 600 hPa reached values of about 12ms^{-1} (Fig. 4.15b). The mid-level wind speed decreased with time in such a way that only very weak vertical shear occurs above 800 hPa after 13 forecast hours, in contrast to the land case. The temporal evolution of the mean meridional wind (Fig. 4.15d) reveals that the maximum occurs at around 700 hPa. The decrease during the system's life-cycle is distinct. A marked difference between both convective systems is that the profile for the convective system over the ocean is dominated by northerlies whereas the system over the ocean is influenced by southerlies.

The vertical variation of the mean zonal wind over land and over water (Fig. 4.15) is characterised by low-level westerly monsoon flow and the easterly flow of the AEJ. The stronger influence of the AEJ on the system over land than on the system over the ocean might be due to the fact that the MCS over West Africa was initiated ahead of the AEW trough, where it remained throughout its lifetime. The location of the convective system ahead of the AEW trough leads to a strong zonal and meridional flow at 600 hPa over land. As the convective systems moved over the Atlantic they also moved into the AEW trough giving weaker meridional flow. The low-level flow is similar in strength over land and ocean, but the AEJ is stronger over land leading to a stronger vertical shear in the early stage of convection over land than over the ocean. Additionally, the shear is much

weaker toward the end of the life-cycle of the convective system over the ocean than to the beginning. In contrast, the shear over land did not change as much.

The horizontally averaged profiles in Fig. 4.15 mask the spatial variability across the convective systems. Over land, the AEJ/AEW flow is rather uniform over the area considered and the inflow ahead of the system has little north-south variation (Fig. 4.9). Over the ocean, the easterly shear in the northern portion of the domain occurs primarily due to the AEJ and in the southern part of the domain due to the combination of westerly monsoon flow at low levels and weak flow at 600 hPa (Fig. 4.10). This spatial variability can be expected to influence the nature of the convection in the developing tropical cyclone. However, previous studies on the interaction between tropical cyclones and vertical shear have not considered such complex environmental flows.

The convective available potential energy (CAPE) is spatially variable over land and over water. Both systems formed in an area with high values of CAPE⁴, of around 1500-2000 J kg⁻¹. High values of CAPE were always present ahead of the systems. However, the magnitude of the CAPE was similar for the system over land and over ocean.

A distinct cold pool developed during the life cycle of the MCS over land (Fig. 4.16) as a result of the storm's downdraught. The cold pool spreads out as a density current with a leading edge that can be seen in the strong potential temperature gradient in Fig. 4.16. As several previous studies have shown, e.g. Rotunno et al. (1988), the cold pools of the individual cells spread out near the surface and combine later to form a large mesoscale cold pool. The cold pool substantially modifies the monsoon flow (Diongue et al., 2002). Over water no cold pool was observed. Cold pools can develop in convection over water but they are usually not as strong and do not cover as large an area as those over land. The lowest model level maybe too high (59 m above the surface layer) to resolve the shallow cold pool.

The downdraughts of the convective system over the ocean (not shown) appear to be not as strong as in the MCS over land (Fig. 4.11c) and there is no distinct cold pool over the eastern Atlantic. Thus there is no mechanism for the convective systems to propagate. The vertical shear over the ocean is about 75% of that over land at the beginning of the

⁴For details on the calculation of CAPE see www.cosmo-model.org.

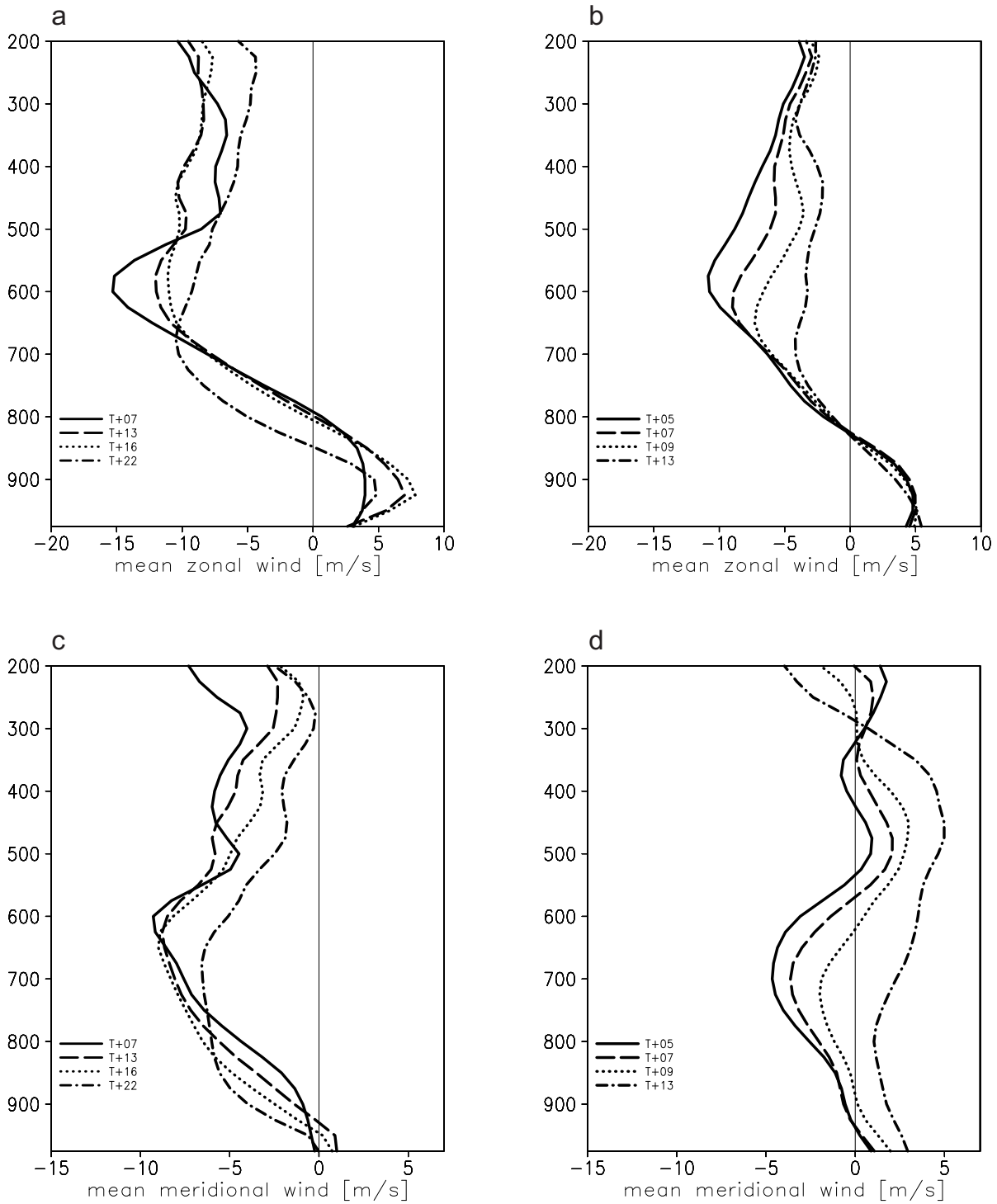


Figure 4.15: Left column: Mean zonal wind (a) and mean meridional wind (c) for the convective system over West Africa averaged over $8.5\text{--}14.5^\circ\text{N}$, $11.0\text{--}5.4^\circ\text{W}$ based on the COSMO run initialised at 12 UTC on 9 September 2006, are displayed for selected times. Right column: Mean zonal (b) and meridional (d) wind for the convective system over the eastern Atlantic averaged over $11.0\text{--}13.8^\circ\text{N}$, $21.2\text{--}18.0^\circ\text{W}$, for different times. Pressure (hPa) is used as the vertical coordinate.

period we discuss and decreases substantially over the 8 hour period shown (Fig. 4.15). Initially, the convective updraught over the ocean is tilted at low levels (Fig. 4.12) but becomes more upright with time as the vertical shear decreases. Both the lack of cold pools and the decrease in shear with time make it more difficult for the convection to be long-lived resulting in a shorter life time. The environment, however, is favourable for new convection. Thus, over the Atlantic there are more convective systems with a moderate intensity rather than a large long-lived mesoscale convective system.

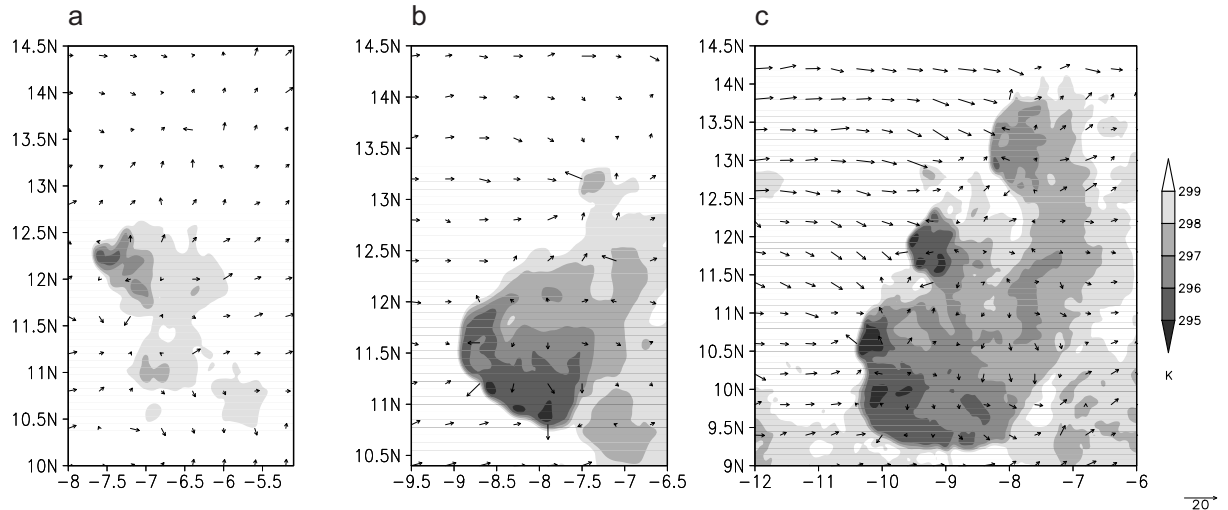


Figure 4.16: Potential temperature (K) and the horizontal wind (m s^{-1}) at 975 hPa for (a) T+13, box B (b, T+16) and box C (c, T+22) based on the COSMO run initialised on 9 September 2006, 12 UTC.

4.2.2 Potential Temperature Budget

Potential temperature budgets were calculated to gain a better understanding of the structural differences between the convective systems over land and over the ocean. Therefore, both systems were divided into characteristic stages of their life-cycle. We defined boxes (shown in Fig. 4.4) that covered the convective system during the different periods. Box A represents the developing phase, box B the mature phase and box C the decaying phase of the MCS over West Africa. Over the Atlantic, the convective system was divided into a highly convectively active period (box D) and its decaying phase (box E).

The potential temperature budget is calculated for the boxes over land and over the ocean (Fig. 4.17). Note, that the residual of the budget calculation amounts to about 2% of the

total potential temperature tendency. It is apparent from all profiles that the potential temperature tendencies due to vertical advection and grid-scale moist processes play a major role in the budget and lead to a net cooling near the surface, almost no net tendency in the mid troposphere and a net warming aloft. The cooling near the surface as a result of the moist processes (evaporation of rain) is strongest in the developing stages of the convective system over land and decreases through the systems life-cycle.

For the MCS over land (Fig. 4.17), the positive potential temperature tendency due to the condensational warming and the negative tendency due to vertical advection in ascent regions, have maximum values between 300 and 700 hPa. The upper-level maximum at around 350 hPa indicates mainly the stratiform region and the deep convective towers. The overall shape of the profile is similar during the three stages, and so illustrated for box B (Fig. 4.17, box B). As the systems progress from the developing to the decaying stage, the maximum potential temperature tendency due to moist processes and vertical advection moved upward from box A to box B and weakened in box C. The low-level cooling due to the evaporation of rain water decreases from box A to box C.

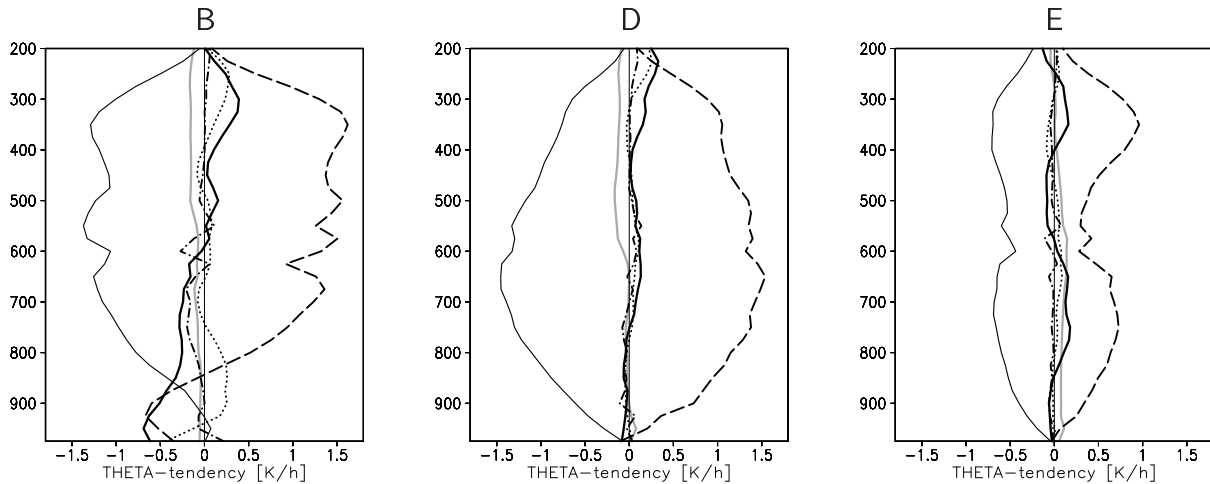


Figure 4.17: The areal averaged profiles of potential temperature tendencies (K h^{-1}): Total tendency (thick black line) and tendencies due to vertical advection (thin black line), moist processes (dashed line), turbulence (dash-dot line), horizontal advection (dotted line), and radiation (grey line). Areal average is taken over box B for the convective system over West Africa based on the COSMO run initialised at 12 UTC on 9 September 2006 (Tab. 4.2). Boxes D and E of the convective system over the Atlantic based on the COSMO run initialised at 00 UTC on 12 September 2006 (Tab. 4.3). Pressure (hPa) is used as the vertical coordinate.

The potential temperature tendency due to turbulence is largest between 550 and 800 hPa and near the surface in all boxes. The former is due to the turbulence in the planetary

boundary layer and the latter can be attributed to the vertical shear of the AEJ. The influence of the jet related turbulence is quite distinct in boxes A and B but appears to be reduced in box C (not shown). As the MCS moves westward, it disrupts the AEJ structure in the area where the convective system can be found and so the dynamics of the system play the major role here.

The contribution of horizontal advection is restricted to the region from the surface up to about 700 hPa and to a region between 200 and 350 hPa. The effect of radiation results in a negative potential temperature tendency which is strongest in boxes A and B and a weak positive tendency in box C.

The potential temperature tendencies are weaker over the ocean (Fig. 4.17, box D) and, as is the case over land, the budget is dominated by a near balance between the tendencies due to vertical advection and moist processes. Weak net warming occurs at around 500-750 hPa as well as above 400 hPa in the growing stage of the convective bursts (box D) over the Atlantic. For both convective systems a net cooling due to vertical and weak horizontal advection occurs near the surface. The upper heating maximum indicates the stratiform region and the deep convective towers of the storm but is not as pronounced as in the case over land. In addition, the impact of the turbulence is not only decreased during the systems life cycle but is also weaker compared to the case over land. Another marked difference between the profiles in boxes B and D is the presence of the strong diabatic cooling below 800 hPa over land. Cooling due to evaporation of precipitation also occurs near the surface over the ocean but only very weakly which is why it is not so clearly visible in Fig. 4.17. Note that the lowest level over the ocean is not shown for consistency. As the convective burst over the ocean weakens (Fig. 4.17, box E), the structure of the potential temperature profile changes significantly. There is a pronounced minimum at 600 hPa in the magnitude of the tendencies due to vertical advection and moist processes, indicating a change in the relative importance of deep ascent, downdraughts, and the stratiform region.

In order to isolate the contribution of different parts of the convective system to the potential temperature budget we partitioned the content of the boxes according to the vertical velocity at 650 hPa (Fig. 4.9 upper row). The terms in the heat budget are averaged over regions with ascent stronger than -2 Pa s^{-1} , regions with descent larger than

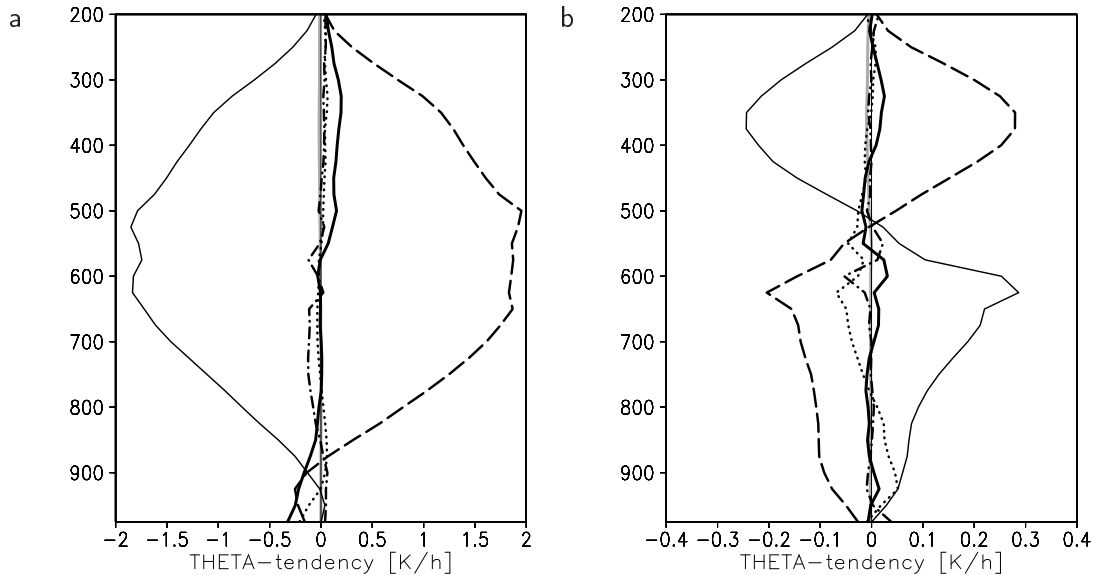


Figure 4.18: As Fig. 4.17, but potential temperature tendencies for regions with (a) strong ascent ($\omega < -2 \text{ Pa s}^{-1}$) and (b) strong descent ($\omega > 2 \text{ Pa s}^{-1}$) at 650 hPa for the convective system over land (box B). Pressure (hPa) is used as the vertical coordinate.

2 Pa s^{-1} , regions with weak ascent ($-2 \text{ Pa s}^{-1} < \omega < 0 \text{ Pa s}^{-1}$) and regions with weak descent ($0 \text{ Pa s}^{-1} > \omega > 2 \text{ Pa s}^{-1}$). The criterion for the partitioning was applied at different levels. The 650-hPa level was chosen, because both updraughts and downdraughts are evident at this level and because the characteristics of the different regions of the MCS were most distinct. As the system over land is tilted, it is not possible to make a completely clear separation between up- and downdraughts in this way. However, the results show that we still capture the essential nature of the systems through this partitioning. This approach is similar to that of Caniaux et al. (1994) but using different criteria for the partitioning.

The potential temperature budgets for the convectively active period of the MCS over land (box B) and the convective burst over the ocean (boxes D and E) are shown in Fig. 4.18 and 4.19. In the region of strong ascent, the magnitude of the potential temperature tendencies of the system over the Atlantic is weaker than that of the system over land. In both cases the net potential temperature changes are very small due to the cancellation between the tendencies due to vertical advection and moist processes. However, the maximum cooling due to vertical advection in the ascent region and the maximum condensational warming occur at higher levels over land than over the ocean consistent with the deeper ascent over land (Fig. 4.11, 4.12).

For the ocean case, the net warming is almost zero between near the surface and 400 hPa with a net warming aloft (Fig. 4.19a,b). The profiles for the boxes over land are characterised, however, by a low-level cooling and an upper level warming (Fig. 4.18a). The low-level cooling over the ocean occurs only between 1000 and 975 hPa and is not shown. The magnitude of the tendency due to vertical advection and due to the moist processes is largest in box D for the convective system over the Atlantic and in boxes A and B for the system over West Africa (not shown). As the convective burst over the ocean weakens, the maximum of the potential temperature tendencies stay at about the same level, but the tendencies decrease more rapidly with height, indicating a shallower and less vigorous ascent region. In these profiles, the effect of horizontal advection and radiation is small.

In the region over land characterised by strong descent at 650 hPa the maximum of condensational heating occurs between 300 and 400 hPa (Fig. 4.18b), illustrating the stratiform region above the mesoscale downdraughts. This heating is opposed by strong cooling due to vertical advection, but there is still a net warming. A further marked feature is the evaporative cooling between about 550 and 800 hPa which initiated the unsaturated downdraughts of the MCS. This effect is largest in the mature state of the system and decreases during the decaying phase. The potential temperature tendency due to turbulence increased from near the surface up to 800 hPa due to the strong vertical shear in relation to the strong downdraughts and in the region above 400 hPa due to strong shear of the outflow. The profiles of strong ascent and descent at 650 hPa for the convective system over land show the typical characteristics of the convective and the anvil region of an MCS.

A significant difference between the convective system over land and over the ocean is seen in the regions with strong descent at 650 hPa. Over the ocean all of the tendency terms are smaller than 0.05 K s^{-1} (not shown), indicating that the downdraughts of the convective system over the ocean are not as strong as in the MCS over land. The regions with weak ascent and weak descent at 650 hPa are, however, of more importance for the net potential temperature tendency (Fig. 4.19c-f). The regions with weak ascent at 650 hPa indicate the presence of shallow convection in the vicinity of the main convective systems, with a maximum due to condensational heating between 600 and 900 hPa. There is a strong negative potential temperature tendency due to vertical advection with a maximum

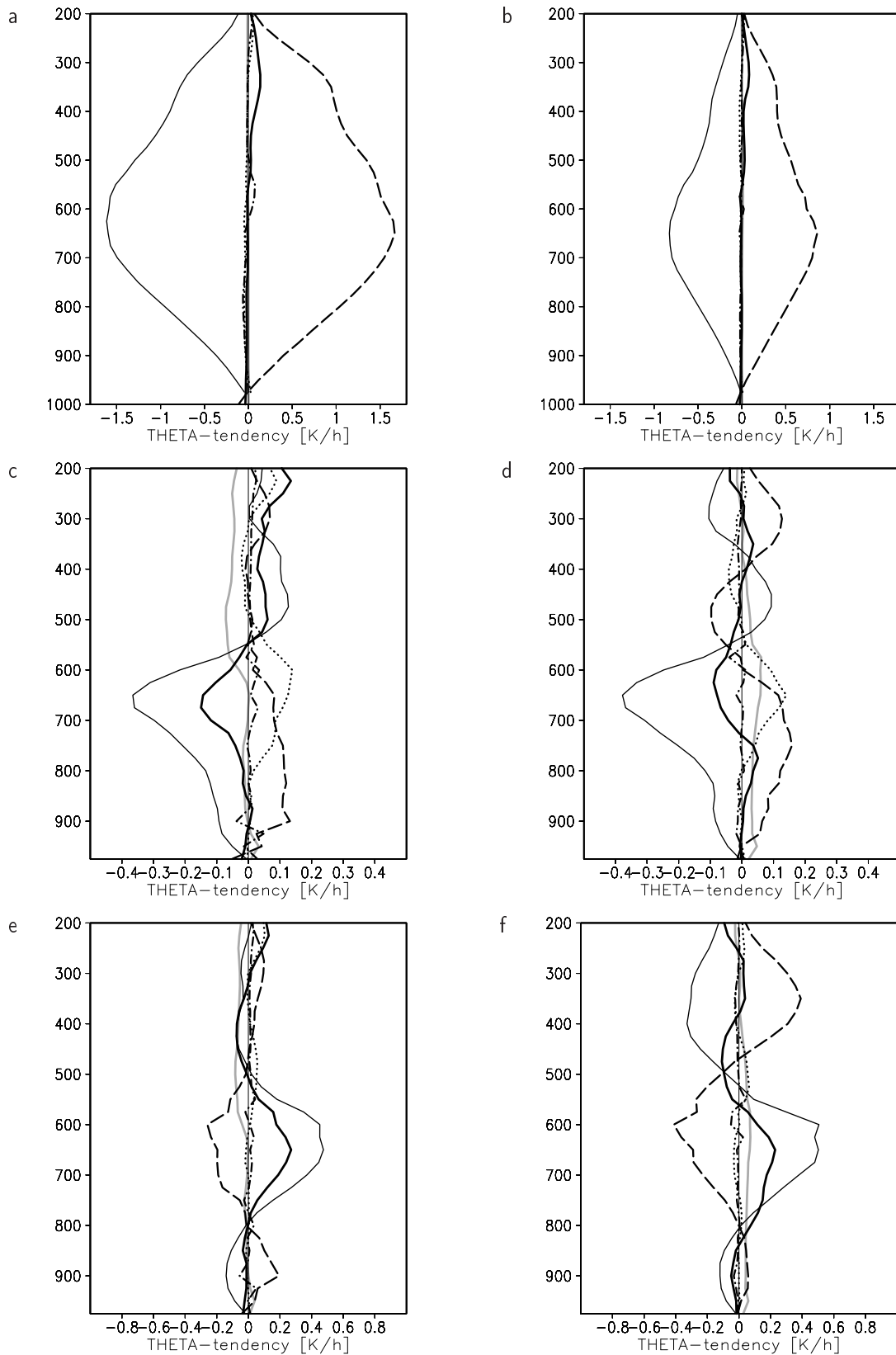


Figure 4.19: As Fig. 4.17, but profiles of potential temperature tendencies for regions with (a, b) strong ascent ($\omega < -2 Pa s^{-1}$), (c, d) weak ascent ($-2 Pa s^{-1} < \omega < 0 Pa s^{-1}$) and (e, f) weak descent ($0 Pa s^{-1} < \omega < 2 Pa s^{-1}$) at 650 hPa for the convective system over the eastern Atlantic. The left column (a,c,e) shows the potential temperature tendencies for box D and the right column (b, d, f) for box E. Pressure (hPa) is used as the vertical coordinate.

between 700 and 600 hPa. At about the same height the horizontal advection leads to a positive tendency. This results in a net temperature decrease, and an increase above about 550 hPa. A second maximum due to condensational heating at around 300 hPa shows that in the decaying phase (Fig. 4.19d) the cirrus shield extends over the region of shallow convection. A pronounced radiative cooling occurs above 600 hPa in Fig. 4.19c. This is due to the fact that at the cloud tops a small negative potential temperature tendency occurs. During the period over which the average was taken, the cloud top height of both the convection in the environment and the cirrus shield arise with time, leading to an average cooling over a deep layer.

In the regions with weak descent at 650 hPa, the profiles between 500 and 750 hPa indicate the presence of downdraughts (Fig. 4.19e). This effect becomes stronger in box E (Fig. 4.19f). This results in a reduction of the mean relative humidity (Fig. 4.14). A marked influence of the stratiform region is seen between 300 and 400 hPa. The low-level condensational heating below 800 hPa can be related to shallow convection in the boundary layer as it is typically seen in the trade wind region. Its presence leads to the low-level maximum in the mean relative humidity (Fig. 4.14).

Caniaux et al. (1994) studied the heat budget of a squall line during COPT 81, but using a two-dimensional model. They found warming in the stratiform part and cooling in the mesoscale downdraughts due to evaporation of rain water. In addition, they observed that the net cooling is a temporal process that occurs when the stratiform region produced enough precipitation to counter the adiabatic warming. The cooling at the anvil base is attributed to the upward transport of low potential temperature and not to melting. Caniaux et al. (1994) also analysed the apparent heat source of the whole system as well as the stratiform parts. Our analysis confirms the structural differences observed by Caniaux et al. (1994) and Lafore et al. (1988), but we do not distinguish between the different heat sources contributions to the tendency due to moist processes. Due to the compensation between condensational heating and vertical advection, the descent regions over land are as important for the total heat budget as the updraughts. With the help of the partitioning described above, the structure of the convection is more evident than in the averages over the entire boxes.

4.2.3 Vorticity Budget

In order to assess how the structural differences described previously impact the dynamics of the systems, we contrast the evolution of the relative vorticity and the PV for the convective systems over land and over water embedded in the same AEW. In particular, we calculate the relative vorticity budget. The development of the convective systems that cross the West African coastline is not addressed in this study as there was a strong interaction with orography.

Over land, the relative vorticity increased between 900 and 500 hPa and decreased notably above 350 hPa. The strongest increase occurred between 600 and 800 hPa (Fig. 4.20a) throughout the period of the MCS shown and the maximum remained at approximately the same height. For the convective system over the ocean (Fig. 4.20b), the vorticity maximum at the beginning of the period of interest in the simulation had a higher magnitude than that over land and occurred at a higher level. Its magnitude did not increase much during the following hours but the height at which the maximum occurred moved downwards. Thus, the relative vorticity decreased between 400 and 600 hPa and increased below 700 hPa. The reduction in the height of the vorticity maximum is particularly marked after 11 hours into the simulation. This process contributes to the intensification and organisation of the tropical depression.

The low-level vorticity is much higher over the ocean than over land due to a low-level vorticity anomaly that moved into the box region. This vorticity anomaly is in fact a secondary heat low that moved over the Atlantic (Fig. 4.21). On 9 September 2006 at 12 UTC a westward extension of the Saharan heat low core occurred. It moved over West Africa along about 18°N in the same manner as described in Grams et al. (2010). A shallow circulation confined to the 1000–800 hPa layer became cut off from the main Saharan heat low and on 10 September 2006 12 UTC can be seen as a secondary heat low at $16\text{--}18^{\circ}\text{N}$, $16\text{--}11^{\circ}\text{W}$ (Fig. 4.21a). Further inspection of the model wind, temperature and humidity fields (Fig. 4.22) confirm the heat-low character of this circulation. The low level temperature maximum was collocated with the maximum of positive relative vorticity. On 9 September at 18 UTC, a low-level vorticity anomaly was located at about 16°W and 20°N and another at 10°W and 17°N (Fig. 4.22a,b). Northeast of these vorticity maxima, bands of high positive relative vorticity occur in a region with marked

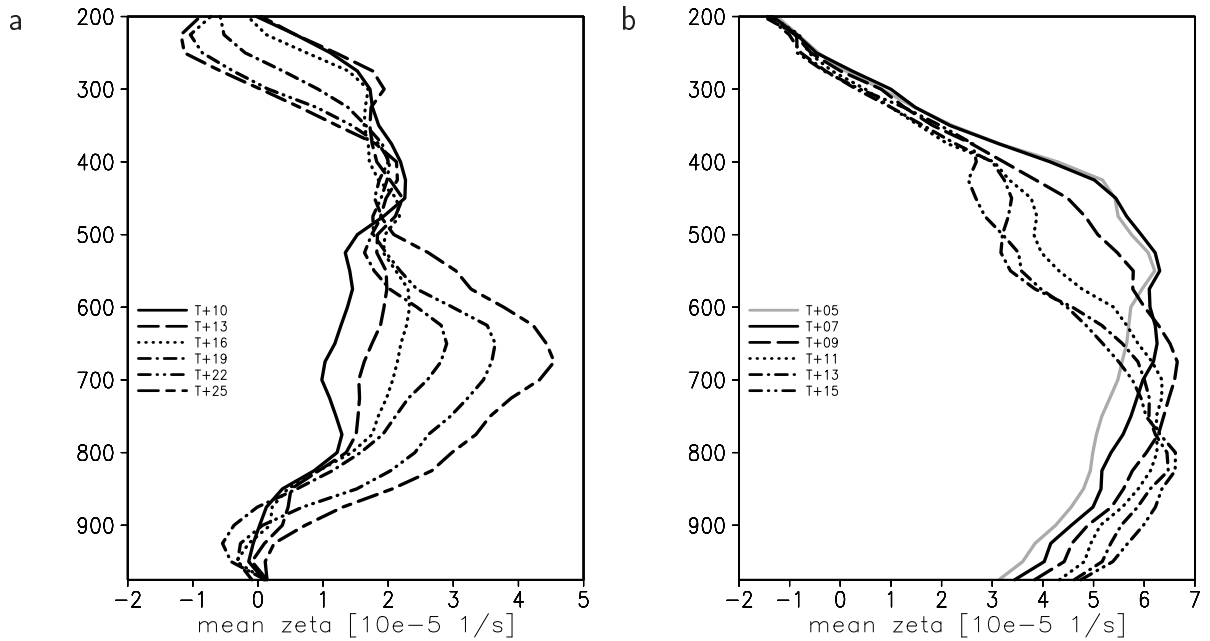


Figure 4.20: (a) Mean vertical component of relative vorticity for the convective system over West Africa based on the COSMO run initialised on 9 September 2006, 12 UTC ($8.5\text{--}14.5^\circ\text{N}$, $11.0\text{--}5.4^\circ\text{W}$) for selected times. (b) The same for the convective system over the eastern Atlantic based on the COSMO run initialised at 00,UTC on 12 September 2006 ($10.5\text{--}14.0^\circ\text{N}$, $22.5\text{--}17.5^\circ\text{W}$) for selected times. Pressure (hPa) is used as the vertical coordinate.

low-level convergence. During the next 12 hours, the relative vorticity maxima move closer together and then merge. On 10 September at about 18 UTC (Fig. 4.22e,f), a tongue of warm air at about 17°W and 19°N crossed the West African coast line and moves over the ocean. This region of relatively warm air extended further south during the next 12 hours (Fig. 4.22g,h) and is associated with significant positive relative vorticity. On the southern fringes of the secondary heat low, a sharp temperature and moisture gradient occurred marking the inter tropical discontinuity. The wind speed increased between 18 UTC and midnight and the air in this region was very dry. The diurnal cycle of the secondary heat low was distinct in the temperature field as well. The flow above the secondary heat low was predominantly easterly, associated with the AEJ (Fig. 4.21b). The enhanced vorticity in the AEW trough was located further inland and was entering the box used for the budget calculations at this time.

The secondary heat low crossed the West African coastline in the evening hours of 11 September. It was located at around $15\text{--}19^\circ\text{N}$ and $16\text{--}20^\circ\text{W}$ over the Atlantic on 11 September at 12 UTC (Fig. 4.21c). At this time the AEW trough reached the West

African coast line and an MCS developed south of Dakar. The secondary heat low moved southwestwards over the ocean and retained warmer temperatures compared to its environment. On 12 September at 00 UTC it started to move into the box over the ocean (Fig. 4.21e). In the southeastern part of the box a relative vorticity maximum occurred associated with the development of the monsoon flow. Thus the initial enhanced low-level vorticity over the ocean (Fig. 4.20b) occurred due to both the secondary heat low and the monsoon circulation. At this time the convective activity over the Atlantic was very low. At 600 hPa, the AEW moved into the box from the east. Six hours later the low-level and the mid-level vorticity maxima began to overlap each other (Fig. 4.21g,h). This is the time when convection is initiated over the Atlantic and the tropical depression starts to develop. A similar contribution of a secondary heat low to tropical cyclogenesis has been observed off Western Australia (M. Reeder, personal communication).

A zonal cross section through one of the low-level vorticity maxima on 9 September (Fig. 4.23a,b) shows the relatively cool and moist air over the Atlantic and the dry warm air over the Sahara (12-8 °W). Strong northerly winds occur below 800 hPa in the region with the strong potential temperature gradient. The region of maximum surface temperatures between about 13.5 and 11 °W collocates with a low-level cyclonic circulation (Fig. 4.23c,d). High positive relative vorticity values occur at around 16 °W in the region with high potential temperature and dry air. As the low-level circulation moves towards the West African coastline it intensifies and reaches higher levels (up to about 700 hPa) with its maximum located at about 920 hPa (Fig. 4.23e,f). This intensification is probably due to stretching, as the Atlantic inflow (Grams et al., 2010) is distinct, leading to a strong baroclinic zone near the West African coast. As the the vorticity anomaly moves over the Atlantic it remains warmer than the environment (18.5-16.5 °W; Fig. 4.23g,h). Between 700 and 850 hPa a relatively warm layer is apparent. On 12 September at 06 UTC, the relatively warm air at around 25 °W extends to the surface (Fig. 4.23k,l). High values of relative vorticity occur at low-levels in the same region and slightly east of it, an even higher relative vorticity anomaly can be found between 700 and 500 hPa. One might hypothesise that the low-level vorticity anomaly associated with relatively warmer air compared to its environment, that initially developed out of a secondary Saharan heat low, aids to transform the cold-cored AEW into a warm core system, and thus, provides favourable conditions for tropical cyclogenesis. Further studies are, however, needed to analyse this.

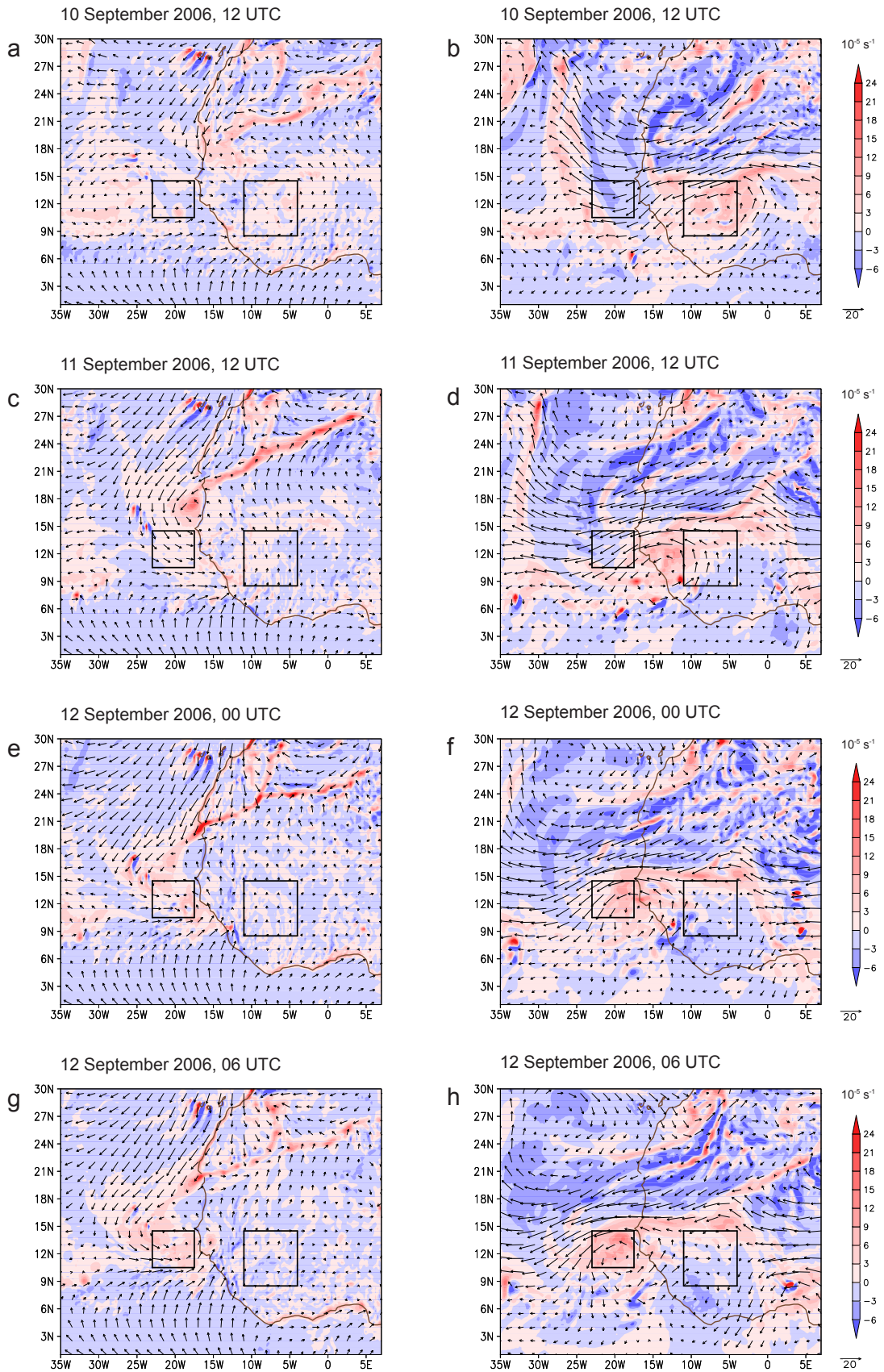


Figure 4.21: Vertical component of relative vorticity and the horizontal wind (m s^{-1}) at 1000 hPa (left column) and 700 hPa (right column) in the ECMWF analysis.

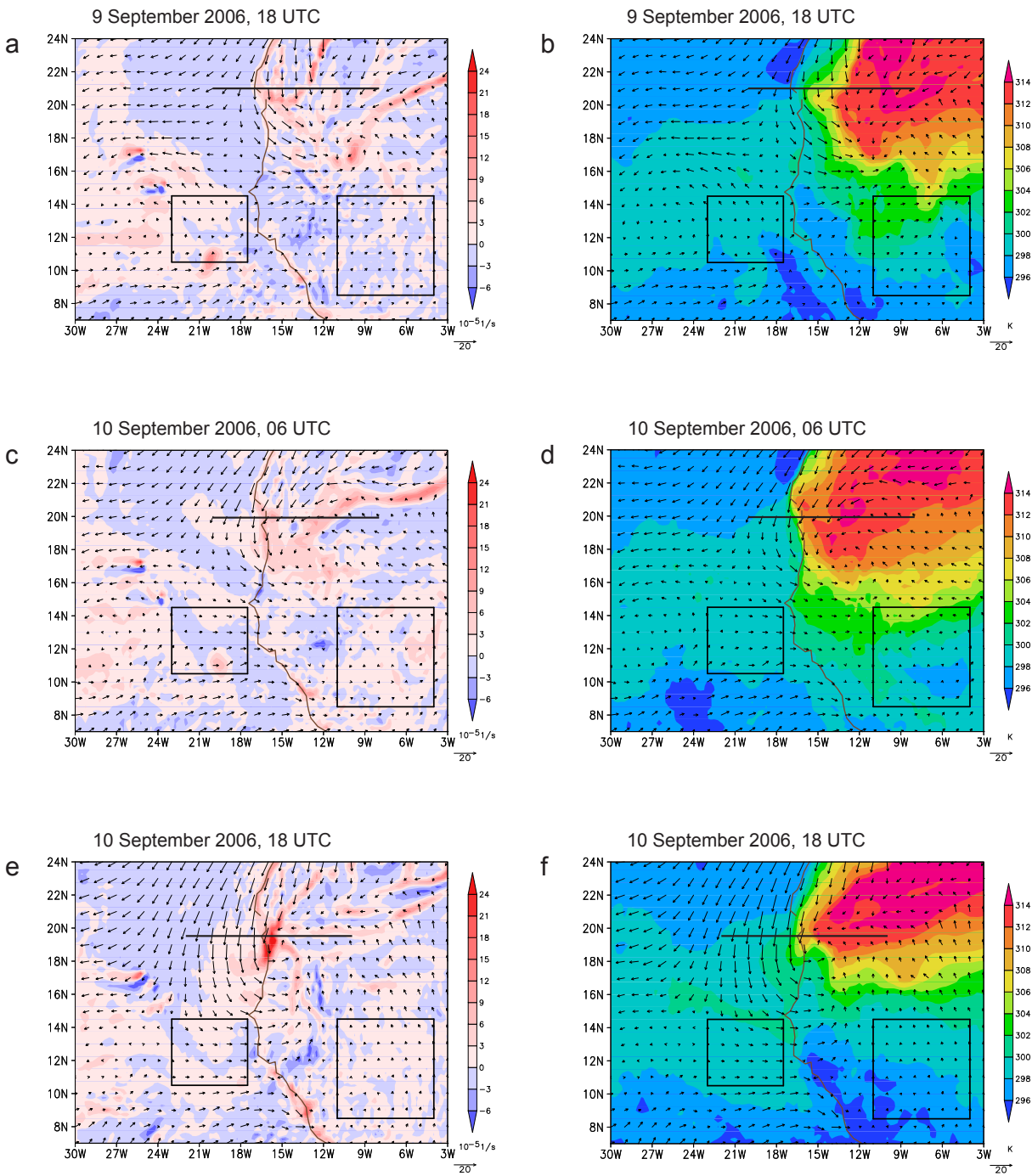


Figure 4.22: Vertical component of relative vorticity (left column), the potential temperature (right column) and the horizontal wind (m s^{-1}) at 975 hPa in the ECMWF analysis. The solid black line denotes the position of the cross sections in Fig. 4.23.

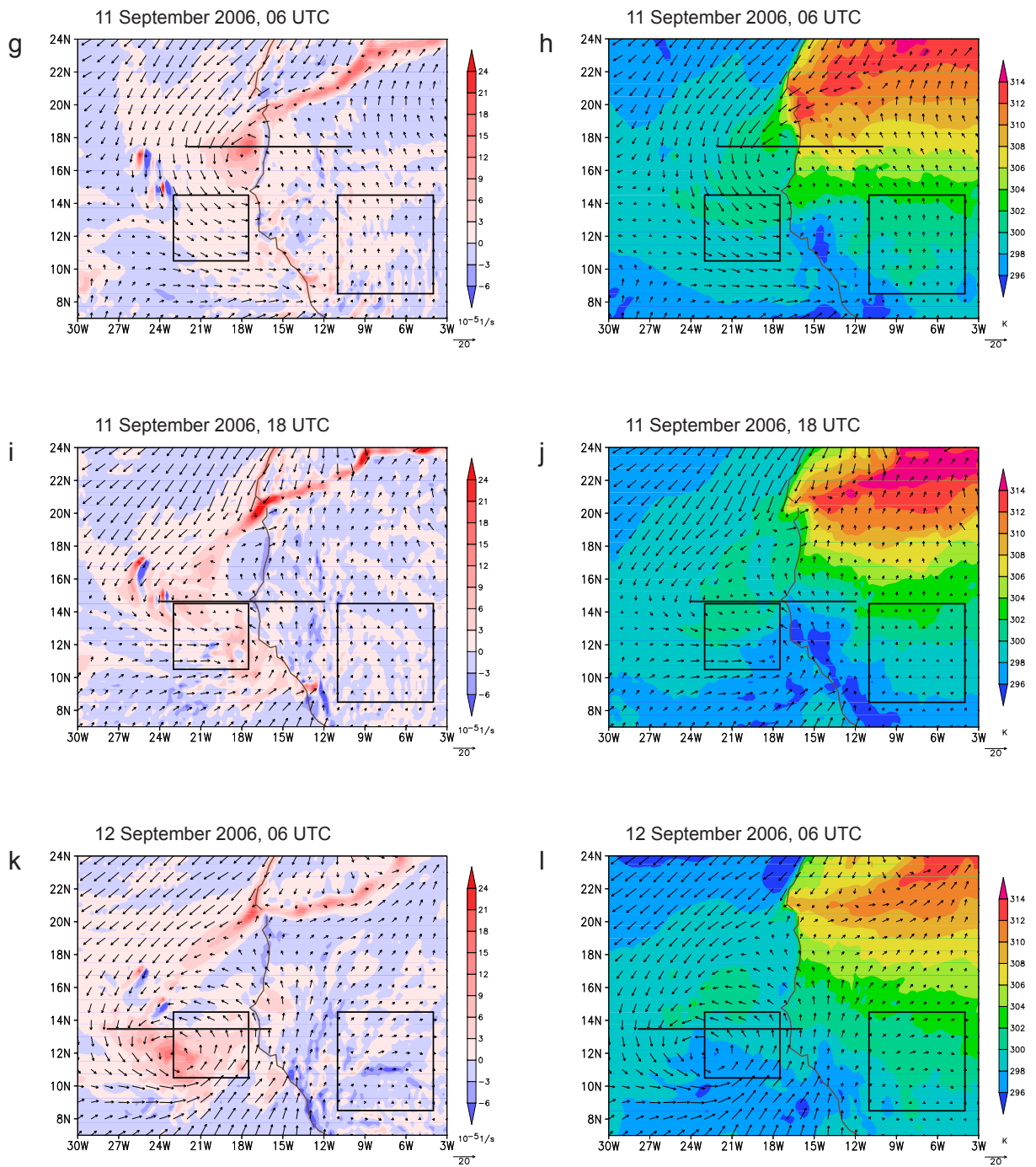


Figure 4.22: (Continued.)

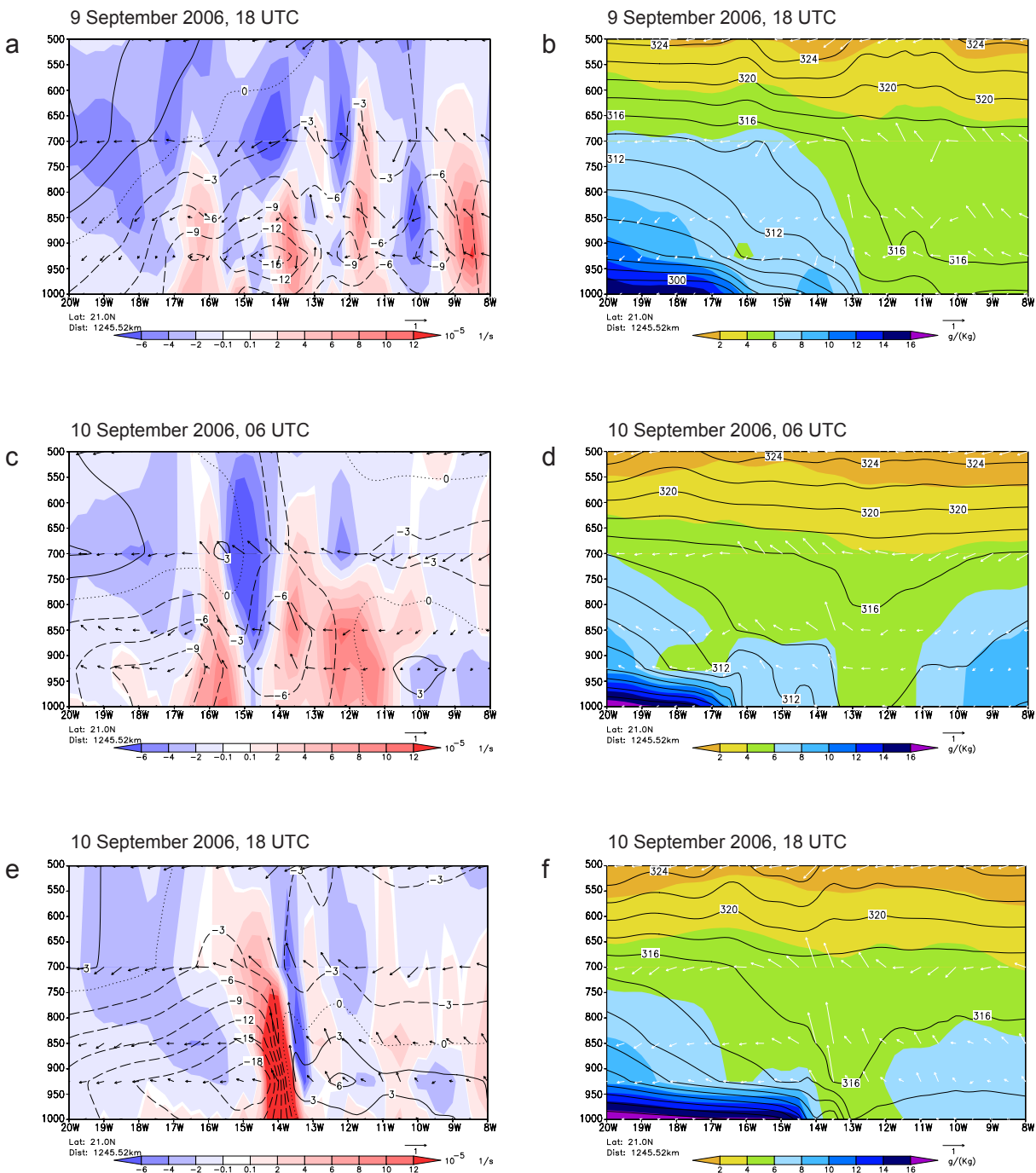


Figure 4.23: Left column: Cross sections of the vertical component of relative vorticity (shaded) and the meridional wind (contour interval 3 m s^{-1}). Right column: Cross section of specific humidity (shaded) and potential temperature (contour interval 2 K) in the ECMWF analysis. The arrows display the wind along the cross section. The position of the cross sections is given in Fig. 4.22. Pressure is the vertical coordinate.

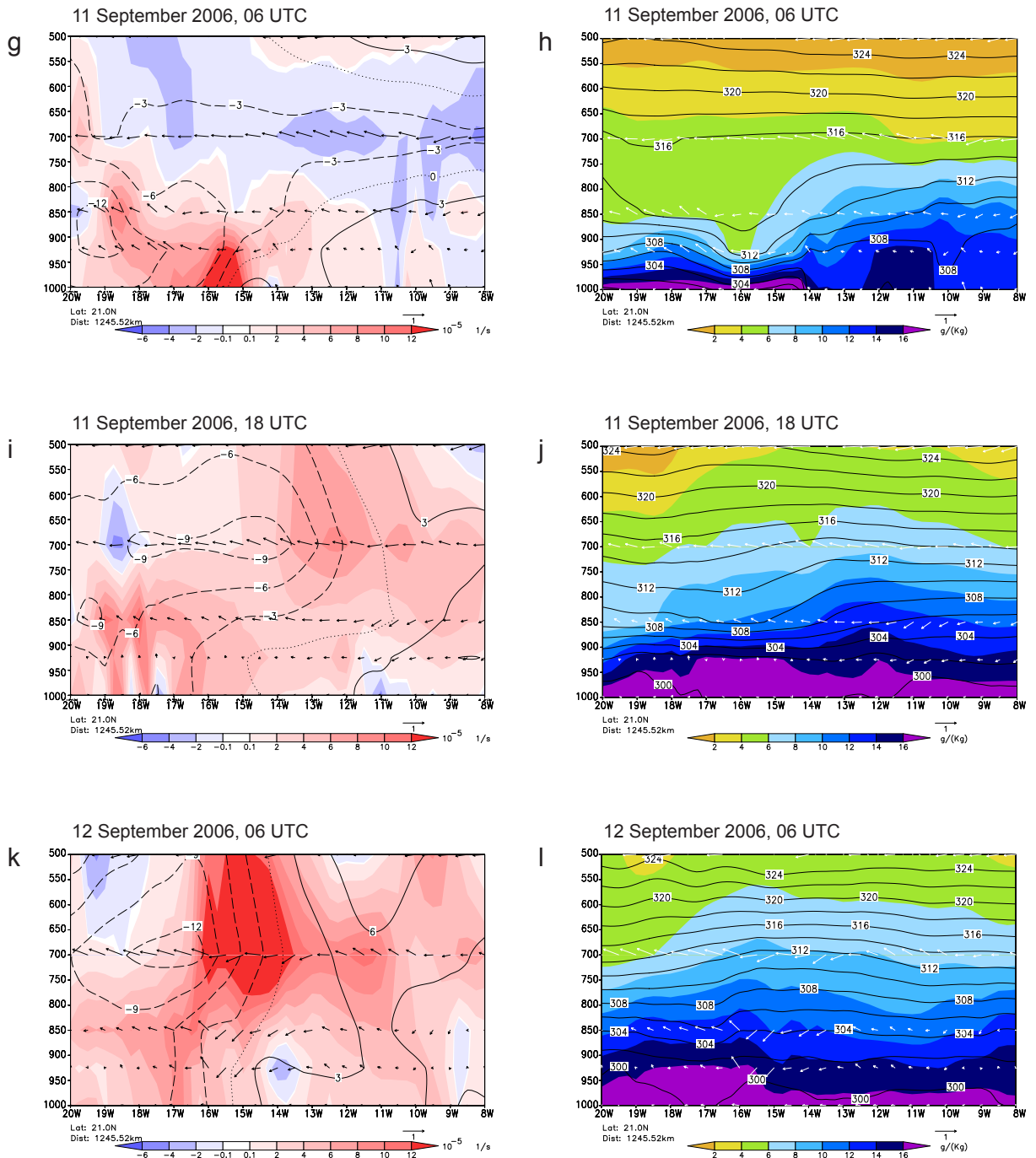


Figure 4.23: (Continued.)

The relative vorticity and PV profiles (Fig. 4.24) exhibit similar characteristics. Over land, the PV increased with time between 900 and 600 hPa and decreased above 300 hPa. The PV maximum remained located around 600 hPa. Over the ocean, the maximum PV occurred at about 500 hPa at the beginning of the period shown. It decreased markedly during the following hours whereas the PV between 700 and 900 Pa increased. As for the relative vorticity, the PV maximum at 700 hPa did not increase after a forecast time of 9 hours but it moved downward until it occurred at about 800 hPa at the end of the period.

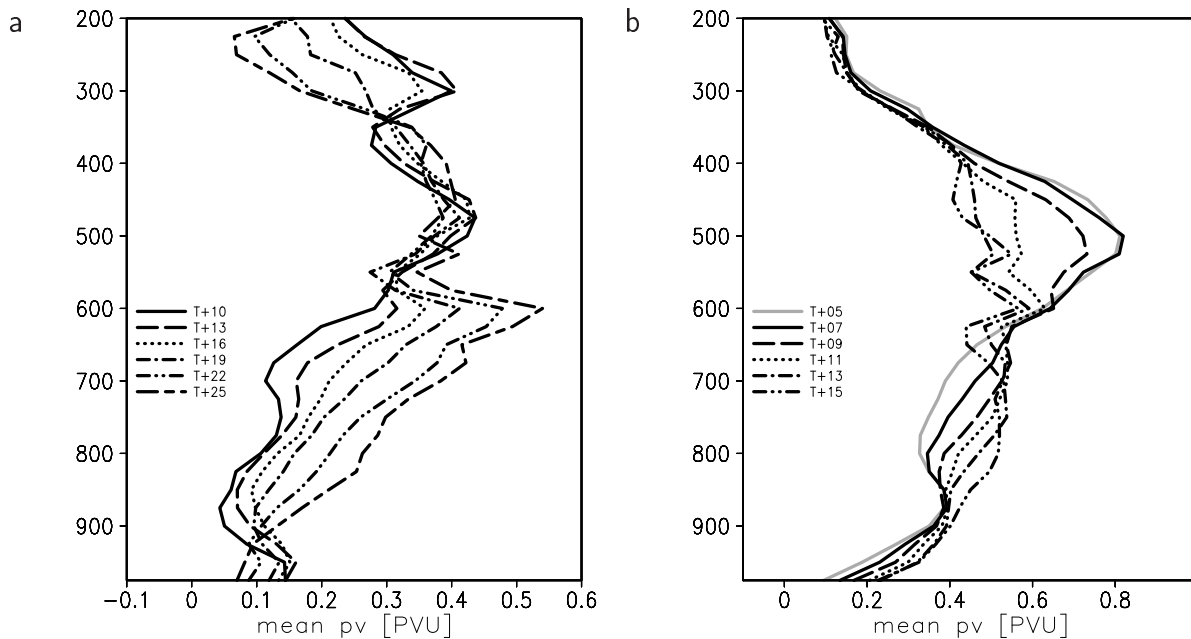


Figure 4.24: (a) Mean potential vorticity for the convective system over West Africa based on the COSMO run initialised on 9 September 2006, 12 UTC ($8.5\text{--}14.5^\circ\text{N}$, $11.0\text{--}5.4^\circ\text{W}$) for selected times. (b) The same for the convective system over the eastern Atlantic based on the COSMO run initialised at 00,UTC on 12 September 2006 ($10.5\text{--}14.0^\circ\text{N}$, $22.5\text{--}17.5^\circ\text{W}$) for selected times. Pressure (hPa) is used as the vertical coordinate.

The spatial vorticity structure leading to the mean profiles shown in Fig. 4.20 is rather complex. We see negative relative vorticity in the lowest levels at the leading edges of the three convective systems embedded in the MCS over West Africa due to the system's cold pool. Between the cold pool and the level of the AEJ, positive relative vorticity occurs in the convective region and negative relative vorticity in the stratiform region. This is reversed above the jet. At the height of the jet we see a more patchy distribution of vorticity (Fig. 4.25b). Below 800 hPa and after a forecast time of about 14 hours, line-end vortices developed at the end of the quasi-linear region of deep convection in system 1

over land. As time proceeds, the other two systems also developed line-end vortices with cyclonic vorticity to the south and anticyclonic vorticity to the north (Fig. 4.25a). These vortices are initiated from the tilting of horizontal vorticity. The effect of stretching helps to strengthen the circulation (Davis and Weisman, 1994).

At a forecast time of about 16 hours system 1 develops an MCV which becomes stronger and larger-scale during the following hours. From 18 hours into the simulation, system 2 develops an MCV also, that was smaller than that of system 1 (Fig. 4.25b; (9.2-8.0 °W, 9.7-10.8 °N) and (8.8-7.8 °W, 11.5-12.3 °N)). At a forecast time of 21 hours, a small vortex develops in the third system. These vortices could be observed between 500 and 700 hPa. They increased the relative vorticity at these levels. All the individual relative vorticity tendencies add up to a strong increase between 600 and 850 hPa.

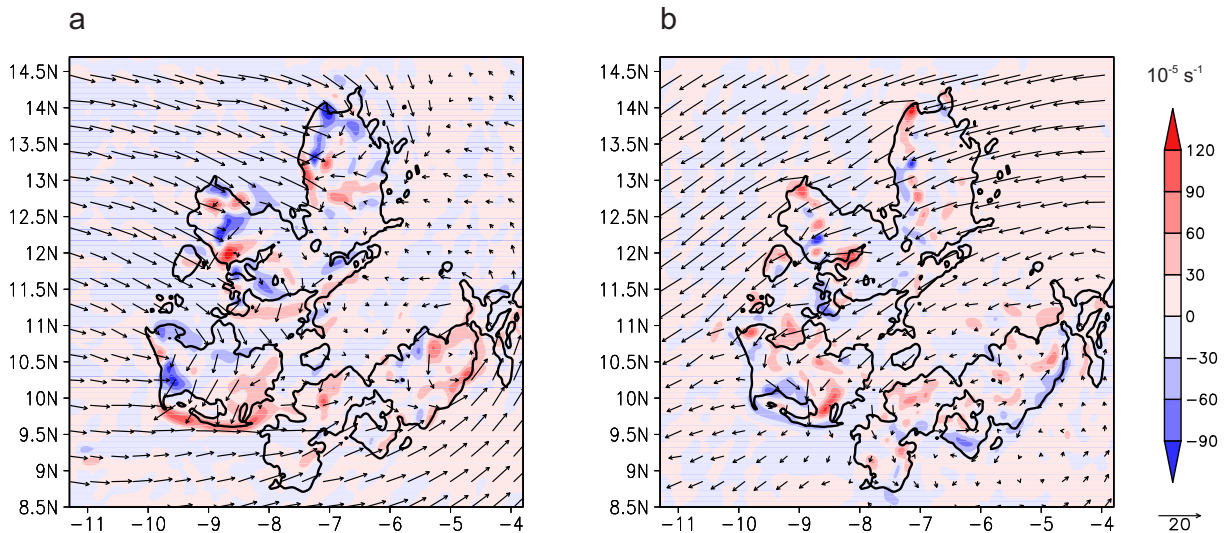


Figure 4.25: The filtered relative vorticity and horizontal wind (ms^{-1}) at (a) 900 hPa and (b) 600 hPa for the convective system over West Africa after 20 forecast hours of the COSMO simulation initialised on 9 September 2006, 12 UTC. The applied filter replaces each grid point by the average of the surrounding 7×7 grid points. The black contour displays the total water content of 60 kg m^{-2} .

Over the ocean, the vorticity decrease seen above 600 hPa is mostly associated with the negative relative vorticity in the southern portion of the region considered (Fig. 4.26 a,b) extending over a larger area. This negative relative vorticity occurs between the westerly outflow from convection in the centre of the box (between about 11.5°N and 12°N) and the easterly flow south of the box associated with an enhanced cyclonic circulation further south. No MCV could be observed, only small-scale cyclonic and anticyclonic vorticity

anomalies (Fig. 4.26). Generally, the convective system over the ocean exhibited less mesoscale organisation than the system over land. The increase at 800 hPa is associated with the vorticity field developing more small-scale positive vorticity anomalies embedded within the large-scale cyclonic flow (Fig. 4.26 b,d). The most marked vorticity anomalies are associated with the strongest convective features described in section 3.1. These are located at (20.5°W, 12.8°N) at 9 h when the convection still appeared influenced by vertical shear, and at (19.9°W, 12.4°N) at 13 h when the stratiform region dominated the convection. In each case there is a mesoscale low-level circulation centre embedded within the larger-scale circulation at the location given.

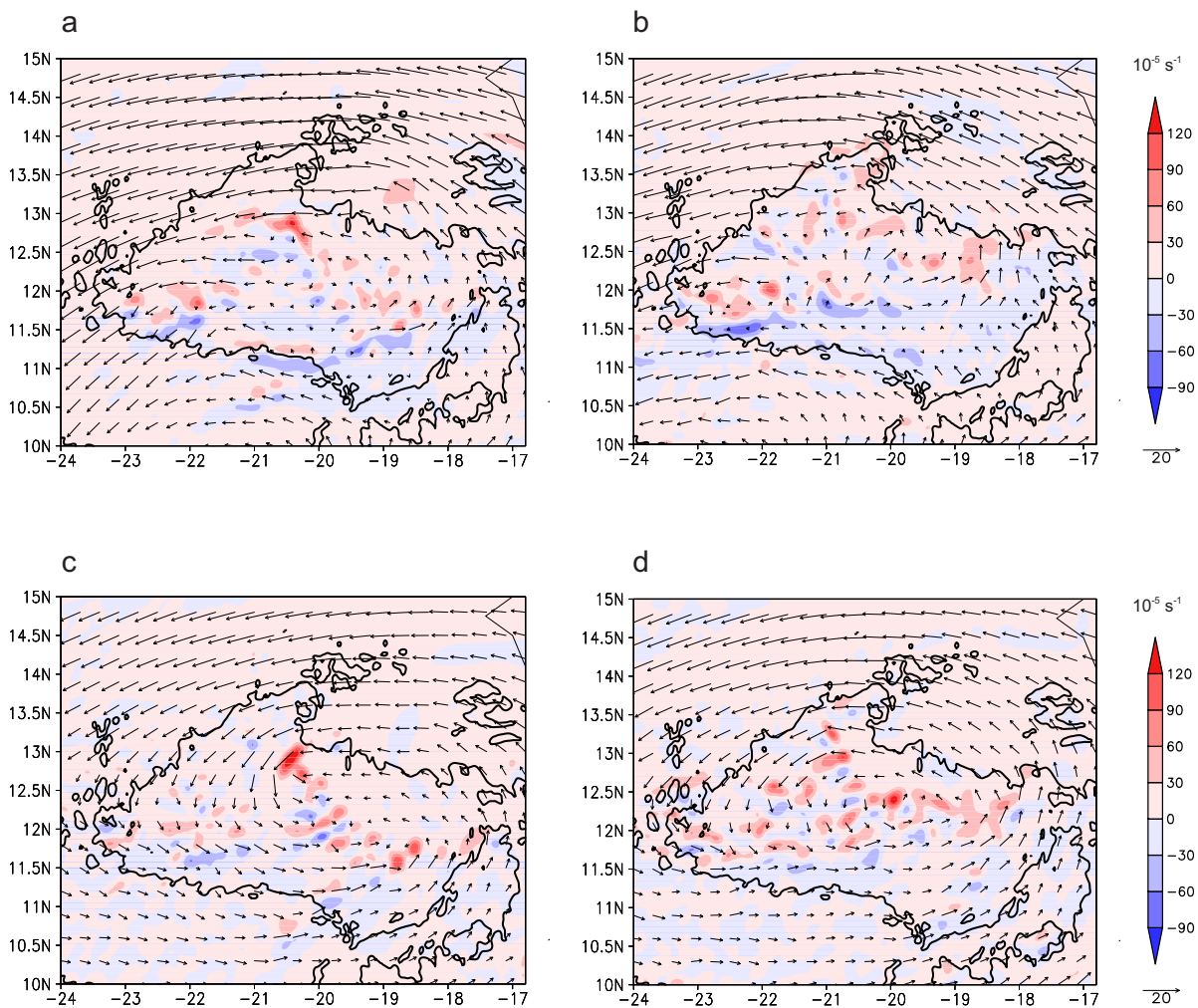


Figure 4.26: The filtered relative vorticity and horizontal wind (m s^{-1}) at 600 hPa (upper row) and 800 hPa (lower row) for the convective system over the eastern Atlantic after (a, c) 9 h and (b, d) 13 forecast hours of the COSMO simulation initialised on 12 September 2006, 00 UTC. The applied filter replaces each grid point by the average of the surrounding 7×7 grid points. The black contour displays the total water content of 60 kg m^{-2} .

We analyse the relative vorticity of the individual systems following the method of DG09. As the heat budget has shown, there is a strong cancellation between the potential temperature tendencies due to diabatic heating and vertical advection, implying that the temperature anomalies are small and the isentropes approximately horizontal. In this case, the net flux of density-weighted PV across a pressure surface is small as has been confirmed with calculations of this flux from the COSMO runs, and the description of the dynamical evolution using vorticity and PV is analogous (Davis and Weisman, 1994). It is advantageous to analyse the vorticity budget since the vorticity flux across pressure surfaces is identically zero (Haynes and McIntyre, 1987) and we avoid the difficulties associated with calculating and interpreting the differences between two large but opposed terms. Arnault and Roux (2010) analyse the vorticity budget for the case of Helene and a non-developing system, but do not apply the flux form of the equation used here. Their study uses the vorticity budget to analyse why one of their cases underwent tropical cyclogenesis whilst the other case decayed. We consider the structure of the convective system themselves and use the vorticity budget to assess the overall impact of the convection on the developing system. Thus these two studies are complementary.

The relative vorticity budget can be found for convection over land (Fig. 4.27a) and over water (Fig. 4.27b) based on hourly model output. The overall balance of the relative vorticity budget is good (compare the grey and black solid lines). Note that rhs is the sum of all terms except friction in equation 3.24, which gives the tendency of the circulation averaged around a box. Some discrepancies occur near the surface and at around 800 hPa over land.

Over land, the relative vorticity tendency is positive between 600 and 850 hPa and negative above 500 hPa. The convergence between the surface and about 700 hPa and divergence in the outflow region of the convective system results in a positive relative vorticity tendency due to vortex stretching in the lower levels and a negative tendency due to vortex compression in the upper levels. The eddy flux, which can be identified with horizontal vorticity advection, leads to a net increase in relative vorticity at mid-levels. The effect due to tilting is a negative relative vorticity tendency below 800 hPa and a slightly positive effect above.

Over water, the total relative vorticity tendency is positive below 700 hPa with its maximum close to the surface. The strong positive effect of convergence in this region is balanced by a negative tendency due to the eddy flux and a weak effect of tilting. Aloft it is the stretching term in particular that leads to the negative relative vorticity tendency with its maximum between 400 and 500 hPa. At this height there is also a negative contribution of the eddy flux. The magnitude of the net relative vorticity changes is larger over the ocean than over the land. The relative vorticity tendency due to tilting is larger at low levels over land than over the ocean and has the opposite sign at 850 hPa. The relative vorticity tendency due to the eddy flux around 700 hPa is larger over land. In addition, the vorticity decrease at upper levels is stronger over land. The maxima of vorticity increase and decrease occur at lower levels over the ocean. These results are in accordance with the total relative vorticity change shown in Fig. 4.20.

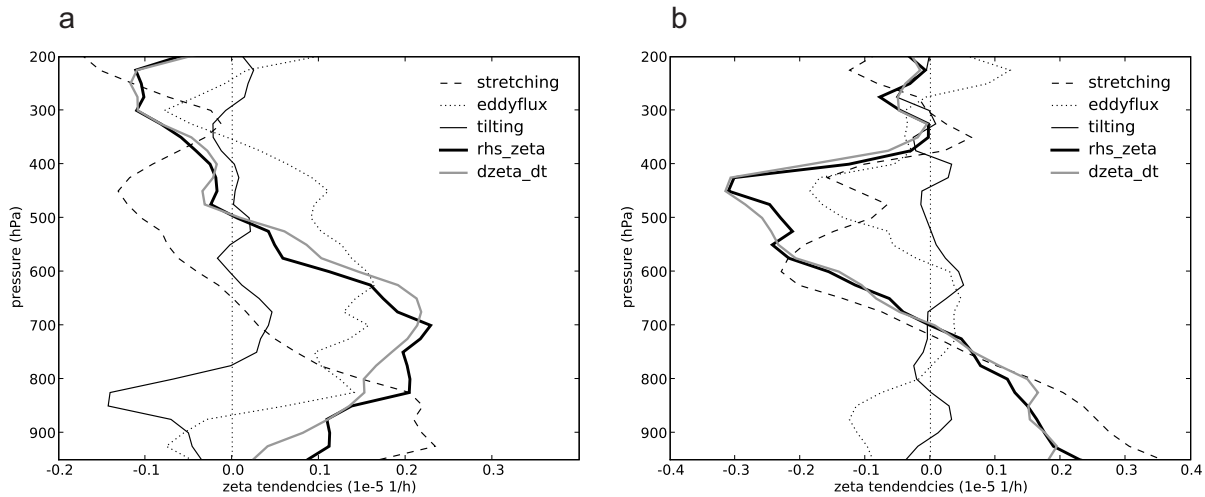


Figure 4.27: Vertical profiles of box-averaged total vorticity change ($dzeta_dt$) is displayed in grey, the sum of hourly rates of changes of vorticity from all rhs term in equation 3.24 except friction (rhs_zeta) is displayed by the thick solid line, eddy flux by the dotted line, stretching by the dashed line, and tilting is displayed by a thin solid line for (a) the convective system over West Africa based on the simulation initialised on 9 September 2006, 12 UTC (T+9 to T+23), and for (b) the convective system over the eastern Atlantic based on the simulation initialised on 12 September 2006, 00 UTC (T+5 to T+15).

Different processes attain importance during the life cycle of the MCS over West Africa and the convective system over the eastern Atlantic. The hourly rate of change of the average relative vorticity, i.e. all terms on the rhs of equation 3.24 except friction, over land (Fig. 4.28a) peaks after 18 hours just below 700 hPa and below 800 hPa. Above 400 hPa the relative vorticity decreases.

The MCS over land consisted of 3 prominent convective systems with different stages of maturity. At the beginning of the period considered (9 to 11 hours into the simulation) the three systems developed very quickly, with system 1 being the strongest. During these two hours a positive relative vorticity tendency occurs below 700 hPa due to stretching and a weakly negative tendency occurs above. As the MCS grows, the vertical vorticity tendency due to stretching increases in magnitude (Fig. 4.28c) and the depth of the layer with vortex stretching increases with time. By the end of the period shown vortex stretching extends up to 600 hPa and has the strongest impact on the net relative vorticity change below 700 hPa. The convective system developed a distinct divergent outflow. Thus, there is vortex compression above 600 hPa. The strongest effect of tilting is mainly restricted to the levels between 800 and 900 hPa. During the system's life cycle the height of the maximum negative tendency due to tilting decreases. Tilting has only a small contribution at mid-levels. Above 600 hPa, the tendency due to tilting is only slightly positive. A large impact at mid-levels results from the eddy flux. As we will see later this presents a striking difference to the relative vorticity budget over the ocean. The eddy flux or horizontal advection of relative vorticity is largest at the height of the AEJ and positive between 450 and 750 hPa (Fig. 4.28b). It is markedly positive at midlevels during the first 3 hours and then again after a forecast time of 17 hours. The relative vorticity tendency due to the eddy flux is negative below about 850 hPa (Fig. 4.28b). This negative tendency becomes stronger with time. Thus the main contribution to the increase in average vorticity is the eddy flux term. For the area over which the budget was calculated the main contribution to the eddy flux appears to be from anomalously positive vorticity being advected inwards at the northeast corner of the box (Fig. 4.25b). To determine how and why the eddy flux term changes the circulation, we calculated the advection of the perturbation absolute vorticity through each of the four vertical surfaces surrounding the box and considered ingoing and outgoing fluxes separately. For this purpose we computed quantities like

$$F_{\text{east}}^{\text{in}} = \int_{A_{\text{east}}^{\text{in}}} u\eta' dA, \quad (4.1)$$

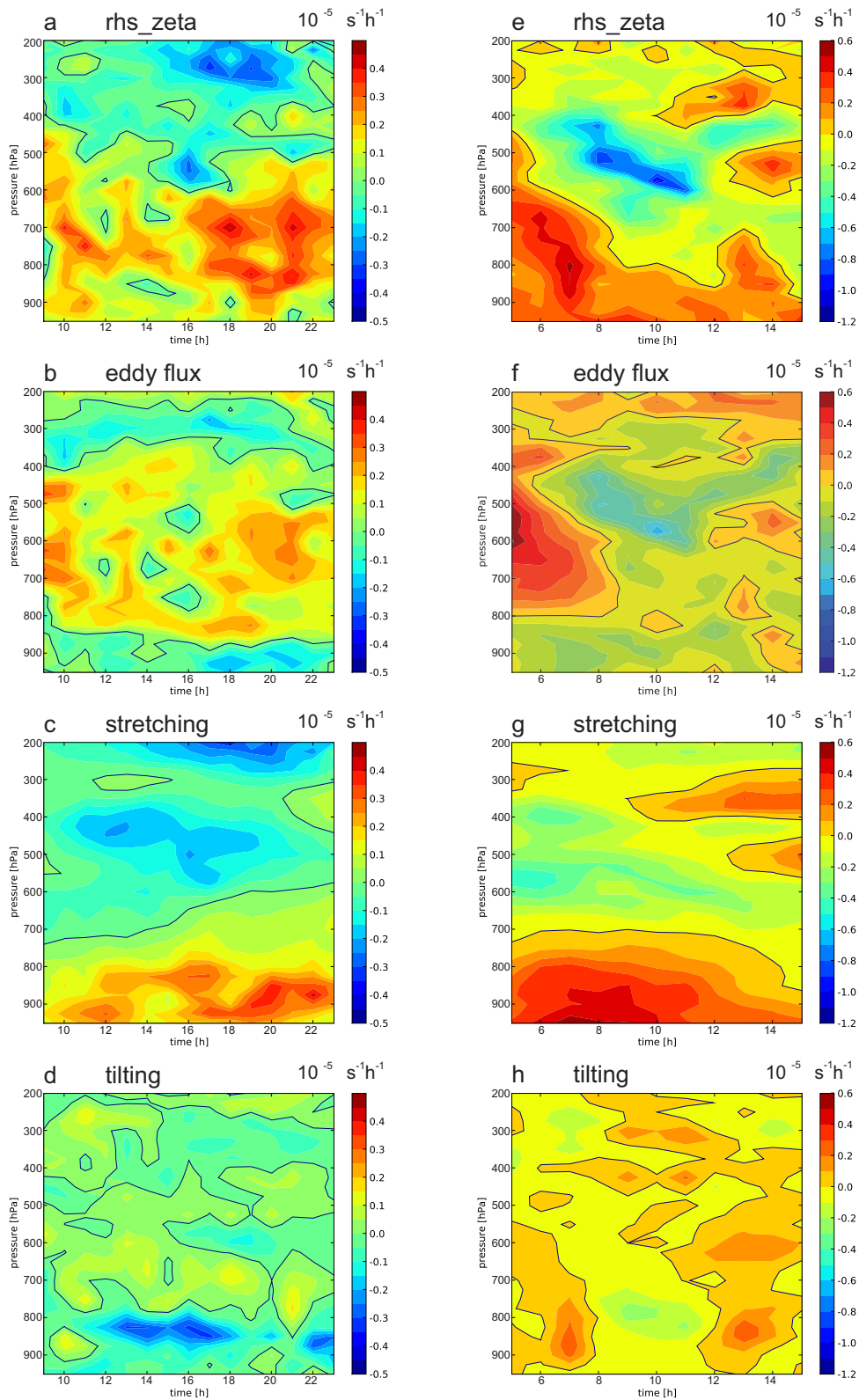


Figure 4.28: (a)-(d): Time–pressure series of hourly changes in box–averaged vorticity representing (a) total relative vorticity tendency (neglecting friction), (b) eddy flux, (c) stretching, and (d) tilting for the MCS over West Africa. The box (11.0 to 4.0°W, 8.5 to 14.5°N) encompasses the convective system throughout the whole time. The forecast hours are shown here based on the model run that was initiated on 9 September 2006, 12 UTC. (e)-(h): As in (a)-(d), but averaged over 23.0-17.5°W and 10.5-14.5°N for the convective burst over the Atlantic. This model run was initiated on 12 September 2006, 00 UTC. Note, the colour scale is different over land and water. The black contour denotes the zero–line.

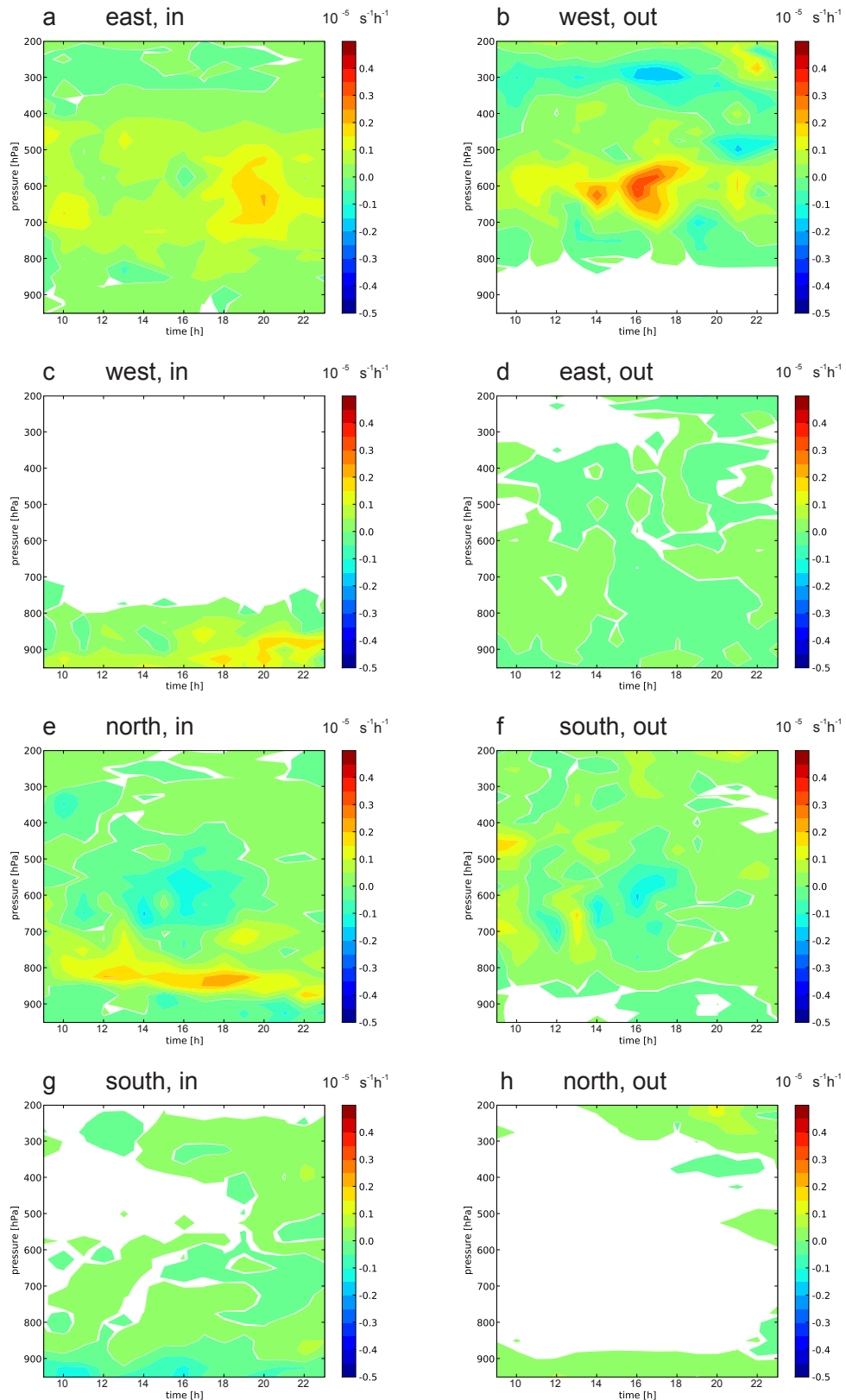


Figure 4.29: The time–pressure series of hourly changes in the eddy flux for the convective system over land. The ingoing (left side) and outgoing (right side) horizontal advection of the perturbation absolute vorticity through each of the four vertical surfaces surrounding the box (details can be found in the text). Positive values refer to a transport of perturbation vorticity into the given direction. Thus, positive values of a quantity labelled with “in” cause an increase, positive values of quantities labelled with “out” an decrease of the integrated vorticity in the box. The white areas indicate regions where no eddy flux in the shown direction occurs.

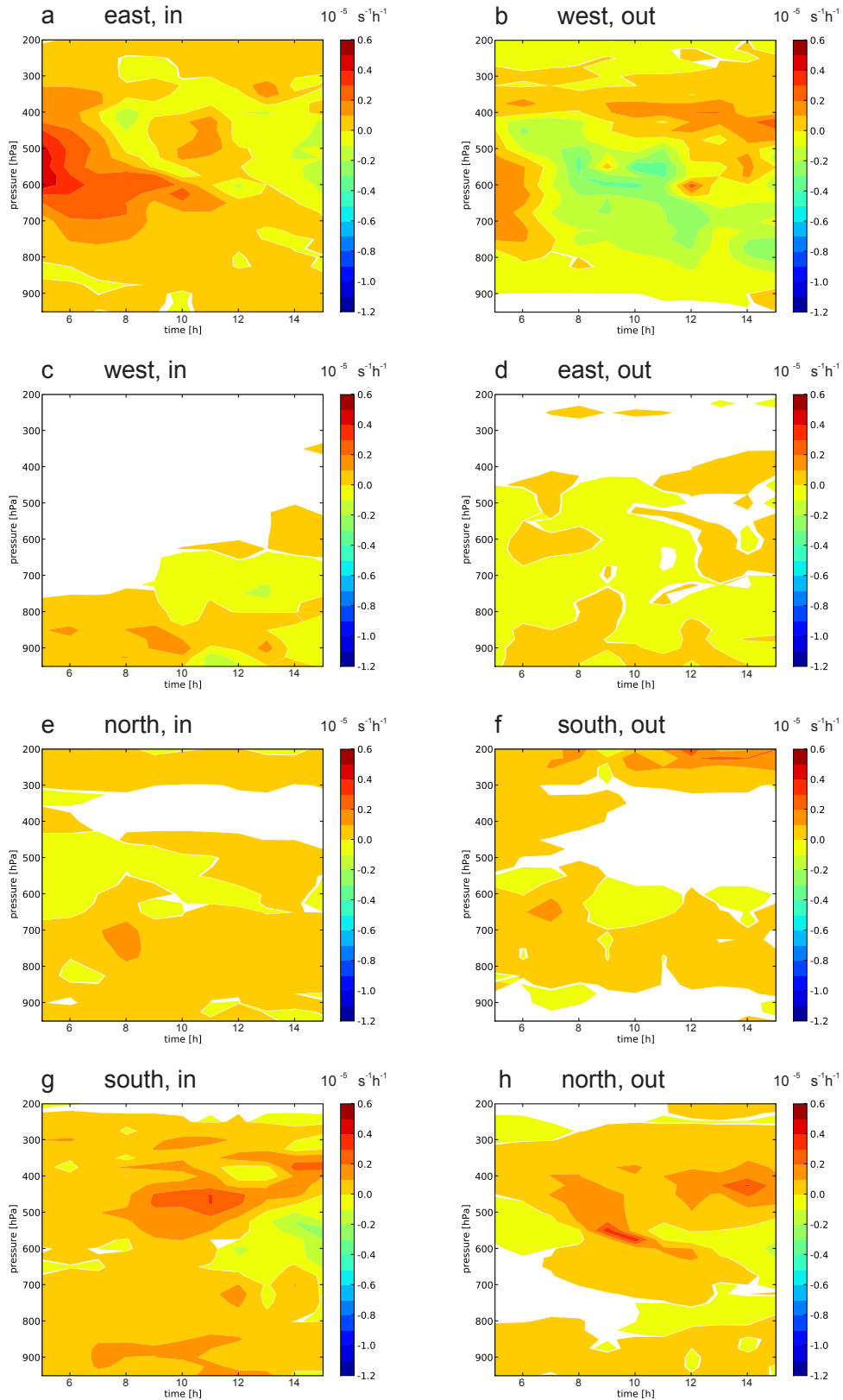


Figure 4.30: The same as Fig. 4.29 but for the convective system over the ocean.

the eddy flux into the box coming through the east side, where $A_{\text{east}}^{\text{in}}$ is the part of the east side of the box for which $u < 0$. The time evolution for all levels of $F_{\text{east}}^{\text{in}}$ and analogously defined quantities for the other sides and directions are shown in Fig. 4.29. Positive values refer to a transport of perturbation vorticity into the given direction. Thus, positive values of a quantity labelled with “in” cause an increase, positive values of quantities labelled with “out” an decrease of the integrated vorticity in the box.

Three main features influence the eddy flux for the convective system over West Africa: the AEJ/AEW, the secondary heat low northwest of the box and the system itself. Anomalously positive vorticity is embedded in the AEW and advected with the AEJ into the box from the east between about 400 and 800 hPa, with the largest values between the forecast hours 7 and 11 and from 18 to 22 (Fig. 4.29a). Between the forecast hours 12 and 19 large amounts of positive absolute vorticity perturbation are advected out of the box by the AEJ at around 600 hPa (Fig. 4.29b). The advection of negative perturbation vorticity to the west can be seen at about 300 hPa due to the convective system’s outflow (Fig. 4.29b). It became stronger as the system developed and reached its maximum at around 16-18 forecast hours. At the northern side, the absolute vorticity perturbation between about 850 and 900 hPa is increased due to a marked low-level inflow of positive relative vorticity (Fig. 4.29e). On the western side of the box, positive perturbation absolute vorticity is also advected into the box below 800 hPa, especially after 18 forecast hours (Fig. 4.29c). This northeasterly flow occurs between the secondary heat low which was located northwest of the box and the monsoon flow to the south (not shown). Negative perturbation vorticity is advected into the box from the northern side between about 500 and 700 hPa between 13 and 18 hours (Fig. 4.29e). Only weakly positive or negative absolute vorticity perturbations are advected out of the eastern, northern and southern sides of the box (Fig. 4.29d,f,h). In summary, positive perturbation vorticity is advected into the box from the eastern and northern side, resulting in high eddy flux values between 700 and 900 hPa during the whole time and between 400 and 700 hPa during the first three hours and from 18 forecast hours on. The decrease from 14 to 17 h occurs due to the outflow of positive absolute vorticity in the west.

The situation over the ocean is rather different (Fig. 4.28e-h). The relative vorticity tendency is strongly positive between the forecast hours 5 and 8 and the height of the

maximum relative vorticity tendency decreases significantly (Fig. 4.28e). Between 600 and 450 hPa the relative vorticity tendency is negative, becomes stronger with time and moves downward. The positive vorticity tendency is not as strong as in the first 3 hours of the period analysed here, but it continues to move downward with time. The decreasing height of the maximum relative vorticity tendency is due to the decrease in height and intensity of the tendency due to eddy flux. Over water, the AEW at 600 hPa moves through the box for which the relative vorticity budget was calculated. The evolution of the eddy flux over water (Fig. 4.28f and Fig. 4.30) appears to be dominated by two factors. The first one is the advection of positive absolute vorticity anomalies at the eastern boundary into the box (Fig. 4.30a) and the advection of negative perturbation absolute vorticity out of the box at the western side (Fig. 4.30b). This is responsible for the initial strongly positive tendency. Between about 600 and 500 hPa and the forecast hours 8 to 12, distinct positive absolute vorticity is advected out of the box, leading to a decrease in the eddy flux (Fig. 4.28f). The second factor is the area of positive absolute perturbation vorticity in the southern portion of the box (Fig. 4.30g). Depending on the flow pattern at the southern boundary this anomaly is at times advected into the box and at other times out of the box. At the southern side of the box, between 550 and 300 hPa, positive absolute vorticity is advected into the box as the results of the outflow of convective systems south of the box analysed here. Due to the related vorticity anomalies the eddy flux results in a positive relative vorticity tendency between 600 and 800 hPa during 8 hours into the simulation and a negative tendency during the next 4 hours (Fig. 4.28f).

As the system grows, the low-level convergence becomes much stronger and reaches its peak intensity during the system's growing and early maturing phase (T+6 to T+10). This results in a strong positive relative vorticity tendency below 700 hPa. The divergence aloft accounts for the negative relative vorticity tendency. At around 12 hours into the simulation, a positive relative vorticity tendency can be observed between 300 and 400 hPa and around 500 hPa, which can be attributed to convergence in the region where stratiform clouds occur. The downdraught at midlevels (Fig. 4.19e,f) and the stratiform region above give the mid-level vortex compression and upper level stretching. The tilting term plays a minor role in the relative vorticity budget. The effect of tilting is weakly positive, in contrast to the system over land, and is found at lower levels when small convective

cells occur at the boundary of the box. The vorticity budget over the ocean illustrates nicely how the tropical cyclogenesis occurs as the AEW moves into the box (Fig. 4.28f) and the subsequent convective events in an environment with preexisting cyclonic vorticity enhance the low-level vorticity (Fig. 4.28g). A distinguishing feature of this case is the role of both the heat low and the monsoon flow in creating the low-level cyclonic environment. We also calculated the relative vorticity budget for the regions with strong ascent and strong descent and we saw a negative relative vorticity tendency at almost all levels but a weak increase below 900 hPa. This is very similar to the results of Chaboureau et al. (2005). The stratiform region in both studies (profiles are not shown) is responsible for the increase in relative vorticity at mid-levels and basically represents the total relative vorticity changes seen in Fig. 4.28a and e. Their case study is somewhat similar to our land case. Both systems occur over West Africa, but their shear profiles are different. However, their squall line developed a big MCV and ours consisted of 3 embedded systems with a different stage of maturity with each of them developing an MCV of different size and intensity and at different times. Chaboureau et al. (2005) assume that the MCV is advected downstream and combined with the AEJ and thus leads to a reinforcement of the AEJ.

An increase in relative vorticity and PV at midlevels was also observed by DG09. An important difference between the present study and that of DG09 is that they used a smaller box that followed the MCV. The boxes used in this study are relatively large and stationary. Additionally, DG09's July case occurs in the midlatitudes over the central U.S. embedded in westerly flow that increases with height throughout the depth of the system. The systems analysed in this study occur in the tropics and are embedded in easterly flow with a pronounced jet maximum at 600 hPa. In another recent study Conzemius and Montgomery (2009) computed an absolute vorticity budget based on an idealised model run with zonally homogeneous vertical wind shear. When we compare our vorticity budget with these and other studies (e.g. Weisman and Davis (1998); Cram et al. (2002)) we see differences in the details of the tilting term, but overall agreement that the stretching term is dominant in the mid troposphere.

4.3 Summary and Discussion

Two convective episodes embedded in the AEW out of which Hurricane Helene developed have been investigated. One developed over West Africa and the other over the eastern Atlantic. The MCS over land was initiated in the afternoon hours on 9 September 2006 ahead of the trough of the AEW which developed on 2 September 2006 at about 33°E. The convective system increased quickly in intensity and size and developed three arc-shaped convective systems moving westward. As the MCS decayed, new convective bursts occurred in the remains of the old MCS. This led to structural changes of the form of a squall line crossing the coastline at around midnight on 11 September. During the next 24 hours, intense convective bursts occurred over the eastern Atlantic. These convective bursts were embedded in a cyclonic circulation which intensified and became a Tropical Depression on 12 September 2006, 12 UTC. The largest and long lived convective burst in this intensification period was analysed here and compared to the MCS over land.

The main difference between both convective systems is that the one over land is tilted, especially during its mature and dissipation stage, and the one over the ocean is upright above 700 hPa. For both systems the region with the strongest updraughts is collocated with the region of maximum diabatic heating. The downdraughts led to the development of anticyclonic relative vorticity at low levels as well as the cold pools. The CAPE in the environment of both convective systems is similar. The shear between 600 and 800 hPa over land is significantly larger over land than for the convective system over the ocean. During the system's life cycle the shear is reduced at mid-levels and increased near the surface as the mean wind speed is increased below 800 hPa due to the downdraughts. This effect is stronger over land than over the ocean. There is hardly any shear at mid-levels over the ocean and the influence of the AEJ is reduced but still apparent over land.

Drier air at mid-levels over land leads to stronger downdraughts and to a strong cold pool which propagates and thus helps the convection to grow upscale into a mature MCS. Over the ocean, the mid-level air is moister, weaker downdraughts occur and no cold pool develops. Without a cold pool there is no mechanism for the convective system to propagate and thus the oceanic convective systems remain smaller. Due to the smaller shear especially towards the end of the analysed period the convection is harder to sustain

and the lifetime is shorter. The environment, however, is favourable for new convection to form. This leads to the succession of smaller convective systems instead of a single, large MCS over land.

The convective systems modify their environment and these changes can be related to the structure of the system itself. The influence on the environment was assessed by calculating potential temperature and relative vorticity budgets for regions encompassing the convective systems. We defined regions with strong ascent and descent as well as with weak ascent and descent according to the vertical velocity at 650 hPa. With the help of this partitioning, the structure of the convective systems is more evident than in the averages over the entire boxes. This enables us to better interpret the total potential temperature tendency.

The potential temperature tendency for the convective systems over West Africa and the eastern Atlantic show a net cooling between 950 and 800 hPa and a net warming above 400 hPa. The potential temperature tendency due to moist processes and due to vertical advection almost counterbalance each other, with their strongest contribution to the potential temperature tendency in the mid troposphere where the maximum occurs at slightly higher levels over land. The presence of stratiform clouds could be clearly distinguished in the budget for the strong descent regions at 650 hPa for the land case. Here, the cooling due to the unsaturated downdraughts is much stronger for the convective system over land than for the convective system over the ocean. The potential temperature tendency due to turbulence contributes to the total potential temperature budget in the lower troposphere and in the mid troposphere due to the shear below the AEJ. Similar observations have been made in previous studies (e.g. Caniaux et al. (1994); Lafore et al. (1988); Yanai et al. (1973)). Over the ocean, the regions of weak ascent and descent at 650 hPa are more important for the net potential temperature tendency than the contribution from the strong descent region. Downdraughts at midlevels occurred, and a stratiform region around 300 and 400 hPa and shallow convection could be observed. We found that the descent regions are as important as the strong convective updraughts for the total heat budget.

Over land, the relative vorticity increased from about 900 to 500 hPa and decreased above 400 hPa. Over the ocean, the relative vorticity between 600 and 400 hPa is relatively high

at the beginning of the observation period and increased up to a forecast time of 9 h. During the following hours the vorticity increased only slightly but the height at which the maximum occurred was lowered significantly. The main reason for the total relative vorticity changes is the tendency due to stretching over the ocean and the eddy flux over West Africa where it led to an increase in vorticity at mid-levels. The tendency due to stretching leads to a negative relative vorticity tendency above 600 hPa over land and over the ocean. It had a positive contribution at low-levels as well as between 300 and 500 hPa towards the end of the analysed period of the convective system over the ocean. The second important component in the relative vorticity budget is the eddy flux. It has a positive tendency at the beginning and towards the end of the observation period for the system over land. Over the ocean it had its strongest effect at the very beginning of the life cycle of the convective system. Its effect decreased as the system reached maturity but positive tendencies occur at midlevels towards the end. The tilting term lead to a mostly negative tendency in the lower troposphere, but provided the smallest contribution to the relative vorticity budget as also shown by other studies (DG09 and Conzemius and Montgomery (2009)). Over the ocean, the increase in relative vorticity and hence potential vorticity was lowered markedly and much stronger than for the system over land. This process plays an important role in the cyclogenesis of Hurricane Helene. During the period analysed over the ocean the convective system was classified a tropical depression.

5

The Saharan Air Layer and Hurricane Helene (2006)

Large amounts of mineral dust are emitted and transported across West Africa and the Atlantic between 9 and 15 September 2006. During this period Hurricane Helene (2006) developed. The aim of this chapter is to investigate the transport of the mineral dust, the impact of the dust–radiation feedback for the African Easterly Wave (AEW) out of which Hurricane Helene (2006) developed, and the radiative effect of the dust on the convective systems and their environment. We use the model system COSMO-ART (Aerosols and Reactive Trace gases) in which the dust emission and dust transport as well as the radiation feedback are implemented.

5.1 Synoptic Situation and the pre-Helene system

On 9 September 2006, a low-level positive vorticity anomaly associated with the westward extension of the Saharan heat low occurred over West Africa at around 10–6°W, 16–19°N (chapter 4). It moved along about 18°N, crossed the West African coast line and then moved towards the southwest, where it merged with a positive vorticity maximum associated with the monsoon depression. When this positive vorticity anomaly was collocated with the vorticity maximum of the AEW, out of which Hurricane Helene (2006) developed, the development of the pre-Helene tropical depression was initiated (chapter 4).

The secondary heat low circulation over West Africa led to strong wind speeds near the surface and, thus, to the emission of significant amounts of mineral dust (Fig. 5.1 region A). Dust was emitted by the gust fronts of the convective systems over land, and due to orographical effects at the Algerian Mountains (Fig. 5.1 region C), the Atlas Mountains (Fig. 5.1 region D), and north and west of the Hoggar (Fig. 5.1 regions E and F). The mineral dust was transported over the Atlantic in the Saharan air layer (SAL). Relatively high values of aerosol optical thickness (AOT) (not shown) occurred north and northeast of the convective systems that developed into a tropical depression, and were present in the vicinity of the storm during the whole genesis period of Hurricane Helene.

The AOT has only moderate intensity compared to other dust events that occurred in March, June and July of 2006, during which the AOTs reached values in the order of 3 (e.g. Stanelle et al. (2010); Bou Karam et al. (2009a,b); Flamant et al. (2009)).

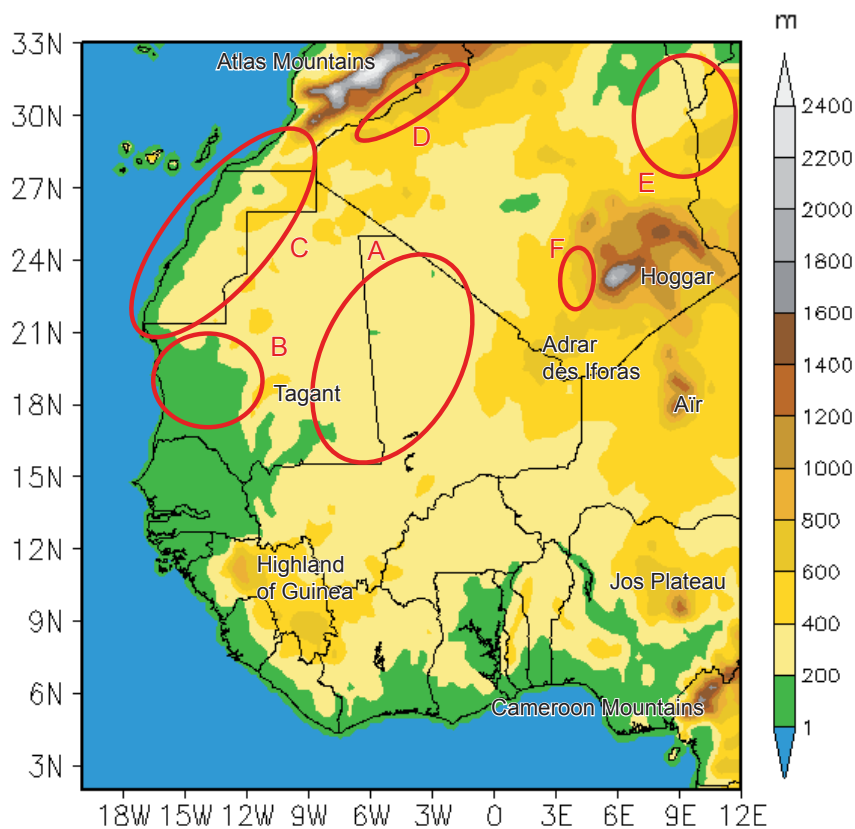


Figure 5.1: Political boundaries of the West African countries, the COSMO model orography (m above mean sea level) with a horizontal resolution of 28 km, and the main source regions of mineral dust (A to F) in the period between 9-14 September 2006.

5.1.1 Model Setup and Observations

The dust events between 9 and 14 September and the associated weather systems over West Africa were simulated using the model system COSMO-ART (chapter 3, section 3.3). The model system COSMO-ART has been developed recently and describes the emission, the transport, and the deposition of gases and aerosols and their feedback on the state of the atmosphere (Vogel et al., 2009). The interaction of the mineral dust particles with cloud microphysics is neglected.

Two model runs were conducted for the model region shown in Fig. 5.2. The first run computes the emission and transport of mineral dust aerosols, and the interaction between aerosols and radiation. Henceforth, this model run will be referred to as the RadDust run. The horizontal resolution is 28 km and the run was initialised on 9 September 2006 at 12 UTC. The convection is parametrised and the dust climatology is not applied, so that only the modelled dust concentrations impact the radiation fields. The emission constant (Eq. 3.7 in Vogel et al. (2006)) is set to 0.8. We use 6-hourly ECMWF operational analyses as initial and boundary data which contain no information about dust concentrations. For the second COSMO-ART run, the NoRadDust run, an identical model setup was used, except that the dust–radiation interaction was switched off. Thus the dust is only a tracer and no interactions involving the dust take place. Observational data was used to validate the RadDust run.

The horizontal distribution of dust is described using Meteosat Second Generation (MSG) Spinning Enhanced Visible and Infrared Imager (SEVIRI). Satellite images are produced from a combination of three infrared channels, namely channel 10 ($12.0\ \mu\text{m}$), channel 9 ($10.8\ \mu\text{m}$) and channel 7 ($8.7\ \mu\text{m}$). False-colour images (available on http://radagast.nerc-essc.ac.uk/SEVIRI_Dust.shtml) are created using an algorithm developed by EUMETSAT which colours the difference between the 12.0 and $10.8\ \mu\text{m}$ channels in red, the difference between the 10.8 and $8.7\ \mu\text{m}$ channels in green, and the $10.8\ \mu\text{m}$ channel in blue (Schepanski et al., 2007). On these composite images, the dust appears pink or magenta.

Daily AOT fields are obtained from the Moderate Resolution Imaging Spectroradiometer (MODIS)/Aqua Deep Blue Collection 051 over desertic surfaces (MOD08 product) and from MODIS/Terra over the ocean.

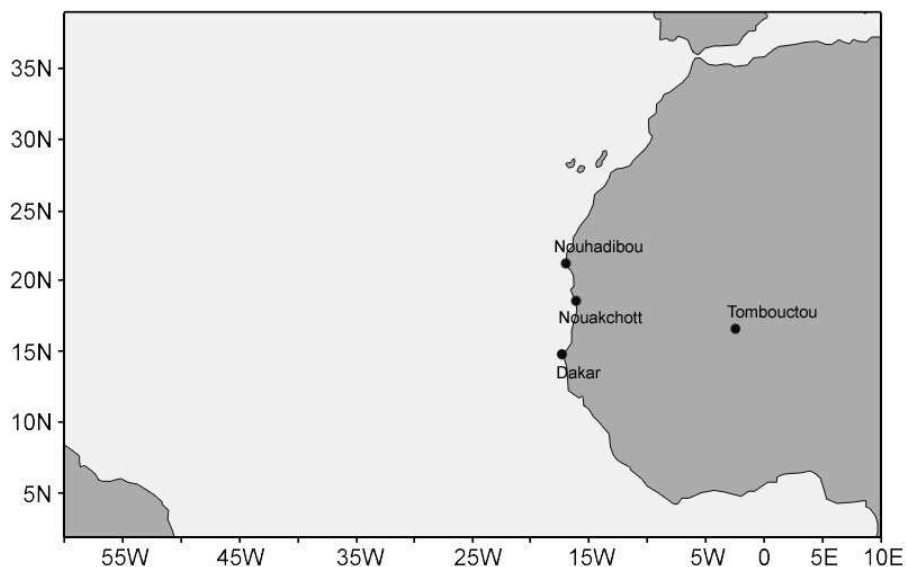


Figure 5.2: Model region for COSMO-ART runs. The model runs were initiated on 9 September 2006 at 12 UTC and have a horizontal resolution of 28.0 km. The model domain compasses 59.0°W-12.0°E and 1.0-39.0°N.

Information about the vertical distribution of dust over West Africa and the Atlantic is provided from the attenuated backscatter profile, or reflectivity profiles, at 532 nm retrieved from the space-born Cloud-Aerosol Lidar with Orthogonal Polarization (CALIOP) onboard the CALIPSO (Cloud-Aerosol Lidar and Infrared Pathfinder Satellite Observation; Winker and Hunt (2007)) satellite with vertical and horizontal resolutions of 60 m and 12 km, respectively. The lidar-derived atmospheric reflectivity at 532 nm is mostly sensitive to aerosols with radii ranging from 0.1 to 5 μm , i.e. dust aerosols (Flamant et al., 2007). The reflectivity is sensitive to aerosol optical properties and concentrations, and to relative humidity in the case of hygroscopic aerosols. The desert dust particles close to the dust source are found to be hydrophobic (Fan et al., 2004). The reflectivity due to desert dust is generally not expected to be sensitive to relative humidity fluctuations. Therefore, the reflectivity is a good approximation for the dust concentration.

The SAL imagery from the Cooperative Institute for Meteorological Satellite Studies (CIMSS) are created by differencing the 12.0 and 10.8 μm infrared channels on the Meteosat-8 satellite. It highlights the presence of dry and/or dusty air between about 600-850 hPa. Both dry air and mineral dust lead to a positive “SAL” signal in these images. Polar air intrusions into the subtropics produce a positive signal in these images that is similar to

that of the SAL. This is because both air masses contain substantial dry air in the lower to middle troposphere.

The total precipitable water (TPW) images are derived from a linear function of the 19, 22 and 37 GHz brightness temperatures available from passive microwave sensors aboard several polar orbiting satellite platforms. The sensors SSM/I (Special Sensor Microwave/Imager) on the DMSP-13/14 (Defence Meteorological Satellite Program) satellites and the AMSR-E (Advanced Microwave Scanning Radiometer–EOS) sensor on the Aqua satellite are used for the shown image. These images were provided by CIMSS also.

5.1.2 Dust Emission and Transport over West Africa

The emission of mineral dust results from a cyclonic vortex embedded in the ITD and a low-level convergence line between 10–0°W and 17–27°N on 9 September 2009 (Fig. 5.3b,c and Fig. 5.1). This dust event with AOTs of up to 1 is distinct in the SEVIRI images (Fig. 5.3a, the encircled region) and is represented nicely by COSMO-ART. The region of the largest dust concentrations moves westward together with the frontal structure that develops in a region characterised by a sharp temperature and humidity gradient and high values of positive relative vorticity between about 21–15°N and about 15–8°W. Strong Harmattan winds from the northeast reach down to about 18°N and turn towards the southwest at lower latitudes. Meanwhile, the moist monsoon flow reaches far north and turns to the northeast, west of the Greenwich meridian. Positive relative vorticity is produced in this convergence zone and dust is emitted due to the increased surface winds (Fig. 5.3f). This feature is restricted to the lower-levels and can not be observed at 700 hPa. However, this frontal zone moves toward the southwest and reaches the Atlantic after 20 forecast hours. The largest amount of mineral dust is emitted north–northwest of the convective system over land which was analysed in chapter 4. As the low-level convective system moves across the West African coast line, large amounts of dust are transported over the Atlantic (Fig. 5.3h,i).

A strong temperature gradient occurs near the surface from about 15°N and 20°N along the West African coast, between the coastal zone and the desertic inland, separating cold stably-stratified maritime air in the west from hot neutrally-stratified air over land.

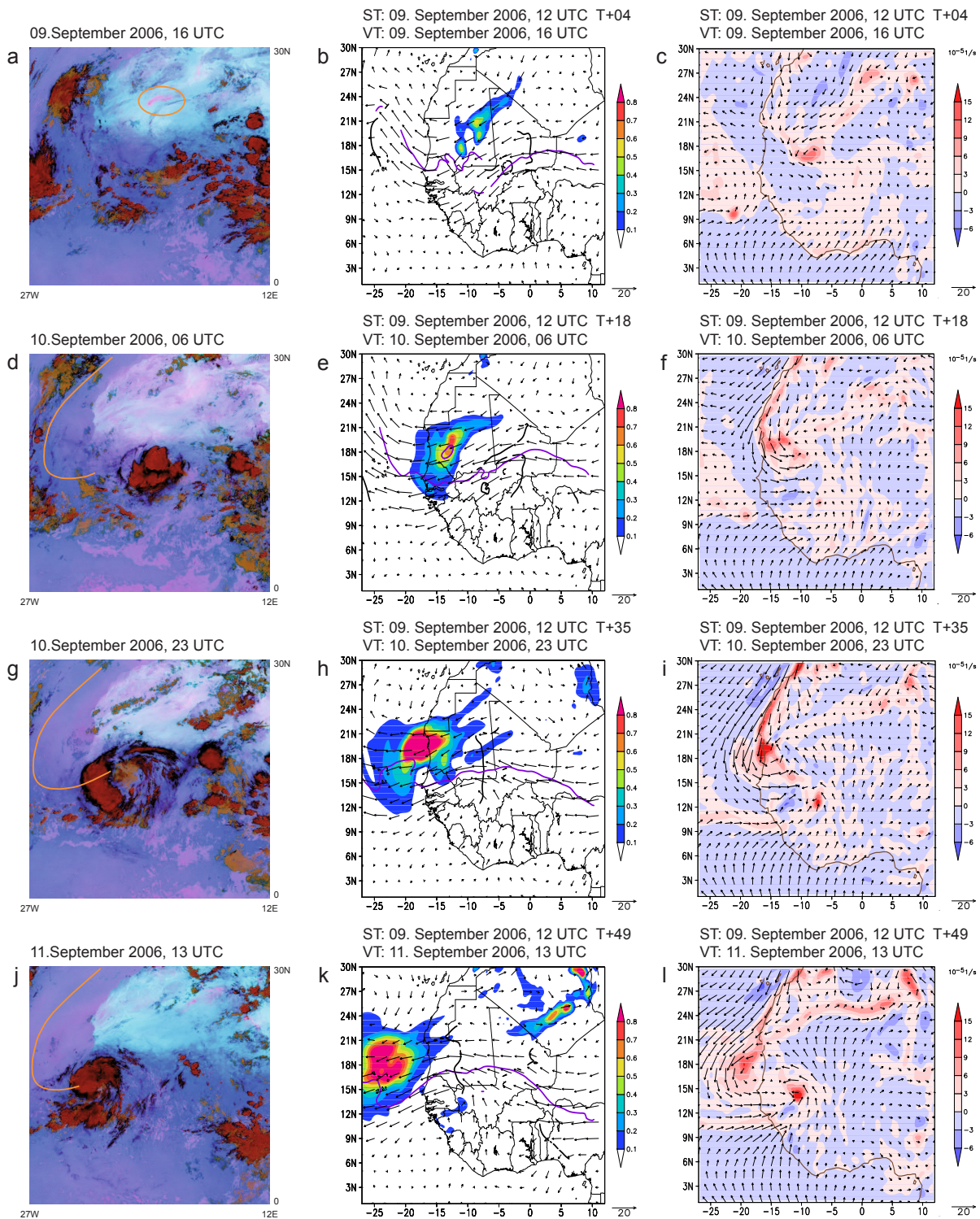


Figure 5.3: Left: SEVIRI dust images from the Meteosat second generation series of satellites. The pink colours indicate the presence of the mineral dust. The orange lines or circles highlight the regions with enhanced dust concentrations. Middle: Modelled aerosol optical thickness (AOT), horizontal wind (m s^{-1}) at 700 hPa as well as the AEW trough (black line) and the AEW (purple line) axes calculated using the method of Berry et al. (2007). Right: Vertical component of relative vorticity (10^{-5} s^{-1}) and horizontal wind speed (m s^{-1}) at 975 hPa. The model results are based on the COSMO-ART run initialised on 9 September 2006, 12 UTC, including the dust–radiation interaction (RadDust).

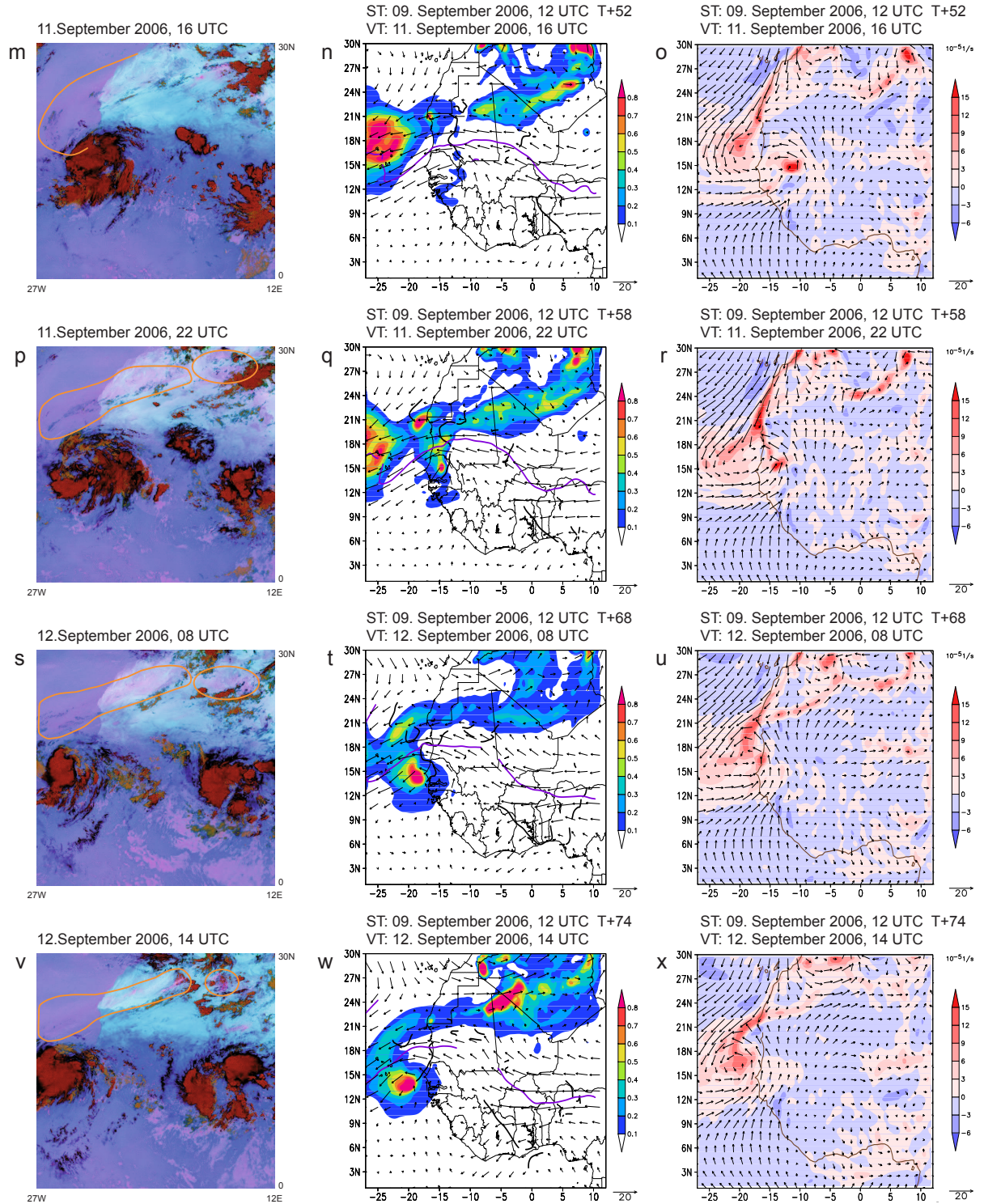


Figure 5.3: Continued.

This low-level front remains stationary during the day (Fig. 5.4a) and moves eastwards in the late afternoon and evening hours (Fig. 5.4b). The most favourable location for frontal propagation is between 17°N and 19°N. This inland propagating front is part of the Atlantic inflow (Grams, 2008; Grams et al., 2010). Along the baroclinic zone of the Atlantic inflow, mineral dust glides up along the isentropes. As the front moves inland, increased mineral dust concentration can be found in the same region. This could be observed almost every day. It was modified, however, by the low-level circulation moving westwards across the West African coastline in the late evening hours on 10 September 2006 (Fig. 5.3f,i), and by the monsoon flow that reaches far north on 11 and 12 September as the monsoon trough over the Atlantic moves westward (Fig. 5.3l,o,r,u). The position of the low-level circulation over the eastern Atlantic leads to a second maximum in the temperature gradient just off shore (Fig. 5.4b). The emission of mineral dust by the Atlantic inflow in this model run is mainly restricted to region B in Fig. 5.1.

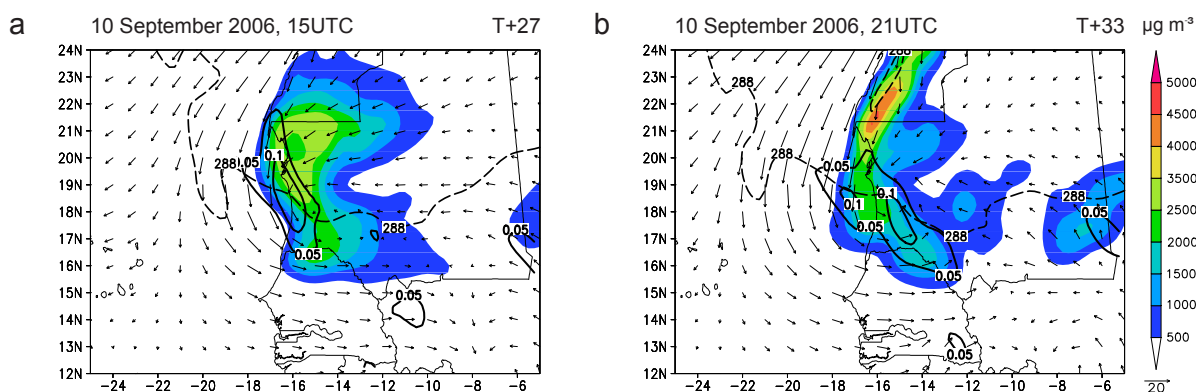


Figure 5.4: The aerosol mass concentration (shaded, $\mu\text{g m}^{-3}$), the temperature gradient (solid black line displaying the 0.05 and 0.1 K km^{-1} contour), the 288 K dewpoint temperature (dashed line) indicating the position of the ITD, and the horizontal wind speed (arrows, m s^{-1}) at 975 hPa on 10 September 2006 at 15 UTC (a), and at 21 UTC (b). Based on the model run initialised on 9 September 2006, 12 UTC including the dust-radiation interaction (RadDust).

Cross sections through the region of largest AOT on 10 September and 11 September (Fig. 5.5) show that the dust is lifted upwards in the region with the strongest potential temperature gradient due to the warm air of the Saharan heat low (SHL) to the northeast and the colder air of the maritime region in the southwest. On 10 September 2006 at 12 UTC, the mineral dust is mostly confined in the Saharan boundary layer (Fig. 5.5b). It appears that a slight inversion separates this layer from the Saharan residual layer. The deep plume of relatively low dust concentrations is likely due to the advection and

uplifting of dust from an earlier dust event further northwest (not shown). Between 12 and 18 UTC on 10 September 2006, the inversion is eroded and the dust is quickly transported up to 600 hPa (Fig. 5.5d). Isentropic upgliding (Bou Karam et al., 2008) in the baroclinic zone between the maritime and the Saharan air is indicated at 1300-1400 km. Mineral dust is also transported upwards by the strong turbulent mixing over the SHL during the day. This effect weakens during the evening hours. The isentropic upgliding occurs in this baroclinic zone which transports the mineral dust up to a height of about 500 hPa, where it descends slightly (Fig. 5.5f). At 700 hPa, significant amounts of dust are transported across the Atlantic. On 11 September 2006 at 06 UTC, two distinct maxima occur in the vertical distribution of the mineral dust mass concentration (Fig. 5.5h). One is located near the surface at the coastline of West Africa, which occurs at around 1500 km, and the other between 800 and 600 hPa towards the southwest. The low-level inversion has reformed so that the dust in the near surface layer is trapped in the boundary layer but the dynamically forced ascent at the baroclinic zone transports the dust above this layer. At midlevels the dust is transported westwards by the AEJ.

Large amounts of mineral dust are distinct offshore of the West African coast between about 15-24°N on 11 September 2006 at about 13 UTC (Fig. 5.3k,l). New dust sources occur in Algeria at about 7-10°E and 28-31°N, and 3-7°E and 23-26°N in the Hoggar region as seen clearly in the satellite image (Fig. 5.3j and region E in Fig. 5.1). During the following hours, the dust concentration just north of the Hoggar Mountains (5-10°E, 27-31°N) increases significantly (Fig. 5.3m,n). Another dust source can be seen in the lee of the Atlas mountains (9-4°W, 28-31°N and region D in Fig. 5.1). Meanwhile, large dust concentrations occur over the Atlantic between 14-21°N and west of 20°. The latter are transported by the AEJ across the Atlantic. A significant amount of dust is transported from the dust regions in the northeastern part of the model domain across West Africa. Mineral dust was also emitted in the Western Sahara during the whole period between 9 to 14 September 2006 due to the strong Harmattan (region C in Fig. 5.1).

In the afternoon hours on 11 September 2006 another significant dust event occurs in Mauritania (Fig. 5.6c) due to the enhanced monsoon flow that reaches far north. The mineral dust is lifted up at about 12°W and 16-18°N. A maximum in dust concentration can also be seen at 800 hPa (Fig. 5.6b) and 700 hPa (Fig. 5.6a). Another maximum in dust

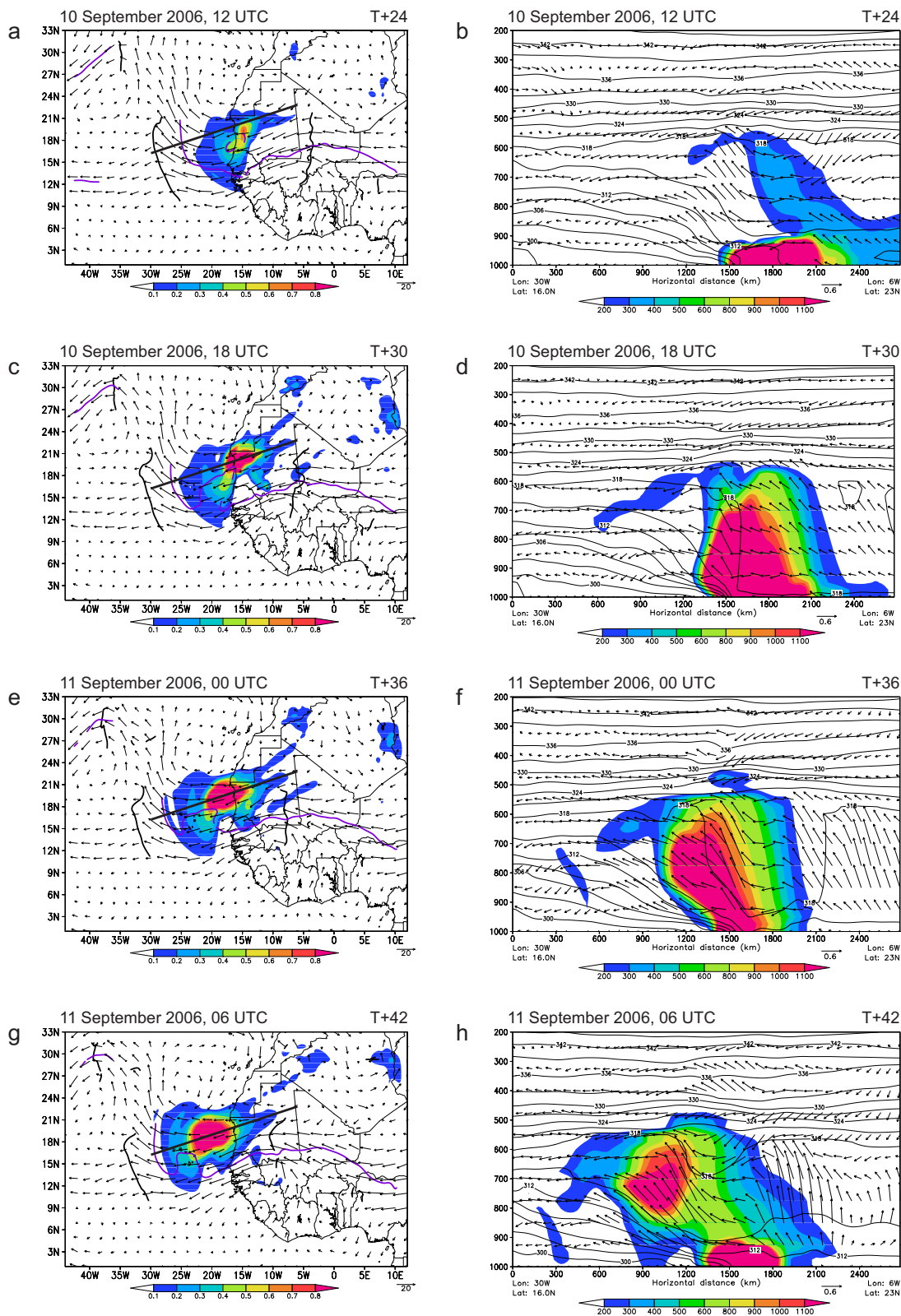


Figure 5.5: The horizontal wind speed (arrows, ms^{-1}) at 700 hPa, the aerosol optical thickness (shaded), the AEW trough (black curvy line) and AEJ (purple line) axes on 10 September 2006, 12 UTC (T+24) (a), 10 September 2006, 18 UTC (T+30) (c), 11 September 2006, 00 UTC (T+36) (e) and 11 September 2006, 06 UTC (T+42) (g) are shown. The black solid line displays the position of the cross section depicting the mineral dust mass concentration in $\mu\text{g m}^{-3}$ in b, d, f, and h at the same times as above. Pressure in the vertical component (b, d, f, h). Based on the model run initialised on 9 September 2006, 12 UTC including the dust–radiation interaction (RadDust).

concentration occurs along the West African coastline north of 22°N in association with a strong Harmattan (Fig. 5.6c). A band of dust enriched air is located north–northeast of the low–level circulation.

During the following hours, the mineral dust concentrations further increase due to new dust emissions. Moreover, the dust is advected westwards by the AEW at 700 hPa (Fig. 5.6d), and northwestwards at 800 (Fig. 5.6e) and 950 hPa (Fig. 5.6f) by the monsoon flow. Additionally, on 12 September at 00 UTC considerable ascent occurs between about 14–20°N along the West African coast. In this region dust is lifted up into the AEW trough, where mineral dust concentration in the order of 300–900 $\mu\text{g m}^{-3}$ can be found (Fig. 5.6d). The dust from the northern dust event is advected towards the south and the dust is lifted up along a northeast–southwest orientated band which collocates with the position of the ITD.

On 12 September 2006 at 04 UTC, the mineral dust from the southern region of high dust concentration at 950 hPa reaches roughly 21°N (Fig. 5.6i). This region is characterised by the convergence between the Harmattan and the monsoon flow. The mineral dust advected by the Harmattan flow and the dust transported by the monsoon flow is partly lifted up in here. The other part rotates cyclonically around the low–level circulation. At 800 hPa, the mineral dust concentration shows a distinct maximum offshore between 16 and 18°N (Fig. 5.6h). At 700 hPa, instead, maximum dust concentrations can not be seen in this region but south of it (Fig. 5.6g).

These individual dust events and the two basic paths of the mineral dust advection lead to an AOT distribution shown in Fig. 5.3q,t,w. On 11 September 2006 at around 22 UTC (Fig. 5.3q), a maximum in AOT is located northeast of Dakar (15–9°W, 16–20°N; region A in Fig. 5.1), which occurs just ahead of the AEW trough axis and south of the AEJ and is transported westwards (Fig. 5.3w). All the previous dust events occurred north of the AEJ at the time of their emission and during the transport across West Africa. The dust from this event, however, is transported along about 15°N over the Atlantic within the AEW out of which Hurricane Helene developed.

Significant amounts of mineral dust are transported into the “ocean box”, used in chapter 4 to analyse the convection in the developing tropical depression. This southern dust

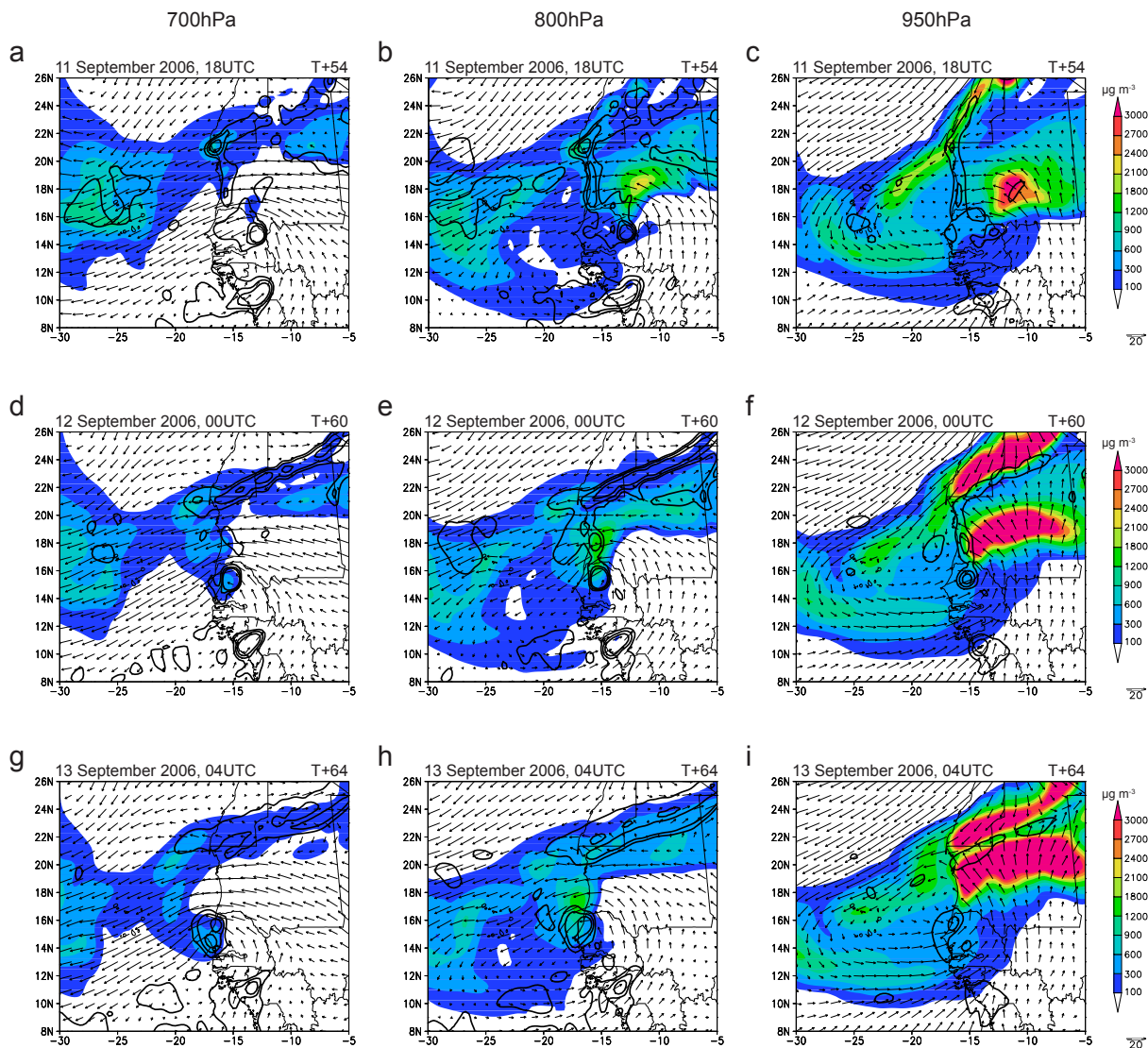


Figure 5.6: Horizontal wind speed (arrows, m s^{-1}), mineral dust mass concentration (shaded, $\mu\text{g m}^{-3}$), and vertical velocity (-1.2 Pa s^{-1} , -0.6 Pa s^{-1} , -0.2 Pa s^{-1} contours, i.e. regions of ascent) at 700 hPa (left), 800 hPa (middle), and 950 hPa (right) on 11 September 2006, 18 UTC and 12 September at 00 UTC and 04 UTC. Based on the model run initialised on 9 September 2006, 12 UTC including the dust–radiation interaction (RadDust).

event can not be seen in the satellite images but could have been masked by the large cirrus shield of the convective system over the Atlantic on 12 September 2006 at about 14 UTC (Fig. 5.3v).

The convective systems over the Atlantic are embedded within a mesoscale mid- and low-level circulation. The low-level circulation was found to be warmer than its environment (chapter 4). The strong Harmattan deflected the mineral dust transport towards the southwest. The strong northwesterly monsoon flow, enhanced the low-level circulation

and the dust spirals around the low-level circulation centre until the low-level and the mid-level circulation centres are collocated (in the late evening hours on 12 September; not shown). From this time on, relatively high AOTs can be found within the centre of the developing tropical depression. During the tropical cyclogenesis, bands of dry and dusty air spiral towards the storm centre.

5.1.3 Comparison with Observational Data

The aerosol optical thickness from MODIS deep blue is shown in Fig. 5.7. Unfortunately, hardly any information is given in the satellite images south of about 15°N . However, enhanced AOTs are distinct between 15 and 21°N and west of 15°W with a local maximum at about 18°N , 17°W on 10 September 2006 (Fig. 5.7a,b) in accordance with the AOT in the model results. The high AOTs in the northeast and east of the model domain are not represented in the COSMO-ART run. This is due to the fact that the dust concentration is zero in the initial and boundary fields. Thus no dust is advected into the model domain. Hence, the dust concentration over the whole model domain is probably slightly low during the entire simulation as it is not possible to include all source regions into the model domain due to computational restriction. On 11 September 2006, high AOTs occur again between 15 - 21°N , in the lee of the Atlas Mountains and north of the Hoggar Mountains in the model run. In the same regions high AOTs are observed in the MODIS image. An elongated band of relatively higher AOTs between the maximum in dust load over the Atlantic and the maximum north of the Hoggar can be seen in the Modis image as well as in the modelled AOT distribution (Fig. 5.7c,d). Maximum AOT at Cap Blanc (17°W , 21°N) is distinct in the modelled and observed AOT. The AOT maximum at the border of Morocco and Algeria is much stronger in the satellite images than in the simulation and the AOT north of the Hoggar Mountains are much weaker than in the simulation on 12 September 2006 (Fig. 5.7e,f). The maxima of the dust concentration appear to occur in the right places in the COSMO-ART simulation, but the overall dust concentrations seems to be too low in the northeastern and eastern part of the model domain.

The Saharan air layer between 12 September 2006, 12 UTC and 14 September 2006, 12 UTC (Fig. 5.8) is very marked to the north and north west of the developing tropical

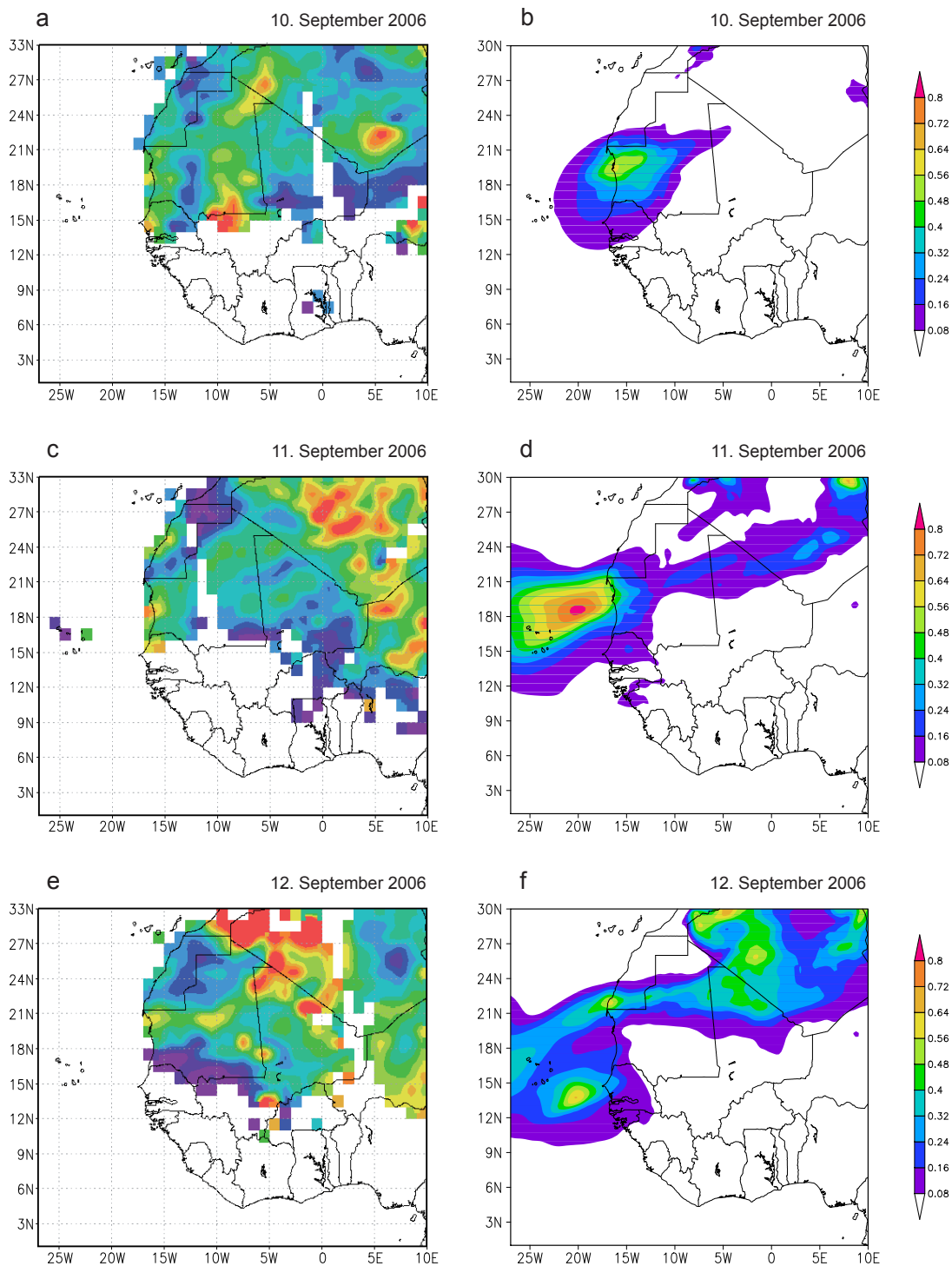


Figure 5.7: Left side: Aerosol optical thickness (AOT) from MODIS on Aqua. These visualisations were produced with the Giovanni online data system, developed and maintained by the NASA Goddard Earth Sciences Data and Information Services Center (GES DISC). Right side: AOT based on the COSMO-ART simulation initialised on 9 September 2006, 12 UTC, including the dust–radiation interaction (RadDust). The AOT was averaged at each grid point over a time period of 24 hours starting at 00 UTC on each day.

depression. The potential temperature anomalies at 700 hPa (not shown) are largest north of the convective system and north of the AEW as well as in the ridge ahead of the AEW in which the pre-Helene system develops. This relatively warm air is also characterised by low values of specific humidity and high AOTs. The highest dust concentrations occur just north of the mid-level circulation centre on 12 September 2006 (Fig. 5.8b). Note, the band with relatively high specific humidity along about 20.5°N and between 18-10°W occurs in the convergence zone between the Harmattan and the monsoon flow. The ITD (Fig. 5.9d) is the border between the hot and dry air in the north and the relatively cold and moist air in the south. This region is also characterised by a positive relative vorticity (see also the elongated bands of positive relative vorticity in Fig. 5.3) and ascent. This leads to increased humidity at 700 hPa and the uplifting of mineral dust.

The satellite SAL imagery shows only the dry and dust enriched air surrounding the convective system in the north-northwest. We cannot assess whether the regions of dusty air were in fact present but could not be detected in cloudy regions. The convective system develops and was organised enough to be classified a tropical depression on 12 September at 12 UTC. During the following 12 hours, the system strengthens further and the region of high AOTs elongates. The dry and warm air ahead of the tropical depression extends down to 10°N as does the SAL shown in the satellite imagery (Fig. 5.8c,d). High dust concentrations are transported across the West African coast north of Cap Blanc as seen in high AOTs in that region and in the dark red region in the corresponding SAL image. As the system develops, dry and wet deposition takes place, which is why the AOTs decrease. The simulated AOT above the storm centre is still higher than in its environment. Bands of relatively dry and dusty air spiral towards the storm's centre in the south and east of the tropical depression on 14 September 2006. In the following hours the system was upgraded a tropical storm and named Helene. During the tropical cyclogenesis, dry air was always present to the west and north of the tropical depression. This is in accordance with the SAL satellite images.

The horizontal AOT distribution appears to be realistic when comparing it to the MODIS AOT in the Terra satellite imagery (Fig. 5.9). High AOTs occur just off shore the West African coastline roughly between Dakar and Cap Blanc on 10 September 2006. The position of the SAL event on 12 September ahead of the AEW out of which Hurricane

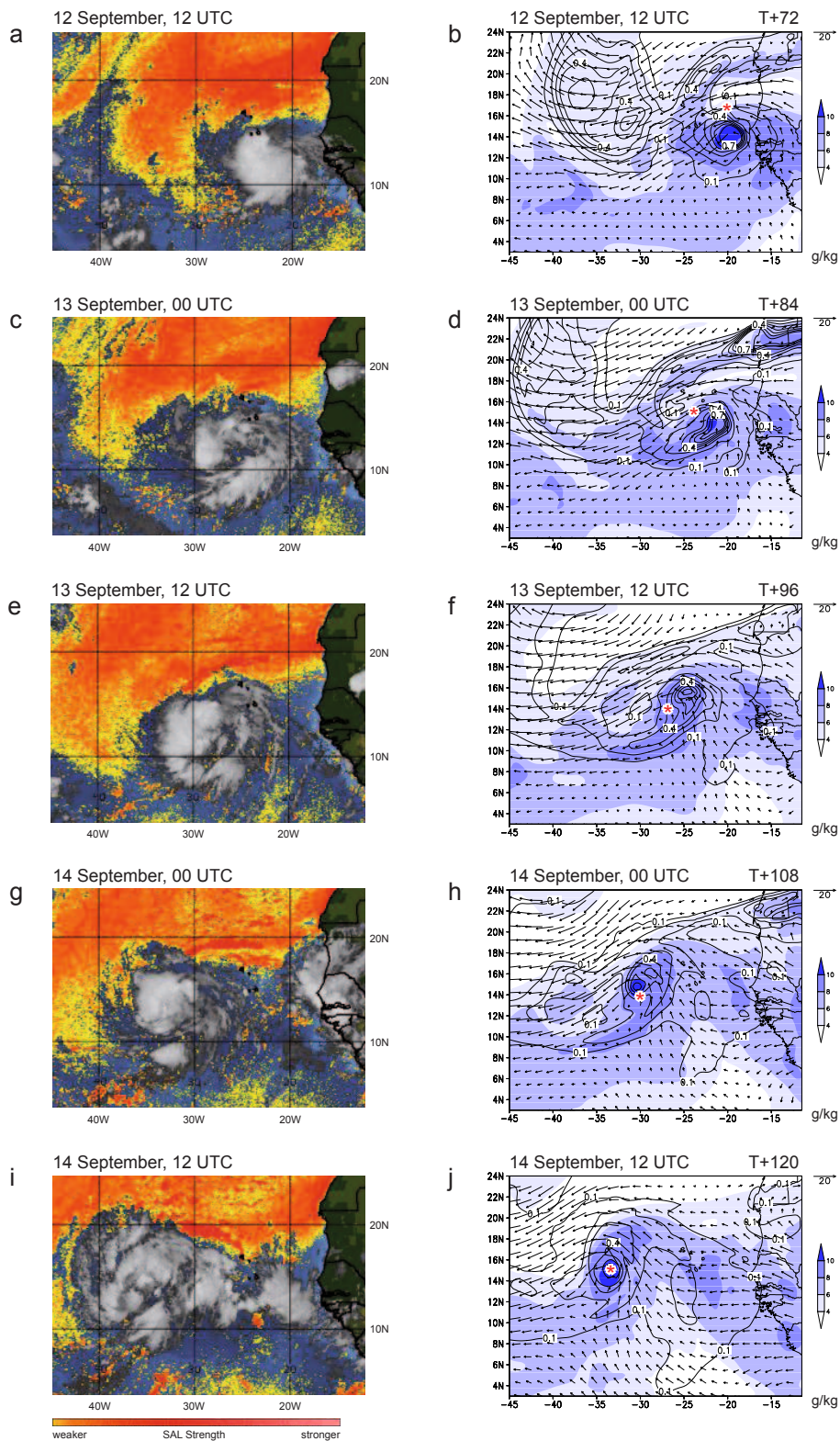


Figure 5.8: Left column: The Saharan air layer (SAL) based on the difference between the 12.0 and $10.8 \mu\text{m}$ infrared channels on the Meteosat-8 satellite. The yellow to dark red colours illustrate weak to very dry and dusty air between about 600–850 hPa. Image courtesy to Jason Dunion (HRD/CIMSS). Right column: Specific humidity (g kg^{-1} , shaded), aerosol optical thickness (contours), and horizontal wind speed (m s^{-1} , arrows) at 700 hPa based on the COSMO-ART run initialised on 9 September 2006, 12 UTC, including the dust–radiation interaction (RadDust). The red star marks the position of the centre of the low-level circulation.

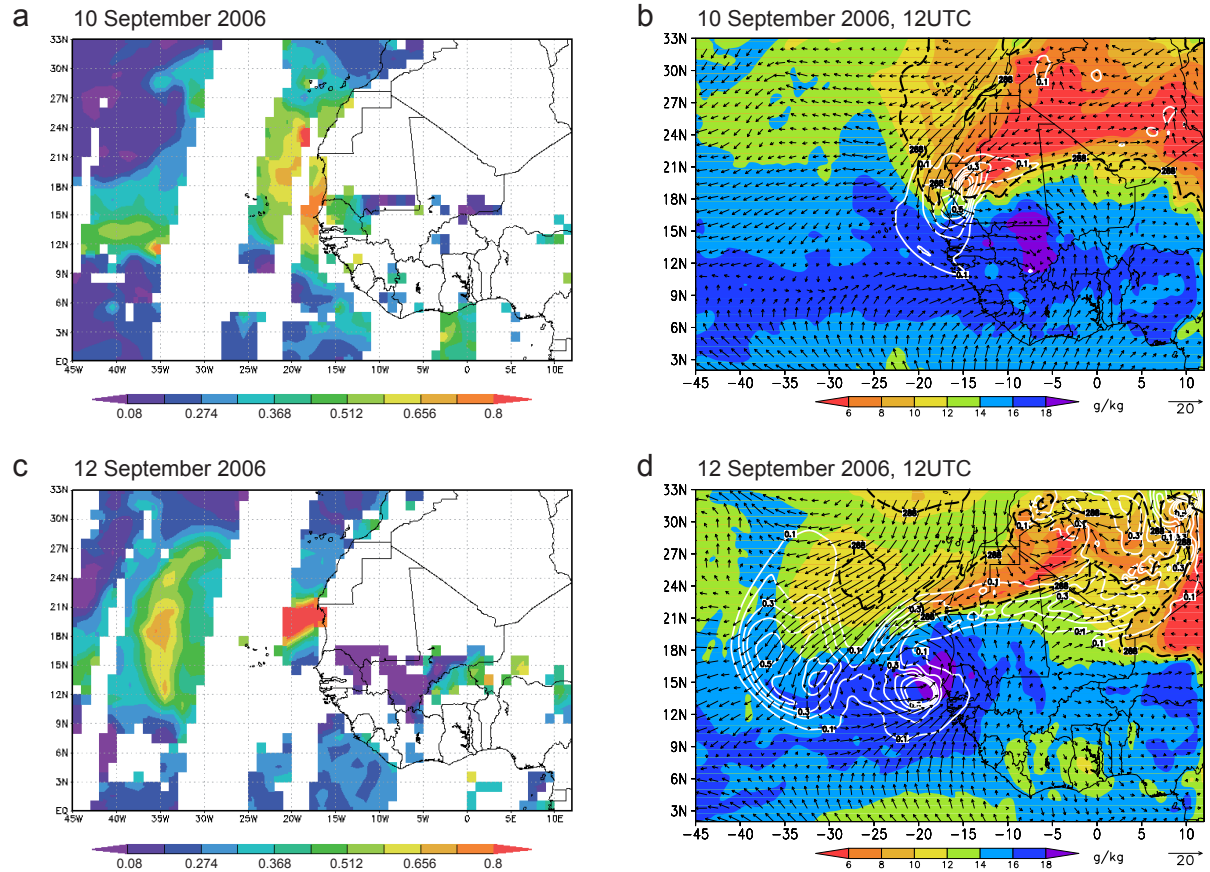


Figure 5.9: Aerosol optical thickness (AOT) from MODIS on Terra on 10 September (a), and 12 September 2006 (c). These visualisations were produced with the Giovanni online data system, developed and maintained by the NASA Goddard Earth Sciences Data and Information Services Center (GES DISC). The specific humidity (g kg^{-1} , shaded), the AOT (white contours with an interval of 0.1), and the 288-K isentrope (black dashed line) on 10 September (b), and 12 September 2006 (d) at 12 UTC, based on the model run RadDust which was initialised on 9 September 2006, 12 UTC.

Helene developed is depicted by the model. The satellite images also show that the highest AOTs occur west and southwest of Cap Blanc which is in accordance with the RadDust model run.

The orange–red colour coded SAL region in the satellite images in Fig. 5.8 highlights regions that are either dry, dust enriched, or both. The AOT distribution in the COSMO-ART RadDust run shows that there is a region of dry air that does not contain mineral dust between both SAL regions over the Atlantic (Fig. 5.8d,f). Forward and backward trajectories showed that this dry air is a result of subsidence. Backward trajectories were calculated for the region displayed in Fig. 5.10c and between 2000 and 3500 m height, i.e. a layer around 700 hPa. This region is characterised by relatively dry air and hardly

any mineral dust. A region of mineral dust concentrations in the order of $100 \mu\text{g m}^{-3}$ can be found westward of the selected region. North of the selected region an anticyclone occurs between about $24\text{--}30^\circ\text{N}$. On 11 September 2006 at 06 UTC, 57 hours prior, the anticyclone is located at about $27\text{--}22^\circ\text{W}$ and $23\text{--}28^\circ\text{N}$. On 9 September 2006 at 23 UTC, the anticyclone can be found at 500 hPa between about $18\text{--}9^\circ\text{W}$ and $23\text{--}32^\circ\text{N}$. Air parcels that originated from the southern region encircled in Fig. 5.10a move towards northwest, and air parcels from the northern encircled region move anticyclonically around the high pressure system. As the anticyclone is displaced westwards, the parcels originating from the southern region in Fig. 5.10a turn towards the southeast in the region illustrated in Fig. 5.10b which is located in the north of the anticyclone. That means that these air parcels also rotate anticyclonically around the high pressure systems while it moves westwards.

On 13 September 2006 at 15 UTC, all air parcels within the selected box (Fig. 5.10c) that show a relative humidity smaller than 30% were traced backwards (Fig. 5.11). The trajectory calculation shows that the air parcels from both regions illustrated in Fig. 5.10a rotate anticyclonically around the high-pressure system and meanwhile, descent (Fig. 5.11a). As this relatively moist air descends it becomes dryer (Fig. 5.11b). On 13 September 2006 at 15 UTC, the air associated with the anticyclone at 500 hPa is very dry (Fig. 5.10a). This non-dust related dry air enhances the moisture gradient in the northwest of the developing tropical depression.

We extend our analysis of the SAL by investigating the moisture distribution in more detail. We compared the vertical integral of cloud water, cloud ice and water vapour, henceforth total water, with the total precipitable water (TPW) from satellite data (Fig. 5.12). The distribution of the dry air in the TPW satellite images is remarkably similar to the total water images based on the COSMO-ART run. On 12 September 2006 at 12 UTC the region with total precipitable water smaller than 35 mm north of Cap Blanc extent to about 18°N and 30°W in the both the satellite image and the model run (Fig. 5.12a,b). The largest values in total water content can be found between about $12\text{--}18^\circ\text{N}$, $21\text{--}17^\circ\text{W}$ in both images, but a region with even higher values in total water occurs southwest of it in the satellite image. During the next 12 hours, the band of dry air extends southwestwards, increasing the temperature gradient northwest of the tropical depression (Fig. 5.12c,d).

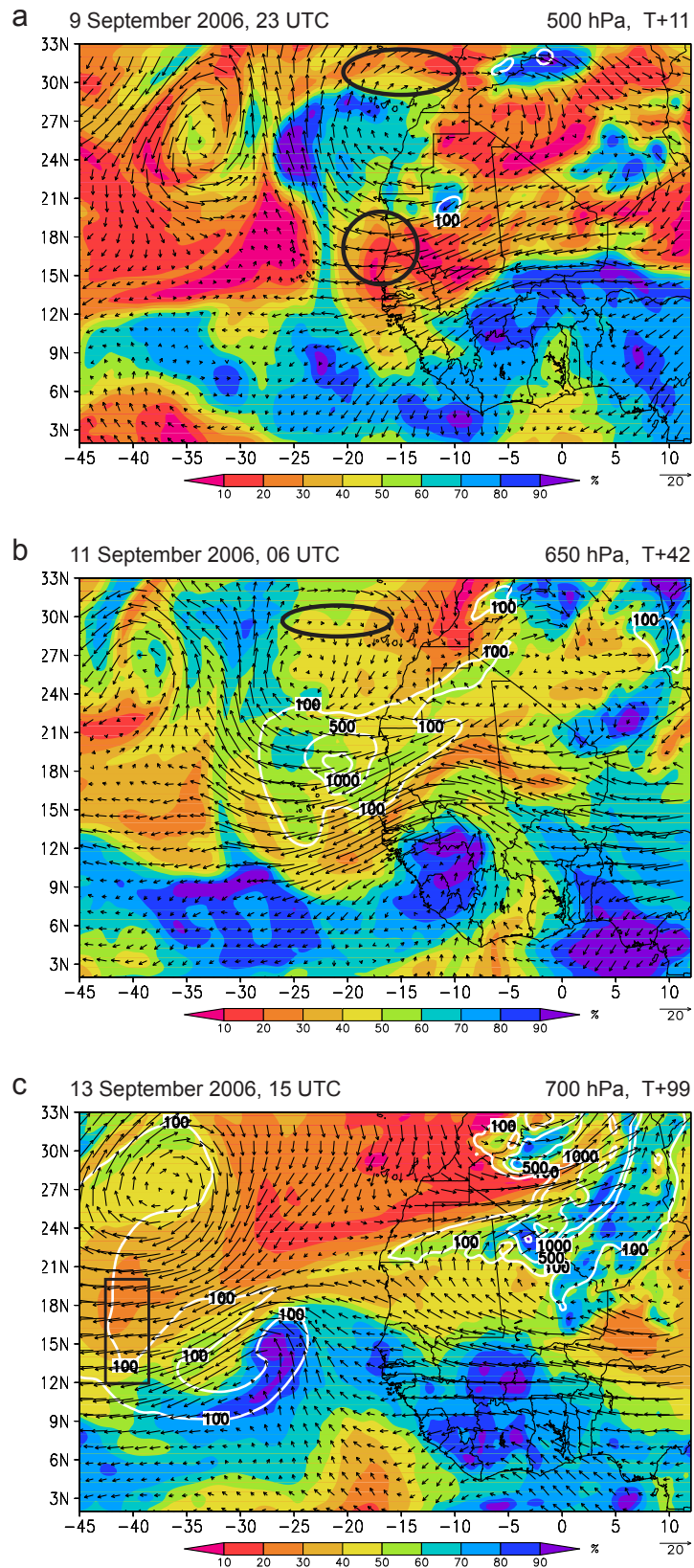


Figure 5.10: The relative humidity (%) at (a) 500 hPa 9 September 2006 at 23 UTC (T+11), (b) 650 hPa on 11 September 2006 at 06 UTC (T+42), and (c) 700 hPa on 13 September 2006 at 15 UTC (T+99). The mineral dust mass concentration ($\mu\text{g m}^{-3}$) is shown in white contours. The black box in (c) indicates the position from where trajectories (Fig. 5.11) were calculated, the encircled regions in (a) give the regions where the trajectories ended, and in (b) the turning point of the trajectories is highlighted. The figure is based on the RadDust model run which was initiated on 9 September 2006 at 12 UTC.

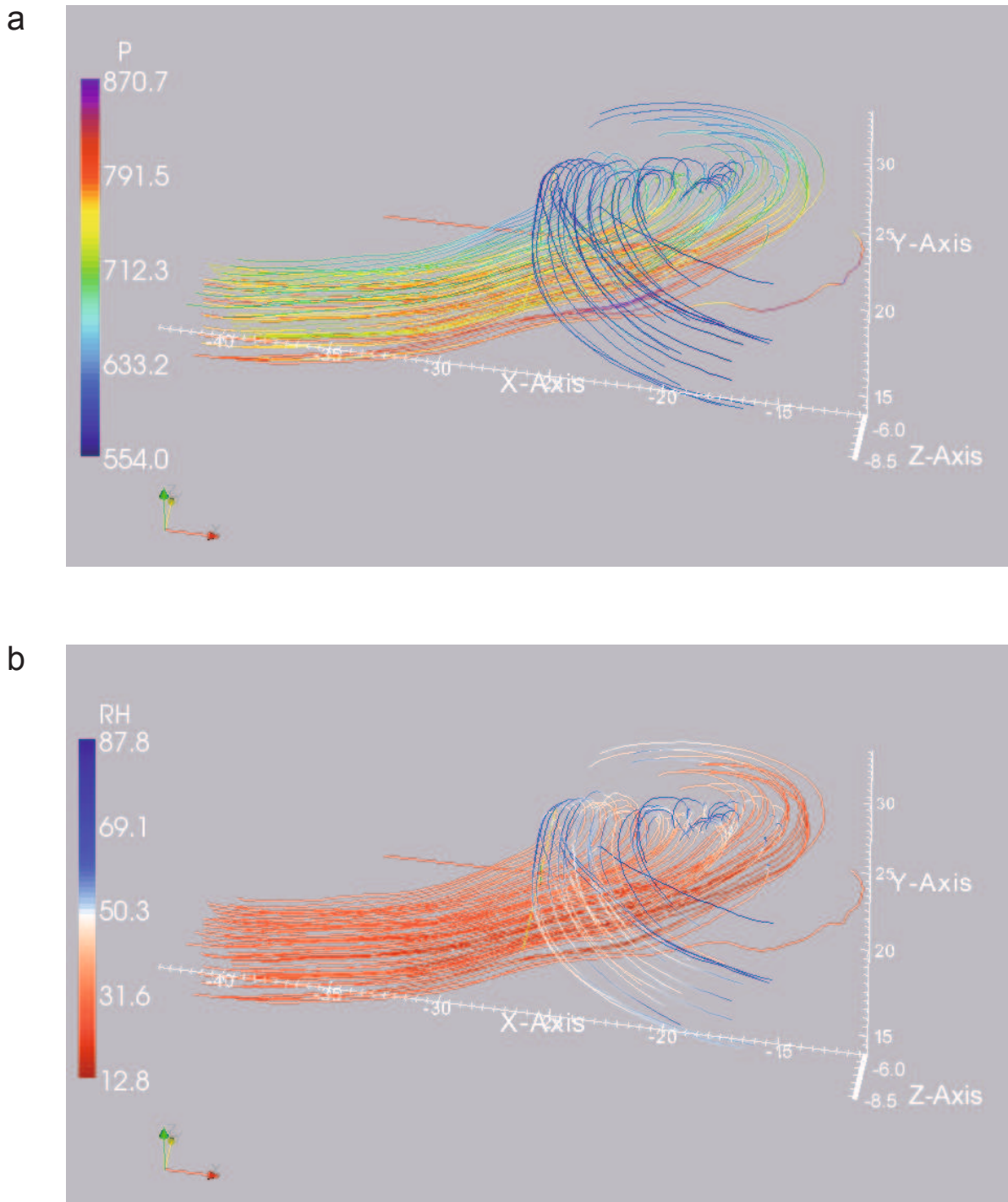


Figure 5.11: Backward trajectories starting on 13 September 2006 at 15 UTC and ending on 09 September 2006, 23 UTC. The horizontal box in which the trajectories originate ranges from 43-39°W, 14-20°N and has extends vertically between 2000-3500 m height, i.e. it is a layer around 700 hPa. Only those trajectories are traced back that have a relative humidity lower than 30%. (a) The pressure (hPa) along the trajectories is displayed in colour, and (b) the relative humidity. The pressure ($\times 100$ hPa) is the vertical coordinate. The trajectories are calculated for the RadDust model run which was initiated on 9 September 2006 at 12 UTC.

Particularly dry air is present on 13 September 2006 at 12 UTC between Cap Blanc and about 30°W north of 22°N in the model data and north of 19°N in the satellite image (Fig. 5.12e,f). A second region of very dry air can be found between 42–37°W and 15–22°N. As the storm further intensifies, a band of high total water values in the southwest and northeast of the storm’s centre can be observed in the satellite and model data (Fig. 5.12g,h). The convective system associated with the high total water has about the same position in both the simulation and the satellite images. Even after a forecast time of 120 hours (Fig. 5.12i,j), the position of the storm, the region of very dry air north of the tropical storm, and the band of moist air are in accordance in both images.

A comparison of the COSMO-ART RadDust run with CALIPSO transects (Fig. 5.12) shows that the vertical extent of the dust layer (Fig. 5.12b,c) appears realistic. The main dust concentration occurs between 700 and 850 hPa in the CALIPSO image, whereas in the model cross section the maximum dust concentration is located near the surface. The northern maximum in dust concentration can be related to the dust source region in the lee of the Atlas Mountains and the southern dust region to the ITD. The modelled maximum dust concentration over land on 11 September at 14 UTC (Fig. 5.12e), owing to the convergence between the Harmattan and the monsoon flow along the ITD, is seen in the satellite image (Fig. 5.12f). Dust is present even above 600 hPa, albeit with low concentrations. The model is able to simulate the high dust concentrations that occur 24 hours later over land (Fig. 5.12g,h) due to strong northerly flow south of the Atlas Mountains and at the ITD, and even the region of much lower concentration between 9 and 8°E. The uplifted dust that reaches altitudes of about 500 hPa is simulated also.

On 11 September 2006 at 15 UTC, the highest dust concentrations over the Atlantic occur at 600 hPa and in the levels below. The uplifted dust region is distinct in the model results as well as in the CALIPSO image (Fig. 5.12k,l). The high concentrations near the surface towards the southern end of the cross section are surprising, as the cross section is located entirely over water. This might be due to the dry and wet deposition of the mineral dust aerosols as this end is closer to the continent, i.e. the source region. The maximum dust concentrations between the near-surface and about 800 hPa are located in the northern part of the low-level circulation which can be related to the SHL. The dust is advected from the source region and spirals towards the circulation centre. High dust

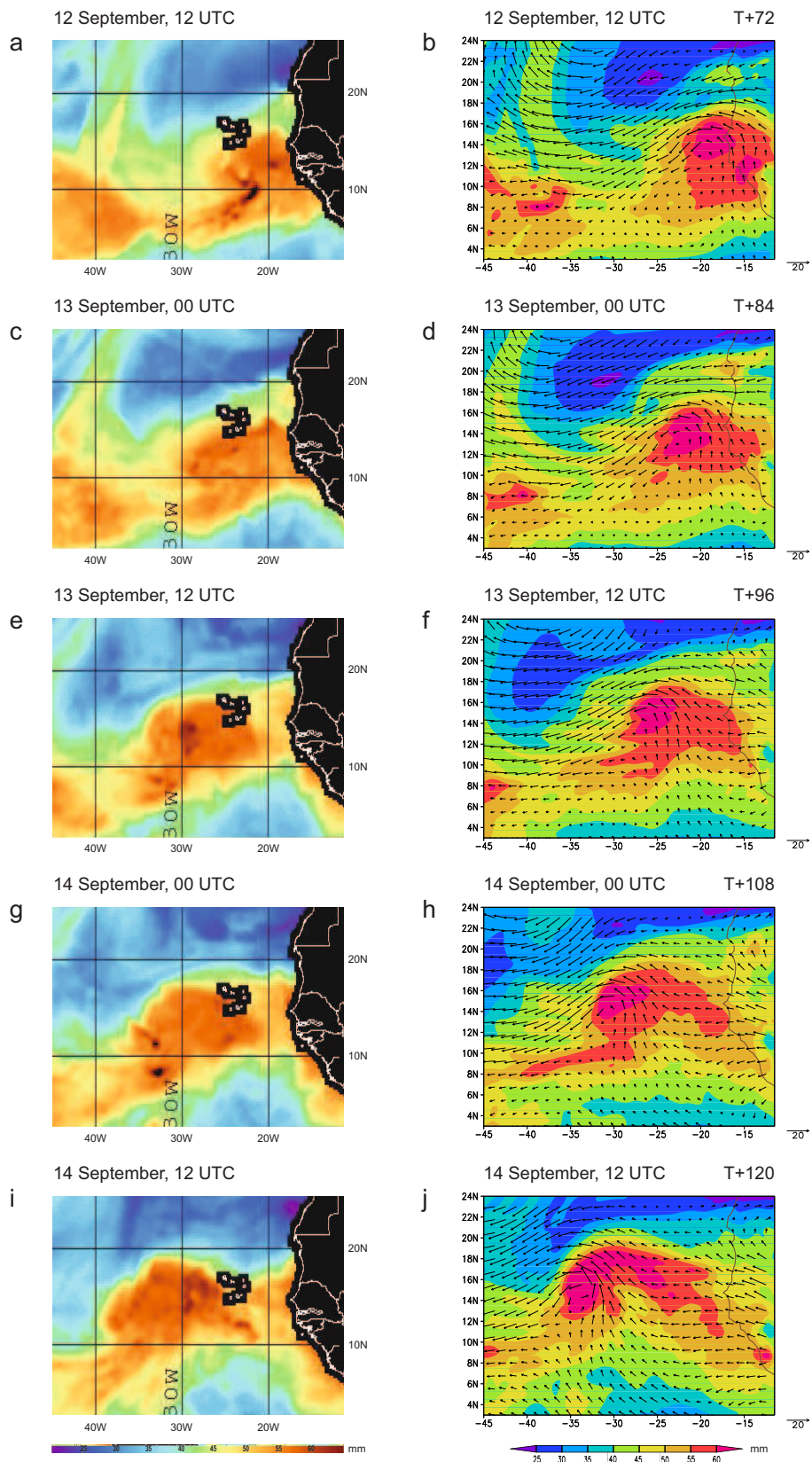
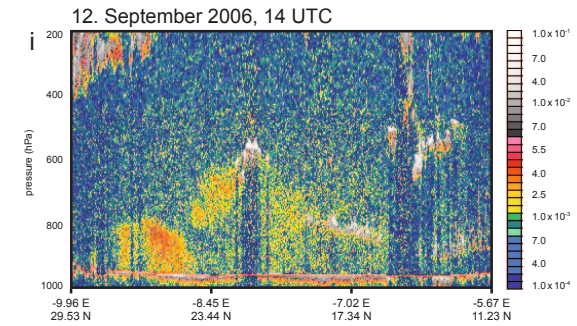
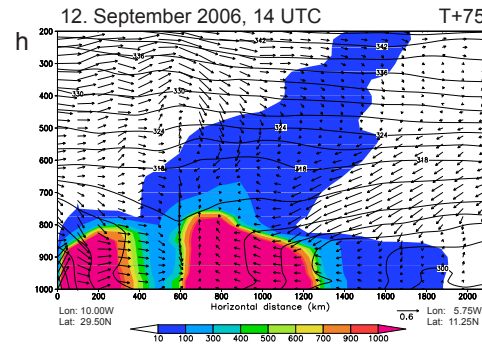
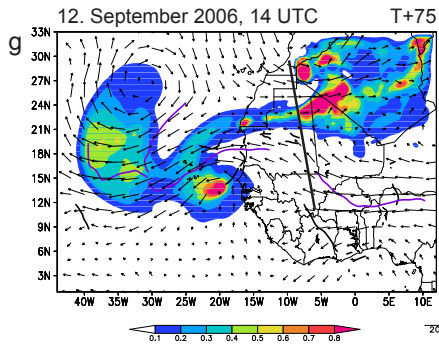
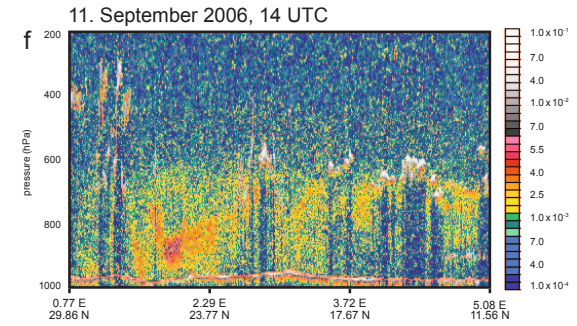
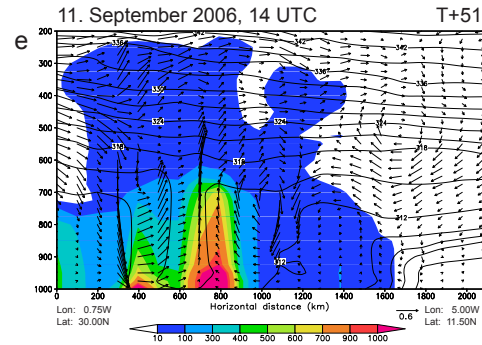
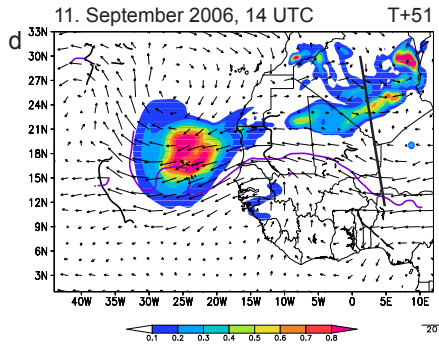
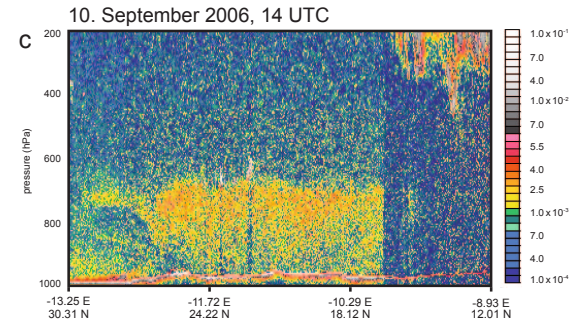
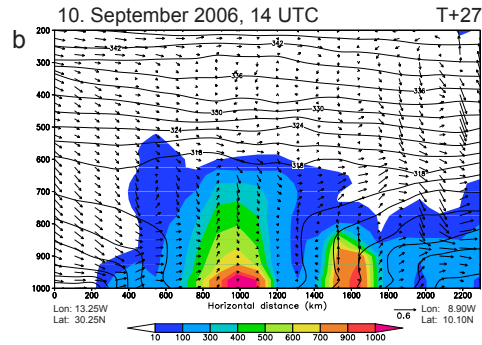
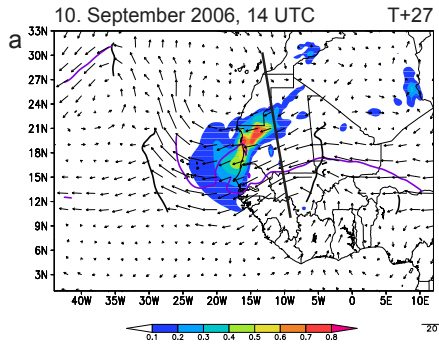


Figure 5.12: Left column: Total precipitable water (TPW) in mm based on the sensors SSM/I on the DMSP-13/14 satellites and the AMSR-E sensor on the Aqua satellite are used for the shown image. The black squares over the Cape Verde Islands occur because TPW is not estimated over ground. Image courtesy to Jason Dunion (HRD/CIMSS). Right column: The vertical integral of cloud water, cloud ice and humidity (mm), and the horizontal wind speed (m s^{-1}) at 700 hPa based on the COSMO-ART run initialised on 9 September 2006, 12 UTC, including the dust-radiation interaction (RadDust).

concentrations between 700 and 800 hPa can be seen in both the CALIPSO transect and the modelled cross section on 12 September at 03 UTC (Fig. 5.12n,o). Also the high low-level concentrations in the northeastern part of the cross section are apparent. They occur in the region around Cap Blanc, where dust concentrations in the order of $3000 \mu\text{g m}^{-3}$ are transported over the Atlantic. Due to deep clouds at the southwestern end of the cross section, the low-level dust concentration can not be seen in the CALIPSO image. A cross section was also taken through the region of weaker AOT ahead of the AEW out of which Hurricane Helene developed (Fig. 5.12q,r). High dust concentrations occurred between 600 and 700 hPa in both cross sections. The high dust concentrations in the southeastern part of the cross section can not be validated with CALIPSO data due to the presence of clouds. There is an indication of the observed uplifted dust concentration to the northwest in COSMO-ART. In general, these comparisons show a reasonable agreement between model results and observations.

Lidar measurements of the aerosol concentration (Fig. 5.13a) onboard the NAMMA DC-8 on 12 September 2006 (Jenkins et al., 2008) along the flight path shown in Fig. 5.13f and g, display the same vertical extent of the dust layer as in the RadDust run (Fig. 5.13b). These measurements also show relatively high mineral dust concentrations near the surface at the northern end of the cross section. Additionally, this dust laden layer is characterised by relatively low specific humidity values in both the measurements and the model results (Fig. 5.13c,d). This indicates that the relatively high dust concentrations in the COSMO-ART simulations at lower levels (Fig. 5.13f) are not unrealistic.

The model representation of moisture and wind fields is validated using radiosoundings from the AMMA database. The locations of the soundings are indicated in Fig. 5.2. The soundings in Dakar (17.49°W , 14.75°N), Senegal, and Tombouctou (4.1°W , 21.85°N), Mali, (Fig. 5.14) illustrate the conditions before the dust events and before the convective systems discussed in chapter 4. The AEJ is located at about 650 hPa in both stations (Fig. 5.14c,d). Tombouctou is located north of the jet and Dakar is located underneath the jet axis in the ridge of the proceeding AEW. The meridional wind is markedly smaller than the zonal wind, although a maximum occurs over Dakar at 650 hPa (Fig. 5.14e) and of the opposite sign in the mid-troposphere over Tombouctou. The moisture profiles of both stations (Fig. 5.14a,b) differ significantly. The near surface air layer is very moist over



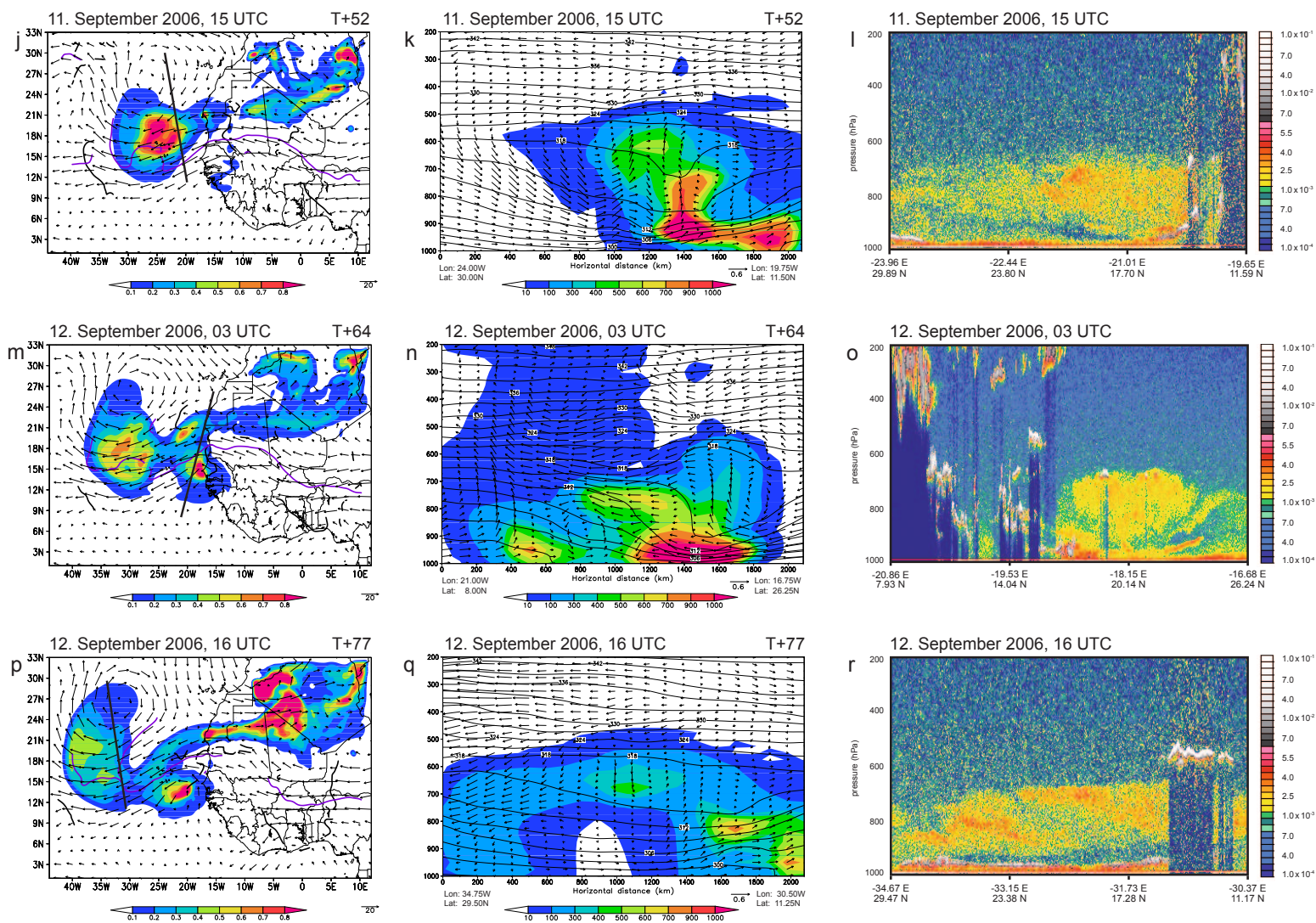


Figure 5.12: Left column: AOT (shaded) and the horizontal wind speed (ms^{-1}) from the COSMO run initialised on 9 September 2006, 12 UTC. The black and purple curly lines denote the AEJ trough and jet axes computed after the method from Berry and Thorncroft (2005), respectively. The straight black lines shows the position of the cross section. Mid-column: The mass concentration (shaded), potential temperature (3-K contour interval), and wind speed (arrows in ms^{-1}) along the cross section shown in the left column. Right column: Vertical damped backscatter coefficient at 532 nm ($\text{km}^{-1} \text{sr}^{-1}$) from CALIPSO. Signal strength is colour coded with blue making weak molecular scatter and very weak scattering on aerosols. Aerosols are shown in yellow, orange and red. Strong cloud signals are given in grey, and weak cloud signals in red and yellow. The validation time is given at the top of every figure and the forecast time is shown in the top right corner for the figures in the left and mid column. The pressure is the vertical coordinate for the cross section.

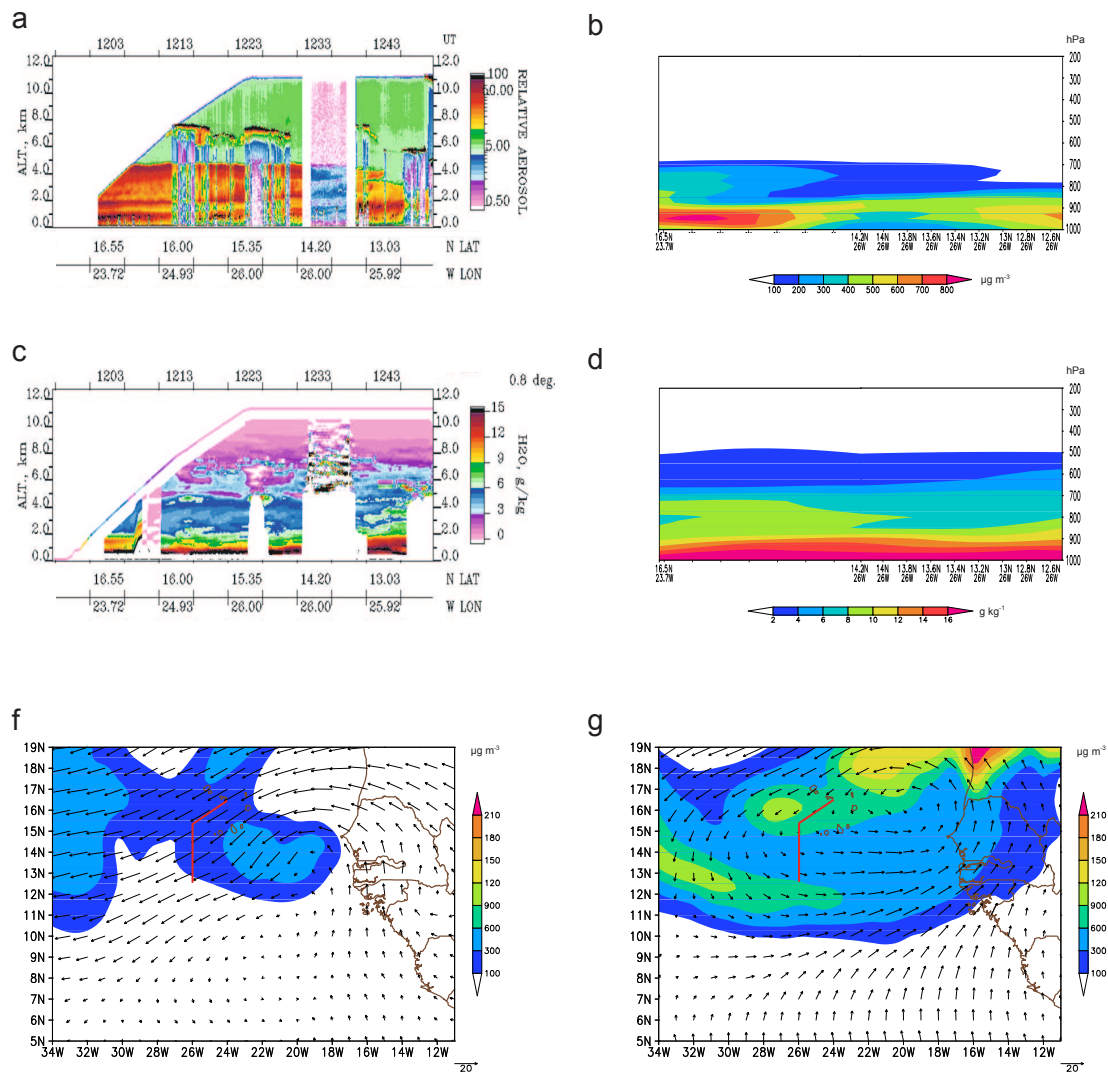


Figure 5.13: (a) NAMMA Lidar Atmospheric Sensing Experiment (LASE) imagery of aerosol scattering between 1200 and 1248 UTC on 12 September 2006. Taken from Jenkins et al. (2008), their Fig. 3. (b) Mineral dust mass concentration ($\mu\text{g m}^{-3}$) along the same transect as in (a) at 12 UTC (T+72) based on the RadDust run initialised on 9 September 2006 at 12 UTC. (c) NAMMA LASE imagery of water vapour mixing ratio between 1200 and 1248 UTC. Taken from Jenkins et al. (2008), their Fig. 3. (d) Specific humidity along the same transect as in (a-c) at 12 UTC (T+72) based on the RadDust run initialised on 9 September 2006 at 12 UTC. (e), (f) Mineral dust mass concentration ($\mu\text{g m}^{-3}$) and horizontal wind (m s^{-1}) at 700 hPa and at 975 hPa, respectively, on 12 September 2006 at 12 UTC (T+72) based on the RadDust run initialised on 9 September 2006 at 12 UTC.

Dakar due to the maritime influence. Between about 14 and 19°N westerly flow (Atlantic inflow) occurs along the West African coast line (Grams et al., 2010). Above this layer in the lower troposphere the relative humidity decreases with height, but increases again at mid-levels. In Tombouctou the lower levels are much drier due to the location of the town at the southern fringes of the Sahara. The mid-levels, however, are relatively moist at the height of the AEJ in the observations but not in the model results. In the model simulation, Tombouctou is located in a region with a sharp moisture gradient at 600 hPa with dry air to the southeast of the station and much moister air to the northwest. At 950 hPa, the station is located at the edge of a region with high AOTs and a low-level convergence to the northwest.

The relation between the dust event and the lower-tropospheric moisture can be seen in the radiosoundings in Nouakchott on 9 September at about 23 UTC and the sounding 12 hours later (Fig. 5.15). On 9 September at about 23 UTC the relative humidity in the 900 to 700 hPa layer is between 40 and 60% due to the Atlantic Inflow. Twelve hours later, this region is characterised by dry air (relative humidity between 20 and 30 %) and high AOTs. At about 600 hPa the relative humidity is high, probably due to the altocumulus at the top of the SAL. Strong low-level negative meridional flow can be observed on 10 September at about 11 UTC, in contrast to the weaker meridional wind 12 hours earlier. The differences in the low-level moisture and zonal wind fields in Nouakchott might be related to a slight misplacement of the low-level circulation in the model run and the associated moisture fields.

The influence of the SAL can be seen in Fig. 5.16 also. Both stations show a moist layer between 500 and 600 hPa which could indicate the characteristic altocumulus at the top of the SAL. Below, the air is very dry in Nouadhibou, which is located at the northern edge of the region with high AOTs on 10 September 2006 at about 11 UTC (Fig. 5.3). The sounding in Nouakchott, which is located within the region of high AOTs, was taken about 12 hours later. Here, the low-level air is still dry, but slightly moister than in Nouadhibou 12 hours before. Strong low-level negative meridional winds can be observed at both stations, as well as low-level easterlies in Nouadhibou and westerlies in Nouakchott, that led to the dust emission. The largest discrepancies between model and observations occur in the meridional wind in Nouakchott and in the zonal wind profile

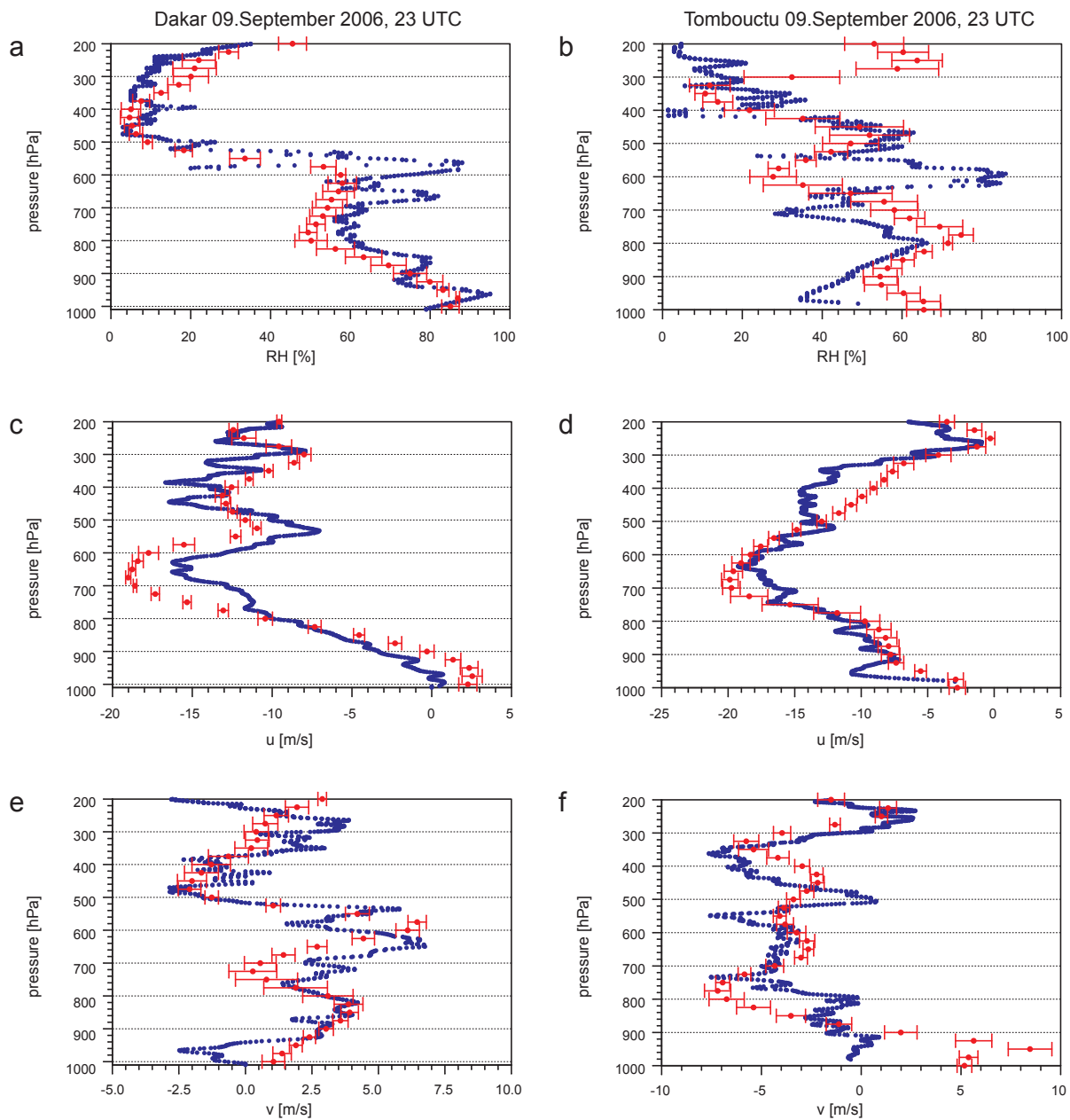


Figure 5.14: Profiles of relative humidity (%) (upper row), the zonal wind (m s^{-1}) (middle row), and the meridional wind from radiosondes, released in Dakar (17.49°W , 14.75°N), Senegal, at (a, c, e) 09 September 2006, 2235 UTC and at (b, d, f) and at 2232 UTC on 9 September 2006 in Tombouctou (4.1°W , 21.85°N), Mali. The radiosounding is displayed by blue dots, and the corresponding model output from the 144-hour COSMO forecast initialised at 12 UTC on 9 September 2006 and including the dust–radiation interaction (RadDust), by red dots. The horizontal bars indicate the standard deviation of the model output in a $0.5^\circ \times 0.5^\circ$ square centred on the closest grid point.

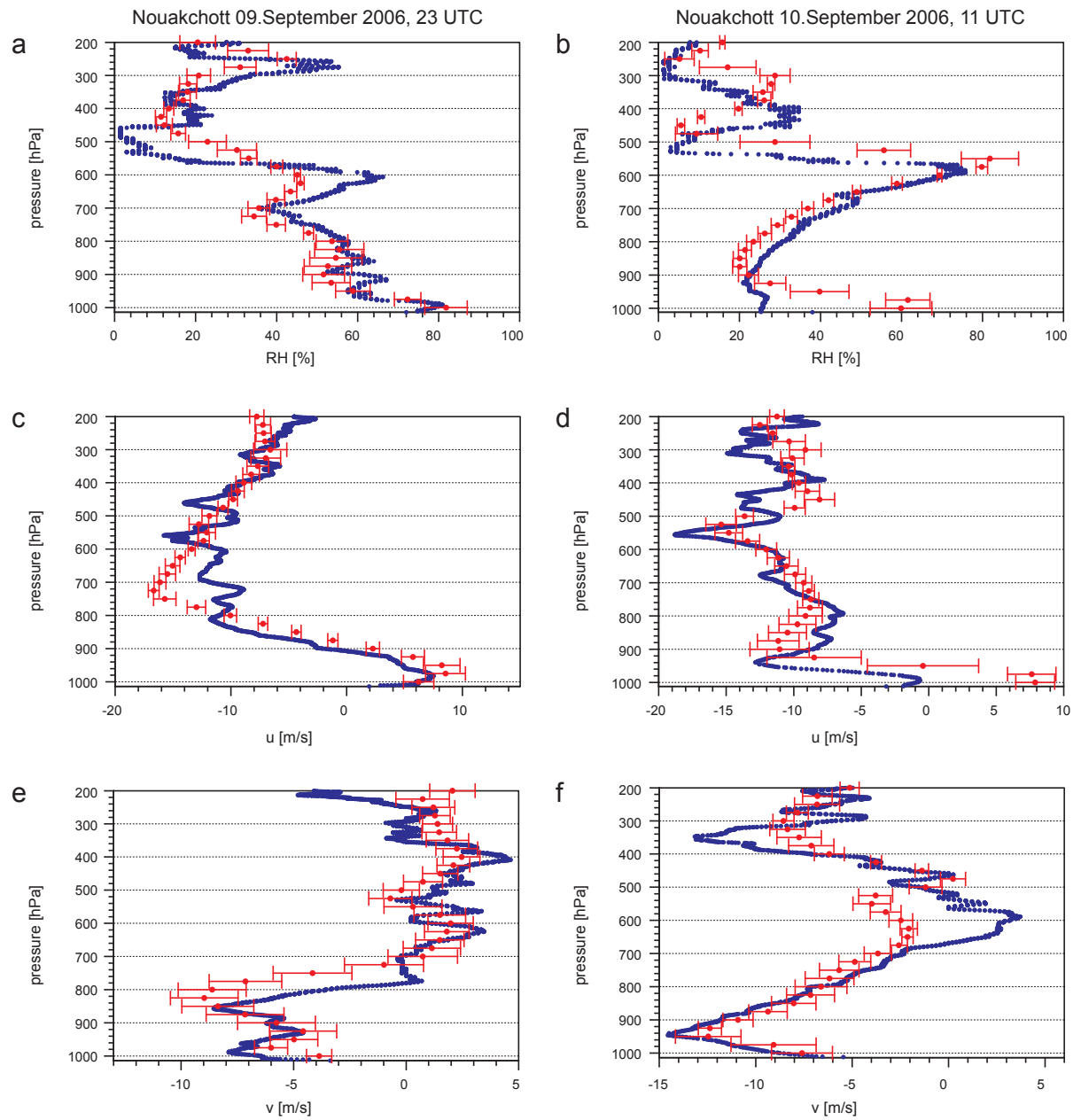


Figure 5.15: The same as Fig. 5.14, but the the radiosounding in Nouakchott (15.57°W , 18.6°N), Mauritania on 09 September 2009, 2234 UTC (left side), and on 10 September at 1042 UTC (right side).

in Nouadhibou. This might be because Nouadhibou on 10 September at about 11 UTC, is located just northwest of the low-level circulation associated as a secondary heat low in the model run. The position of this circulation feature might be slightly misplaced leading to errors in the wind profile. Nouakchott is situated in a region with strong low-level gradients. The region with maximum negative meridional wind is located about 2° west of the station at 980 hPa and in the northeast at 600 hPa.

The comparisons between the COSMO-ART run RadDust, and the satellite images illustrating the atmospheric dust load, as well as the comparison with the AMMA radiosoundings show that the model represents the atmospheric conditions reasonably well, and that the model run can be used to analyse the effect of the dust on its environment.

5.2 The Impact of the Dust–Radiation Feedback

To assess the effect of mineral dust in the atmosphere during the cyclogenesis of Hurricane Helene, we compare the simulation in which the dust interacts with the radiation scheme (RadDust) with the simulation in which dust acts as a passive tracer (NoRadDust).

Several differences occur in the potential temperature, zonal and meridional wind fields during the simulated period. The most marked, however, is the intensification of the monsoon trough on 12 September 2006. The potential temperature at 950 hPa north of the low-level circulation centre is about 4 K higher in the RadDust run than in the NoRadDust run (Fig. 5.17d). In this region high dust concentrations can be found (Fig. 5.17b). The mineral dust particles absorb the incoming shortwave radiation and thus the potential temperature increases. A broad region west of the circulation centre is also characterised by an increase in low-level potential temperature due to the absorption of shortwave radiation by mineral dust particles. A marked temperature decrease up to 4 K occurs over land north of about 18°N . It can partly be attributed to an elevated dust layer that is located at around 900 hPa in this region. The mineral dust absorbs the incoming shortwave radiation and the temperatures in this dust layer increase (not shown). Below, the temperatures decrease as the shortwave radiation is reduced. Associated with these potential temperature differences we see an increase in the easterlies and northerlies

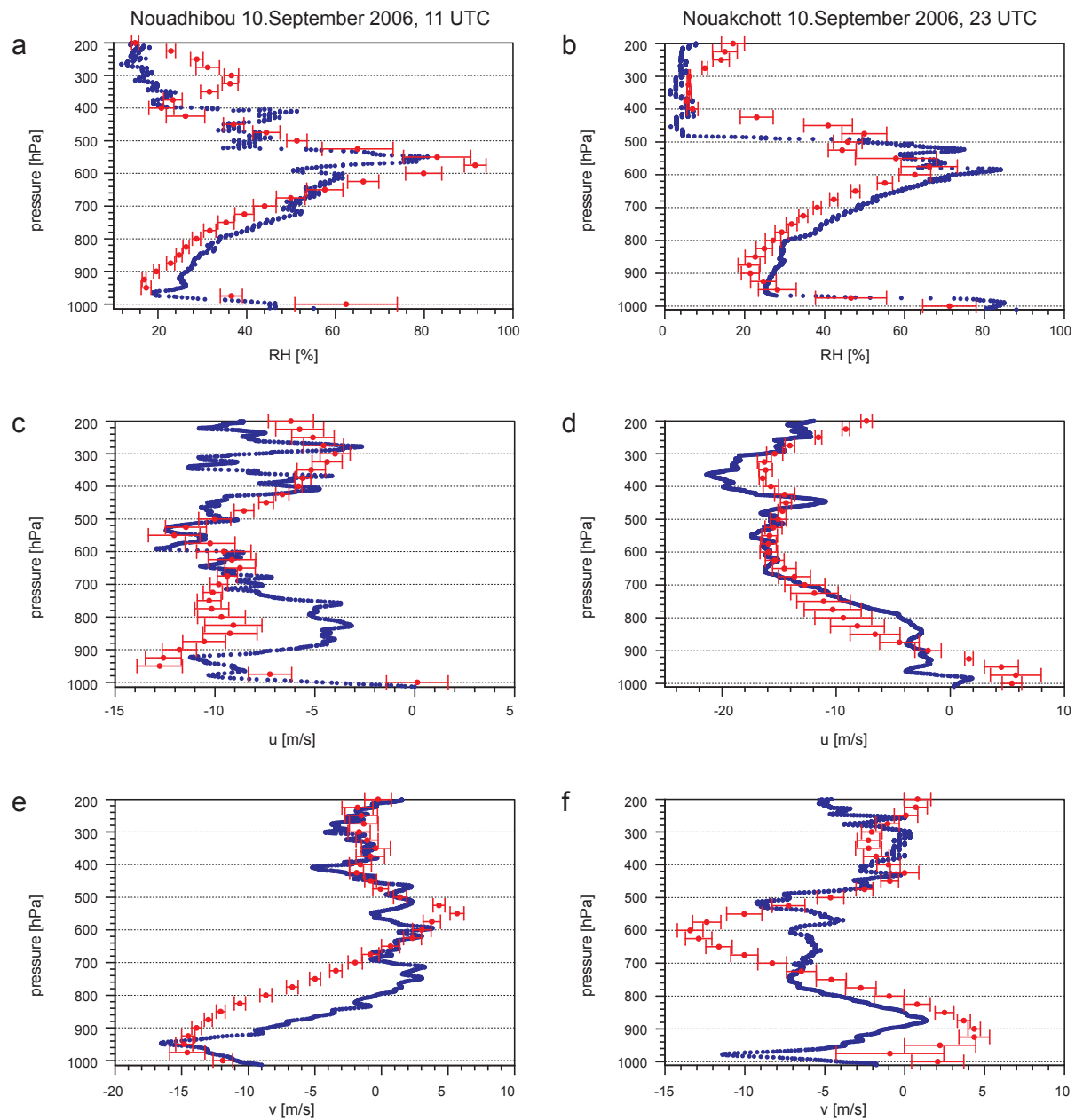


Figure 5.16: The same as Fig. 5.14, but the the radiosounding in Nouadhibou (17.2°W , 20.56°N), Mauritania on 10 September 2009, 1035 UTC (left side), and in Nouakchott (15.57°W , 18.6°N), Mauritania, on 10 September at 2236 UTC (right side).

north of the low-level circulation, and an increase in the westerlies and southerlies south of the low-level circulation (Fig. 5.17f) in the RadDust run. This is an indication that the monsoon trough has intensified and the low-level vorticity has increased.

At 700 hPa, at the northern edge of the largest dust concentrations in the AEW trough at about 22°W and 16°N (Fig. 5.17a) the temperatures in the RadDust run are up to 2K higher than in the NoRadDust run (Fig. 5.17c). The region between 25-18°W and 12-17°N is also characterised by strengthening of the northeasterlies, and by strengthening of the southwesterlies between 23-12°W and 9-12°N (Fig. 5.17e). The anomalies at 700 hPa have a smaller horizontal extent than those at 950 hPa.

Moreover, large amounts of dust are transported at low levels towards the northwest, partly by the eastern branch of the low-level circulation over the Atlantic, whereas parts of the dust are lifted up along the west African coast between Dakar and Cap Blanc and transported westwards by the AEJ. Relatively high dust concentrations occur also in the region of the low-level convergence line over west Africa (see also Fig. 5.3x). A tongue of dust enriched air moves towards the circulation centre (Fig. 5.17b). Although some of the thermodynamical changes are clearly associated with the direct interaction between dust and radiation at the time in question, others cannot be directly connected, indicating that changes in the circulation have occurred due to the dust-radiation interaction at previous times.

The differences between both model runs in the vertical are illustrated by north-south cross section through the centre of the low-level circulation centre at the position indicated in Fig. 5.17a,b. The near surface temperatures north of 16°N are higher in the RadDust run on 12 September 2006, 12 UTC (Fig. 5.18d), as well as the temperatures between 900 and about 500 hPa. This mid-level temperature increase results from the enhanced dust concentration in this region (Fig. 5.18b), particularly in the northern part of the cross section. Within the near surface and uplifted dust layer, a potential temperature increase occurs due to the absorption of radiation by the dust particles (direct aerosol effect). Below the uplifted dust layer, the reduction of incoming shortwave radiation leads to a cooling (14-16°N and 900-700 hPa). Above 500 hPa a potential temperature decrease can be observed. Between about 16 and 18°N a sharp gradient in westerly and easterly winds marks the low-level circulation centre. The stronger low-level circulation in the RadDust

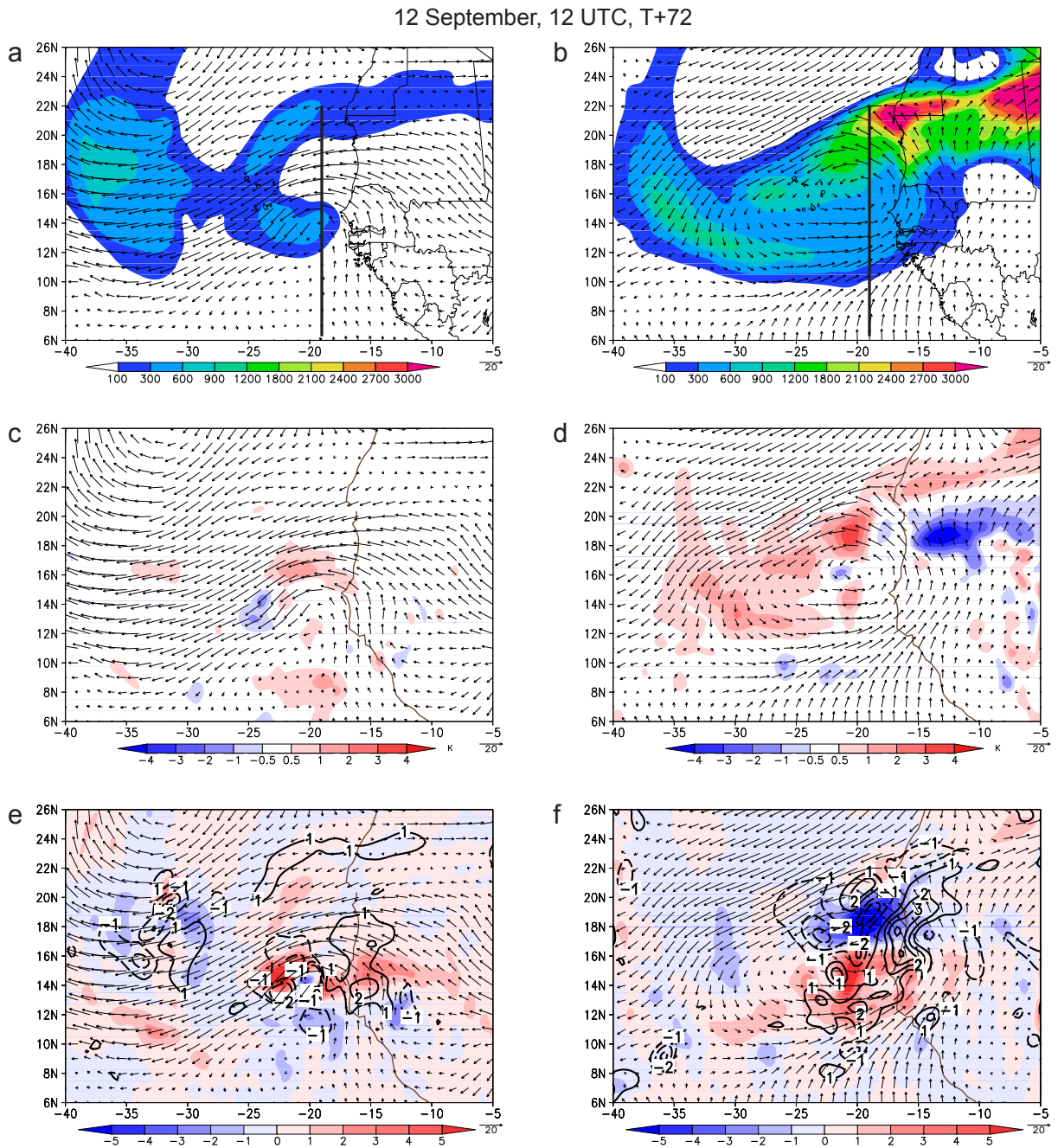


Figure 5.17: The mineral dust mass concentration ($\mu\text{g m}^{-3}$) at 700 hPa (a) and 950 hPa (b) in the RadDust model run. Differences between the RadDust and NoRadDust model runs in potential temperature (shaded, K) at 700 hPa (c) and 950 hPa (d), as well as in zonal wind (m s^{-1} , shaded) and meridional wind (2 m s^{-1} contour interval) at 700 hPa (e) and 950 hPa (f). The dotted line denotes the zero line. The horizontal wind speed (arrows in m s^{-1}) from the RadDust run is shown on 12 September 2006 at 12 UTC (T+72) at 700 hPa (left) and at 950 hPa (right).

12 September, 12 UTC, T+72

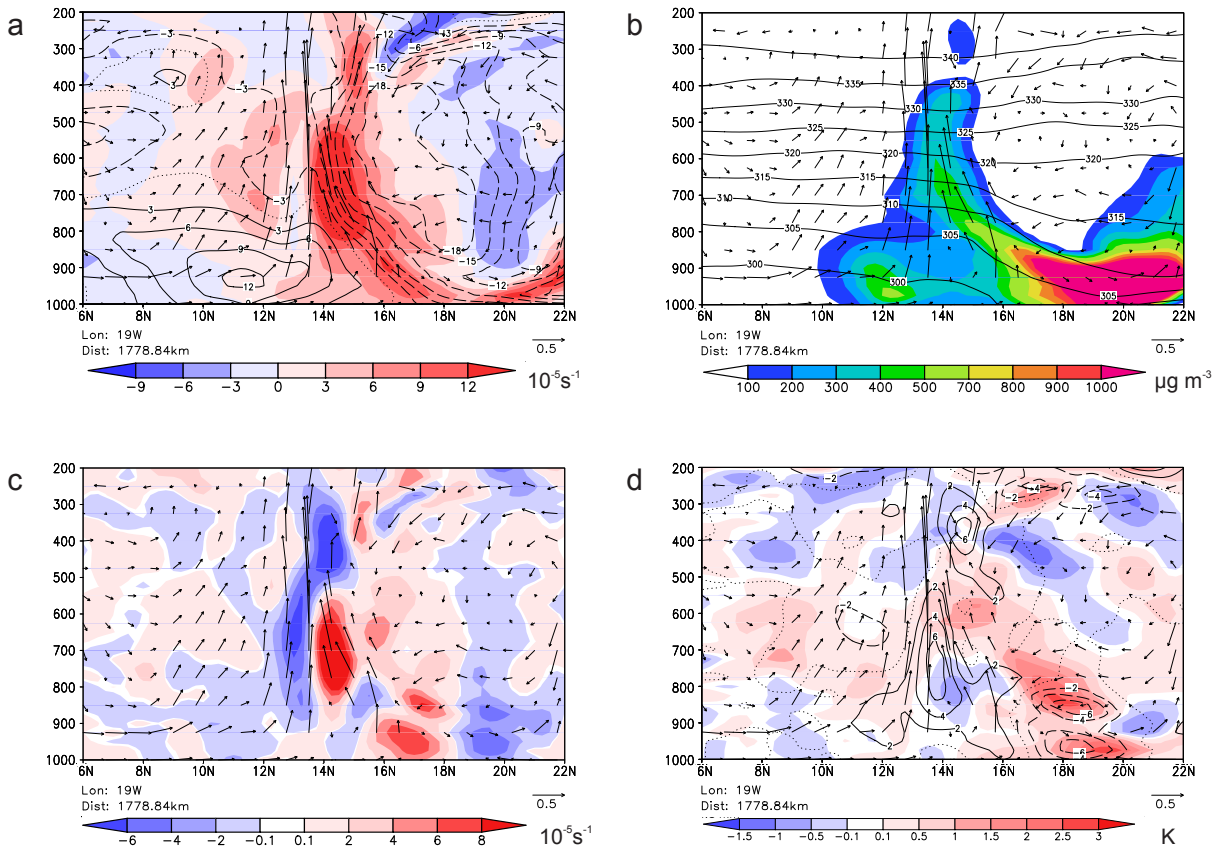


Figure 5.18: Cross sections on 12 September 2006 at 12 UTC (T+72) through the circulation shown in Fig. 5.17 along 19°W . (a) The vertical component of the relative vorticity (shaded) and the zonal wind speed (3 m s^{-1} contour interval), and (b) the mass concentration ($\mu\text{g m}^{-3}$) as well as the potential temperature (5 K contour interval) of the RadDust model run initialised on 9 September 2006 at 12 UTC. Differences between the RadDust and NoRadDust model runs in (c) the vertical component of relative vorticity (contours, 10^{-5} s^{-1}), and (d) potential temperature (shaded) as well as the zonal wind speed (contours, m s^{-1}). The wind field (arrows) along the cross sections is shown in all images.

run is also indicated by the positive relative vorticity anomaly in the same region (Fig. 5.18c). The dipole structure in the relative vorticity differences illustrates the the position of the centre of circulation differs in both runs.

The differences between the RadDust and the NoRadDust runs become more distinct with time. On 15 September 2006 at 06 UTC, the centre of tropical storm Helene had a lower potential height in the RadDust run than in the NoRadDust run (Fig. 5.19a) indicating that the tropical storm develops faster in the RadDust run. Warm air can be found in the north and northwest of the storm in both runs. The system had a warm core in both runs, but the displacement of the storm's centre by about 2° is distinctly visible (Fig. 5.19b).

The potential temperatures in the northeast are higher in the RadDust run. Here high dust concentrations occur (Fig. 5.19d). Dust concentrations in the order of $220 \mu\text{g m}^{-3}$ can be found in the storm's centre in the RadDust run and even higher values southwest of it, and in a narrow band in the north and northeast of the storm's centre. The position of the largest dust concentrations in the NoRadDust run is slightly displaced according to the position of the storm, but no particularly enhanced dust concentrations occur in the storm's centre. Moreover, the region characterised with dust concentration of $70 \mu\text{g m}^{-3}$ covers a larger area in the RadDust run. The region with high dust concentration and high potential temperatures northeast of the tropical storm is also quite dry (Fig. 5.19c). West–northwest of the storm there is a sharp gradient in dust concentration and total water, which is the integral of cloud water, cloud ice and humidity in both runs. The region in between is very dry and as previously shown, a result from subsiding air from upper levels. This comparison indicates that the tropical storm Helene is stronger in the RadDust run.

5.3 Summary and Discussion

The AEW out of which Hurricane Helene (2006) developed, the associated weather systems and mineral dust sources, as well as the dust transport were simulated using the model system COSMO-ART. Two model runs were conducted with the same model set up, except one model run includes the dust–radiation interaction (RadDust) and the other run does not (NoRadDust). The RadDust run was compared to satellite images illustrating the AOT, the SAL, and the TPW. In addition, radiosoundings from Dakar, Nouakchott, Nouadhibou and Tombouctou from the AMMA campaign were compared to the model results. The agreement between the observations and the model results for the whole simulation period was found to be reasonably good.

The main source regions of mineral dust for this case study were the convergence zone between the dry and hot Harmattan and the moist and relatively cool monsoon flow along the ITD, the convergence zone between the maritime air of the Atlantic inflow and the Saharan air, the strong Harmattan in the Western Sahara, the lee of the Atlas Mountains, the Algerian Mountains and the Hoggar. Large amounts of dust were uplifted at the ITD

15 September 2006, 06 UTC, T+138

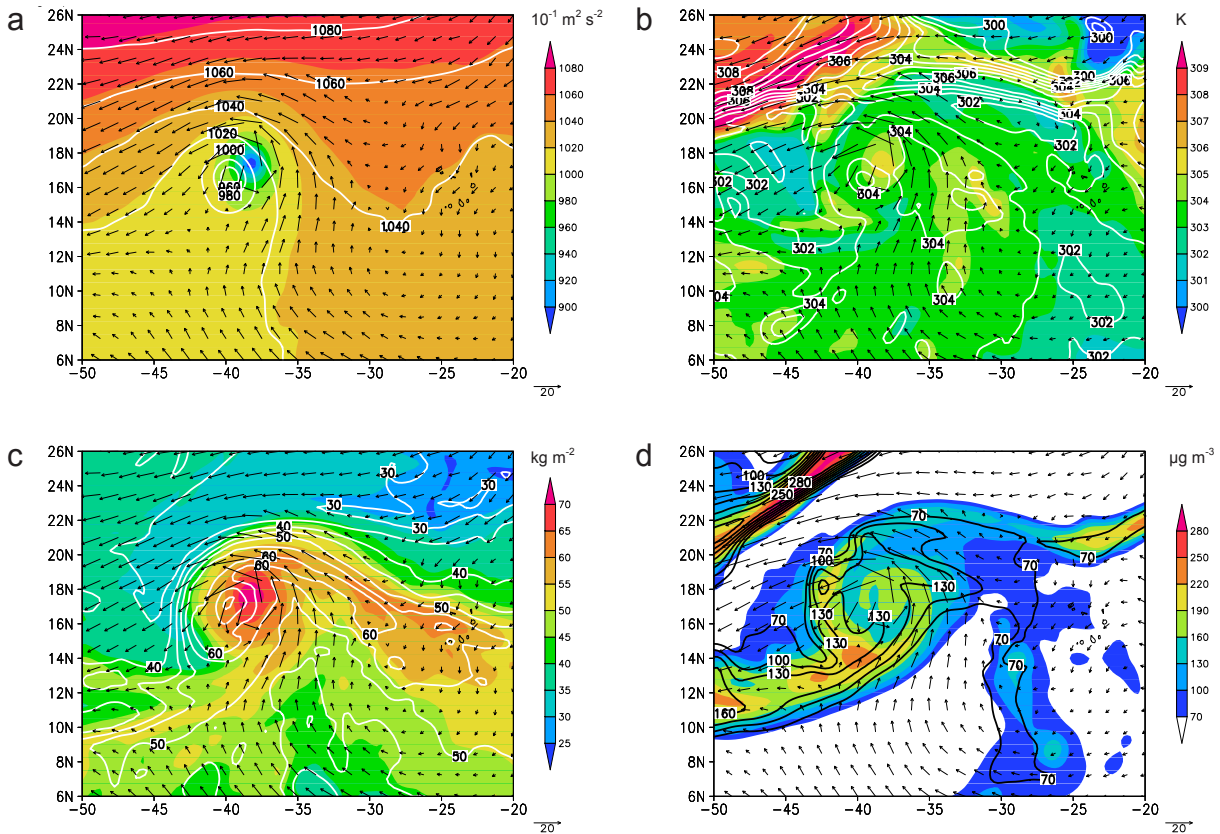


Figure 5.19: (a) The geopotential ($10^{-1} \text{ m}^2 \text{ s}^{-2}$) at 900 hPa, (b) the potential temperature (K) at 850 hPa, (c) the vertical integral of cloud water, cloud ice and humidity (kg m^{-2}) at 1000 hPa, and (d) the mineral dust concentration ($\mu\text{g m}^{-3}$) at 850 hPa, for the RadDust run (shaded) and the NoRadDust run (contours). Additionally, the horizontal wind field in the RadDust run is shown at the given levels on 15 September 2006 at 06 UTC (T+138).

and ahead of the Atlantic inflow, and thus transported by the AEJ across West Africa and the Atlantic. Mineral dust was also transported in association with the low-level circulation and the large monsoon trough, that could be found off shore the west African coastline on 12 September 2006 with the monsoon flow reaching north up to about 22°N . Large amounts of mineral dust occurred north of the AEJ axis. On 11 September 2006 in the afternoon hours, a dust event was initiated east of Dakar within the trough of the AEW out of which Hurricane Helene developed. This mineral dust was transported along two pathways. On the one hand, the dust was lifted up over Mauritania close to the region where it was emitted, and predominantly between about $15\text{--}19^\circ\text{N}$ along the West African coast line. It reached heights of about 600 hPa and was advected westwards by the AEW. On the other hand, the dust is transported northwestwards by the low-level monsoon flow.

The Harmattan and the monsoon flow converged along a northeast–southwest orientated band (17°W , 20° and 8°W , 25°N). In this region the dust is partly lifted and the other part rotated cyclonically around the low–level circulation. Thus the mineral dust is both lifted up into the AEW trough, and advected at lower levels by the monsoon flow into the centre of the low–level monsoon circulation.

When the low–level and the mid–level relative vorticity anomaly related to the AEW are collocated on 12 September 2006 in the late afternoon hours, dust can be seen in the centre of the developing tropical depression. The dust concentration in the storm’s centre decreases with time due to wet and dry deposition, but relatively high AOTs can be observed in the centre when Helene reached hurricane intensity. During the development from a tropical depression to a mature hurricane, bands of dry air spiralled towards the storm centre and a dry intrusion occurs west and southeast of the storm, close to the centre.

The comparison between the RadDust and NoRadDust model runs showed that the potential temperature increased in the near–surface and uplifted mineral dust regions due to the absorption of radiation by aerosol particles. In the regions below the elevated dust layer, cooling occurs due to the reduction of incoming shortwave radiation. The northeasterly and the southwesterly winds are stronger in the RadDust run than in the NoRadDust run, leading to a stronger monsoon trough. From this time on the low–level circulation was distinctly stronger in the RadDust run. The pre-Helene system was stronger, i.e. the zonal and meridional wind was stronger and hence the relative vorticity, in the RadDust run than in the NoRadDust run.

Cross sections showed that in the RadDust run a strong potential temperature increase occurred between 950 and about 700 hPa north of the low–level circulation in the region with the largest dust concentrations. Dust concentration in the order of $300\text{--}500\ \mu\text{g m}^{-3}$ can be found near within the centre of the low–level circulation and markedly higher values north of it between 12 and 13 September. From 14 September on, distinct amounts of dust are located in the storm’s centre. Differences in the geopotential and other fields showed that the developing tropical cyclone is distinctly stronger in the RadDust run. The tropical storm in the NoRadDust run is located about 2° further southwest than the storm in the RadDust run. Additionally, the warm–core structure is more marked.

It appears that in this modelled case, the mineral dust acts to enhance the developing tropical cyclone.

The development of Hurricane Helene (2006) was also analysed and compared to a non-developing case at the end of August 2006 by Reale et al. (2009). Their tropical storm Helene occurred at about the same position as our system on 14 September 2006 at 00 UTC, and they also observed dry air in the north–northwest of Helene. Reale et al. (2009) argue that the temperature anomaly within the vorticity column is a result of the tropical storm’s development. In our case study, however, it appears that the increased temperatures due to the dust enhance the warm core. They state that different amounts of dust have a different impact on the thermal structure of the atmosphere. The dust was advected into the circulation of their non–developing case, and was assumed to lead to an increase in static stability and hence a suppression of the tropical cyclogenesis. In our RadDust run, however, the mineral dust was advected into the centre of the pre–Helene system.

The effect of dust on the tropical cyclogenesis is assumed to depend on the intensity of the dust event, i.e. the mineral dust mass concentrations. The dust concentrations or the AOTs for the Helene case were relatively low compared to other mineral dust events in West Africa (e.g. Stanelle, 2008; Bou Karam et al., 2009a,b; Flamant et al., 2009). The temperature increase due to the absorption of radiation by the dust particles in the present case led to warming in the TC core, which in turn enhanced the system. This may not be the case for more intense dust outbreaks. The main difference to previous studies (e.g. Dunion and Velden, 2004) is that the dust in the present study occurs partly in regions that are relatively moist, especially in the vicinity of the storm’s centre. If the air is dry and dust enriched then it is likely to suppress convection as pointed out by several other studies. Another difference between our model study and previous studies (e.g. Reale et al., 2009; Sun et al., 2009) is that their model simulations contain the dust, temperature and humidity information via the assimilation of Atmospheric Infrared Sounder (AIRS) data, whereas COSMO-ART simulates the emission and the transport of mineral dust based on the current mineral dust distribution. Further studies are needed to investigate the effect of the mineral dust on the dynamics that led to the tropical

cyclogenesis and the dynamics of the tropical cyclone. Such studies could include the calculation of potential temperature and potential vorticity budgets.

6

Summary and Conclusions

The African easterly wave out of which Hurricane Helene (2006) developed and the convective systems over West Africa and the eastern Atlantic embedded in this AEW between 9-15 September 2006 were investigated in this study. The differences and similarities between the convective systems over land and over water were studied by simulating the events with the COSMO model at a horizontal resolution of 2.8 km. During this period, significant amounts of mineral dust were present over West Africa and over the Atlantic. The effect of the mineral dust on these convective systems, their environment, and on the development of Hurricane Helene was investigated using the model system COSMO-ART at a horizontal resolution of 28 km.

The mesoscale convective system over land, embedded in the AEW out of which Hurricane Helene developed, was initiated in the afternoon hours on 9 September 2006 ahead of the trough of the AEW. This MCS increased quickly in intensity and size, and developed three arc-shaped convective systems moving westward. As the MCS decayed, new convective bursts occurred in the remains of the old MCS leading to a north-south orientated band of thunderstorms, which crossed the West African coastline at around midnight on 11 September. During the next 24 hours, intense convective bursts occurred over the eastern Atlantic. These convective bursts were embedded in a cyclonic circulation, which intensified and became a Tropical Depression on 12 September 2006, 12 UTC. The largest and most long lived convective burst in this intensification period was analysed here and compared to the MCS over land.

The convective available potential energy (CAPE) in the environment of the convective systems over land and over the ocean was similar. In both systems the region with the strongest updraughts was collocated with the region of maximum diabatic heating. The convective system over the ocean was upright above 700 hPa, whereas the one over the land was tilted with height away from the direction of motion. Over land the shear was stronger and the air was drier at midlevels (600-800 hPa). This resulted in stronger downdraughts and, hence, in a marked cold pool which allowed the system to propagate westwards towards a region with high CAPE and low-level high equivalent-potential temperature air that feeds the convective systems, and to grow upscale into a mature MCS. As the oceanic convective systems had no cold pool and, thus, no mechanism to propagate, they remained smaller. Due to the smaller shear the convection was harder to sustain and the lifetime was shorter. The environment, however, was favourable for new convection to form. This led to the succession of smaller convective systems instead of a single, large MCS over land.

Over land the MCS was initiated ahead of the AEW trough, where it remained throughout its lifetime. As the convective systems moved over the Atlantic they moved into the AEW trough. During the convective system's lifecycle, the environmental vertical shear of the horizontal wind was reduced significantly over the ocean and only slightly over land.

The interaction of the convective systems with their environment could be related to the structure of the systems themselves, i.e. the convective and stratiform regions. The influence of the MCSs was assessed by calculating potential temperature and relative vorticity budgets for regions encompassing the convective systems. We defined regions with strong ascent and descent as well as with weak ascent and descent according to the vertical velocity at 650 hPa. With the help of this partitioning, the structure of the convective systems was more evident than in the averages over the entire boxes.

The potential temperature tendencies for the convective systems over West Africa and the eastern Atlantic showed a net cooling between 950 and 800 hPa and a net warming above 400 hPa. Between these layers there were hardly any net changes detectable. The potential temperature tendency due to moist processes and due to vertical advection almost counterbalanced each other, with their strongest contribution to the potential temperature tendency in the mid troposphere, where the maximum occurred at slightly higher levels

over land. In contrast to the ocean case, the presence of stratiform clouds was evident in the budget for the strong descent regions at 650 hPa for the land case. The cooling due to unsaturated downdraughts was much stronger for the convective system over land than for the convective system over the ocean. Over land, the potential temperature tendency due to turbulence contributed significantly to the total potential temperature budget in the lower troposphere and in the mid troposphere due to the shear below the AEJ. In contrast to the MCSs over land, the regions of weak ascent and weak descent over the ocean at 650 hPa contributed more strongly to the net potential temperature tendency than the contribution from the strong descent region. Furthermore, we found that the weak descent regions were as important as the strong convective updraughts for the total heat budget. Downdraughts at midlevels occurred, a stratiform region around 300-400 hPa and shallow convection could be observed.

Over land, the relative vorticity increased from about 900 to 500 hPa, especially from the mature state of the convective system on, and decreased above 400 hPa. Over the ocean, the relative vorticity between 600 and 400 hPa was relatively high at the beginning of the observation period and increased up to a forecast time of 9 h. During the following hours the vorticity increased only slightly but the height at which the maximum occurred was lowered significantly. The main reason for the total relative vorticity changes over the ocean was the tendency due to vortex stretching that led to a relative vorticity increase at lower levels. The positive contribution at low-levels was smaller over the land than over the ocean. The tendency due to vortex compression resulted in a negative relative vorticity tendency above 600 hPa over land and over the ocean. Over West Africa, the eddy flux, i.e. the horizontal advection of absolute perturbation vorticity, led to an increase in vorticity at mid-levels. The eddy flux had a positive contribution at the beginning and towards the end of the observation period for the system over land due to the advection of positive perturbation vorticity into the box by the AEW. Between 14 and 18 forecast hours positive perturbation vorticity was advected out of the box. Additionally, in association with the low-level circulation northwest of the box, positive perturbation vorticity was advected into the box at low-levels through the northern and western side. Over the ocean, the eddy flux term caused an increase in relative vorticity at the very beginning of the life cycle of the convective system. This effect decreased as the system reached maturity but

positive tendencies occurred at midlevels towards the end. The tilting term provided the smallest contribution to the relative vorticity budget. It led to a mostly negative tendency in the lower troposphere over land, and an increase in relative vorticity over the ocean.

The PV budget shows that the PV increased between 900 and 600 hPa and decreased above due to diabatic effects and horizontal advection of PV for the convective systems over land. Over the ocean the PV increase was not as strong but the height at which the PV maximum was located was lowered significantly. Similar effects could be observed for the relative vorticity budget. Initially, the circulation in the AEW trough was horizontally elongated and had a southwest–northeast orientation. During the period of investigation, the circulation became more circular and intensified. This increased low–level PV could have enhanced the low–level monsoon flow behind the system, and possibly strengthened the trough of the AEW and the AEJ.

A remarkable feature contributed to the formation of Hurricane Helene. A secondary heat low was separated from the main heat low over the Sahara and moved over the Atlantic. This positive relative vorticity anomaly that was confined to the lowest levels moved towards the southwest over the ocean while the northeastern trade winds increased and the monsoon flow developed. Meanwhile, the AEW at 700 hPa propagated over West Africa. As the mid–level AEW anomaly moved over the low–level cyclonic circulation, convection was initiated and the pre–Helene tropical depression developed.

To assess the effect of the mineral dust on the above described convective systems and the cyclogenesis of Hurricane Helene, two COSMO-ART model runs were conducted. The only difference in the setup of the two model runs was that one model run included the dust–radiation interaction (RadDust) and the other run did not (NoRadDust).

The main source regions of mineral dust were in this case the convergence zone between the dry and hot Harmattan and the moist and relatively cool monsoon flow along the ITD, the convergence zone between the maritime air of the Atlantic inflow and the Saharan air, the lee of the Atlas Mountains, the Algerian Mountains and the Hoggar. Large amounts of dust were lifted up at the ITD and ahead of the Atlantic inflow, and transported across West Africa and the Atlantic by the AEJ. Mineral dust was also transported in association with the low–level circulation and the monsoon trough.

Large amounts of mineral dust were present north of the AEJ axis. A strong dust event was initiated east of Dakar within the trough of the AEW out of which Hurricane Helene developed. The mineral dust released in this event was transported along two pathways. On the one hand, dust was lifted up over Mauritania close to the region where it was emitted, predominantly along the West African coast line between Dakar and Cap Blanc, reached the height of the AEJ and was advected westwards by the AEW. On the other hand, dust was transported northwestwards by the low-level monsoon flow. A part of it was lifted up in the northeast-southwest orientated band in which the monsoon flow and the Harmattan converge. The other part rotated cyclonically around the low-level circulation. Thus mineral dust was advected into the centre of the low-level monsoon circulation by the monsoon flow .

The dust was transported northwestwards by the monsoon flow and rotated cyclonically around the monsoon trough, was advected later by the strong northeasterly winds, and spiralled towards the centre of the low-level circulation. From this time on, significant amounts of dust were present in the low-level circulation centre that was associated with the secondary heat low. When the low-level and the mid-level relative vorticity anomaly related to the AEW were collocated, non-negligible dust concentrations could be observed in the centre of the developing tropical depression. The dust concentration in the storm's centre decreased with time due to wet and dry deposition, but a still relatively high optical thickness could be observed in the centre when Helene was upgraded to hurricane intensity. During the development from a tropical depression to a mature hurricane, bands of dry air spiralled towards the storm centre and a dry intrusion formed west and southeast of the storm, close to the centre.

The results from the RadDust run were compared to satellite imagery and radiosoundings obtained during the AMMA campaign. The agreement between the observations and the model results was found to be reasonably good. The comparison between the RadDust and the NoRadDust model runs shows that the potential temperature increased in the low-level and uplifted mineral dust regions due to the absorption of radiation by aerosol particles. In the regions below the SAL, cooling was caused by the indirect aerosol effect. The northeasterly and the southwesterly winds were stronger in the RadDust run than in the NoRadDust run, leading to a more pronounced monsoon trough. The low-level

circulation, the tropical depression and the tropical storm were distinctly stronger in the RadDust run.

In the RadDust run a considerable potential temperature increase occurred between 950 and about 500 hPa. Significant amounts of dust could be found between the surface and about 500 hPa, even in the tropical storm's centre. Markedly higher dust concentrations could be found north of the storm. Differences in the zonal wind field showed that the developing tropical depression was distinctly stronger in the RadDust run. The position of the storm in both runs differed, too. At the end of the model runs the tropical storm in the NoRadDust run was located about 2° further southwest than the storm in the RadDust run. Additionally, the warm-core structure was more marked. The centre of the tropical storm in the RadDust run had a lower geopotential and a warmer warm core. Thus, the mineral dust in the RadDust run acted to enhance the developing tropical cyclone.

In this study we contrasted the influence of convective systems over land and over the ocean on the vorticity structure of their environment. We related the changes in the nature of the convection over land and over the ocean to changes in the environment. For this purpose we computed heat and vorticity budgets. Over land, the increased mid- to lower tropospheric circulation modified the propagation characteristics of the AEW. Over water, the character of the convection appeared to be undergoing a transition from that of an MCS in a vertically sheared environment to that of vortical hot towers, which is an important step for tropical cyclogenesis. However, in the convective burst considered there was still a significant stratiform component present in the system, along with unsaturated downdraughts in its decaying phase. Further study is needed to quantify how these changes in the nature of the convection impact the route to tropical cyclogenesis. Future studies could also analyse the development and the characteristics of the secondary heat low and investigate how it interacts with the AEW to trigger cyclogenesis. The analysis could be applied to other cases in order to generalise these results. Furthermore, an interesting extension of this work would be to quantify the impact of convection on the AEW using PV inversion techniques.

The comparison between the RadDust and NoRadDust model runs showed that in this case the dry and dusty air that is associated with the low-level circulation which developed as a westward extension of the secondary heat low, and the SAL at mid-levels, appears

to aid the transformation from a cold–cored system to a warm–cored system, which is a crucial step on the way to tropical cyclogenesis. As the horizontal resolution is a critical factor when modelling tropical cyclogenesis and the SAL, future work needs to include high–resolution model runs which resolve the convection in order to investigate the effect of the SAL. Potential temperature and relative vorticity budgets could also be conducted for the RadDust and NoRadDust runs to analyse the effect of the dust on the dynamics. Moreover, dust can influence the formation of clouds and should therefore be included in the model cloud microphysics.

List of Symbols

A	area
$A_{\text{east}}^{\text{in}}$	the part of the east side of the box for which $u < 0$
B_q	buoyant acceleration
C	circulation
c_{pd}	specific heat capacity of dry air at constant pressure
c_{pv}	specific heat capacity of dry air at constant volume
Δt	finite time interval
$\Delta V = \Delta x \Delta y \Delta z$	finite volume element
$\frac{d}{dt} = \frac{\partial}{\partial t} + \vec{v} \cdot \nabla$	total (Lagrangian) time derivative operator
$\frac{\partial}{\partial t}$	local (Eulerian) time derivative operator
η	absolute vorticity
f	Coriolis parameter
\vec{F}	frictional force
$F_{\text{east}}^{\text{in}}$	eddy flux into the box coming through the east side
F_h	horizontal saltation flux
F_v	vertical saltation flux
\vec{F}_x	turbulent flux of water constituent x
\vec{g}	apparent acceleration due to gravity
H	turbulent flux of sensible heat
\vec{i}	unit vectors in x direction
I_l	phase transition rate for liquid water
I_f	phase transition rate for ice
\vec{j}	unit vectors in y direction

\vec{k}	unit vectors in z direction
\vec{K}	the relative vorticity flux vector
λ	geographical longitude
l	$2\omega \cos \varphi$
L_S	latent heat of sublimation
L_V	latent heat of vapourisation
\vec{n}	unit vector normal to the boundary of the closed region
$\nabla = \frac{\partial}{\partial x}\vec{i} + \frac{\partial}{\partial y}\vec{j} + \frac{\partial}{\partial z}\vec{k}$	gradient operator
∇_h	horizontal gradient operator
ω	vertical velocity in pressure coordinates
$\vec{\Omega}$	constant angular velocity due to earth rotation
p	pressure
p_0	pressure of reference state
φ	geographical latitude
Ψ	any mass specific quantity
$\Psi = \bar{\Psi} + \Psi'$	Reynolds average where $\bar{\Psi}$ denotes the mean value and Ψ' the deviation
$\Psi = \hat{\Psi} + \Psi''$	mass-weighted average where $\hat{\Psi}$ denotes mass-weighted mean and Ψ'' the deviation from $\hat{\Psi}$
$\vec{P}_{l,f}$	precipitation flux for liquid water and ice
$q_x = \rho_x / \rho$	mass fraction (specific content) of constituent $x = d, v, l, f$
q_v	specific humidity
Q_h	rate of diabatic heating or cooling
\vec{R}	flux density of solar and thermal radiation
R_d	gas constant of dry air
R_v	gas constant of water vapour
ρ	density
ρ_0	density of reference state
ρ_x	partial density of mixture constituent x

$\rho = \sum_x \rho_x$	total density of the air mixture
$\tau_{scatter}$	optical thickness of scattering
$\tau_{absorbr}$	optical thickness of absorption
θ	potential temperature
θ_e	equivalent potential temperature
t	time
T	temperature
T_0	temperature of reference state
\mathbb{T}	Reynolds stress tensor (turbulent flux of momentum)
u	zonal wind
u_*	threshold friction velocity
$\nu = \rho^{-1}$	specific volume
v	meridional wind
v_h	horizontal velocity
$\vec{v} = \vec{v}(u, v, w)$	velocity relative to the rotating earth
$\vec{v}_{l,f}^T$	terminal velocity of constituent l,f
w	vertical velocity
$x = d, v, l, f$	index for mixture constituent: dry air (d), water vapour (v), liquid (l), and frozen water (f)
z	height
z_0	roughness length at the surface
ζ	vertical component of vorticity (relative vorticity)

List of Abbreviations

AEJ	African Easterly Jet
AEW	African Easterly Waves
AI	Aerosol Index
AIRS	Atmospheric Infrared Sounder
AMMA	African Monsoon Multidisciplinary Analyses
AMSR-E	Advanced Microwave Scanning Radiometer - EOS
AOT	Aerosol Optical Thickness
ART	Aerosols and Reactive Trace gases
BQ	buoyancy
CALIOP	Cloud–Aerosol Lidar with Orthogonal Polarization
CALIPSO	Cloud–Aerosol Lidar and Infrared Pathfinder Satellite Observation
CAPE	Convective Available Potential Energy
CFL	Courant–Friedrich–Levi criterion
CIMSS	Cooperative Institute for Meteorological Satellite Studies
COMP	computational effects
COSMO	Consortium for Small–scale Modelling
<i>d</i>	dry
DMSP	Defense Meteorological Satellite Program
DWD	Deutscher Wetterdienst (German Weather Service)
E	East
EOS	Earth Observing System
EUMETSAT	European Organisation for the Exploitation of Meteorological Satellites

<i>f</i>	water in solid state (frozen)
Fig.	Figure
FAST	fast waves
GATE	GARP Atlantic Tropical Experiment
GARP	Global Atmospheric Research Program
GRAALS	General Radiative Algorithm Adapted to Linear-type Solutions
HADV	horizontal advection
HAPEX-Sahel	Hydrology-Atmosphere Pilot Experiment in the Sahel
HRD	Hurricane Research Division
ITD	Inter Tropical Discontinuity
IFS	Integrated Forecast System
ITF	Inter Tropical Front
IMK	Institut für Meteorologie und Klimaforschung
IMPETUS	Integratives Management Projekt für einen Effizienten und Tragfähigen Umgang mit Süßwasser in Westafrika
INT2LM	Interpolation to Lokal Model grid
ITCZ	Inter Tropical Convergence Zone
<i>l</i>	liquid
LAGRANTO	LAGRangian ANalysis TOol
LFC	Level of Free Convection
MADEsoot	Modal Aerosol Dynamics Model for Europe extended by Soot
MCM	computational mixing (horizontal diffusion)
MCS	Mesoscale Convective System
MCV	Mesoscale Convective Vortex
METEOSAT	METEOrological SATellite
MLB	lateral boundary relaxation
MMC	subgrid scale moist convection
MODIS	Moderate Resolution Imaging Spectroradiometer
MRD	Rayleigh damping

MSG	Meteosat Second Generation
MTD	turbulent mixing
N	North
NAMMA	NASA African Monsoon Multidisciplinary Analyses
NASA	National Aeronautics and Space Administration
NHC	National Hurricane Center
NOAA	National Oceanic and Atmospheric Administration
NoRadDust	COSMO-ART model run without dust–radiation interaction
PBL	Planetary Boundary Layer
PV	Potential Vorticity
PVU	Potential Vorticity Unit ($10^{-6} \text{ K kg}^{-1} \text{ m}^2 \text{ s}^{-1}$)
RAD	solar and thermal radiation
RadDust	COSMO-ART model run including the dust–radiation interaction
rhs	right hand side
S	South
SAL	Saharan Air Layer
SEVIRI	Spinning Enhanced Visible and Infrared Imager
SHL	Saharan Heat Low
SLOW	Slow modes
SQ	cloud condensation and evaporation
SRL	Saharan Residual Layer
SSM/I	Special Sensor Microwave/Imager
Tab.	Table
TOMS	Total Ozone Mapping Spectrometer
TPW	Total Precipitable Water
UTC	Universal Time Coordinated
v	vapour
VADV	vertical advection
VHT	vortical hot tower

W	West
WAM	West African Monsoon

Bibliography

- Ackermann, I. J., H. Hass, M. Memmesheimer, A. Ebel, F. B. Binkowski, and U. Shankar, 1998: Modal aerosol dynamics model for Europe: development and first application. *Atmos. Environ.*, **32**, 2981–2999.
- Alfaro, S. C. and L. Gomes, 2001: Modeling mineral aerosol production by wind erosion: emission intensities and aerosol size distributions in source areas. *J. Geophys. Res.*, **106**, 18 075–18 084.
- Arakawa, A. and V. R. Lamb, 1981: A potential enstrophy and energy conserving scheme for the shallow water equations. *Mon. Wea. Rev.*, **109**, 18–36.
- Arnault, J. and F. Roux, 2009: Case study of a developing African easterly wave: an energetic point of view. *J. Atmos. Sci.*, **66**, 2991–3020.
- , 2010: Comparison between two case studies of developing and non developing African easterly waves during NAMMA and AMMA/SOP-3: absolute vertical vorticity budget. *Mon. Wea. Rev.*, **138**, 1420–1445.
- Avila, L. A. and R. J. Pasch, 1992: Atlantic tropical systems of 1991. *Mon. Wea. Rev.*, **120**, 2688–2696.
- , 1995: Atlantic tropical systems of 1993. *Mon. Wea. Rev.*, **123**, 887–896.
- Berry, G. J. and C. D. Thorncroft, 2005: Case study of an intense African easterly wave. *Mon. Wea. Rev.*, **133**, 752–766.
- Berry, G. J., C. D. Thorncroft, and T. Hewson, 2007: African easterly waves during 2004 - Analysis using objective techniques. *Mon. Wea. Rev.*, **135**, 1251–1267.
- Bishop, C. H. and A. J. Thorpe, 1994: Potential vorticity and the electrostatics analogy: quasi-geostrophic theory. *Q. J. R. Meteorol. Soc.*, **120**, 713–731.

- Bister, M. and K. E. Emanuel, 1997: The genesis of Hurricane Guillermo: TEXMEX analyses and a modeling study. *Mon. Wea. Rev.*, **125**, 2662–2682.
- Blackadar, A. K., 1957: Boundary layer wind maxima and their significance for the growth of nocturnal inversions. *Bull. Amer. Meteor. Soc.*, **38**, 283–290.
- Bohren, C. F. and D. R. Huffman, 1983: *Absorption and Scattering of Light by Small Particles*. John Wiley and Sons, New York.
- Bolton, D., 1984: Generation and propagation of African squall lines. *Q. J. R. Meteorol. Soc.*, **110**, 695–721.
- Bou Karam, D., C. Flamant, P. Knippertz, O. Reitebuch, P. Pelon, M. Chong, and A. Dabas, 2008: Dust emissions over the Sahel associated with the West African Monsoon inter-tropical discontinuity region: a representative case study. *Q. J. R. Meteorol. Soc.*, **134**, 621–634.
- Bou Karam, D., C. Flamant, M. C. T. P. Tulet, J. Pelon, and E. Williams, 2009a: Dry cyclogenesis and dust mobilization in the inter tropical discontinuity of the West African monsoon: a case study. *J. Geophys. Res.*, **114**, D05115, doi:10.1029/2008JD010952.
- Bou Karam, D., C. Flamant, P. Tullet, J.-P. Chaboureau, A. Dabas, and M. C. Todd, 2009b: Estimate of Sahelian dust emissions in the intertropical discontinuity region of the West African monsoon. *J. Geophys. Res.*, **114**, D013106, doi:10.1029/2008JD011444.
- Braun, D., 2006: Hurricane Helene. Tropical cyclone report, Available from http://www.nhc.noaa.gov/pdf/TCR-AL082006_Helene.pdf.
- Braun, S. A. and C.-L. Shie, 2008: Examination of the influence of the Saharan air layer on hurricanes using data from TRMM, MODIS, and AIRS. Extended abstract, 28th Conference on Hurricanes and Tropical Meteorology, 28 April - 2 May 2008 Orlando, Florida, USA.
- Buckle, C., 1996: *Weather and Climate in Africa*. Addison-Wesley Longman Ltd., Harlow, U. K.
- Burpee, R. W., 1972: The origin and structure of easterly waves in the lower troposphere of North Africa. *J. Atmos. Sci.*, **29**, 77–90.

-
- , 1974: Characteristics of North African easterly waves during the summers of 1968 and 1969. *J. Atmos. Sci.*, **31**, 1556–1570.
- , 1975: Some features of synoptic-scale waves based on a compositing analysis of GATE data. *Mon. Wea. Rev.*, **103**, 921–925.
- Caniaux, G., J.-L. Redelsperger, and J.-P. Lafore, 1994: A numerical study of the stratiform region of a fast-moving squall line. Part I: General description and water and heat budgets. *J. Atmos. Sci.*, **51**, 2046–2074.
- Carlson, T. N., 1969a: Some remarks on African disturbances and their progress over the tropical Atlantic. *Mon. Wea. Rev.*, **97**, 716–726.
- , 1969b: Synoptic histories of three African disturbances that developed into Atlantic hurricanes. *Mon. Wea. Rev.*, **97**, 256–276.
- Carlson, T. N. and S. G. Benjamin, 1980: Radiative heating rates for Saharan dust. *J. Atmos. Sci.*, **37**, 193–213.
- Carlson, T. N. and J. M. Prospero, 1972: The large-scale movement of Saharan air outbreaks over the northern equatorial Atlantic. *J. Appl. Meteor.*, **11**, 283–297.
- Chaboureau, J.-P., S. Evan, A.-S. Daloz, and F. Roux, 2005: Numerical simulation of the 15-17 August 2004 West-African mesoscale convective system. Proceedings, 1st AMMA International Conference, Dakar, Senegal, 28 November - 4 December 2005.
- Charney, J. G. and M. Stern, 1962: On the stability of internal baroclinic jets in a rotating atmosphere. *J. Atmos. Sci.*, **19**, 159–172.
- Chatenet, B., B. Marticorena, L. Gomes, and G. Bergametti, 1996: Assessing the micro-ped size distribution of desert soils erodible by wind. *Sedimentology*, **43**, 901–911.
- Conzemius, R. J. and M. T. Montgomery, 2009: Clarification on the generation of absolute and potential vorticity in mesoscale convective vortices. *Atmos. Chem. Phys.*, **9**, 7591–7605.
- Cook, K. H., 1999: Generation of the African easterly jet and its role in determining West African precipitation. *J. Climate*, **12**, 1165–1184.

- Cram, T. M., M. T. Montgomery, and R. F. A. Hertenstein, 2002: Early evolution of vertical vorticity in a numerically simulated idealized convective line. *J. Atmos. Sci.*, **59**, 2113–2127.
- Crank, J. and P. Nicolson, 1947: A practical method for numerical evaluation of solutions of partial differential equations of the heat conduction type. *Camb. Phil. Soc.*, **43**, 50–67.
- Davies, H. C., 1976: A lateral boundary formulation for multi-level prediction models. *Q. J. R. Meteorol. Soc.*, **102**, 405–418.
- , 1983: Limitations of some common lateral boundary schemes used in regional NWP models. *Mon. Wea. Rev.*, **111**, 1002–1012.
- Davis, C. A. and T. J. Galarneau, 2009: The vertical structure of mesoscale convective vortices. *J. Atmos. Sci.*, **66**, 686–704.
- Davis, C. A. and M. L. Weisman, 1994: Balanced dynamics of mesoscale vortices produced in simulated convective systems. *J. Atmos. Sci.*, **51**, 2005–2030.
- Diaz, H. F., T. N. Carlson, and J. M. Prospero, 1976: A study of the structure and dynamics of the Saharan air layer over the northern equatorial Atlantic during BOMEX. Tech. Memo. ERL WMPO-32, National Hurricane and Experimental Meteorology Laboratory NOAA.
- Diongue, A., J.-P. Lafore, J.-L. Redelsperger, and R. Roca, 2002: Numerical study of a Sahelian synoptic weather system: initiation and mature stages of convection and its interaction with the large-scale dynamics. *Q. J. R. Meteorol. Soc.*, **128**, 1899–1927.
- Doms, G., J. Förstner, E. Heise, H.-J. Herzog, M. Raschendorfer, R. Schrodin, T. Reinhardt, and G. Vogel, 2005: A description of the nonhydrostatic regional model LM. Part II: Physical parameterization. COSMO documentation, Deutscher Wetterdienst, Offenbach, Germany, www.cosmo-model.org.
- Doms, G. and U. Schättler, 2002: A description of the nonhydrostatic regional model LM. Part I: Dynamics and Numerics. COSMO documentation, Deutscher Wetterdienst, Offenbach, Germany, www.cosmo-model.org.

-
- Dudhia, J., M. W. Moncreiff, and D. W. K. So, 1987: The two-dimensional dynamics of West African squall lines. *Q. J. R. Meteorol. Soc.*, **131**, 121–146.
- Dunion, J. P. and C. S. Velden, 2004: The impact of the Saharan air layer on the Atlantic tropical cyclone activity. *Bull. Amer. Meteor. Soc.*, **85**, 353–365.
- Duvel, J., 1990: Convection over tropical Africa and the Atlantic Ocean during northern summer. Part II: Modulation by easterly waves. *Mon. Wea. Rev.*, **118**, 1855–1868.
- Eldridge, R. H., 1957: A synoptic study of West African disturbance lines. *Q. J. R. Meteorol. Soc.*, **83**, 303–314.
- Engelstaedter, S., I. Tegen, and R. Washington, 2006: North African dust emissions and transport. *Earth-Science Reviews*, **79**, 73–100.
- Engelstaedter, S. and R. Washington, 2007: Atmospheric controls on the annual cycle of North African dust. *J. Geophys. Res.*, **112**, D03 103, doi:10.1029/2006JD007195.
- Ertel, H., 1942: Ein neuer hydrodynamischer Wirbelsatz. *Meteorol. Z.*, **59**, 277–281.
- Evan, A. T., J. Dunion, J. A. Foley, A. K. Heidinger, and C. S. Velden, 2006a: New evidence for a relationship between Atlantic tropical cyclone activity and African dust outbreaks. *Geophys. Res. Lett.*, **33**, 9813, doi:10.1029/2006GL026408.
- Evan, A. T., A. K. Heidinger, and P. Knippertz, 2006b: Analysis of winter dust activity off the coast of West Africa using a new 24-year over-water advanced very high resolution radiometer satellite dust climatology. *Geophys. Res. Lett.*, **111**, 2210, doi:10.1029/2005GL006336.
- Fan, S. M., L. W. Horowitz, H. Levi, and W. J. Moxim, 2004: Impact on air pollution on wet deposition of mineral dust aerosols. *Geophys. Res. Lett.*, **32**, L02 104, doi:10.1029/2003GL0118501.
- Fink, A. H., 2006: Das westafrikanische Monsunsystem. *Promet*, **32**, 114–122.
- Fink, A. H. and A. Reiner, 2003: Spatio-temporal variability of the relation between African easterly waves and West African squall lines in 1998 and 1999. *J. Geophys. Res.*, **108**, 4332.

- Fink, A. H., D. G. Vicent, and V. Ermert, 2006: Rainfall types in the West African Sudanian zone during the summer monsoon 2002. *Mon. Wea. Rev.*, **134**, 2143–2164.
- Flamant, C., J.-P. Chaboureau, D. J. Parker, C. M. Taylor, J.-P. Cammas, O. Bock, F. Timouk, and J. Pelon, 2007: Airborne observations of the impact of a convective system on the planetary boundary layer thermodynamics and aerosol distribution in the West African monsoon inter-tropical discontinuity region. *Q. J. R. Meteorol. Soc.*, **133**, 1–28.
- Flamant, C., C. Lavaysse, M. C. Todd, J.-P. Chaboureau, and J. Pelon, 2009: Multi-platform observations of a representative springtime case of Bodélé and Sudan dust emission, transport and scavenging over West Africa. *Q. J. R. Meteorol. Soc.*, **135**, 413–430.
- Fortune, M., 1980: Properties of African squall lines inferred from time-lapse satellite imagery. *Mon. Wea. Rev.*, **108**, 153–168.
- Frank, N. L., 1970: Atlantic tropical systems of 1969. *Mon. Wea. Rev.*, **98**, 307–314.
- Fritsch, J. M., J. D. Murphy, and J. S. Kain, 1994: Warm core vortex amplification over land. *J. Atmos. Sci.*, **51**, 1780–1807.
- Gamache, J. F. and R. A. Houze, 1982: Mesoscale air motions associated with a tropical squall line. *Mon. Wea. Rev.*, **110**, 118–135.
- Gantner, L. and N. Kalthoff, 2010: Sensitivity of a modelled life cycle of a mesoscale convective system to soil conditions over West Africa. *Q. J. R. Meteorol. Soc.*, **136(s1)**, 471–482.
- Goutorbe, J. P., T. Lebel, A. J. Dolman, J. H. C. Gash, P. Kabat, Y. H. Kerr, B. Monteny, S. D. Prince, J. N. M. Stricker, A. Tinga, and J. S. Wallace, 1997: An overview of HAPEX-Sahel: a study in climate and desertification. *J. Hydrol.*, **105**, 915–929.
- Grams, C. M., 2008: The Atlantic inflow: atmosphere-land-ocean interaction at the south western edge of the Saharan heat low. Master's thesis, Institut für Meteorologie und Klimaforschung, Universität Karlsruhe, Karlsruhe, Germany.
- Grams, C. M., S. C. Jones, J. Marsham, D. J. Parker, J. M. Haywood, and V. Heuveline, 2010: The Atlantic inflow to the Saharan heat low: observations and modelling. *Q. J.*

-
- R. Meteorol. Soc.*, **136(s1)**, 125–140.
- Gray, W. M., 1968: Global view of the origins of tropical disturbances and storms. *Mon. Wea. Rev.*, **96**, 669–700.
- , 1979: Hurricanes: their formation, structure and likely role in the tropical circulation. *Meteorology Over Tropical Oceans*, Shaw, D. B., Ed., Roy. Meteor. Soc., James Glaisher House, Grenville Place, Bracknell, Berkshire, RG12 1BX, 155–218.
- Hadley, G., 1735: Concerning the Cause of the General Trade-Winds. *Philos. Trans. Roy. Soc. London*, **39**, 58–62.
- Hall, N. M. J., G. N. Kiladis, and C. D. Thorncroft, 2006: Three-dimensional structure and dynamics of African easterly waves. Part II: Dynamic Modes. *J. Atmos. Sci.*, **63**, 2231–2245.
- Harr, P. A., R. L. Elsberry, and J. C. L. Chan, 1996: Transformation of a large monsoon depression to a tropical storm during TCM-93. *Mon. Wea. Rev.*, **124**, 2625–2643.
- Hastenrath, S., 1994: *Climate dynamics of the Tropics: an updated edition of climate and circulation of the Tropics*. Kluwer Academic Publishers, 488 pp.
- Haynes, P. H. and M. E. McIntyre, 1987: On the evolution of vorticity and potential vorticity in the presence of diabatic heating and frictional or other forces. *J. Atmos. Sci.*, **44**, 828–841.
- , 1990: On the conservation and impermeability theorems for potential vorticity. *J. Atmos. Sci.*, **47**, 2021–2031.
- Haywood, J., P. Francis, S. Osborne, M. Glew, N. Loeb, D. T. E. Highwood, G. Myhre, P. Formenti, and E. Hirst, 2003: Radiative properties and direct radiative effect of Saharan dust measured by the C-130 aircraft during SHADE: 1. Solar spectrum. *J. Geophys. Res.*, **108**, 8577, doi:10.1029/2002JD002687.
- Helmert, J., B. Heinold, I. Tegen, O. Hellmuth, and M. Wendisch, 2007: On the direct and semidirect effects of Saharan dust over Europe: a modeling study. *J. Geophys. Res.*, **112**, D13 208, doi:10.1029/2006JD007444.

- Hendricks, E. A., M. T. Montgomery, and C. A. Davis, 2004: The role of “vortical” hot towers in formation of tropical cyclone Diana (1984). *J. Atmos. Sci.*, **61**, 1209–1232.
- Herbert, F., 2007: The physics of potential vorticity. *Meteorol. Z.*, **16**, 243–254.
- Hill, C. M. and Y.-L. Lin, 2003: Initiation of a mesoscale convective complex over the Ethiopian Highlands preceding the genesis of Hurricane Alberto (2000). *Geophys. Res. Lett.*, **30**, 1232–1236.
- Hodges, K. I. and C. D. Thorncroft, 1997: Distribution and statistics of African mesoscale convective weather systems based on the ISCCP Meteosat imagery. *Mon. Wea. Rev.*, **125**, 2821–2837.
- Hoose, C., 2004: Numerische Simulation zur Ausbreitung von Mineralstaub auf der regionalen Skala. Master’s thesis, Institut für Meteorologie und Klimaforschung, Universität Karlsruhe, Karlsruhe, Germany.
- Hoose, C., U. Lehmann, R. Erdin, and I. Tegen, 2008: The global influence of dust mineralogical composition on heterogeneous ice nucleation in mixed-phase clouds. *Environ. Res. Lett.*, **3**, doi:10.1088/1748-9326/3/2/025003.
- Hoskins, B. J., M. E. McIntyre, and A. W. Robertson, 1985: On the use and significance of isentropic potential vorticity maps. *Q. J. R. Meteorol. Soc.*, **111**, 877–946.
- Houze, R. A., 1977: Structure and dynamics of a tropical squall-line system. *Mon. Wea. Rev.*, **105**, 1540–1567.
- , 2004: Mesoscale Convective Systems. *Rev. Geophys.*, **42**, 1–43.
- Houze, R. A. and A. K. Betts, 1981: Convection in GATE. *Rev. Geophys.*, **19**, 541–576.
- Jacobsen, I. and E. Heise, 1982: A new economic method for the computation of the surface temperature in numerical models. *Beitr. Phys. Atm.*, **55**, 128–141.
- Janicot, S. and B. Sultan, 2006: The large-scale context on the West African Monsoon in 2006. *Newsletter of the Climate Variability and Predictability Programme (CLIVAR)*, **41**, 11–17.
- Jenkins, G. S., A. S. Pratt, and A. Heymsfield, 2008: Possible linkage between Saharan dust and tropical cyclone rain band invigoration in the eastern Atlantic during

-
- NAMMA-06. *Geophys. Res. Lett.*, **35**, L08 815, doi:10.1029/2008GL034 072.
- Jones, C., N. Mahowald, and C. Luo, 2003: The role of easterly waves on African dust transport. *J. Climate*, **16**, 3617–3628.
- Jones, T. A., D. J. Cecil, and J. Dunion, 2007: The environmental and inner-core conditions governing the intensity of Hurricane Erin (2001). *Wea. Forecasting*, **22**, 708–2725.
- Karyampudi, V. M. and T. Carlson, 1988: Analysis and numerical simulations of the Saharan air layer and its effects on easterly wave disturbances. *J. Atmos. Sci.*, **45**, 3102–3136.
- Karyampudi, V. M., S. P. Palm, J. A. Regan, H. Fang, W. B. Grant, R. M. Hoff, C. Moulin, H. F. Pierce, O. Torres, E. V. Browell, and S. H. Melfi, 1999: Validation of the Saharan dust plume conceptual model using Lidar, Meteosat, and ECMWF data. *Bull. Amer. Meteor. Soc.*, **80**, 1045–1075.
- Karyampudi, V. M. and H. F. Pierce, 2002: Synoptic-scale influence of the Saharan air layer on tropical cyclone genesis over the Eastern Atlantic. *Mon. Wea. Rev.*, **130**, 3100–3128.
- Kessler, E., 1969: On the distribution and continuity of water substance in atmospheric circulation models. *Meteor. Monographs*, **10**, Americ. Meteor. Soc. Boston, MA.
- Kieu, C. Q. and D.-L. Zhang, 2009: Genesis of Tropical Storm Eugene (2005) from merging vortices associated with ITCZ breakdowns. Part I: Observational and modeling analyses. *J. Atmos. Sci.*, **65**, 3419–3439.
- Kiladis, G. N., C. D. Thorncroft, and N. M. J. Hall, 2006: Three-dimensional structure and dynamics of African easterly waves. Part I: Observations. *J. Atmos. Sci.*, **63**, 2212–2230.
- Klemp, J. B., 1987: Dynamics of tornadic thunderstorms. *Ann. Rev. Fluid Mech.*, **19**, 369–402.
- Klemp, J. B. and R. B. Wilhelmson, 1978: The simulation of three-dimensional convective storm dynamics. *J. Atmos. Sci.*, **35**, 1070–1096.

- Klüpfel, V., 2008: Analyse eines Staubsturms über Westafrika anhand von Modellergebnissen (COSMO-ART) und Messungen (GERBILS). Seminararbeit, Institut für Meteorologie und Klimaforschung, Universität Karlsruhe, Karlsruhe, Germany.
- Knievel, J. C. and R. H. Johnson, 2002: The kinematic of a midlatitude, continental mesoscale convective system and its mesoscale vortex. *Mon. Wea. Rev.*, **130**, 1749–1770.
- Knippertz, P., 2008: Dust emissions in the West African heat trough - the role of the diurnal cycle and of extratropical disturbances. *Meteorol. Z.*, **17**, 001–011.
- Knippertz, P., C. Deutscher, K. Kandler, T. Müller, O. Schulz, and L. Schütz, 2007: Dust mobilization due to density currents in the Atlas region: observations from the SAMUM 2006 field campaign. *J. Geophys. Res.*, **111**, D21 109, doi:10.1029/2007JD008 774.
- Knippertz, P. and A. Fink, 2006: Synoptic and dynamic aspects of an extreme springtime Saharan dust outbreak. *Q. J. R. Meteorol. Soc.*, **132**, 1153–1177.
- Kuo, Y.-H., R. J. Reed, and S. Low-Nam, 1992: Thermal structure and airflow in a model simulation of an occluded marine cyclone. *Mon. Wea. Rev.*, **120**, 2280–2297.
- Lafore, J.-P. and M. W. Moncrieff, 1989: A numerical investigation of the organization and interaction of the convective and stratiform regions of tropical squall lines. *J. Atmos. Sci.*, **58**, 1079–1090.
- Lafore, J.-P., J.-L. Redelsperger, and G. Jaubert, 1988: Comparison between a three-dimensional simulation and dopplar radar data of a tropical squall line: transport of mass, heat and moisture. *J. Atmos. Sci.*, **45**, 3483–3500.
- Laing, A. and J. M. Fritsch, 1993: Mesoscale convective complexes in Africa. *Mon. Wea. Rev.*, **121**, 2254–2263.
- Laing, A., V. Levizzani, and R. Carbone, 2005: The diurnal cycle and propagation of precipitating convection in Africa. Proceedings, 1st AMMA International Conference, Dakar, Senegal, 28 November - 4 December 2005.
- Landsea, C. W., 1993: A climatology of intense (or major) Atlantic hurricanes. *Mon. Wea. Rev.*, **121**, 1703–1713.

-
- Landsea, C. W., G. D. Bell, W. M. Gray, and S. B. Goldenberg, 1998: Extremely active 1995 Atlantic hurricane season: environmental conditions and verification of seasonal forecasts. *Mon. Wea. Rev.*, **126**, 1174–1193.
- Lau, K. M. and K. M. Kim, 2007: Cooling of the Atlantic by Saharan dust. *Geophys. Res. Lett.*, **34**, L23 811, doi:10.1029/2007GL031 538.
- Laurent, H., N. D’Amato, and T. Lebel, 1998: How important is the contribution of the mesoscale convective complexes to the Sahelian rainfall. *Phys. Chem. Earth.*, **23**, 629–633.
- Lin, Y.-H., K. I. Robertson, and C. M. Hill, 2005: Origin and propagation of a disturbance associated with an African easterly wave as a precursor of Hurricane Alberto (2000). *Mon. Wea. Rev.*, **133**, 3276–3298.
- Lu, H. and Y. Shao, 1999: A new model for dust emission by saltation bombardment. *J. Geophys. Res.*, **104**, 16 827–16 841.
- Machado, L., J.-P. Duvel, and M. Desbois, 1993: Diurnal variations and modulations by easterly waves of the size distribution of convective cloud clusters over West Africa and the Atlantic Ocean. *Mon. Wea. Rev.*, **121**, 37–49.
- Maddox, R., 1980: Mesoscale convective complexes. *Bull. Amer. Meteor. Soc.*, **61**, 1374–1387.
- Mallet, M., P. Tulet, D. Serça, F. Solmon, O. D. J. Pelon, V. Pont, and O. Thouron, 2009: Impact of dust aerosols on the radiative budget, surface heat fluxes, heating rate profiles and convective activity over West Africa during March 2006. *Atmos. Chem. Phys.*, **9**, 7143–7160.
- Marshall, J. H., D. J. Parker, C. M. Grams, C. M. Taylor, and J. M. Haywood, 2008: Uplift of Saharan dust south of the intertropical discontinuity. *J. Geophys. Res.*, **113**, doi:10.1029/2008JD009 844.
- Mathon, V. and H. Laurent, 2001: Life cycle of Sahelian mesoscale convective cloud systems. *Q. J. R. Meteorol. Soc.*, **127**, 337–406.
- Mathon, V., H. Laurent, and T. Lebel, 2002: Mesoscale convective system rainfall in the Sahel. *J. Appl. Meteor.*, **41**, 1081–1092.

- McGarry, M. M. and R. J. Reed, 1978: Diurnal variations in convective activity and precipitation during Phase II and III of GATE. *Mon. Wea. Rev.*, **106**, 101–113.
- Mellor, G. L. and T. Yamada, 1974: A hierarchy of turbulent closure models for planetary boundary layers. *J. Atmos. Sci.*, **31**, 1791–1806.
- Messenger, C. J., D. J. Parker, O. Reitebuch, C. M. Taylor, and J. M. Haywood, 2010: Structure and dynamics of the Saharan heat low during the West African monsoon 2006 onset: observations and analyses from the research flights of 14 and 17 July 2006. *Q. J. R. Met. Soc.*, **136(s1)**, 107–124.
- Mohr, K. I. and C. D. Thorncroft, 2006: Intense convective systems in West Africa and their relationship to the African easterly jet. *Q. J. R. Meteorol. Soc.*, **132**, 163–174.
- Montgomery, M. T. and J. Enagonio, 1998: Tropical cyclogenesis via convectively forced vortex Rossby waves in a three-dimensional quasi-geostrophic model. *J. Atmos. Sci.*, **55**, 3176–3207.
- Montgomery, M. T. and R. J. Kallenbach, 1997: A theory of vortex Rossby waves and its application to spiral bands and intensity changes in hurricanes. *Q. J. R. Meteorol. Soc.*, **123**, 435–465.
- Montgomery, M. T., M. E. Nicholls, T. M. Cram, and A. B. Saunders, 2006: A vortical hot tower route to tropical cyclogenesis. *J. Atmos. Sci.*, **63**, 355–386.
- Nicholson, S. and J. Grist, 2003: The seasonal evolution of the atmospheric circulation over West Africa and equatorial Africa. *J. Climate*, **16**, 1013–1030.
- Omotosho, J. B., 2003: The separate contributions of squall lines, thunderstorms and the monsoon to the total rainfall in Nigeria. *J. Climatol.*, **5**, 543–552.
- Paradis, D., J.-P. Lafore, J.-L. Redelsperger, and V. Balaji, 1995: African easterly waves and convection. Part I: Linear simulations. *J. Atmos. Sci.*, **52**, 1657–1679.
- Parker, D. J., R. Burton, A. Diongue-Niang, R. Ellis, M. Felton, C. M. Taylor, C. D. Thorncroft, P. Bessemoulin, and A. Tompkins, 2005a: The diurnal cycle of the West African monsoon circulation. *Q. J. R. Meteorol. Soc.*, **131**, 2839–2860.

-
- Parker, D. J., C. D. Thorncroft, R. Burton, and A. Diongue-Niang, 2005b: Analysis of the African easterly jet using aircraft observations from the JET2000 experiment. *Q. J. R. Meteorol. Soc.*, **131**, 1461–1482.
- Payne, S. W. and M. M. McGarry, 1977: The relationship of satellite inferred convective activity to easterly waves over West Africa and the adjacent ocean during phase III of GATE. *Mon. Wea. Rev.*, **105**, 413–420.
- Petterssen, S., 1956: *Weather analysis and forecasting. Vol. I, Motion and motion systems.* McGraw-Hill.
- Prospero, J. M. and T. N. Carlson, 1972: Vertical and areal distributions of Saharan dust over the western equatorial North Atlantic Ocean. *J. Geophys. Res.*, **77**, 5255–5265.
- Prospero, J. M., P. Ginoux, O. Torres, S. E. Nicholson, and T. E. Gill, 2002: Environmental characterization of global sources of atmospheric soil dust identified with the Nimbus 7 Total Ozone Mapping Spectrometer (TOMS) absorbing aerosol product. *Rev. Geophys.*, **40**, 1002, doi:10.1029/2000RG000095.
- Pytharoulis, I. and C. D. Thorncroft, 1999: The low-level structure of African easterly waves in 1995. *Mon. Wea. Rev.*, **127**, 2266–2280.
- Raymond, D. J., 1992: Nonlinear balance and potential-vorticity thinking at large Rossby number. *Q. J. R. Meteorol. Soc.*, **118**, 987–1015.
- Raymond, D. J. and H. Jiang, 1990: A theory for long-lived mesoscale convective systems. *J. Atmos. Sci.*, **47**, 3067–3077.
- Reale, O., W. K. Lau, K.-M. Kim, and E. Brin, 2009: Atlantic tropical cyclogenetic processes during SOP-3 NAMMA in the GEOS-5 global data assimilation and forecast system. *J. Atmos. Sci.*, **66**, 3563–5253.
- Redelsperger, J.-L., A. Diongue, A. Diedhiou, J.-P. Ceron, M. Diop, J.-F. Gueremy, and J.-P. Lafore, 2002: Multi-scale description of a Sahelian synoptic weather system representative of the West African monsoon. *Q. J. R. Meteorol. Soc.*, **128**, 1229–1257.
- Redelsperger, J.-L., C. D. Thorncroft, A. Diedhiou, T. Lebel, D. J. Parker, and J. Polcher, 2006: African Monsoon, Multidisciplinary Analysis (AMMA): an international research project and field campaign. *Bull. Amer. Meteor. Soc.*, **87**, 1739–1746.

- Reed, R. J. and K. D. Jaffe, 1981: Diurnal variation of summer convection over West Africa and the tropical Eastern Atlantic during 1974 and 1978. *Mon. Wea. Rev.*, **109**, 2527–2534.
- Reed, R. J., D. C. Norquist, and E. E. Recker, 1977: Structure and properties of synoptic-scale wave disturbances as observed during phase III of GATE. *Mon. Wea. Rev.*, **105**, 317–333.
- Reed, R. J., M. T. Stoelinga, and Y.-H. Kua, 1992: A model-aided study of the origin and evolution of the anomalously high potential vorticity in the inner region of a rapidly deepening marine cyclone. *Mon. Wea. Rev.*, **120**, 893–913.
- Riehl, H., 1954: *Tropical Meteorology*. McGraw-Hill, 329 pp.
- Riehl, H. and J. S. Malkus, 1958: On the heat balance in the equatorial trough zone. *Geophysica*, **6**, 503–538.
- Riemer, N., H. Vogel, B. Vogel, and F. Fiedler, 2003: Modelling aerosols on the mesoscale- γ : treatment of soot aerosol and its radiative effects. *J. Geophys. Res.*, **108**, D19, doi:10.1029/2003JD003448.
- Rinke, R., 2008: Parametrisierung des Auswaschens von Aerosolpartikeln durch Niederschlag. Ph.D. thesis, Institut für Meteorologie und Klimaforschung, Universität/Forschungszentrum Karlsruhe, Karlsruhe, Germany.
- Ritchie, E. A. and G. Holland, 1997: Scale interaction during the formation of typhoon Irving. *Mon. Wea. Rev.*, **125**, 1377–1396.
- Ritchie, E. A., J. Simpson, W. T. Liu, J. Halverson, C. Velden, K. F. Brueske, and H. Pierce, 2003: Present day satellite technology for hurricane research: a closer look at formation and intensification scale interaction during the formation of typhoon Irving. *Hurricane! Coping With Disaster*, Simpson, R., Ed., AGU, Washington, D. C., chap. 12, 249–289.
- Ritter, B. and J.-F. Geleyn, 1992: A comprehensive radiation scheme for numerical weather prediction models with potential application in climate models. *Mon. Wea. Rev.*, **120**, 303–325.

-
- Rotunno, R., J. B. Klemp, and M. L. Weisman, 1988: A theory for strong, long-lived squall lines. *J. Atmos. Sci.*, **45**, 463–458.
- Rowell, D. and J. Milford, 1993: On the generation of African squall lines. *J. of Climatol.*, **6**, 1181–1193.
- Schepanski, K., I. Tegen, B. Laurent, B. Heinold, and A. Macke, 2007: A new Saharan dust source activation frequency map derived from MSG-SEVIRI IR-channels. *Geophys. Res. Lett.*, **34**, L18 803, doi:10.1029/2007GL030 168.
- Schmidt, J. M. and W. R. Cotton, 1990: Interactions between upper and lower tropospheric gravity waves on squall line structure and maintenance. *J. Atmos. Sci.*, **47**, 1205–1222.
- Schwendike, J. and S. C. Jones, 2010: Convection in an African Easterly Wave over West Africa and the eastern Atlantic: a model case study of Helene (2006). *Q. J. R. Meteorol. Soc.*, **136(s1)**, 364–396.
- Shu, S. and L. Wu, 2009: Analysis of the influence of Saharan air layer on tropical cyclone intensity using AIRS/Aqua data. *Geophys. Res. Lett.*, **36**, L09 809, doi:10.1029/2009GL037 634.
- Simpson, J., E. A. Ritchie, G. J. Holland, J. Halverson, and S. Stewart, 1997: Mesoscale interactions in tropical cyclone genesis. *Mon. Wea. Rev.*, **125**, 2643–2661.
- Slinn, S. A. and W. G. N. Slinn, 1980: Prediction for particle deposition on natural waters. *Atmos. Environ.*, **27**, 2495–2502.
- Sommeria, G. and J. Testud, 1984: COPT 81. A field experiment designed for the study of dynamics and electrical activity of deep convection in continental tropical regions. *Bull. Amer. Meteor. Soc.*, **65**, 4–10.
- Stanelle, T., 2008: Wechselwirkungen von Mineralstaubpartikeln mit thermodynamischen und dynamischen Prozessen in der Atmosphäre über Westafrika. Ph.D. thesis, Institut für Meteorologie und Klimaforschung, Universität/Forschungszentrum Karlsruhe, Karlsruhe, Germany.
- Stanelle, T., B. Vogel, H. Vogel, D. Bäumer, and C. Kottmeier, 2010: Feedback between dust particles and atmospheric processes over West Africa in March 2006 and June

2007. *Atmos. Chem. Phys. Discuss.*, **10**, 7553–7599.
- Stohl, A., L. Haimberger, M. P. Scheele, and H. Wernli, 2001: An intercomparison of three trajectory models. *Meteorol. Appl.*, **8**, 127–135.
- Sun, D., W. K. M. Lau, M. Kafatos, Z. Boybeyi, G. Leptoukh, C. Yang, and R. Yang, 2009: Numerical simulations on the impacts of the Saharan air layer on Atlantic tropical cyclone development. *J. Climate*, **22**, 6230–6250.
- Tegen, I., B. Heinold, M. Todd, J. Helmert, R. Washington, and O. Dubovik, 2006: Modeling soil dust aerosol in the Bodélé depression during BoDEx campaign. *Atmos. Chem. Phys.*, **6**, 4171–4211.
- Tegen, I., A. A. Lacis, and I. Fung, 1996: The influence on climate forcing of mineral aerosols from disturbed soils. *Nature*, **380**, 419–422.
- Thorncroft, C. D., 1995: An idealized study of African easterly waves. Part III: More realistic basic states. *Q. J. R. Meteorol. Soc.*, **121**, 1589–1614.
- Thorncroft, C. D. and M. Blackburn, 1999: Maintenance of the African easterly jet. *Q. J. R. Meteorol. Soc.*, **125**, 763–786.
- Thorncroft, C. D. and K. I. Hodges, 2001: African easterly wave variability and its relationship to tropical cyclone activity. *J. Climate*, **14**, 1166–1179.
- Thorncroft, C. D. and B. Hoskins, 1994a: An idealized study of African easterly waves. Part I: A linear view. *Q. J. R. Meteorol. Soc.*, **120**, 953–982.
- Thorncroft, C. D. and B. J. Hoskins, 1994b: An idealized study of African easterly waves. Part II: A nonlinear view. *Q. J. R. Meteorol. Soc.*, **120**, 983–1015.
- Thorncroft, C. D., D. J. Parker, R. R. Burton, M. Diop, J. H. Ayers, H. Barjat, S. Devereau, A. Diongue, R. Dumelow, D. R. Kindred, N. M. Price, M. Saloum, C. M. Taylor, and A. M. Tompkins, 2003: The JET2000 Project: aircraft observations of the African easterly jet and African easterly waves. *Bull. Amer. Meteor. Soc.*, **84**, 337–351.
- Tiedtke, M., 1989: A comprehensive mass flux scheme for cumulus parameterization in large-scale models. *Mon. Wea. Rev.*, **117**, 1779–1800.

-
- Todd, M. C., S. Raghavan, G. Lizcano, and P. Knippertz, 2008: Regional model simulations of the Bodélé low-level jet of northern Chad during the Bodélé Dust Experiment (BoDEx 2005). *J. Climate*, **21**, 995–1012.
- Tory, K. J., N. E. Davidson, and M. T. Montgomery, 2007: Prediction and diagnosis of tropical cyclone formation in an NWP system. Part III: Diagnosis of developing and nondeveloping storms. *J. Atmos. Sci.*, **64**, 3195–3213.
- Tory, K. J., M. T. Montgomery, and N. E. Davidson, 2006a: Prediction and diagnosis of tropical cyclone formation in an NWP system. Part I: The critical role of vortex enhancement in deep convection. *J. Atmos. Sci.*, **63**, 3077–3090.
- Tory, K. J., M. T. Montgomery, N. E. Davidson, and J. D. Kepert, 2006b: Prediction and diagnosis of tropical cyclone formation in an NWP system. Part II: A diagnosis of tropical cyclone formation. *J. Atmos. Sci.*, **63**, 3077–3090.
- Vogel, B., C. Hoose, H. Vogel, and C. Kottmeier, 2006: A model of dust transport applied to the Dead Sea area. *Meteorol. Z.*, **15**, doi: 10.1127/0941-2948/2006/0168.
- Vogel, B., H. Vogel, D. Bäumer, M. Bangert, K. Lundgren, R. Rinke, and T. Stanelle, 2009: The comprehensive model system COSMO-ART - radiative impact of aerosol on the state of the atmosphere on the regional scale. *Atmos. Chem. Phys.*, **9**, 8661–8680.
- Washington, R. and M. C. Todd, 2006: Atmospheric controls on mineral dust emission from the Bodélé depression, Chad: intraseasonal to interannual variability and the role of the low level jet. *Geophys. Res. Lett.*, **32**, L17701, doi:10.1029/2005GL023597.
- Weisman, M. L., 1993: The genesis of severe, long-lived bow echos. *J. Atmos. Sci.*, **50**, 645–670.
- Weisman, M. L. and C. A. Davis, 1998: Mechanisms for the generation of mesoscale vortices within quasi-linear convective systems. *J. Atmos. Sci.*, **55**, 2603–2622.
- Weisman, M. L., J. B. Klemp, and R. Rotunno, 1988: Structure and evolution of numerically simulated squall lines. *J. Atmos. Sci.*, **45**, 1990–2013.
- Weisman, M. L. and R. Rotunno, 2004: “A theory for strong long-lived squall lines” revisited. *J. Atmos. Sci.*, **61**, 361–382.

- Wernli, H., 1997: A Lagrangian-based analysis of extratropical cyclones. II: A detailed case study. *Q. J. R. Meteorol. Soc.*, **123**, 1677–1706.
- Wernli, H. and H. C. Davies, 1997: A Lagrangian-based analysis of extratropical cyclones. I: The method and some applications. *Q. J. R. Meteorol. Soc.*, **123**, 467–489.
- Whitaker, J. S., L. W. Uccellini, and K. F. Brill, 1988: A model-based diagnostic study of the rapid development phase of the President’s Day cyclone. *Mon. Wea. Rev.*, **116**, 2337–2365.
- Willoughby, H. E. and M. E. Rahn, 2004: Parametric presentation of the primary hurricane vortex. Part I: Observations and evaluation of the Holland (1980) model. *Mon. Wea. Rev.*, **132**, 3033–3048.
- Winker, D. M. and B. Hunt, 2007: First results from CALIOP, Proc. Third Symposium on LIDAR Atmospheric Applications. 87th AMS Annula Meeting, San Antonio Texas, 15-18 January 2007, American Meteorological Society.
- Wong, S. and A. E. Dessler, 2005: Supression of deep convection over the tropical North Atlantic by the Saharan air layer. *Geophys. Res. Lett.*, **32**, 9808, doi:10.1029/2004GL022295.
- Yanai, M., S. Esbensen, and J. H. Chu, 1973: Determination of bulk properties of tropical cloud clusters from large-scale heat and moisture budgets. *J. Atmos. Sci.*, **30**, 611–627.
- Zhang, D.-L. and N. Bao, 1996a: Oceanic cyclogenesis as induced by a mesoscale convective system moving offshore. Part I: A 90-h real-data simulation. *Mon. Wea. Rev.*, **124**, 1449–1469.
- , 1996b: Oceanic cyclogenesis as induced by a mesoscale convective system moving offshore. Part II: Genesis and thermodynamic transformation. *Mon. Wea. Rev.*, **124**, 2206–2226.
- Zhang, H., G. M. McFarquhar, S. M. Saleeby, and W. R. Cotton, 2007: Impact of Saharan dust as CCN on the evolution of an idealized tropical cyclone. *Geophys. Res. Lett.*, **34**, doi:10.1029/2007GL029876.
- Zipser, E., 1977: Mesoscale and convective-scale downdrafts as distinct components of the squall line structure. *Mon. Wea. Rev.*, **105**, 1568–1589.

Acknowledgments

I would like to express my gratitude to my supervisor, Prof Sarah Jones, for suggesting this exiting topic and for her guidance, faith, and constant support. The many hours Sarah Jones was available for discussion are greatly appreciated and were always a huge source of motivation for me.

I would like to thank Prof Klaus Beheng for taking the co-correctorship, for thoroughly reading the thesis, and for his critical questions and comments that immensely helped to improve this thesis.

The PhD-scholarship from the state of Baden-Württemberg and funding from the EU-Integrated Project African Monsoon Multidisciplinary Analyses (AMMA) are acknowledged.

Many thanks go to Jason Dunion and Chris Velden for providing the SAL and TPW imagery. I would like to thank Andreas Schmidt for creating the Meteosat images. Much of the observational data used here was obtained from the AMMA database. Radiosoundings from the stations Bamako, Dakar, Nouakchott, Tombouctou, and Nouadhibou were made available due to the efforts of Jean-Blaise Ngamini and his team at ASECNA.

I am grateful to the Deutscher Wetterdienst for letting me use their COSMO model, and to Heike Vogel and Bernhard Vogel for their kind support with COSMO-ART and their interest in my work.

I am grateful to Leonhard Gantner for assisting with COSMO and to Christian Grams for providing code for the potential temperature budget. This work benefited from discussions with Chris Davis, Patrick Harr, Jean-Philippe Lafore, David Nolan, Frank Roux and Uli Blahak.

Many thanks go to Norbert Kalthoff for taking me to Burkina Faso, Africa, and giving me the chance to experience mesoscale convective systems in the pre-onset phase of the West African monsoon 2006. I had a great time in Dano.

I would like to thank Olgica Birnmeier for her warm encouragements and for being the good soul of the IMK. Many thanks go to Friederike Schönbein for her help with all the administrative work, and to Gerhard Brückel for his support with IT problems and especially data storage problems caused by several terabytes of data generated for this thesis.

I am very much obliged to Sebastian Salopiata for his support, kindness, patience, and knowing so many tricks with InDesign. I am indebted to Leonhard Scheck (a.k.a. H.B. or T.H.) for his technical and general support, and all the encouraging tea hours. I also would like to kindly thank Christian Grams, Tanja Stanelle, Doris Anwender, Julia Keller, and Simon Lang for all their help. Sebastian, Leonhard, Christian, Tanja, Doris, Julia, and Simon I would like to thank you for being tremendously good friends. I also would like to thank everyone at the IMK for creating such a lively and kind atmosphere.